

AD/A-003 305

THE SHOCK AND VIBRATION BULLETIN. PART 4.  
UNDERWATER PROBLEMS, ENVIRONMENTS AND  
MEASUREMENTS

Naval Research Laboratory  
Washington, D. C.

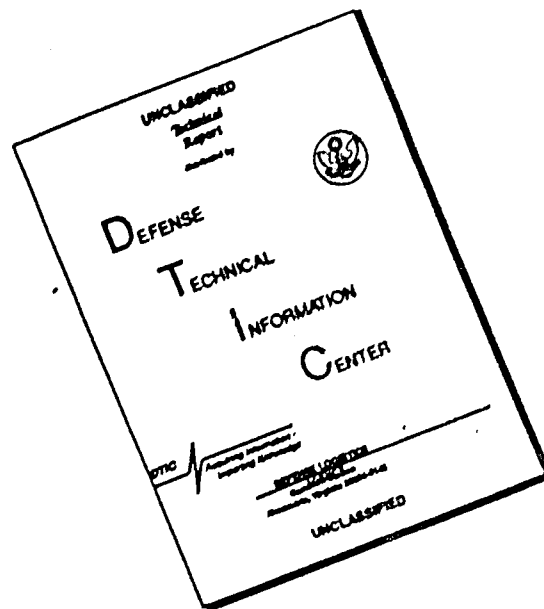
August 1974

DISTRIBUTED BY:

**NTIS**

National Technical Information Service  
U. S. DEPARTMENT OF COMMERCE

# DISCLAIMER NOTICE



THIS DOCUMENT IS BEST QUALITY AVAILABLE. THE COPY FURNISHED TO DTIC CONTAINED A SIGNIFICANT NUMBER OF PAGES WHICH DO NOT REPRODUCE LEGIBLY.

023119

Bulletin 44  
(Part 4 of 5 Parts)

AD A003305

# THE SHOCK AND VIBRATION BULLETIN

Part 4  
Underwater Problems, Environments and Measurements

AUGUST 1974

Reproduced by  
NATIONAL TECHNICAL  
INFORMATION SERVICE  
U S Department of Commerce  
Springfield VA 22151

A Publication of  
THE SHOCK AND VIBRATION  
INFORMATION CENTER  
Naval Research Laboratory, Washington, D.C.

FOR DISSEMINATION PURPOSES ONLY

NOT TO BE USED FOR SALE  
OR DISTRIBUTION

May  
be removed from  
Shock and Vibration Information Center  
Naval Research Laboratory, Code 6020  
Washington, D.C. 20340



DDC  
RECEIVED  
JAN 21 1975  
D

Office of  
The Director of Defense  
Research and Engineering

Approved for public release; distribution unlimited.

#3 - AD - A003304

143

ACCESSION FOR	
NTIS	White Section <input checked="" type="checkbox"/>
DDC	Bull Section <input type="checkbox"/>
UNANNOUNCED	<input type="checkbox"/>
JUSTIFICATION	
BY	
DISTRIBUTION/AVAILABILITY CODES	
Dist.	AVAIL. and SPECIAL
A21	

## SYMPOSIUM MANAGEMENT

### THE SHOCK AND VIBRATION INFORMATION CENTER

Henry C. Pusey, Director  
 Edward H. Schell  
 Rudolph H. Volin  
 J. Gordon Showalter

#### Bulletin Production

Graphic Arts Branch, Technical Information Division,  
 Naval Research Laboratory



**Bulletin 44**  
**(Part 4 of 5 Parts)**

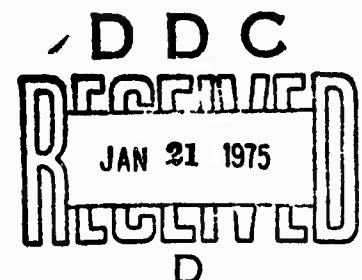
# **THE SHOCK AND VIBRATION BULLETIN**

**AUGUST 1974**

**A Publication of  
THE SHOCK AND VIBRATION  
INFORMATION CENTER  
Naval Research Laboratory, Washington, D.C.**

The 44th Symposium on Shock and Vibration was held at the Rice Hotel and Lyndon B. Johnson Space Center, Houston, Texas on 4-7 December 1973. The National Aeronautics and Space Administration was the host.

**Office of  
The Director of Defense  
Research and Engineering**



# CONTENTS

## PAPERS APPEARING IN PART 4

### Underwater Problems

APPLICATION OF MECHANICAL IMPEDANCE CONCEPTS TO THE COUPLING PROBLEM OF STRUCTURES IN SHOCK ENVIRONMENT .....	1
R. Aquilina and L. Gaudriot, Center D-Etudes et de Recherches Techniques Sous-Marines, Direction Des Constructions Et Armes Navales, Toulon, France	
THE NAVY LARGE FLOATING SHOCK PLATFORM-PART I: PHYSICAL DESCRIPTION AND CAPABILITIES .....	11
C.G. Schrader, West Coast Shock Facility, San Francisco, California	
THE NAVY LARGE FLOATING SHOCK PLATFORM-PART II: SHOCK CHARACTERISTICS .....	13
E.W. Clements, Naval Research Laboratory, Washington, D.C.	
THE EFFECT OF UNIFORM EXTERNAL PRESSURIZATION ON THE DYNAMIC RESPONSE OF ISOTROPIC CYLINDRICAL SHELLS .....	21
F.J. Dzialo, University of Massachusetts, Amherst, Massachusetts	
ON DEFINING TIME DOMAINS FOR RADIATION DAMPING AND ADDED MASS EFFECTS IN FLUID-STRUCTURAL INTERACTION .....	41
A.V. Clark Jr., Naval Research Laboratory, Washington, D.C.	

### Environments and Measurements

HARPOON MISSILE FLIGHT ENVIRONMENTAL MEASUREMENT PROGRAM ..	51
V.S. Noonan, J.L. Gubser and R.D. Harmening, McDonnell Douglas Astro- nautics Company, St. Louis, Missouri	
NARROW BAND TIME HISTORY ANALYSIS OF TRANSPORT AIRCRAFT VIBRATION DATA .....	79
R.E. Thaller and J. Pearson, Air Force Flight Dynamics Laboratory, Wright- Patterson AFB, Ohio	
PRELIMINARY MEASUREMENT AND ANALYSIS OF THE VIBRATION EN- VIRONMENT OF COMMON MOTOR CARRIERS .....	87
W.N. Sharpe, T.J. Kusza, F.W. Sherman and J.W. Goff, School of Packaging, Michigan State University, East Lansing, Michigan	

THE DYNAMIC ENVIRONMENT OF LANDING CRAFT . . . . .	101
M.B. Gens, Sandia Laboratories, Albuquerque, New Mexico	
A RESONANCE-TYPE BACK-TO-BACK CALIBRATOR FOR ACCELEROMETERS .	123
J.A. Macinante, N.H. Clark, B.H. Cresswell, CSIRO, Division of Applied Physics, National Standards Laboratory, Sydney, Australia	
A NEW TRANSVERSE CALIBRATOR FOR ACCELEROMETERS . . . . .	131
J.A. Macinante, N.H. Clark, and B.H. Cresswell, CSIRO, Division of Applied Physics, National Standards Laboratory, Sydney, Australia	

## PAPERS APPEARING IN PART 1

### Summaries of Papers Presented at 44th Symposium

## PAPERS APPEARING IN PART 2

### Invited Papers

#### SPACE SHUTTLE DYNAMICS

Mr. Robert F. Thompson, Manager, Space Shuttle Program, Lyndon B.  
Johnson, Space Center, Houston, Texas

#### VIKING DYNAMICS — AN OVERVIEW

Dr. Richard E. Snyder, NASA Langley Research Center, Hampton, Virginia

#### VIKING ORBITER — DYNAMICS OVERVIEW

Mr. Ben K. Wada, Jet Propulsion Laboratory, Pasadena, California

#### VIKING LANDER DYNAMICS

Mr. Joseph C. Pohlen, Martin Marietta Aerospace, Denver, Colorado

### Structural Dynamics

#### PERFORMANCE OF STATISTICAL ENERGY ANALYSIS

R.F. Davis and D.E. Hines, McDonnell Douglas Astronautics Company,  
Huntington Beach, California

#### PREDICTION OF SHOCK ENVIRONMENTS BY TRANSFER FUNCTION MEASUREMENT TECHNIQUES

G.C. Kao, J.M. Cantril, G.D. Shipway, Wyle Laboratories, Huntsville,  
Alabama, and M.A. Boyd, U.S. Army Corps of Engineers, Huntsville, Alabama

**DETERMINATION OF GUIDEWAY ROUGHNESS FROM CONSTRUCTION  
TOLERANCES**

B.J. Brock, Vought Systems Division LTV Aerospace Corporation,  
Dallas, Texas

**SELECTED SYSTEM MODES USING THE DYNAMIC TRANSFORMATION WITH  
MODAL SYNTHESIS**

E.J. Kuhar, General Electric Company, Philadelphia, Pennsylvania

**STRUCTURAL DYNAMICS COMPUTATIONS USING AN APPROXIMATE  
TRANSFORMATION**

C.S. O'Hearne and J.W. Shipley, Martin Marietta Aerospace, Orlando, Florida

**DETERMINATION OF GUIDEWAY ROUGHNESS FROM CONSTRUCTION  
TOLERANCES**

B.J. Brock, Vought Systems Division LTV Aerospace Corporation,  
Dallas, Texas

**SELECTED SYSTEM MODES USING THE DYNAMIC TRANSFORMATION WITH  
MODAL SYNTHESIS**

E.J. Kuhar, General Electric Company, Philadelphia, Pennsylvania

**STRUCTURAL DYNAMICS COMPUTATIONS USING AN APPROXIMATE  
TRANSFORMATION**

C.S. O'Hearne and J.W. Shipley, Martin Marietta Aerospace, Orlando, Florida

**LINEAR LUMPED-MASS MODELING TECHNIQUES FOR BLAST  
LOADED STRUCTURES**

W.J. Liss, Jr. and N.J. DeCapua, Bell Laboratories, Whippany, New Jersey

**DEVELOPMENT AND CORRELATION: VIKING ORBITER ANALYTICAL  
DYNAMIC MODEL WITH MODAL TEST**

B.K. Wada, J.A. Garba and J.C. Chen, Jet Propulsion Laboratory, Pasadena,  
California

**MODAL TEST RESULTS OF THE VIKING ORBITER**

E.L. Leppert, B.K. Wada, Jet Propulsion Laboratory, Pasadena, California,  
and R. Miyakawa, Martin-Marietta Aerospace, Denver, Colorado (assigned  
to the Jet Propulsion Laboratory)

**IMPLEMENTATION OF INTERACTIVE GRAPHICS TO A TRANSIENT  
RESPONSE RING CODE**

R.W. Buchanan, T.N. Vogel and P.G. Underwood, Lockheed Missiles and  
Space Company, Sunnyvale, California

**COMPUTER GENERATED DISPLAYS OF STRUCTURES IN VIBRATION**

H.N. Christiansen, Brigham Young University, Provo, Utah

**VIBRATION REDUCTION BY USING BOTH THE FINITE ELEMENT STRAIN  
ENERGY DISTRIBUTION AND MOBILITY TECHNIQUES**

J. J. Sciarra, Boeing Vertol Company, Philadelphia, Pennsylvania

**INFLUENCE OF ELASTIC SUPPORTS ON NATURAL FREQUENCIES OF  
CANTILEVER BEAMS**

R.F. Solberg, Jr., Southwest Research Institute, San Antonio, Texas

**PAPERS APPEARING IN PART 3**

**Shock Testing**

**DIGITALLY CONTROLLED TRANSIENT WAVEFORM TESTING —  
ALTERNATE METHOD TO SLOW SINE SWEEP**

B.K. Kim, Jet Propulsion Laboratory, Pasadena, California

**COMPARISON OF SHOCK SPECTRUM TECHNIQUES AND THE METHOD  
OF LEAST FAVORABLE RESPONSE**

A.F. Witte and R.J. Wolf, Kaman Sciences Corporation, Colorado Springs,  
Colorado

**APPLICATION OF LEAST FAVORABLE RESPONSE TECHNIQUES INCORPO-  
RATING FIELD DATA FOURIER TRANSFORM PHASE ANGLE**

R.J. Wolf and A.F. Witte, Kaman Sciences Corporation, Colorado Springs,  
Colorado

**MATCHING SHOCK SPECTRA WITH SUMS OF DECAYING SINUSOIDS COMPEN-  
SATED FOR SHAKER VELOCITY AND DISPLACEMENT LIMITATIONS**

D.O. Smallwood and A.R. Nord, Sandia Laboratories, Albuquerque,  
New Mexico

**A CASE FOR DAMPED OSCILLATORY EXCITATION AS A NATURAL  
PYROTECHNIC SHOCK SIMULATION**

D.B. Nelson and P.H. Prasthofer, Sandia Laboratories, Livermore, California

**DEVELOPMENT OF A PYROTECHNIC SHOCK TEST FACILITY**

D.R. Powers, McDonnell Douglas Astronautics Company, Santa Monica,  
California

**STUDY OF AN EXPERIMENTAL TECHNIQUE FOR APPLICATION TO  
STRUCTURAL DYNAMIC PROBLEMS**

R.F. Snell, McDonnell Douglas Astronautics Company, Huntington Beach,  
California

**TIMewise OUTPUT OF PYROTECHNIC BOLTS**

V.H. Neubert, The Pennsylvania State University, University Park, Pennsylvania  
and R.P. Parker, Uniroyal Research Center, Middlebury, Connecticut

**PYROTECHNIC SHOCK REDUCTION**

S.N. Prescott, Jet Propulsion Laboratory, Pasadena, California

**IMPACT TESTING WITH THE 35-FOOT CENTRIFUGE**

J.V. Otts, Sandia Laboratories, Albuquerque, New Mexico

**FRAGMENT VELOCITIES FROM EXPLODING LIQUID PROPELLANT TANKS**

R.L. Bessey, Southwest Research Institute, San Antonio, Texas

### Shock Analysis

#### PIPING DESIGN FOR HYDRAULIC TRANSIENT PRESSURE

C.C. Huang, R.J. Bradshaw, Jr., U.S. Army Engineer Division, Huntsville, Alabama and H.H. Yen, Sperry-Rand Corporation, Huntsville, Alabama

#### POPPING MOTOR DOME SHOCK DURING FIRST STAGE SEPARATION ON POSEIDON MISSILE FLIGHTS

L.R. Pendleton and R.L. Henrikson, Lockheed Missiles and Space Company, Sunnyvale, California

#### SCALING OF WATER IMPACT DATA FOR SPACE SHUTTLE SOLID ROCKET BOOSTER

R. Madden, H.A. Wright, Bolt Beranek and Newman, Inc., Cambridge, Massachusetts and D.A. Kross, NASA Marshall Space Flight Center, Huntsville, Alabama

### PAPERS APPEARING IN PART 5

### Isolation and Damping

#### DESIGN OF CONSTRAINED LAYER TREATMENTS FOR BROAD TEMPERATURE DAMPING

D.I.G. Jones, Air Force Materials Laboratory, Wright-Patterson AFB, Ohio

#### REDUCTION OF INTERIOR CABIN NOISE LEVELS IN A HELICOPTER THROUGH ADDITIVE DAMPING

J.P. Henderson, Air Force Materials Laboratory, Wright-Patterson AFB, Ohio and A.D. Nashif, University of Dayton, Dayton, Ohio

#### VIBRATION DAMPING AND ISOLATION WITH ENERGY ABSORBING COMPOSITES

J. Nunes, Brunswick Corporation, Skokie, Illinois

#### SUPPRESSION OF TORSIONAL VIBRATION WITH ZERO TORSIONAL STIFFNESS COUPLINGS

J.M. Vance, University of Florida, Gainesville, Florida and R.A. Brown, E.I. du Pont de Nemours and Company, Inc., Wilmington, Delaware

### Vibration Testing and Analysis

#### DEVELOPMENT OF SAM-D MISSILE RANDOM VIBRATION RESPONSE LOADS

P.G. Hahn, Martin Marietta Aerospace, Orlando, Florida

#### EVALUATION OF BLOCKED ACOUSTIC PRESSURE ON STIFFENED CYLINDRICAL SHELLS

V.M. Conticelli, Aeritalia S.p.A., Naples, Italy, and G.C. Kao, Wyle Laboratories, Huntsville, Alabama

**REDUCTION OF HULL NOISE AND VIBRATION BY CENTER OF PERCUSSION  
ROADARM DESIGN**

D.D. Ustick, U.S. Army Tank-Automotive Command, Warren, Michigan

**SYNCHRONIZATION AND PHASE ANGLE OF TWO UNBALANCED ROTORS**

M. Paz, University of Louisville, Louisville, Kentucky, P.H. Schrader and  
R. Blackmon, Vibrating Equipment Division, Rexnord, Inc., Louisville, Kentucky

**EXPERIMENTAL INVESTIGATION OF THE DYNAMIC RESPONSE OF  
CANTILEVER ANTISOTROPIC PLATES**

R.L. Sierakowski, University of Florida, Gainesville, Florida and C.T. Sun,  
Iowa State University, Ames, Iowa

**SPACECRAFT VIBRATION TEST LEVEL COST OPTIMIZATION STUDY**

J.P. Young, NASA Goddard Space Flight Center, Greenbelt, Maryland

**FLIGHT QUALIFICATION OF SPECIAL EQUIPMENT**

J. Pearson and R.E. Thaller, Air Force Flight Dynamics Laboratory, Wright-  
Patterson AFB, Ohio

**THE USE OF LISSAJOUS FIGURES IN VIBRATION TESTING**

J.D. Ray, Memphis State University, Memphis, Tennessee and C.W. Bert,  
University of Oklahoma, Norman, Oklahoma

**STRUCTURAL DYNAMIC RESPONSE ANALYSIS OF ROCKET TEST SLEDS**

T.N. Gardner, Mechanics Research Incorporated, Los Angeles, California

**CONSIDERATION OF THE RESPONSE OF A SLED BORNE MISSILE**

A.R. Glaser, Rockwell International, Columbus, Ohio and L.C. Mixon,  
6585th Test Group, Holloman AFB, New Mexico

**FLOW-INDUCED VIBRATIONS OF A GLASS-REINFORCED PLASTIC  
SONAR DOME**

D.A. King, Rockwell International Corporation, Anaheim, California

**AERO-ACOUSTIC ENVIRONMENT OF A RECTANGULAR CAVITY WITH A  
LENGTH TO DEPTH RATIO OF FOUR**

L.L. Shaw and D.L. Smith, Air Force Flight Dynamics Laboratory, Wright-  
Patterson AFB, Ohio

**RESPONSE OF LINEAR DYNAMICAL SYSTEMS UNDER NONSTATIONARY  
RANDOM EXCITATIONS**

T.S. Sankar and D. Doan, Sir George Williams University, Montreal, Canada

**MEANS OF CONTROLLING THE DYNAMIC MOTION OF BOTTOM MOORED  
MINE CASES EXPOSED TO HIGH CURRENT**

J.J. O'Neill, J. Berezow and J.E. Goeller, Naval Ordnance Laboratory, Silver  
Spring, Maryland

# UNDERWATER PROBLEMS

## APPLICATION OF MECHANICAL IMPEDANCE CONCEPTS TO THE COUPLING PROBLEM OF STRUCTURES IN SHOCK ENVIRONMENT

Robert AQUILINA  
Centre d'Etudes et Recherches Techniques Sous-Marines  
DIRECTION DES CONSTRUCTIONS ET ARMES NAVALES  
TOULON, FRANCE

Lionel GAUDRIOT  
Société METRAVIB  
LYON, FRANCE

The paper describes a tentative approach to the problem of hull-equipment interaction in an under water shock environment, by the way of mechanical impedance techniques. Two different methods are used to analyse point impedance of submarine hulls, by sinusoidal and transient excitation. Measurements give a spring-like behaviour of the hull in the frequency range of interest for rigidly fixed equipments. Underwater shock experiments on a shock test section have confirmed this result. However this description is not sufficient. The hypothesis of a viscous damper-like behaviour of the hull at higher frequencies is invoked to account for the phenomena that are observed during the first while of the shock response.

### 1 - INTRODUCTION

A research program has been undertaken these last years by the French Navy to improve its knowledge of the shock environment of submarine equipments. The purpose is to work up better methods for shock resistance design and particularly to obtain better shock input values. Such a process has been made possible by improvements in shock measurements techniques and in analysis of the dynamic behaviour of structures.

The amount of work devoted to these problems has not permitted to develop an extensive program of full scale experiments and thus has induced us to concentrate on a more fundamental aspect of the dynamic interaction phenomena between the hull and the supported equipments. Though we are conscious, from the experience of other Navies, that this procedure is quite less sure, nevertheless we hope that we shall get a very useful understanding of the basic principles. Obviously the risk is eventually to get unable to process a too much sophisticated information.

Our first approach of the interaction phenomena is concerned with the case of medium weight equipments (up to a few tons) fixed to the hull through sufficiently stiff supports (rubber mounts being excluded).

The problem is considered under following aspects :

- Impedance characterization of the hull at the fixture points,
- Modal identification of fixed-base equipment,
- Mechanical coupling between the two connected parts.
- Determination of shock input signals in unloaded hull condition.

The study is conducted in an experimental way by various dynamical analysis techniques on one hand, and by underwater explosions in a full scale submarine test section on the other.

To validate the hypothesis of our approach resulting from dynamical analysis of hull and equipment, we have extracted the major part of the useful information directly from the time history of the signals recorded during shock tests. So we have been brought to improve significantly our various filtering methods in the frequency and also in the space domains and we have consequently fully realized up to what point the philosophy of some shock measurements specialists of US NAVY was pertinent.



The work is now in progress. First results have made it possible to point out some simple ideas that we are going to present ; many questions remain yet.

## II - POINT IMPEDANCE OF THE HULL

Point impedance measurements have been made on the hull of the submarine section. This experimental facility consists in the full scale section of a conventional submarine (diameter : 5 m, length : 16 m). The hull was immersed up to the level of the hatch and the flotation tanks were full of water.

Two types of excitation of the hull have been used :

- Sinusoidal force signal provided by an electrodynamic shaker of limited strength (200 N) (Figure 1).

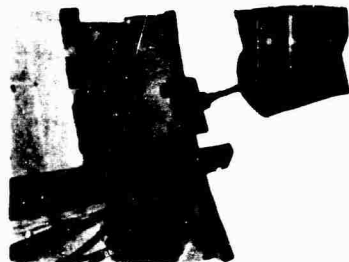


Fig. 1a - Sinusoidal Excitation of Hull



Fig. 1b - Sinusoidal Excitation of a Rigidly fixed Mass

- Shock impulse force supplied by the percussion of an anvil spring device fastened to the hull, by a guided drop mass (Figure 2). In this case, the impedance is obtained by a FOURIER ana-

lysis of the transient signals : force and acceleration. Results are displayed on following diagrams for the case of an exciting force normal to rib, 45° downward, in the middle of the immersed section.

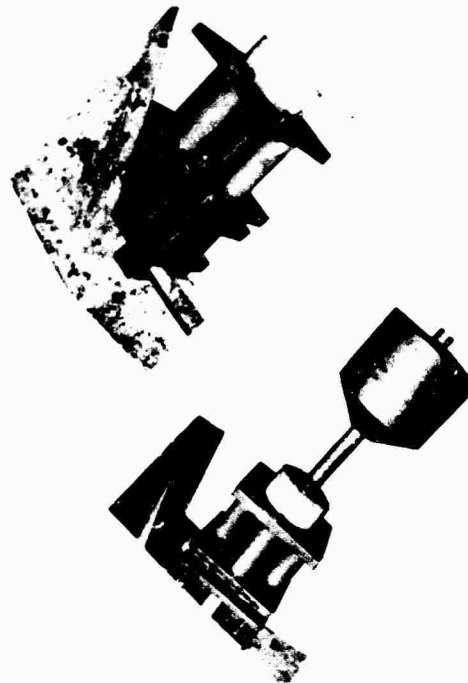


Fig. 2 - Transient Excitation of Hull

- Figure 3 shows the force, acceleration and displacement signals delivered by piezoelectric force and acceleration transducers. It immediately appears that the displacement is roughly proportional to the force. So in the frequency range of interest the hull has a spring like behaviour. After the first pulse, a low frequency oscillation (a few Hz) is occurring in the displacement signal. It tends to confuse with the erroneous integration of the piezoelectric transducer noise. That low frequency behaviour has been analysed with other kinds of transducers : piezoresistive and servo accelerometers.

The FOURIER analysis of the signals has allowed to assess the accuracy of these first conclusions. On Figure 4a we can see the compliance function computed with an FFT algorithm of 1024 points. This compliance is rather complex in its details but the spring-like behaviour is easily pointed out again at medium frequency.

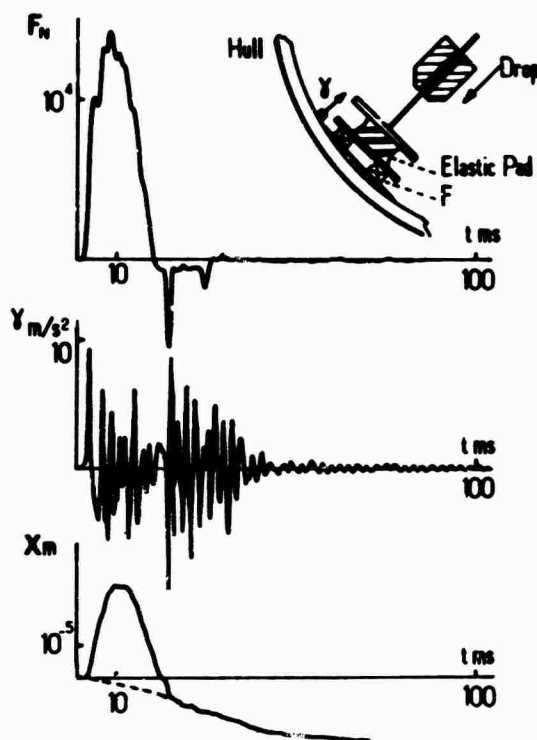


Fig. 3 - Shock excitation of Hull  
Time signals

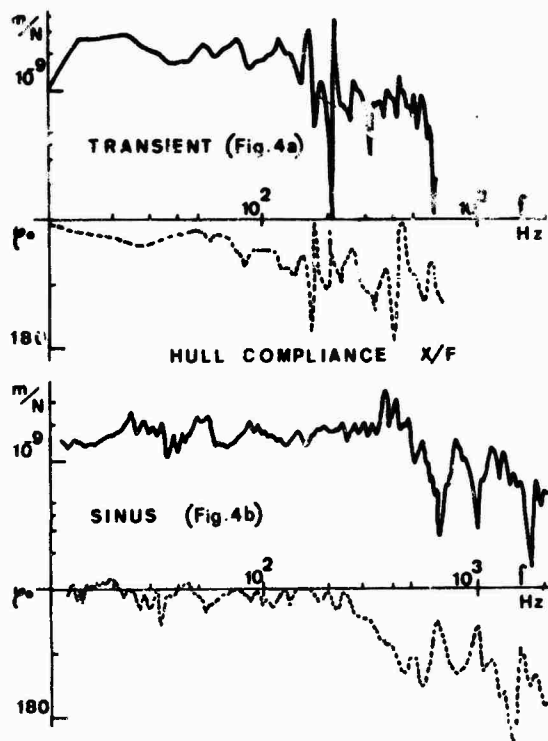


Fig. 4 - Point Impedance of Hull  
Shock and Sinusoidal Excitation

The Figure 4b gives the compliance function measured at a similar point under a sinusoidal excitation by the usual techniques of mechanical impedance. The results are in agreement with the preceding ones. We notice a resonance tendency around the hoop frequency of the hull. Above that frequency, the compliance can be considered as resulting from the cumulative effects of a lot of higher frequencies modes. The average behaviour is to be related to the point impedance of an equivalent infinite plate which is known as being real. So the global behaviour of the hull on that range of frequency may be roughly described by a viscous damper.

An additional verification of the actual existence of the medium frequency stiffness has been carried out by loading the hull with a rigidly secured mass of 2.5 t and by measuring the resonance frequencies of the system. Results have credited the value of the stiffness previously estimated (Fig. 5).

From another point of view, we have found out, by measuring again the compliance of the hull in the vicinity of the fixture points of the mass, that this function is quite similar to that in unloaded conditions (Fig. 5). So the input impedance of the hull may be considered as being quite independant of the near supported equipments.

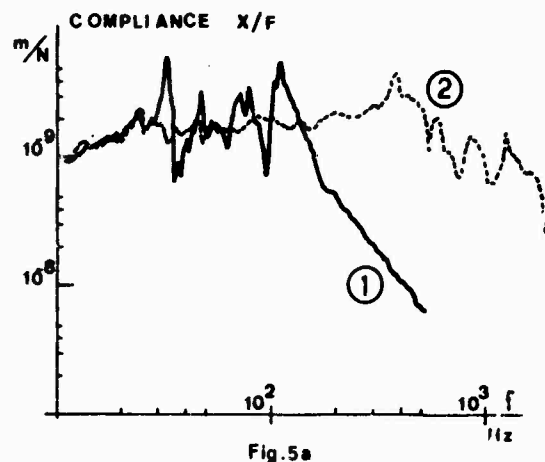


Fig. 5a

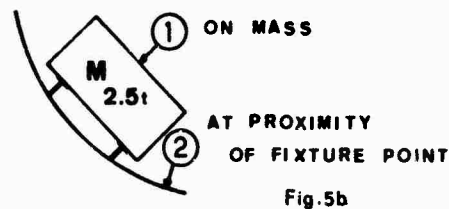


Fig. 5b

Fig. 5 - Point Impedance of Hull  
Influence of Loading Mass

Presently, similar tests are undertaken in different types of French submarines. Measurements are extended to the low frequency range with percussion excitation.

### III - MODAL IDENTIFICATION OF THE FIXED BASE EQUIPMENT

The choice of the fixed base modal description of equipments has been made by the US Navy many years ago. We have adopted this point of view. The main advantage in our sense is that this description fits well with the calculation of the response to a given input shock motion of translation of the base. It is suited also to formulate the equipment-hull dynamical interaction on the basis of the measured hull compliance matrix.

In the case of a base of limited dimensions, the modal fixed base parameters may be determined experimentally. The base is materialized by the table of an electro-dynamical shaker, the equipment being secured to it through force transducers, the signals of which are summed up to get the resultant force. The modal parameters: frequency, modal mass, damping factor are obtained from the mass apparent function by an identification process (Fig. 6a). Transfer functions displacement/force and strain/force are measured simultaneously in order to give the modal shapes and modal particular strains by the same separation procedure.

Such a technique succeeded when applied to light-weight models of structures (Fig. 6b) and can be extended easily to medium weight equipments (1 t). Presently, we are rather oriented to perform the same analysis by shock techniques by fixing the equipment on the anvil of a shock machine and making a FOURIER analysis of the transient wave to get the related transfer functions.

Medium weight shock machines are so able to accommodate equipments of up to 3 t weight. For heavier ones it seems to us that the measurements must be made in situ, by point impedance of the equipment fixed to a submarine hull, the fixed base hypothesis being of quite less a value in such a case.

An important limit to these general principles of description and analysis of the dynamics of equipment is their non linear behaviour which we often met with at high level of excitation.

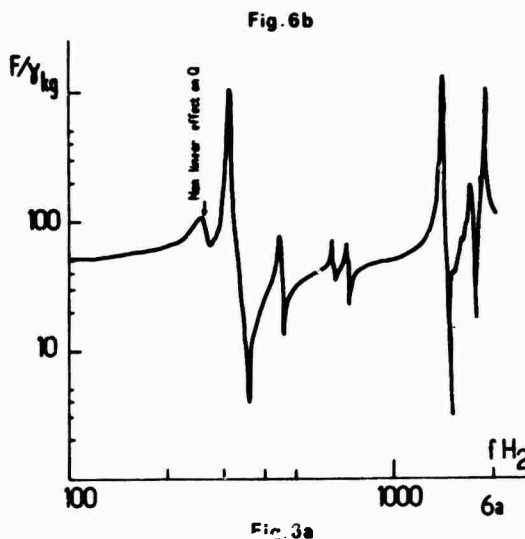
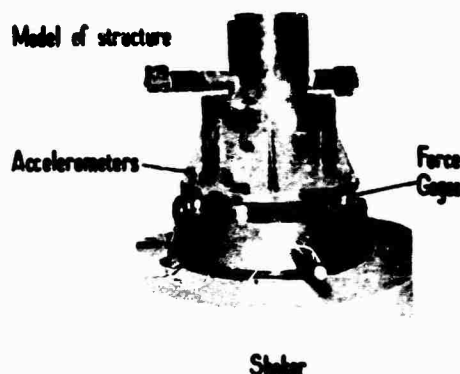


Fig. 6 - Fixed base impedance measurement on Electro-dynamical shaker

### IV - INTERACTION WITH HEAVY OSCILLATORS

#### 1) Coupling with a single oscillator

As the spring-like behaviour of the hull corresponds to the frequency range of fixed base first resonances of equipments we are dealing with, we consider in a first step the simplified following linear model of interaction (Fig. 7a) with an SDOF oscillator.

$\gamma_o(t)$ ,  $V_o(t)$  are then the shock motions that can be measured at the fixture points in unloaded conditions. With a loading oscillator of mass  $M$  and natural frequency  $\omega_1$ , the FOURIER transform of the acceleration  $\gamma(t)$  is :

$$\gamma(\omega) = \frac{\omega_o^2}{\omega_o^2 - \omega^2} \gamma_o(\omega)$$

with

$$\omega_o^2 = \frac{K \omega_1^2}{K + M \omega_1^2}$$

or with non dimensional frequency parameters :

$$\Omega_1 = \omega_1 (M/K)^{1/2}$$

$$\gamma(\Omega) = \gamma_o(\Omega) \frac{\Omega_o^2}{\Omega_o^2 - \Omega^2}$$

with  $\Omega_o^2 = \frac{\Omega_1^2}{1 + \Omega_1^2} \quad (1)$

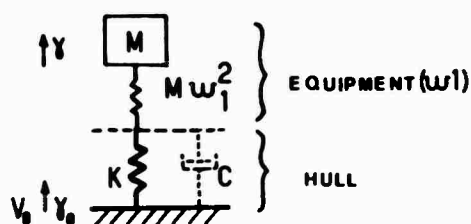


Fig. 7a

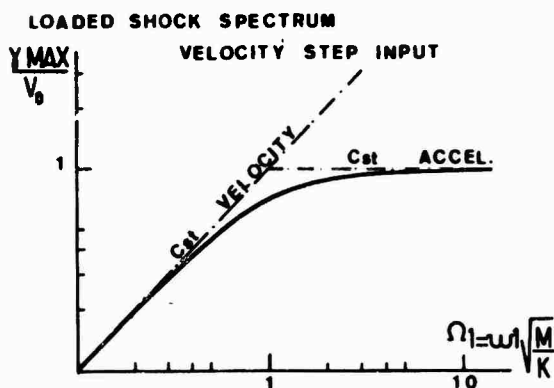


Fig. 7b

Fig. 7 - Coupling with Heavy SDOF Spring Effect

The right-hand member of the equation is the response of an unloading oscillator of frequency  $\Omega_o$ . The loaded case can be deduced from it by the frequency transform (1). With a unit step velocity  $V_o H(t)$  the acceleration shock spectrum is : (Fig. 7b).

$$\frac{\gamma_{MAX}(\theta)}{V_o} = \Omega_o = \left( \frac{\Omega_1^2}{\Omega_1^2 + 1} \right)^{1/2}$$

For a practical use with a definite hull stiffness  $K$ , we obtain a Design Shock Spectrum to the following example (Fig. 8).

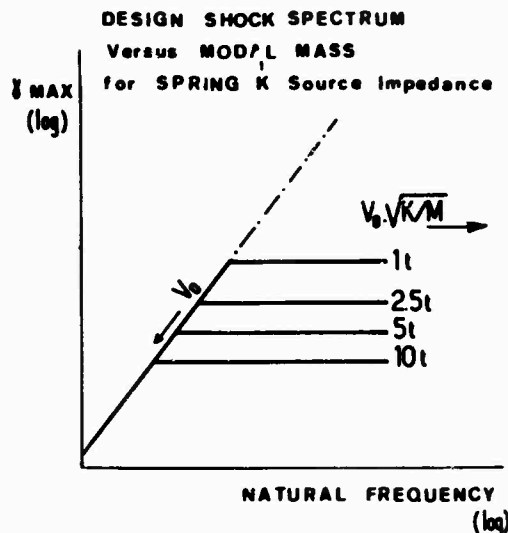
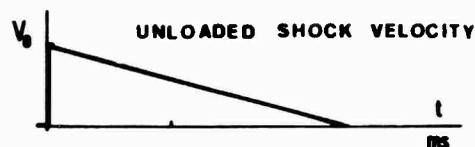


Fig. 8 - Design Shock Spectrum for Underwater Explosion

At low frequencies, the spectrum design value is equal to  $V_o$ . At high frequencies, the limit acceleration value is  $V_o \sqrt{\frac{K}{M}}$ .

The shapes and values obtained in that manner are close to the shock standards used by Navies of several nations.

If we admit that for higher frequencies the impedance of the hull tends to be equivalent to that of a viscous damper of coefficient  $C$  ( $\omega \gg \frac{K}{C}$ ), the model turns to be : (Fig. 9a).

The transfer function is :

$$\gamma(\omega) = \gamma_o(\omega) \frac{1}{1 + j \frac{M}{C} \omega - \frac{\omega^2}{\omega_1^2}}$$

With a velocity step input  $V_o H(t)$  the shock spectrum of the loaded acceleration has the following shape (Fig. 9b).

This simplified description of the two principal effects of the hull impedance shows how the Design Shock Spectrum may be modified according to the relative values of the characteristic frequencies  $\sqrt{\frac{K}{M}}$  and  $\frac{C}{M}$ , compared with the transition frequency  $\frac{C}{M}$ . When these phenomena are not sufficiently separated, it seems better to compute directly the response of the system with the complete model.

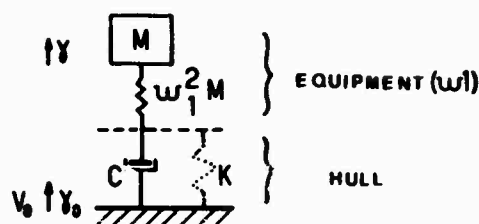


Fig. 9a

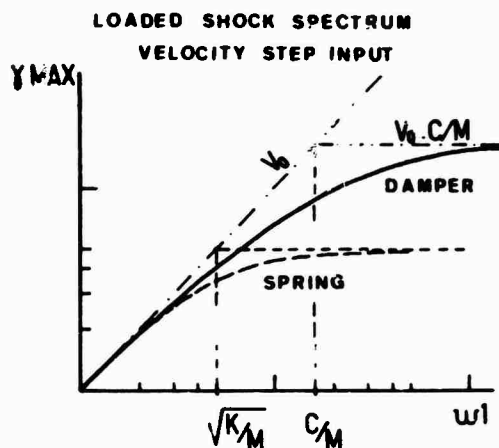


Fig. 9b

Fig. 9 - Coupling with Heavy SDOF  
Damping Effect

## 2) Coupling with a multi-degree of freedom system

In a simplified approach, we consider a system with a predominant mode loading the hull, the other ones having negligible reaction effects at the fixture level. We consider then the shock spectrum of the acceleration  $\gamma_n(t)$ .

For a velocity step  $V_0 H(t)$  the velocity  $V_0(t)$  has the following shape : (Fig. 10a).

$$V_0(\theta) = V_0 H(\theta) \left[ 1 - \Omega_0^2 \cos(\Omega_0 \theta) \right]$$

$$\Omega_0^2 = \frac{\Omega_1^2}{1 + \Omega_1^2} \quad \text{and} \quad \theta = t \sqrt{\frac{K}{M}}$$

$$\gamma_n(\theta) = V_0 H(\theta) \left[ \delta(\theta) (1 - \Omega_0^2) + \Omega_0^3 \sin(\Omega_0 \theta) \right]$$

We are induced to define the stock spectrum of  $\gamma_n(\theta)$ .

We calculate :

$$\gamma_n(\theta) = \frac{\Omega_n}{\Omega_n^2 - \Omega_0^2} \left\{ \left[ \Omega_n^2 (1 - \Omega_0^2) - \Omega_0^2 \right] \sin(\Omega_n \theta) + \Omega_0^3 \Omega_n \sin(\Omega_0 \theta) \right\} H(\theta) V_0 \quad (2)$$

A conservative evaluation of  $\gamma_n \text{ MAX}(\Omega_n)$  consists in the sum of the maximal absolute values of the two terms in the right-hand member of (2). The related shock spectra are given on figure 10b.

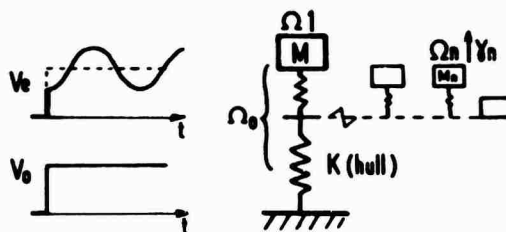


Fig. 10a

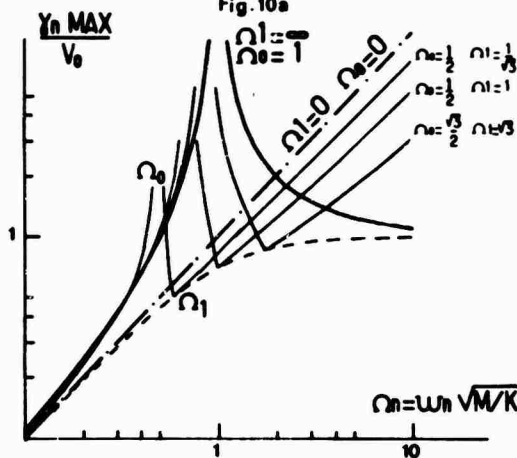


Fig. 10b

Fig. 10 - Shock Spectrum at fixture point  
of a loading SDOF

We can notice from it that :

- if  $\Omega_n \ll \Omega_0$  the same velocity step spectrum is preserved,
- if  $\Omega_n = \Omega_0$  the oscillator is excited at resonance,
- if  $\Omega_n = \Omega_1$  the shock spectrum value is that defined for the prevailing mode,
- if  $\Omega_n \gg \Omega_1$  the spectrum tends toward a reduced velocity step spectrum :

$$V_0 (1 - \Omega_0^2) = V_0 \left( \frac{1}{1 + \Omega_1^2} \right)$$

For either case :  $\Omega_n \ll \Omega_0$  or  $\Omega_n \gg \Omega_1$ , it is possible under certain conditions to take into account the loading effects of secondary modes on the source impedance (stiffness  $K$  and stiffness  $K$  in parallel with stiffness  $M \omega_1^2$ ), by a procedure similar to that described before.

In the most general case, the interactions between the modes through the hull impedance must be taken into account, it is then necessary to set in action analytical procedures in order to obtain modal responses.

For this purpose, we have chosen the FOURIER technique. The transfer functions of the whole system are calculated and give the possibility to obtain the responses to a given input signal by FFT Algorithm.

The figure 11 shows the velocity response of the three modes system (Fig. 11a) to the "vertical rise triangular" velocity input.

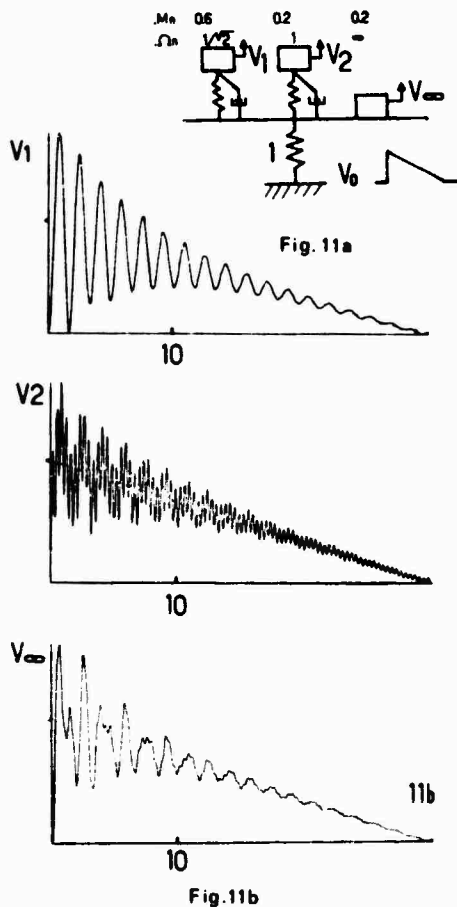


Fig. 11 - Velocity response of a three-modes System by FFT algorithm

## V - EXPERIMENTS IN SHOCK ENVIRONMENT

### 1) Measurements

The problem of shock measurements is known to be a difficult one. The difficulties are due to the severity of the severity of the transducers mechanical environment, and to the need to discriminate the useful part of the information among predominant erroneous or non significant signals. So the measurement system must be organized specifically for each specific case with a complementary use of the following transducers and signal processing techniques :

- Piezoresistive accelerometers rather than piezoelectric ones in order to avoid shift and low frequency cut off problems,
- Mechanical filters to protect the transducer and to be adapted to the frequency range of interest,
- Spatial filtering by mixing of several transducers to point out some particular ensemble effects,
- Use of strain gauges, and force transducers at fixture, to identify the shock input motion in its effects,
- Time history signal processing with filtering techniques to separate modal responses and with integration to obtain velocity information,
- Shock spectrum analysis of the signal previously conditioned by the mentioned method.

### 2) Unloaded shock characteristics

Unloaded shock spectra have been acquired by various experiments with underwater explosions in our shock test section. They assume a constant velocity shape in frequency range from a few Hz to a few kHz as it is usually accepted.

The analysis of the integrated acceleration signal has confirmed that fact and led us to admit that the shock input is an approximate velocity step with a short rise time ( $< 0.5$  ms) and a long decay time (Fig. 8).

### 3) Experimental investigation of coupling effect

Experiments have been made with a heavy loading mass (a few tonnes), and various fixture conditions. We describe one of them which is quite significant of the hull behaviour.

A 2.5 t mass is fastened to the hull through a very stiff seating (Fig. 12a). According to the presented model of the hull, the equivalent diagram is (Fig. 12b).

Acceleration and velocity measured at the top of the mass are plotted on Figure 12c. The velocity is oscillating around the step input  $V_0$  with two periods relative to two successive phases of the phenomena.

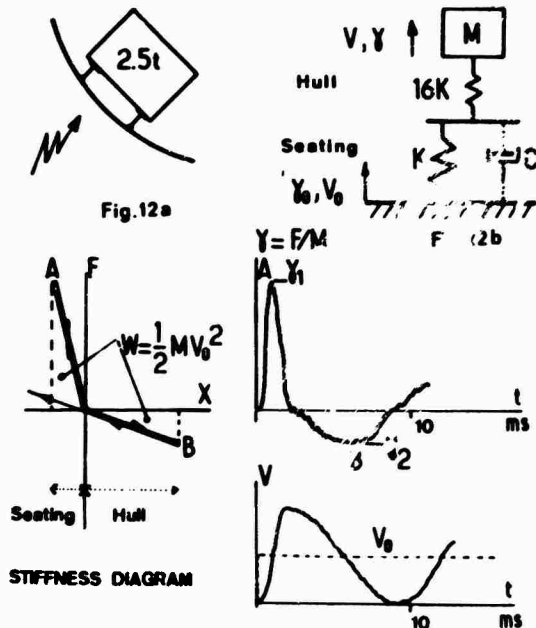


Fig. 12c

Fig. 12 - Underwater Explosion  
Experimental Results on 2.5 t Mass (Rigid Mount)

In the first milliseconds, the velocity step is directly transferred through the equivalent viscous damper  $C$  to the oscillating system:  $M$ ,  $16K$  and the resulting maximal acceleration is  $\gamma_1 = V_0 \sqrt{\frac{16K}{M}}$ ,

Then the mass oscillates on the two springs in series ( $\neq K$ ) and the acceleration is  $\gamma_2 = -V_0 \sqrt{\frac{K}{M}}$ .

Thus we are induced to take into account successively two aspects of the impedance which bring about two quite different values of the acceleration in opposite directions.

The viscous damper is considered as active during the little while when the hull acts like an infinite plate.

When the boundary effects take place due to reflection and propagation around the cylinder, the behaviour of the hull turns to be that of a simple spring.

With this hypothesis, the duration of the damper effect might be estimated to be equal to

a characteristic propagation delay of the elastic waves of the order of the hoop mode period.

Such an experiment gives another possibility to validate the measured values of  $K$  et  $C$ .

This case can be reasoned by using energy transfer concepts. In the first phase, the energy  $\frac{1}{2}MV_0^2 = \frac{1}{2}M^2V_0^2 \frac{1}{16K}$  is transferred from the stiffness  $16K$  to the mass. In the second phase this kinetic energy is transferred back from the mass to the stiffness  $K$ :  $\frac{1}{2}MV_0^2 = \frac{1}{2} \frac{M^2V_0^2}{K}$  (Fig. 12).

From accelerations  $\gamma_1$  and  $\gamma_2$  it is then possible to deduce the reaction forces at the fixture point.

This way of reasoning is suited to non linear stiffness behaviour as in the following experiment (Fig. 13a).

The same mass is fastened to its seating with Belleville springs. The acceleration and velocity signals (Fig. 13b) show the successive actions of variable stiffness in series. Each time the acceleration  $\gamma(t)$  (or the transmitted force) is controlled by the most flexible spring in operation.

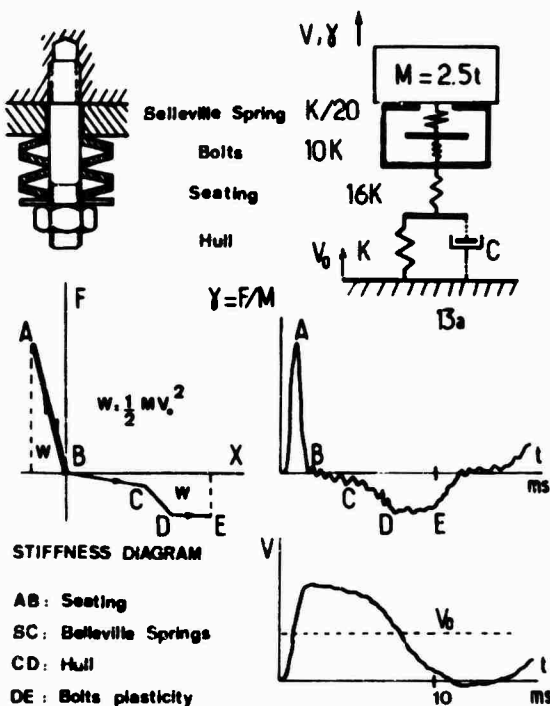


Fig. 13b

Fig. 13 - Underwater Explosion  
Experimental Results  
on 2.5 t Mass (Non Linear Mount)

Energy transfer calculation makes it possible to access the stress level which is reached in every part of the fixture system including the region of plasticity.

## VI - CONCLUSION

The results that have been described are concerned with a limited number of experimental configurations. However they already allow us to obtain a first view of the hull-equipment behaviour, in a certain range of mass and resonant frequencies.

Mechanical impedance techniques have shown a spring-like behaviour of the point impedance of the hull in the frequency range of interest for rigidly fixed equipments. Underwater shock experiments on a shock test section have confirmed this result.

This first view incites us to deal with the time input velocity signals as basic data for analysing the interaction phenomena. The resulting Design Shock Spectra are close to the values and shapes commonly used.

However, this description is not wholly convenient. The hypothesis of a viscous damper-like behaviour of the hull at higher frequencies is invoked to account for the phenomena that are observed during the first while of the shock response.

The damping effect has been related to the characteristic impedance of an equivalent infinite plate. So, that temporary effect exists until reactive behaviour takes place, after propagation and reflections of elastic waves.

This interpretation is quite incomplete and does not account for the effect of water on impedance and water-cavitation. These phenomena would have to be investigated. Simulations on hull models under water and in air may bring out the predominant influence of hull or water on the source impedance, and ascertain the origin of its stiffness-damper aspect.



The Navy Large Floating Shock Platform  
Part 1: Physical Description and Capabilities

C.G. Schrader  
West Coast Shock Facility  
San Francisco, California

Equipment to be installed on Navy ships must be tested and/or designed to meet Navy shock specification standards. The previous capability for direct testing extended to items weighing 40,000/60,000 lb. The Large Floating Shock Platform has now been constructed and calibrated, and its shock characteristics are compatible with those of the previously existing test devices. Direct-testing capability for shipboard shock can now be extended to items weighing some 400,000 lb.

**BACKGROUND**

The Navy requires that equipments intended for shipboard use be shock tested, if possible, to the specifications of MIL-S-901. The testing machines specified in the current version of MIL-S-901 are capable of accommodating test loads of up to 60,000 lb.

In 1969 the West Coast Shock Facility, San Francisco, California was tasked by the Naval Research Laboratory, Washington, D.C. to conduct a conceptual study for a Large Floating Shock Platform (LFSP) which would be capable of shock testing loads of 60,000 to 320,000 lb. This study indicated that if the LFSP were to be designed as a scaled-up version of the Floating Shock Platform (FSP), some economies would have to be made. These were accomplished by changing the steel from HY 80 to HTS and bottom structure from an inner deck to open framing.

In 1971, WCSF was tasked by Naval Ship Systems Command (as part of Operation DIVE UNDER, Phase II) to prepare contract plans and specifications. The LFSP was built in accordance with these and was delivered to WCSF in February 1973.

**DESCRIPTION**

The LFSP is a rectangular, flat-bottomed barge 50 ft long by 30 ft beam (Fig. 1). The sides and ends are shock-resistant to a height of 12 ft above the bottom, and are continued a further 6 ft in height by a lighter bulwark. The shock-resistant bottom, sides and ends are constructed of 1-1/2" HTS plate strongly reinforced with gussets and stiffeners; the bulwarks are 3/8" HTS plate. The bottom 3 ft of the LFSP is occupied by an egg-crate arrangement of longitudinal and athwartship



Fig. 1 - The Large Floating Shock Platform

stiffeners with cell size of approximately 4 ft square. The upper edges of these stiffeners are capped by flanges 8 in. wide x 3 in. thick, forming a mounting plane to which the test load is attached by a suitable foundation structure. The LFSP is covered by a three section canopy 18 ft high at its center. The maximum overall dimensions of test items which can be accommodated are 46 ft x 26 ft x 32 ft high, although for higher items a special cover could be fitted instead of the standard canopy. Empty, the LFSP draws 62 in; with an added load of 500,000 lb, the draft would increase to about 124", leaving a freeboard of 20 in. on the

shock-resistant sides. With allowance for fixturing, this implies that test items weighing up to 400,000 lb can be handled provided the weight distribution of the installation satisfies stability requirements.

Figure 2 shows the Floating Shock Platform (FSP) installed in the LFSP as a calibration test load. The FSP is 28 ft x 16 ft x 10 ft high.

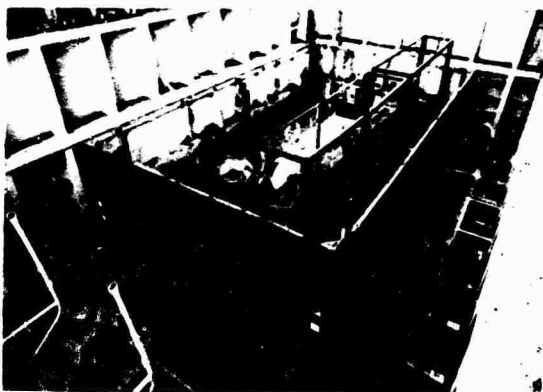


Fig. 2 - FSP installed as test load

Figure 3 shows a close-up of one of the three mounting plates forming the foundation for the FSP.

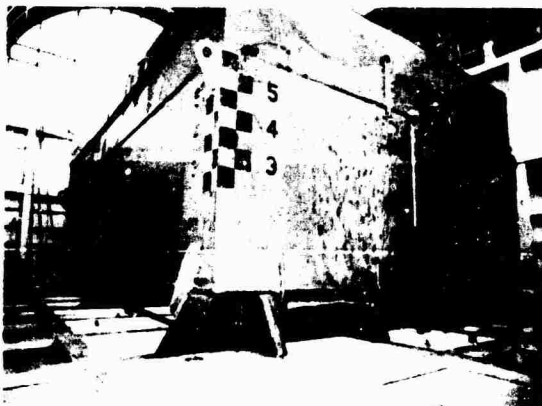


Fig. 3 - Mounting plate detail

The shock environment on board the LFSP is developed by detonating a 300 lb charge at a depth of 20 ft a selected distance from it. The size and depth of the charge, and the location of the test site, are chosen to minimize disturbance to the surroundings. The charge parameters result in venting of the bubble on its first expansion, preventing interaction of its pulsations with the bottom. The test is conducted with the LFSP at a distance of 900 ft from the nearest structure, the pier which serves as the base for the test operation and on which the test control station is located. The geometry of the test array is tightly controlled. The position of the LFSP is fixed by an LCM tensioning through an outhaul line against a hold-back line from the LFSP to the pier. The charge location is fixed relative to the LFSP by a small boat tensioning through a charge-outhaul line against a standoff bridle from the charge float to the LFSP. Following the test, the LFSP is winched back to the pier by a retrieval line, with assistance from the LCM. In addition to the LCM and the small boat which handles the charge-outhaul line, a sonar boat is employed to patrol the test area as a precaution against fish-kills, and a Yard tug stands by to assist in case of emergency.

Operational procedures are described in detail in Reference (1).

#### CONCLUSION

A calibration test series of fourteen shots was completed during May 1973. No substantial difficulties were encountered in operations as outlined above, and test results indicate that the LFSP will not be affected structurally by repeated tests at the probable specification severities.

This work was sponsored by Naval Ship Systems Command under Element 63714, Project S4815.

#### REFERENCE:

1. "Operation Manual for Large Floating Shock Platform (LFSP)" NAVSHIPYD HUNTERS PT Technical Report 10-73 of July 1973.

## The Navy Large Floating Shock Platform

### Part II: Shock Characteristics

E.W. Clements  
Naval Research Laboratory  
Washington, D.C.

Equipment to be installed on Navy ships must be tested and/or designed to meet Navy shock specification standards. The previous capability for direct testing extended to items weighing 40,000/60,000 lb. The Large Floating Shock Platform has now been constructed and calibrated, and its shock characteristics are compatible with those of the previously existing test devices. Direct-testing capability for shipboard shock can now be extended to items weighing some 400,000 lb.

#### BACKGROUND

In order to maximize the combat effectiveness of its ships the Navy requires that shipboard equipment be designed to resist the damaging effects of shock caused by the explosion of enemy weapons, and be tested (if possible) by exposure to shock similar to this before acceptance. It is thus necessary to have a means for generating controlled shock environments similar to those found on shipboard; this is needed both for acceptance testing and to provide a tool for design and development. The Navy has such a means in the family of machines specified in MIL-S-901 for acceptance testing. This family is comprised of the Lightweight Shock Machine (for loads up to 400 lb), the Mediumweight Shock Machine (250-6000 lb) and the Floating Shock Platform (6000-60,000 lb). Those machines have little in common in design or operation, but are highly compatible in the shock environments they provide to their test loads. They have now been joined by the Large Floating Shock Platform (LFSP), which has a test load capacity of up to 400,000 lb.

#### CALIBRATION TEST SERIES

The LFSP, described in Part I of this paper, was subjected to an eight-shot calibration test series in May 1973. This was preceded by a preliminary series of six shots in March 1973, shortly after the LFSP was delivered to the West Coast Shock Facility (WCSF). Both series were performed by personnel from WCSF and the Naval Research Laboratory (NRL), Washington, D.C.

The first series was conducted against the empty LFSP; following this, a Floating Shock

Platform (FSP) was installed in the LFSP as a test load. Four shots of the second series were fired against the LFSP with this load condition, the inner bottom of the FSP was filled with water to increase the load, and the final four shots were fired.

The charge size for all shots was 300 lb, and the charge depth 20 feet. These parameters were partially set by geographical considerations, e.g., the depth of water available and the proximity of buildings, etc. With charges of this size and depth the bubble vented on the first expansion. The gross displacement of the LFSP is thus much smaller than that of the FSP, since it is due to the shock wave rather than to riding the water displaced by the bubble. The primary control variable for operation of the LFSP is the charge standoff, the horizontal distance between the position of the charge and the closest point of the LFSP. The secondary control variable is the charge orientation, i.e., whether it is closest to a side or an end of the LFSP. The major effect of standoff is to control the severity of the shock produced, that of orientation to change the relative severity of its components in the athwartship and fore-and-aft directions. The standoff was varied from 120 feet to 45 feet. Charges were fired against both sides and both ends with no added load in the LFSP and against the port side and stern with added load. Details of the shot geometries are given in Table I.

Table I  
LFSP Calibration Test  
Shot Schedule

Shot No.	Date 1973	Near Side	Standoff ft	Added Load klb
1	28 Feb	Port	70	0
2	1 Mar	Port	55	0
3	2 Mar	Port	45	0
4	5 Mar	Stern	45	0
5	6 Mar	Starboard	45	0
6	7 Mar	Bow	45	0
7	7 May	Port	120	112.6
8	9 May	Port	70	112.6
9	10 May	Port	45	112.6
10	16 May	Stern	45	112.6
11	17 May	Port	70	176.9
12	18 May	Port	45	176.9
13	22 May	Port	45	176.9
14	23 May	Stern	45	176.9

#### TEST LOAD

The FSP employed as a test load was connected to the LFSP mounting plane by three edgewise plates running athwartships, one near each end and one amidships. Shock-protected racks within the FSP contained recorders, instrumentation components and firing control circuitry. Also within the FSP was a concentrically mounted single-degree-of-freedom (SDOF) system, a 5,000-lb concrete block supported by an elaborate spring system. This was designed some years ago by NSRDC for another project, and its only important mode was that of simple vertical translation at a fixed base frequency of 30 Hz. The total weight added to the LFSP was 112.6K lb, increased to 176.9K lb later by filling the FSP inner bottom with water. The mounting system was extremely stiff; even with these large weights the translation frequencies of the total mass lumped on the total spring of the plates would be about 300 Hz and 240 Hz. The behavior of the sdoof should thus be essentially the same as if it had been attached directly to the LFSP.

#### INSTRUMENTATION

For the first series of tests, transducers were installed to measure velocity at five locations on the LFSP bottom. These transducers were accelerometers in a shock-mitigating housing with integrating electronics. For the second series of tests more of these transducers were added on the LFSP mounting plane at the base of the FSP mounting plates and within the FSP. Strain gages were installed on the LFSP shell plating at its mid-section and on its central athwartship stiffener. The output signals were recorded on magnetic tape. After each shot the tapes were played back through an

integrator on a string oscillograph providing a strip recording of velocity and displacement vs. time for each velocity transducer, and strain versus time for each strain gage. A few of the velocity records were also fed into an analog shock spectrum analyzer.

#### LFSP VELOCITIES

The waveforms of velocities measured in the LFSP are affected principally by the location and orientation of the measurement. The magnitude of the velocity (in a given direction) decreases as the distance between the point of measurement and the charge increases. This gives a general increase in velocity as the charge standoff is reduced, and also a considerable variation in the velocities measured throughout the LFSP for a given shot. The shapes of the waveforms are mainly determined by the orientation of the measurement. Those in the vertical and horizontal-parallel\* directions have sharp rises (~ 1 ms) and gradual declines (~ 50 ms) accompanied by structure-related frequencies up to ~ 1 KHz. The horizontal-transverse† velocities consist of the structural frequencies amplitude-modulated by a

\* The horizontal-parallel direction is the horizontal direction parallel to the line from the plan position of the charge to the nearest point of the LFSP, i.e., athwartship for a side shot, fore-and-aft for an end shot.

† The horizontal-transverse direction is the horizontal direction perpendicular to the line from the plan position of the charge to the nearest point of the LFSP.

fairly fast rise ( $\sim 10$  ms) and slow decline ( $\sim 300$  ms) (Fig. 1). Velocities measured on the shell plating and the LFSP mounting plane on top of the stiffeners are similar, although those on the plating have higher magnitudes and sharper rises, so sharp that it is likely that a substantial fragment of the energy content lies at frequencies above the 2 KHz pass limit of the velocity transducer. Thus the measurements made on the plating must be considered less reliable than those on the mounting plane or FSP. Regarding the mounting-plane velocities, the variation of peak vertical velocity with measurement location is such that the greatest is 1.75 times the smallest. This variation is enough to obscure some of the other points of interest, and it is convenient to speak of the average value of all measured values in a given direction and at a given type of location--viz., the average vertical mounting-plane velocity or the average athwartship FSP velocity, etc.

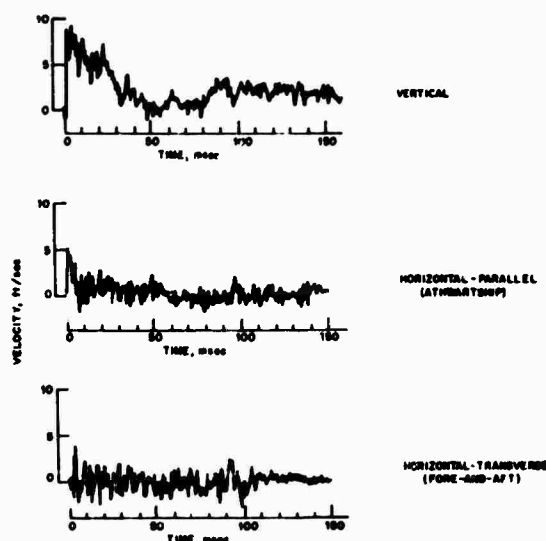


Fig. 1 - Typical velocity waveforms measured on the LFSP mounting plane.

The variation is less for horizontal-parallel velocities, and slight for horizontal-transverse. On the average, the variation in peak velocity with measurement orientation is 1:7:3 for vertical: horizontal-parallel: horizontal-transverse. The essential effect of charge orientation (end shot vs side) is to determine which of the LFSP axes (athwartship and fore-and-aft) is aligned with which of the test axes (horizontal-parallel and horizontal-transverse). It would be expected that the average peak velocities would be slightly lower for end shots than for side, since the average point of the LFSP is more removed from the change in this orientation. There is such a decrease, but it is not consistent and is of an amount which could be expected from normal variation between nominally identical shots. The

peak velocities on the plating shows no effect from an increase in load from 0 to 112.6K lb, and a substantial decrease for an increase from 112.6 to 176.3K lb. The mounting plane peak velocities show a similar decrease for an increase in load weight from 112.6 to 176.3K lb. These effects are summarized in Fig. 2A & 2B, showing average peak velocities vs standoff.

#### LOAD (FSP) VELOCITIES

The velocity waveforms measured in the FSP are similar to those found at the same locations when the FSP is operated alone (1), implying that because the mounting structure is stiffer than the inherent structure of the FSP (free-free beam mode  $\sim 120$  Hz) the details of the local FSP structure are dominant in fixing the details of a particular measured waveform. Most of the transducers in the FSP were placed around its perimeter close to the mounting plates, the regions most rigidly coupled to the LFSP mounting plane. The waveforms here resemble those of the associated LFSP waveforms with the addition of a discernible sinusoidal component. Those measured towards the FSP center are located over cells, and have a more strongly sinusoidal nature. The magnitudes and the variations of magnitude are greater in the FSP than at the LFSP mounting plane. The highest peak velocities are those from the central locations above cells, but those about the perimeter are also higher and more variable from place to place than those in the LFSP. In the vertical direction, the highest peak velocity is 2.5 times the smallest, and the average peak is 1.5 times the average peak at the LFSP mounting plane. In the two horizontal directions the variation over location is much less, and the average peak values are substantially the same in the FSP and the LFSP. The ratio of average peak velocities in the FSP is 1:45:15 (vertical:horizontal-parallel:horizontal-transverse). The influences of the test parameters are much the same as on the LFSP velocities, save that the vertical FSP velocity is more strongly reduced by increasing load weight (Fig. 3).

#### LOAD (SDOF) RESPONSES

The SDOF response was measured by a single accelerometer sensing vertical motion centrally located on top of its mass. The signal from this transducer, its integral and double integral were played back on strip charts. The acceleration curve carries a small amount of high-frequency hash for the first couple of cycles, but after this dies down the curve, like those of velocity and displacement, is a clean, highly-damped sinusoidal at a frequency of 29.4 Hz. The measured peak values are tabulated in Table II.

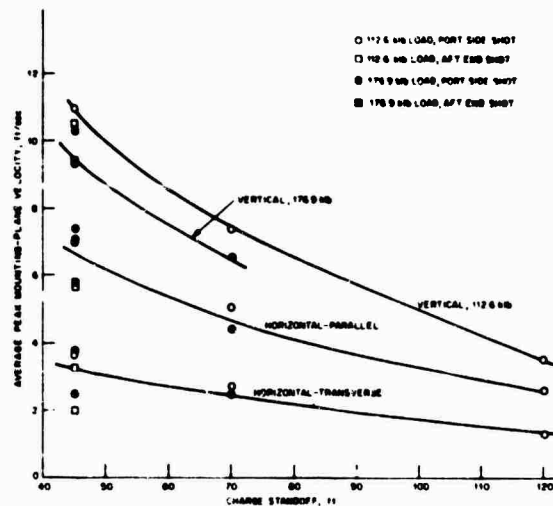
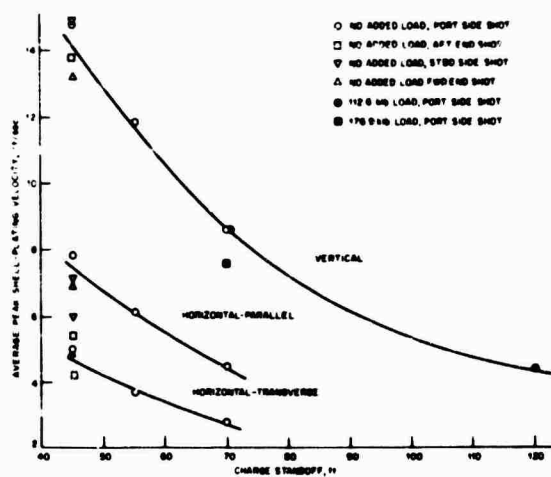


Fig. 2 - The variation of average peak velocity with charge standoff - A, on the shell-plating; B, on the LFSP mounting plane.

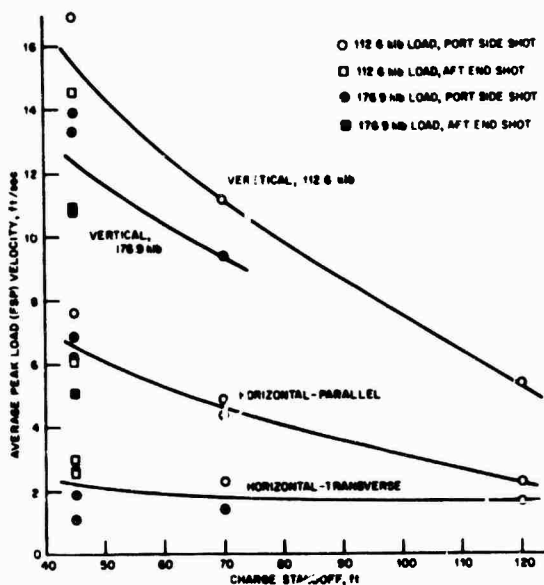


Fig. 3 - Variation of average peak load (FSP) velocities as a function of charge standoff.

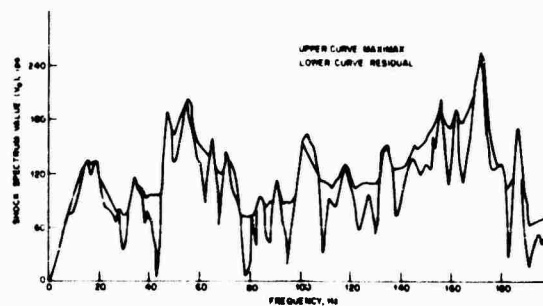


Fig. 4 - A typical shock spectrum derived from a velocity recording.

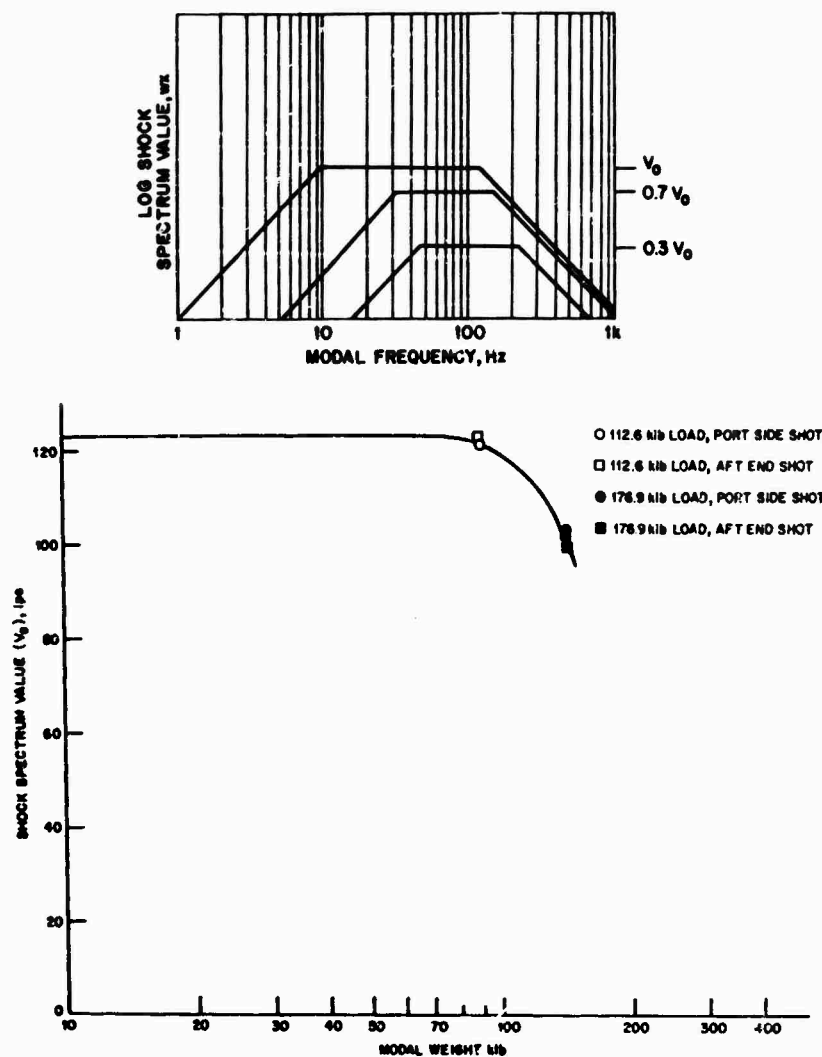


Fig. 5 - Design shock spectra for the LFSP-A, the variation of shock spectrum value with modal frequency and component direction; B, the variation with modal weight.

#### LFSP SHOCK SPECTRA

Shock spectra were derived from the recordings of some of the vertical velocities at the LFSP mounting plane. These generally show a velocity-shock nature below about 40 Hz, and a few interaction peaks above, as in Fig. 4. The dips at around 30 and 40 Hz are present in some degree in all of these spectra and in the absence of any knowledge of the modal description of the test load structure the average level of the maximax spectrum in this region is taken as the shock spectrum value. The dis-

placement and acceleration limits can be set from the integrals and slopes of the velocity curves, since for a set of massless oscillators, such as define the shock spectrum, the peak relative displacement for low frequencies is the maximum displacement of the shock motion, and the peak acceleration at high frequencies is the maximum acceleration involved in the shock motion. The data at hand do not indicate a change in corner frequency with weight.

Table II  
S90F Responses

Shot No.	Rear Side	Standoff ft	Added Load klb	Peak S90F Acceler. g	Response Velocity ft/sec	Displ. in.
7	Port	120	112.6	45	5.6	.49
8	Port	70	112.6	63	8.6	1.35
9	Port	45	112.6	88	13.3	2.40
10	Stern	45	112.6	106	11.7	1.96
11	Port	70	176.9	56	8.9	1.47
13	Port	45	176.9	91	14.2	2.07
14	Stern	45	176.9	87	12.0	2.22

Data for larger loads may do so. Next the variation of the shock spectrum value with modal weight must be determined. This has been attempted on the basis of the assumptions that the shock spectrum value components are related much as peak velocity components, and that the weight in the lowest frequency mode is some 80% of the total. The first is reasonable for linear systems, the second a rule of thumb for simple systems in uniaxial translation. Under these assumptions the shock spectra curves of Fig. 5A & 5B are obtained.

The variation of  $V_o$  with modal weight is shown in Fig. 5B for 45 ft standoff, and is 124 ips for modal weights up to about 90K lb, declining to 102 ips at 142K lb. This curve should continue to decline, and eventually level off at some value; its structure will become clearer as data are accumulated through use. A straight line connecting the points for the two load conditions on a linear plot has the equation

$$V_o(\text{ips}) = 156 - .38 \times \text{modal weight (K lb)}.$$

The variation of  $V_o$  with standoff is shown in Fig. 6.

#### STRUCTURAL EFFECTS

During the first six shots (LFSP unloaded) minor cracking of the welds associated with some of the side stiffeners occurred. These were repaired, and no cracking was observed on the subsequent shots. The strain gages showed elastic behavior of the LFSP structure with the exception of the installation on the bottom plating at the center of the cell closest to the charge. For a shot at 45 ft standoff, this showed a set of 100 to 200  $\mu\text{in/in.}$  For a given shot geometry, the peak strains were higher with the greater load. However, the differences between the peak strains for the two nominally identical shots were about twice as great as the difference between the lesser of these and the shot with the lower load and the same standoff. Since it is not likely that a standoff of less than 45 ft will be required, the LFSP structure should not be significantly affected by normal use.

#### SUMMARY

The Large Floating Shock Platform has extended the Navy's shock testing capability to loads of about 400,000 lb. In its essential shock characteristics the LFSP behaves in much the same way as the FSP, although some details (for example, gross motion) are different. The LFSP will be included as a prescribed

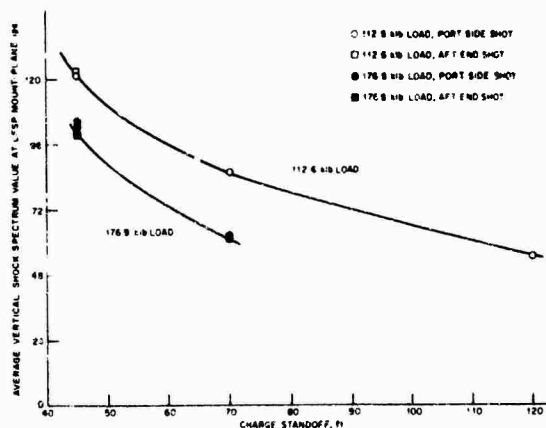


Fig. 6 - The effect of charge standoff and load on shock spectrum value

Figure 5A shows the variation of shock spectrum value with modal frequency for each component direction. The corner frequencies are: Vertical, 9.5 and 117 Hz; horizontal-parallel, 31 and 154 Hz; horizontal-transverse, 59 and 171 Hz. The shock spectrum values are: vertical,  $V_o$ ; horizontal-parallel,  $.7 V_o$ ;



testing device in future editions of MIL-S-901. Under what will probably be its normal operating conditions the LFSP will be essentially an elastic machine, so that its structure and shock characteristics should change little with use. It would be desirable to obtain information on the LFSP's behavior with extremely large loads in order to extend the curve of shock spectrum value vs modal weight. This information should become available as large items are tested.

#### ACKNOWLEDGEMENTS

The author expresses his gratitude to the members of the operating team, C. Schrader, S. Giannoccolo, G. Volpe and S. Vogensen, all of WCSF, and the instrumentation team, C. Cunningham, E. Judd and C. Lamb of NRL, and W. Luksa and C. Parker of WCSF.

This work was sponsored by the Naval Ship Systems Command under Project No. S4415.

#### REFERENCES

1. NRL Report 7396, "Shipboard Shock and Navy Devices for its Simulation," E. W. Clements, July 14, 1972.
2. "Shock Measurement System Development," M.W. Oleson, Report of NRL Progress, pp. 16-27, October 1967.

#### DISCUSSION

Mr. Mador (Electric Boat): Do you intend to use a similar size charge in conducting MIL-S-901C tests for this large barge as you do on the smaller barges?

Mr. Schrader: This is a 300 lb. charge.

Mr. Mador: Yes, I realize that you use that for the instrumentation shock characteristics. But if you were to use this platform for qualification of large components what would your charge geometry be?

Mr. Schrader: The 300 lbs. charge would be used with a 20 ft. depth. The closest in standoff would be 50 ft. and the next would be 65, 80, and then 1 inch at 100 ft.

Mr. Berezow (Naval Ordnance Laboratory): You mentioned that the bubble was vented from the primary pulse, was that because of the 300 lb. charge?

Mr. Schrader: Yes, as you probably know about 45% of the energy of the explosive that we used is in the bubble. If we were closer to the bottom this bubble would then migrate to the bottom and bounce on the bottom several times before it would vent, and so we used the shallow 20 ft. standoff to let the bubble blow to the surface to give us some airborne noise in lieu of exciting all of the residents of the area who might think that an earthquake

was present.

Mr. Roberts (Raytheon Company): Did you feel that you could have had an oscillating bubble if you had a small charge? Did that affect it?

Mr. Schrader: Yes we could, but that would have meant that we wouldn't have as good a velocity distribution throughout the whole barge; and as it is, the minimum to the maximum velocity distribution ranged about 1.75.

Mr. Roberts: In previous reports I noticed that there were oscillating bubbles with smaller charges. I was trying to figure out why in some cases they were oscillating and in other cases they did not.

Mr. Schrader: With the small floating shock platform, if the water is deep enough, the bubble, as you previously indicated, will pulsate about three times before it vents. This usually doesn't bother anything because most things are broken in that first millisecond rise and the only time this bubble gets to be annoying is if there is a low frequency system.

Mr. White (Bettis Atomic Power): Do you have plans to build an additional large barge? You had implied that this was the only one in existence. I was wondering if you had plans to build one for the East Coast.

Mr. Schrader: No, not that I know of. These larger tests are rather expensive and I don't think that they are planned as regular production tests. These tests that will provide information for prototype equipment, such as a large reduction gear, not every piece of machinery will be tested this way maybe Mr. Sullivan has some ideas on this.

Mr. Sullivan (NAVSEC): The requirements for this barge have already been written into a revised MIL-S-901 that is presently going through the mill, so this will be included. Again since it is a unique facility I don't anticipate that we will automatically divert all large pieces of equipment through this, but it will be alternative to a formal dynamic analysis. We would hope that more equipment is diverted for tests rather than strictly analysis.

Mr. Duffy (General Electric Company): Do you have any data on relative costs between the small platform and the large platform?

Mr. Schrader: The costs of this test seemed to run about 20 or 30% more than with the small platform, and this is just conducting the tests. The installation of the bigger equipment can be pretty expensive, it depends on what kind of equipment. This foundation cost us about \$20,000 to be installed.

Mr. Welch: Is this large enough to shock test the largest item of equipment aboard a Naval

combatent ship? I can answer for machinery, turbines, gears, and turbine generator sets and say that it is. I have some question about boilers and perhaps reactor components. I think that this large floating shock platform rounds out the Naval shock testing and shock analysis capacity in a very fine and complete fashion. It has been the experience of those who have used dynamic analysis that it is very effective in the early stages of design. It is a design method in that it permits one to make changes during design. But because of the necessarily mathematical complexities it tends to be rather gross in the math models that one develops for the dynamic analysis, or rather gross in their concept of the dynamical system. Furthermore it generally does not take into account the cross effects, the cross couplings that exist between the directions of shock; on the other hand the shock barge test tends to be very detailed and an apparatus subjected to the shock barge test generally gets an extensive shock in all directions, and although there may be some criticism about the arbitrary nature of the shock barge test, it at least encompasses detailed elements of an apparatus that are often neglected when one math models the apparatus for dynamic analysis. Furthermore it takes into effect sometimes very valid cross effects which are important to the actual shock resistance of machinery.

Mr. Schrader: All of the test loads that have been considered for tests on the barge looked as if they would be accommodated. There might be a stability problem with some of the hardware that has a very high center of gravity, but off hand I don't know of any machinery that won't fit into this.

Mr. Sullivan: Originally we attempted to come up with a size that would satisfy our projected requirements. It will take all the boilers that the Navy has made, including the LHA boiler which is the biggest boiler ever made for shipboard service. There may be some other components in the reactor area that we cannot handle.

Mr. Schrader: I agree with Mr. Welch wholeheartedly that these tests are very ingenious in finding out one weak point that somebody has not calculated in their dynamic design and that 6th mode which was not considered to be important. These tests have been very surprising in the way that they will point out things to you. As an example, in the calibration series the welding rod that was used to fasten this foundation into the FSP it started to crack at the joint and we couldn't understand it so we took a careful look at the rods that were used and lo and behold it was an incorrect rod. This had started the crack and you may have noticed that we put some little gussets to spread out the load at the cracking point and we had to re weld things; but it is rather interesting how shock in a test like this can pick out that one flaw in a whole system just like that.

# THE EFFECT OF UNIFORM EXTERNAL PRESSURIZATION ON THE DYNAMIC RESPONSE OF ISOTROPIC CYLINDRICAL SHELLS

Frederick J. Dzialo  
Civil Engineering Department  
University of Massachusetts  
Amherst, Massachusetts

Following Flugge's derivation for the buckling of cylindrical shells, the equations of motion for dynamic loading of isotropic cylindrical shells subjected to an external uniform pressure have been formulated. The equations of motion neglect the effect of rotatory inertia and shear, and in general are applicable to cylindrical shells whose structural wave length is significantly greater than the thickness of the shell; however as pointed out by J.E. Greenspon [3], Flugge's theory which includes bending and membrane effects is good at even the shorter wave lengths, provided the thickness of the shell is not too great, that is the ratio of inside radius to outside is less than 0.5. The normal mode theory was utilized to provide dynamic solutions for the equations of motion.

Solutions are also provided for the Timoshenko-type theory, and comparisons are made between the two theories by considering and neglecting in-plane inertia forces.

Comparison of results is exemplified by a numerical example which considers the effect of an external pressure on the dynamic response of a shell supported by a thin diaphragm and subjected to a localized unit impulse.

## INTRODUCTION

In a recent paper [1], E.N.K. Liao and P. G. Kessel investigated the dynamic response of a cylindrical shell with initial stress, and subjected to general three-dimensional surface loads. This paper presented general solutions for both Flugge's and Donnell's equations for a simply supported cylindrical shell, as well as analytical solutions for a stationary radial point force and a stationary couple.

The purpose of this paper is to investigate the effect of an external uniform pressure on the dynamic response of isotropic cylindrical shells. Following Flugge's [2] derivation for the buckling of cylindrical shells, the equations of motion are formulated. The equations of motion neglect the effect of rotatory inertia and shear, and in general are applicable to shells whose structural wave length is significantly greater than the thickness of the shell; however as pointed out by J.E. Greenspon [3], Flugge's theory which includes bending and membrane effects is good at even the shorter wave lengths provided the shell is not too thick; that is the ratio of inside radius to outside radius is less than

0.5. The equations, useful in calculating displacements and stresses for impulsive loads applied to a comparatively small region of the shell, are found by utilizing the classical normal theory which provides dynamic solutions for the equations of motion as well as natural boundary conditions for a cylindrical shell subjected to an external uniform pressure.

Solutions are also provided for the Timoshenko-type theory, and comparisons are made between the two theories by considering and neglecting in-plane inertia forces.

Comparison of results is exemplified by a numerical example which considers the effect of an external uniform pressure on the dynamic response of a shell simply supported by a thin diaphragm, and subjected to a localized unit impulse.

## Equations of Motion

Following Flugge's [2] exact derivation for the buckling of cylindrical shells, the differential equations of motion for impulsive loading of cylindrical shells subject to an external uniform pressure become:

$$a N_x' + a N_{\phi}' - p a (u'' - w') - P u'' + a^2 p_x \\ = \rho h a^2 \frac{\partial^2 u}{\partial t^2}$$

$$a N_{\phi}' + a N_x' - a Q_{\phi}' - p a (v'' + w') - P v'' + a^2 p_{\phi} \\ = \rho h a^2 \frac{\partial^2 v}{\partial t^2} \quad (1-3)$$

$$-a Q_{\phi}' - a Q_x' - a N_{\phi}' - p a (u' - v' + w'') \\ - P w'' + a^2 p_r = \rho h a^2 \frac{\partial^2 w}{\partial t^2} \quad (1-3)$$

where

$$Q_{\phi} = \frac{M_{\phi}' + M_x'}{a} \quad Q_x = \frac{M_x' + M_{\phi}'}{a}$$

$$N_{\phi} = \frac{D}{a} (v' + w + v u') + \frac{K}{a^3} (w + w'')$$

$$N_x = \frac{D}{a} (u' + v v' + v w) - \frac{K}{a^3} w''$$

$$N_{\phi x} = \frac{D}{a} \frac{1-v}{2} (u' + v') + \frac{K}{a^3} \frac{1-v}{2} (u' + w'')$$

$$N_{x\phi} = \frac{D}{a} \frac{1-v}{2} (u' + v') + \frac{K}{a^3} \frac{1-v}{2} (v' - w'')$$

$$M_{\phi} = \frac{K}{a^2} (w + w'' + v w'')$$

$$M_x = \frac{K}{a^2} (w'' + v w'' - u' - v v')$$

$$M_{\phi x} = \frac{K}{a^2} (1-v) (w'' + \frac{1}{2} u' - \frac{1}{2} v')$$

$$M_{x\phi} = \frac{K}{a^2} (1-v) (w'' - v') \quad (4-13)$$

Substitution of equations (4) through (13) into equations (1) through (3) yields:

$$u'' + \frac{(1-v)}{2} u'' + \frac{1+v}{2} v'' + v w' \\ + k \left( \frac{1-v}{2} u'' - w''' + \frac{1-v}{2} w'' \right) \\ - q_1 (u'' - w') - q_2 u'' + \frac{p_x(x, t) a^2}{D} \\ = \frac{\rho h a^2}{D} \frac{\partial^2 u}{\partial t^2}$$

$$\frac{1+v}{2} u'' + v'' + \frac{1-v}{2} v'' + w' \\ + k \left( \frac{3}{2} (1-v) v'' - \frac{3-v}{2} w''' \right) \\ - q_1 (v'' + w') - q_2 v'' + \frac{p_{\phi}(x, t) a^2}{D} \\ = \frac{\rho h a^2}{D} \frac{\partial^2 v}{\partial t^2} \\ v u' + v' + w + k \left( \frac{1-v}{2} u'' - u''' - \frac{3-v}{2} v''' \right) \\ + w''' + 2 w'' + w'' + 2 w'' + w \\ + q_1 (u' - v' + w'') + q_2 w'' \\ - \frac{p_r(x, t) a^2}{D} = \frac{-\rho h a^2}{D} \frac{\partial^2 w}{\partial t^2} \quad (14-16)$$

where

$$k = h^2 / 12 a^2 \quad q_1 = p a / D \quad q_2 = P / D = q_1 / 2$$

## Orthogonality and Modal Vibrations

For free vibrations, equations (14) through (16) may be written as follows

$$\alpha_5 u'' + \alpha_2 u'' + \frac{1+v}{2} v'' + \alpha_3 w' \\ + k \left( \frac{1-v}{2} w'' - w''' \right) = \frac{\rho h a^2}{D} \frac{\partial^2 u}{\partial t^2} \\ \frac{1+v}{2} u'' + \alpha_4 (v'' + w') + \alpha_1 v'' \\ - \frac{k}{2} (3-v) w''' = \frac{\rho h a^2}{D} \frac{\partial^2 v}{\partial t^2} \\ \alpha_3 u' + \alpha_4 v' + (2k + 1 - \alpha_4) w'' + k \left( \frac{1-v}{2} u'' \right. \\ \left. - u''' - \frac{3-v}{2} v''' + w''' + 2 w'' + w'' \right. \\ \left. + \left( \frac{k+1}{k} \right) w \right) + (1 - \alpha_5) w'' = \frac{-\rho h a^2}{D} \frac{\partial^2 w}{\partial t^2} \quad (17-19)$$

where

$$\alpha_1 = \frac{1-v}{2} (1 + 3k) - q_2$$

$$\alpha_2 = \frac{1-v}{2} (1 + k) - q_1$$

$$\alpha_3 = (v + q_1) \quad \alpha_4 = 1 - q_1 \quad \alpha_5 = 1 - q_2$$

Equations (17) through (19) yield the natural frequencies and mode shapes. The orthogonality condition for the mode shapes is derived by assuming that the displacements  $u$ ,  $v$ , and  $w$  for the  $n$ th mode have the form

$$u = u_n(x, \phi) e^{i \omega_n t}, \quad v = v_n(x, \phi) e^{i \omega_n t}, \\ w = w_n(x, \phi) e^{i \omega_n t} \quad (20)$$

Finding the orthogonality condition involves the following steps:

1. the  $n$ th terms of expressions (20) are inserted into equations (17) through (19), and the resulting equations are multiplied by  $u_m(x)$ ,  $v_m(x)$  and  $w_m(x)$ , respectively, integrated over the domain, and added;
2. the  $m$ th terms of expressions (20) are inserted into equations (17) through (19), and the resulting equations are multiplied by  $u_n(x)$ ,  $v_n(x)$ , and  $w_n(x)$ , respectively, integrated over the domain, and added;
3. the equation resulting from Step 2 is subtracted from the equation resulting from Step 1; it is integrated by parts, and use is made of equations (4) through (13) to obtain the final orthogonality relation. The orthogonality condition may be written as follows:

$$\begin{aligned}
 (\omega_n^2 - \omega_m^2) \int_0^L \rho h (u_n u_m + v_n v_m + w_n w_m) dx = \\
 = u_n (N_{xm} + p w_m - P \frac{\partial u_m}{\partial x}) \\
 + v_n (N_{x\phi m} - \frac{M_{x\phi m}}{a} - P \frac{\partial v_m}{\partial x}) \\
 - w_n (Q_{xm} + P \frac{\partial w_m}{\partial x}) + M_{xm} \frac{\partial w_n}{\partial x} \\
 - u_m (N_{xn} + p w_n - P \frac{\partial u_n}{\partial x}) \\
 - v_m (N_{x\phi n} - \frac{M_{x\phi n}}{a} - P \frac{\partial v_n}{\partial x}) \\
 + w_m (Q_{xn} + P \frac{\partial w_n}{\partial x}) - M_{xn} \frac{\partial w_m}{\partial x} \Big|_0^L = 0, \\
 m \neq n
 \end{aligned} \quad (21)$$

where the natural boundary conditions at  $x=0$  and  $L$  are:

Fixed:

$$u = v = w = \frac{\partial w}{\partial x} = 0 \quad (22)$$

Hinged:

$$u = v = w = 0 \quad M_x = 0 \quad (23)$$

Simply Supported:

$$w = 0 \quad M_x = 0$$

$$N_{x\phi} - \frac{M_{x\phi}}{a} - P \frac{\partial v}{\partial x} = 0 \quad N_x + p w - P \frac{\partial u}{\partial x} = 0 \quad (24)$$

Free:

$$M_x = 0 \quad Q_x + P \frac{\partial w}{\partial x} = 0$$

$$N_{x\phi} - \frac{M_{x\phi}}{a} - P \frac{\partial v}{\partial x} = 0 \quad N_x + p w - P \frac{\partial u}{\partial x} = 0 \quad (25)$$

#### Integral of the Square of Eigenfunctions

The integral of the square of the eigenfunctions is evaluated from equation (21) by a limiting process. For any prescribed boundary condition, the evaluation of the integral may be determined as follows:

$$\begin{aligned}
 \int_0^L \rho h [u_n^2(x) + v_n^2(x) + w_n^2(x)] dx \\
 = \lim_{\omega_m \rightarrow \omega_n} (-1/2\omega_m) \frac{d}{d\omega_m} \left[ u_n (N_{xm} + p w_m - P \frac{\partial u_m}{\partial x}) \right. \\
 + v_n (N_{x\phi m} - \frac{M_{x\phi m}}{a} - P \frac{\partial v_m}{\partial x}) - w_n (Q_{xm} + P \frac{\partial w_m}{\partial x}) \\
 + M_{xm} \frac{\partial w_n}{\partial x} - u_m (N_{xn} + p w_n - P \frac{\partial u_n}{\partial x}) \\
 - v_m (N_{x\phi n} - \frac{M_{x\phi n}}{a} - P \frac{\partial v_n}{\partial x}) \\
 \left. + w_m (Q_{xn} + P \frac{\partial w_n}{\partial x}) - M_{xn} \frac{\partial w_m}{\partial x} \right]_0^L
 \end{aligned}$$

To determine the natural frequencies and mode shapes, equations (17) through (19) may be solved by assuming

$$\begin{aligned}
 u &= A e^{\lambda x/a} \cos(m\phi) e^{i\omega_{nm} t} \\
 v &= B e^{\lambda x/a} \sin(m\phi) e^{i\omega_{nm} t} \\
 w &= C e^{\lambda x/a} \cos(m\phi) e^{i\omega_{nm} t}
 \end{aligned} \quad (27)$$

Inserting equation (27) into equations (17) through (19) yields equation (28):

$$[\alpha_5 \lambda^2 - m^2 \alpha_2 + \rho h a^2 \omega_{nm}^2 / D] A + \left( \frac{1+\nu}{2} \right) m B$$

$$+ [\alpha_3 \lambda - k \left( \frac{1-\nu}{2} \right) m^2 \lambda - k \lambda^3] C = 0$$

$$- \left( \frac{1+\nu}{2} \right) m \lambda A - [\alpha_4 m^2 - \alpha_1 \lambda^2 - \rho h a^2 \omega_{nm}^2 / D] B$$

$$- [\alpha_4 m - k \left( \frac{3-\nu}{2} \right) m \lambda^2] C = 0$$

$$[\alpha_3 \lambda - k \left( \frac{1-\nu}{2} \right) m^2 \lambda - k \lambda^3] A + [\alpha_4 m - k \left( \frac{3-\nu}{2} \right) m \lambda^2] B$$

$$+ [1 - (2k+1-\alpha_4) m^2 + (1-\alpha_5) \lambda^2 + k \{ (\lambda^2 - m^2)^2 + 1 \}]$$

$$- \rho h a^2 \omega_{nm}^2 / D] C = 0 \quad (28)$$

The characteristic equation is found by setting the determinant of the set of equations (28) equal to zero. To determine the eigenvalues,  $\omega_{nm}^2$ , the following method is utilized: A value of  $\omega_{nm}^2$  is guessed and inserted into the characteristic equation. The characteristic equation will yield eight roots. For unequal roots, equations (27) may be written as follows:

$$u = \sum_{i=1}^8 A_i e^{\lambda_i x/a} (\cos m \phi e^{i \omega_{nm} t})$$

$$v = \sum_{i=1}^8 B_i e^{\lambda_i x/a} (\sin m \phi e^{i \omega_{nm} t})$$

$$w = \sum_{i=1}^8 C_i e^{\lambda_i x/a} (\cos m \phi) e^{i \omega_{nm} t} \quad (29)$$

where for each  $\lambda_i$  there exists a relationship between the amplitudes  $A_i$ ,  $B_i$  and  $C_i$  from the determinant of equation (28).

Equations (29) with the necessary boundary conditions will lead to a determinant  $|a_{ij}| = 0$  versus  $\omega_{nm}^2$ . The eigenvalues,  $\omega_{nm}^2$ , are those for which  $|a_{ij}| = 0$ . At a point,  $\omega_{nm}^2$ , when  $|a_{ij}| = 0$ , the ratio of the amplitudes  $A_i$ ,  $B_i$  and  $C_i$  can be calculated from the determinant of equation (28).

#### Solutions for Forced Vibrations

Equations (17) through (19) may be solved by assuming

$$u = \sum_{n=0}^{\infty} u_n(x, \phi) q_n(t) \quad v = \sum_{n=0}^{\infty} v_n(x, \phi) q_n(t) \\ w = \sum_{n=0}^{\infty} w_n(x, \phi) q_n(t) \quad (30)$$

Substituting the above equations into equations (14) through (16), and utilizing the orthogonality condition (21) yields the following:

$$q_n(t) = \frac{\int_0^{2\pi} \int_0^L \int_0^a t P \sin \omega_n(t-\tau) d\lambda dx d\phi}{\omega_n \int_0^{2\pi} \int_0^L \int_0^a \rho h (u_n^2 + v_n^2 + w_n^2) dx d\phi} \quad (31)$$

where

$$P = p_x(x, \phi, \lambda) u_n + p_\phi(x, \phi, \lambda) v_n + p_r(x, \phi, \lambda) w_n$$

For an impulsive loading as shown in Figure 1, equation (31) becomes

$$q_n(t) = \frac{\int_{(\tau-\epsilon_1)/a}^{(\tau+\epsilon_1)/a} \int_{(\tau-\epsilon_2)/a}^{(\tau+\epsilon_2)/a} P \sin \omega_n(t-\tau) d\lambda dx d\phi}{\omega_n \int_0^{2\pi} \int_0^L \int_0^a \rho h (u_n^2 + v_n^2 + w_n^2) dx d\phi} \quad (32)$$

For a concentrated impulsive loading equation (31) becomes

$$q_n(t) = \lim_{\epsilon_1 \rightarrow 0, \epsilon_2 \rightarrow 0} \int_{(\tau-\epsilon_1)/a}^{(\tau+\epsilon_1)/a} \int_{(\tau-\epsilon_2)/a}^{(\tau+\epsilon_2)/a} P \sin \omega_n(t-\tau) d\lambda dx d\phi \\ \times \frac{1}{\omega_n \int_0^{2\pi} \int_0^L \int_0^a \rho h (u_n^2 + v_n^2 + w_n^2) dx d\phi} \quad (33)$$

where

$$p_x = \frac{P_x}{4\epsilon_1 \epsilon_2} \quad p_\phi = \frac{P_\phi}{4\epsilon_1 \epsilon_2} \quad p_r = \frac{P_r}{4\epsilon_1 \epsilon_2}$$

#### Solution for Impulse

Consider an impulse per unit area,  $i_x(x, \phi)$ ,  $i_\phi(x, \phi)$  and  $i_r(x, \phi)$  acting on the cylinder for an infinitely short time. The cylinder may now be considered to be vibrating freely with the following initial conditions:

At  $t = 0$ :

$$u = v = w = 0 \quad (34)$$

$$\frac{\partial u}{\partial t} = \frac{i_x(x, \phi)}{\rho h} \quad \frac{\partial v}{\partial t} = \frac{i_\phi(x, \phi)}{\rho h} \\ \frac{\partial w}{\partial t} = \frac{i_r(x, \phi)}{\rho h} \quad (35)$$

The displacements for free vibrations are given as:

$$\begin{aligned}
u &= \sum_{m=0}^{\infty} u_n (A_m \cos \omega_m t + B_m \sin \omega_m t) \\
v &= \sum_{m=0}^{\infty} v_n (A_m \cos \omega_m t + B_m \sin \omega_m t) \\
w &= \sum_{m=0}^{\infty} w_m (A_m \cos \omega_m t + B_m \sin \omega_m t) \quad (36)
\end{aligned}$$

Substituting the initial conditions into equation (36) and making use of orthogonality yields the following

$$\begin{aligned}
u &= \sum_{m=0}^{\infty} u_m B_m \sin \omega_m t & v &= \sum_{m=0}^{\infty} v_m B_m \sin \omega_m t \\
w &= \sum_{m=0}^{\infty} w_m B_m \sin \omega_m t \quad (37)
\end{aligned}$$

where

$$B_m = \frac{1}{\omega_n} \frac{\int_0^{2\pi} \int_0^l (i_x u_m + i_\phi v_m + i_r w_m) dx d\phi}{\int_0^{2\pi} \int_0^l \rho h (u_m^2 + v_m^2 + w_m^2) dx d\phi} \quad (38)$$

For a distributed impulse as shown in Figure 1, equation (38) becomes

$$B_m = \frac{\int_{(n-\epsilon_1)/a}^{(n+\epsilon_1)/a} \int_{\zeta-\epsilon_2}^{\zeta+\epsilon_2} [i_x u_m + i_\phi v_m + i_r w_m] dx d\phi}{\omega_n \int_0^{2\pi} \int_0^l \rho h (u_m^2 + v_m^2 + w_m^2) dx d\phi} \quad (39)$$

For a concentrated impulse, equation (38) becomes

$$B_m = \lim_{\substack{\epsilon_1 \rightarrow 0 \\ \epsilon_2 \rightarrow 0}} \frac{\int_{(n-\epsilon_1)/a}^{(n+\epsilon_1)/a} \int_{\zeta-\epsilon_2}^{\zeta+\epsilon_2} [i_x u_m + i_\phi v_m + i_r w_m] dx d\phi}{\omega_n \int_0^{2\pi} \int_0^l \rho h (u_m^2 + v_m^2 + w_m^2) dx d\phi} \quad (40)$$

where

$$i_x = \frac{I_x}{4\epsilon_1 \epsilon_2} \quad i_r = \frac{I_r}{4\epsilon_1 \epsilon_2} \quad i_\phi = \frac{I_\phi}{4\epsilon_1 \epsilon_2}$$

#### Equations of Motion for Timoshenko Theory [4]

Equations (1) through (3) can be reduced to those presented by Timoshenko by assuming the following conditions:

- The circumferential strain  $\epsilon_\phi$ ,  $\epsilon_x$  and  $\gamma_{x\phi}$  are equal to zero in calculation of  $X_\phi$  and  $X_{x\phi}$ .
- Membrane forces are not affected by bending stresses, nor bending moments by membrane stresses.

Assumptions (a) and (b) yield  $N_{\phi x} = N_{x\phi}$  and  $M_{\phi x} = M_{x\phi}$ . Assuming  $\epsilon_\phi = (v' + w)/a$ ;  $u' = 0$ , and  $\gamma_{x\phi} = (u' + v')/a = 0$ , equations (1) through (3) become:

$$\begin{aligned}
a N_x'' + a N_{\phi x}'' + p a (v'' + w') + a^2 p_x &= \rho h a^2 \frac{\partial^2 u}{\partial t^2} \\
a N_\phi'' + a N_{x\phi}'' - a Q_\phi - P v'' + a^2 p_\phi &= \rho h a^2 \frac{\partial^2 v}{\partial t^2} \\
-a Q_\phi' - a Q_x' + a N_\phi - p a (w'' + w) - P w'' - a^2 p_r &= \rho h a^2 \frac{\partial^2 w}{\partial t^2} \quad (41-43)
\end{aligned}$$

The membrane forces and moments from equations (6) through (13) become

$$\begin{aligned}
N_\phi &= \frac{D}{a} (v' + w + v u') \\
N_{\phi x} &= \frac{D}{a} \left( \frac{1-v}{2} \right) (u' + v') \\
M_\phi &= \frac{K}{a^2} (-v' + w'' + v w'') \\
M_{\phi x} &= \frac{K}{a^2} (1-v) (w'' - v') \quad (44)
\end{aligned}$$

$$\begin{aligned}
N_x &= \frac{D}{a} (u' + v v' + v w') \\
N_{x\phi} &= \frac{D}{a} \left( \frac{1-v}{2} \right) (u' + v') \\
M_x &= \frac{K}{a^2} (w'' + v w'' - v v'') \\
M_{x\phi} &= \frac{K}{a^2} (1-v) (w'' - v')
\end{aligned}$$

Substitution of equations (44) into equations (41) through (43) yields the following:

$$\begin{aligned} u'' + \left(\frac{1+\nu}{2}\right)v'' + \frac{1-\nu}{2}u'' + \nu w' + q_1(v'' + w') \\ + \frac{a^2 p_x}{D} = \frac{\rho h a^2}{D} \frac{\partial^2 u}{\partial t^2} \\ \left(\frac{1+\nu}{2}\right)u'' + v'' + \left(\frac{1-\nu}{2}\right)v'' + w'' - k[w'' + w'''] \\ + k[(1-\nu)v'' + v'''] - q_2 v'' + \frac{a^2 p}{D} = \frac{\rho h a^2}{D} \frac{\partial^2 v}{\partial t^2} \\ \nu u' + v' + w + k[w'' + 2w''' + w'''] - k[v'''] \\ + (2-\nu)v'' + q_2 w'' + q_1(w'' + w) \\ - \frac{a^2 p_r}{D} = \frac{\rho h a^2}{D} \frac{\partial^2 w}{\partial t^2} \end{aligned} \quad (45-47)$$

Equations (45) through (47) may be written

$$\begin{aligned} u'' + \frac{1-\nu}{2}u'' + \beta_1 v'' + \beta_2 w' + \frac{a^2 p_x}{D} \\ = \frac{\rho h a^2}{D} \frac{\partial^2 u}{\partial t^2} \\ \left(\frac{1+\nu}{2}\right)u'' + \beta_3 v'' + \beta_4 v'' + w'' - k(w'' + w''') \\ + \frac{a^2 p}{D} = \frac{\rho h a^2}{D} \frac{\partial^2 v}{\partial t^2} \\ \nu u' + v' + \beta_5 w + k(w'' + 2w''' + w''') \\ - k[v'''] + (2-\nu)v'' + q_2 w'' + q_1 w'' \\ - \frac{a^2 p_r}{D} = \frac{\rho h a^2}{D} \frac{\partial^2 w}{\partial t^2} \end{aligned} \quad (48-50)$$

where

$$\begin{aligned} \beta_1 &= \frac{1+\nu}{2} + q_1 & \beta_2 &= \nu + q_1 \\ \beta_3 &= k + 1 & \beta_4 &= (1-\nu)(k + 0.5) - q_2 \\ \beta_5 &= 1 + q_1 \end{aligned}$$

#### Illustrative Example for Cylinder Supported by Thin Diaphragm

##### Flügge's Theory

For a cylinder supported by a thin diaphragm the following displacements satisfy the natural boundary conditions as derived from the orthogonality conditions:

$$\begin{aligned} u &= \sum_m \sum_n U_{mn} \cos m\phi \cos \frac{n\pi x}{l} \\ v &= \sum_m \sum_n V_{mn} \sin m\phi \sin \frac{n\pi x}{l} \\ w &= \sum_m \sum_n W_{mn} \cos m\phi \sin \frac{n\pi x}{l} \end{aligned} \quad (51)$$

To determine the natural frequencies and mode shapes the determinant for the frequency equation becomes:

$$\begin{aligned} -[\alpha_5 \left(\frac{n\pi a}{l}\right)^2 + m^2 \alpha_2 - \frac{\rho h a^2}{D} \omega_{nm}^2] U_{mn} \\ + \left[\left(\frac{1+\nu}{2}\right)(m) \left(\frac{n\pi a}{l}\right)\right] V_{mn} \\ + [\alpha_3 \left(\frac{n\pi a}{l}\right) - k \left(\frac{1-\nu}{2}\right) m^2 \left(\frac{n\pi a}{l}\right) + k \left(\frac{n\pi a}{l}\right)^3] W_{mn} = 0 \\ \frac{(1+\nu)}{2} (m) \left(\frac{n\pi a}{l}\right) U_{mn} - [\alpha_4 m^2 + \alpha_1 \left(\frac{n\pi a}{l}\right)^2 \\ - \frac{\rho h a^2}{D} \omega_{nm}^2] V_{mn} \\ - [\alpha_4 m + k \left(\frac{3-\nu}{2}\right) (m) \left(\frac{n\pi a}{l}\right)^2] W_{mn} = 0 \\ -[\alpha_3 \left(\frac{n\pi a}{l}\right) - \frac{k(1-\nu)}{2} (m^2) \left(\frac{n\pi a}{l}\right) + k \left(\frac{n\pi a}{l}\right)^3] U_{mn} \\ + [\alpha_4 m + k \left(\frac{3-\nu}{2}\right) (m) \left(\frac{n\pi a}{l}\right)^2] V_{mn} = 0 \\ + [1 - (2k+1-\alpha_4) m^2 - \left(\frac{n\pi a}{l}\right)^2 (1-\alpha_5) \\ + k \{ \left(\frac{n\pi a}{l}\right)^2 + m^2 \}^2 + k - \frac{\rho h a^2}{D} \omega_{nm}^2] W_{mn} = 0 \end{aligned} \quad (52)$$

The ratios of the mode shapes are defined as:

$$\begin{aligned} \alpha_{mn} &= \frac{U_{mn}}{W_{mn}} = \frac{-CD + BE}{AD - B^2} \\ \beta_{mn} &= \frac{V_{mn}}{W_{mn}} = \frac{-AE + BC}{AD - B^2} \end{aligned} \quad (53)$$

where

$$\begin{aligned} A &= -\alpha_5 \left(\frac{n\pi a}{l}\right)^2 - m^2 \alpha_2 + \frac{\rho h a^2}{D} \omega_{nm}^2 \\ B &= \frac{1+\nu}{2} m \left(\frac{n\pi a}{l}\right) \end{aligned}$$



$$C = \alpha_3 \left( \frac{n\pi a}{l} \right) - k \left( \frac{1-\nu}{2} \right) m^2 \left( \frac{n\pi a}{l} \right) + k \left( \frac{n\pi a}{l} \right)^3$$

$$D = -\alpha_4 m^2 - \alpha_1 \left( \frac{n\pi a}{l} \right)^2 + \frac{\rho h a^2}{D} \omega_{mn}^2$$

$$E = -\alpha_4 m - k \left( \frac{3-\nu}{2} \right) m \left( \frac{n\pi a}{l} \right)^2$$

#### Solutions for Forced Vibrations

From equations (30) and (31) the dynamic displacements become

$$\begin{aligned} u &= \sum_m \sum_n U_{mn} \cos m\phi \left( \cos \frac{n\pi x}{l} \right) q_{mn}(t) \\ v &= \sum_m \sum_n V_{mn} \sin m\phi \left( \sin \frac{n\pi x}{l} \right) q_{mn}(t) \quad (54) \\ w &= \sum_m \sum_n W_{mn} \cos m\phi \left( \sin \frac{n\pi x}{l} \right) q_{mn}(t) \end{aligned}$$

where

$$\begin{aligned} q_{on}(t) &= \int_0^{2\pi} \int_0^l \int_0^t [p_x(x, \phi, \lambda) U_{on} \cos \frac{n\pi x}{l} \\ &\quad + p_r(x, \phi, \lambda) W_{on} \sin \frac{n\pi x}{l}] \\ &\quad \times \frac{\sin \omega_{on}(t - \lambda) d\lambda dx d\phi}{\omega_{on} \rho h \pi l (U_{on}^2 + W_{on}^2)} \\ &\quad m = 0 \quad (55) \end{aligned}$$

$$\begin{aligned} q_{nm}(t) &= \int_0^{2\pi} \int_0^l \int_0^t [p_x(x, \phi, \lambda) U_{nm} \cos m\phi \cos \frac{n\pi x}{l} \\ &\quad + p_\phi(x, \phi, \lambda) V_{nm} \sin m\phi \sin \frac{n\pi x}{l} \\ &\quad + p_r(x, \phi, \lambda) W_{nm} \cos m\phi \sin \frac{n\pi x}{l}] \\ &\quad \times \frac{\sin \omega_{nm}(t - \lambda) d\lambda dx d\phi}{\omega_{nm} \rho h \frac{\pi l}{2} (U_{nm}^2 + V_{nm}^2 + W_{nm}^2)} \\ &\quad m \neq 0 \quad (56) \end{aligned}$$

#### Solution for Radial Impulse

a. Unit Step Load Distributed over Area ( $2\epsilon_1 \times 2\epsilon_2$ )

$$\begin{aligned} u &= \sum_{n=1}^{\infty} \sum_{i=1}^s \alpha_{noi} Q_{noi}(t) \cos \frac{n\pi x}{l} \\ &\quad + \sum_{n=1}^{\infty} \sum_{m=1}^{\infty} \sum_{i=1}^s \alpha_{nmi} Q_{nmi}(t) \times \cos \frac{n\pi x}{l} \cos m\phi \\ v &= \sum_{n=1}^{\infty} \sum_{m=1}^{\infty} \sum_{i=1}^s \beta_{nmi} Q_{nmi}(t) \sin \frac{n\pi x}{l} \sin m\phi \\ w &= \sum_{n=1}^{\infty} \sum_{i=1}^s Q_{noi}(t) \sin \frac{n\pi x}{l} \\ &\quad + \sum_{n=1}^{\infty} \sum_{m=1}^{\infty} \sum_{i=1}^s Q_{nmi}(t) \sin \frac{n\pi x}{l} \cos m\phi \quad (57) \end{aligned}$$

where

$$\begin{aligned} Q_{noi}(t) &= \frac{4}{\rho h \pi^2} \frac{\epsilon_1}{a} \left\{ \frac{1}{n} \cdot \frac{1}{\alpha_{noi}^2 + 1} \sin \frac{n\pi \xi}{l} \sin \frac{n\pi \epsilon_2}{l} \right\} \\ &\quad \times \left\{ \frac{1 - \cos \omega_{noi} t}{\omega_{noi}^2} \right\} \quad (58) \end{aligned}$$

$$\begin{aligned} Q_{nmi}(t) &= \frac{8}{\rho h \pi^2} \left\{ \frac{1}{nm(\alpha_{nmi}^2 + \beta_{nmi}^2 + 1)} \cos \frac{m\pi}{a} \sin \frac{n\pi \xi}{l} \right. \\ &\quad \times \left. \sin \frac{m\pi \epsilon_1}{a} \sin \frac{n\pi \epsilon_2}{l} \right\} \left\{ \frac{1 - \cos \omega_{nmi} t}{\omega_{nmi}^2} \right\} \quad (59) \end{aligned}$$

and

s = 1 with in-plane inertia neglected  
s = 3 with in-plane inertia included

b. Solutions for Unit Impulse

Solutions for a unit impulse can be found by differentiating with respect to time the solutions for a unit function.  $Q_{noi}(t)$  and  $Q_{nmi}(t)$  become:

$$Q_{noi}(t) =$$

$$\frac{4}{\rho h \pi^2} \frac{\varepsilon_1}{a} \left\{ \frac{1}{n} \cdot \frac{1}{\alpha_{noi}^2 + 1} \sin \frac{n\pi z}{l} \sin \frac{n\pi \varepsilon_2}{l} \right\} \cdot \left\{ \frac{\sin \omega_{noi}(t)}{\omega_{noi}} \right\} \quad (60)$$

$$Q_{nmi}(t) =$$

$$\frac{8}{\rho h \pi^2} \left\{ \frac{1}{\alpha_{nmi}^2 + \beta_{nmi}^2 + 1} \cos \frac{m\pi}{a} \sin \frac{n\pi z}{l} \right. \\ \left. \cdot \sin \frac{m\pi \varepsilon_1}{a} \sin \frac{n\pi \varepsilon_2}{l} \right\} \cdot \left\{ \frac{\sin \omega_{nmi}(t)}{\omega_{nmi}} \right\} \quad (61)$$

### c. Dynamic Strains and Stresses

Having determined the dynamic displacements, the dynamic middle surface strains and stresses are determined from the following relationships [1]:

$$\varepsilon_x = \frac{\partial u}{\partial x}$$

$$\varepsilon_\phi = \frac{1}{a} \left( \frac{\partial v}{\partial \phi} + w \right)$$

$$\gamma_{x\phi} = \frac{1}{a} \frac{\partial u}{\partial \phi} + \frac{\partial v}{\partial x}$$

$$\sigma_x = \frac{E}{1 - \nu^2} (\varepsilon_x + \nu \varepsilon_\phi)$$

$$\sigma_\phi = \frac{E}{1 - \nu^2} (\varepsilon_\phi + \nu \varepsilon_x) \quad (62)$$

$$\tau_{x\phi} = \frac{E}{2(1 + \nu)} \gamma_{x\phi}$$

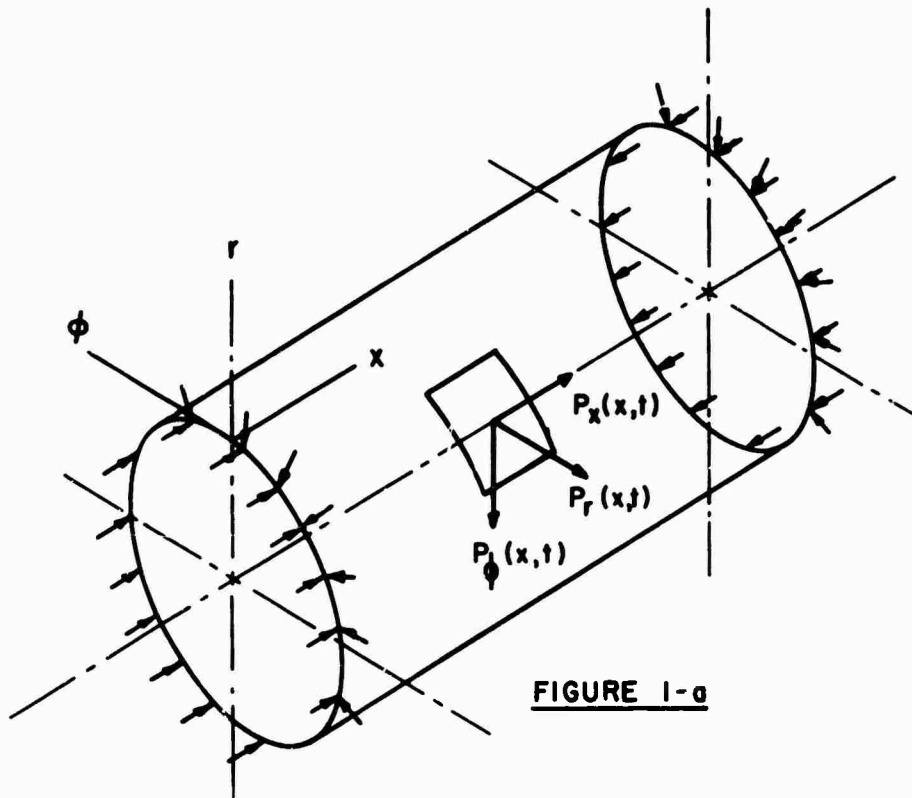


**FIGURE 1-a**

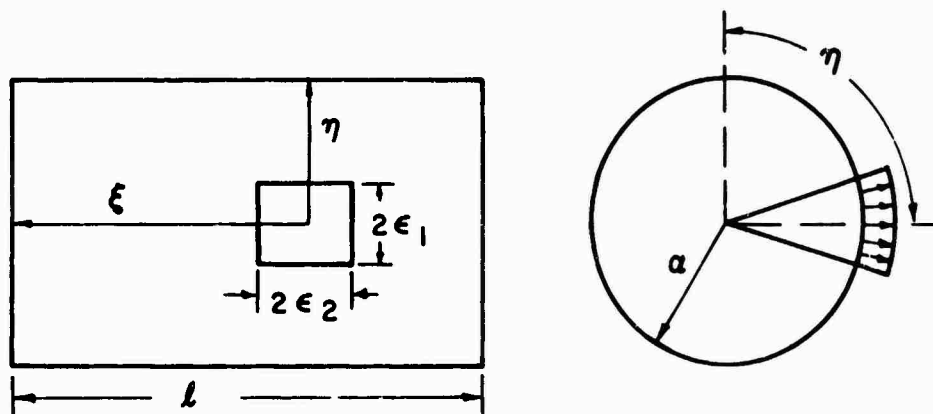


**FIGURE 1-b**

# Data for Illustrative Example

$h = 1.2$  inches       $a = 60$  inches  
 $l = 24$  inches       $c = 12$  inches  
 $c_1 = 2$  inches       $c_2 = 2$  inches  
 $\eta = 0$  radians       $\nu = 0.33333$        $n = 1 - 30$   
 $m = 0 - 29$        $P_c(\text{Flugge}) = 5083.855$  psi.  
 $P_c(\text{Timoshenko}) = 5071.793$  psi.  
 $E = 30 \times 10^6$  psi.

TABLE I

EFFECT OF EXTERNAL UNIFORM PRESSURE ON  
FUNDAMENTAL FREQUENCY (CYCLES/SEC.)

Flugge's Theory			
$h/2a = 0.01$	$l/2a = 0.2$	$P_c = 5083.855$ p.s.f.	
$P/P_c$	$n, m$	$f$	
0	1, 6	461.46	
0.2	1, 7	422.42	
0.4	1, 7	374.72	
0.6	1, 8	313.82	
0.8	1, 8	230.72	
0.95	1, 9	115.63	
0.98	1, 9	73.13	
1.00	1, 9	0.00	

TABLE II

EFFECT OF EXTERNAL UNIFORM PRESSURE  
ON LOWER FREQUENCIES (CYCLES/SEC.)

Flugge's Theory			
$n = 1$			
$P/P_c = 0$			
$m$	$f_1$	$f_2$	$f_3$
0	572.40	2579.58	4471.88
1	565.22	2601.76	4508.18
2	545.75	2666.71	4615.37
3	519.28	2770.30	4788.65
4	492.44	2907.31	5021.12
5	471.53	3072.65	5304.90
6	461.46*	3261.81	5632.13
7	465.25	3470.96	5995.59
8	483.95	3696.87	6389.04
9	517.04	3936.83	6807.24
10	563.17	4188.57	7245.89

$P/P_c = 0.5$

$f_1$	$f_2$	$f_3$
537.79	2572.29	4467.77
529.15	2594.27	4503.96
505.12	2658.64	4610.85
470.58	2761.32	4783.66
431.69	2897.20	5015.50
394.67	3061.23	5298.54
365.24	3248.95	5624.92
348.42	3456.57	5987.48
347.99*	3680.88	6379.98
365.62	3919.18	6797.20
400.58	4169.22	7234.85

\* Fundamental frequency

TABLE III

EFFECT OF EXTERNAL UNIFORM PRESSURE ON  
HIGHER FREQUENCIES (CYCLES/SEC.)

Flugge's Theory			
$n = 3$			
$P/P_c = 0$			
$m$	$f_1$	$f_2$	$f_3$
0	1893.26	7738.74	13404.75
1	1902.11	7745.76	13416.82
2	1910.69	7766.78	13452.99
3	1925.04	7801.68	13513.04
4	1945.25	7850.26	13596.67
5	1971.41	7912.26	13703.44

$F/P_c = 0.5$

$f_1$	$f_2$	$f_3$
1807.77	7716.86	13392.16
1810.44	7723.81	13404.20
1818.46	7744.65	13440.26
1831.89	7779.25	13500.14
1850.85	7827.42	13583.54
1875.45	7888.90	13690.02

TABLE III (continued)

$n = 5$			
$P/P_c = 0$			
$m$	$f_1$	$f_2$	$f_3$
0	5091.63	12897.91	22339.84
1	5094.85	12902.10	22347.08
2	5104.51	12914.67	22368.80
3	5120.61	12935.60	22404.95
4	5143.16	12964.84	22455.46
5	5172.16	13002.34	22520.24

$P/P_c = 0.5$			
$f_1$	$f_2$	$f_3$	
4998.41	12861.43	22318.82	
5001.56	12865.59	22326.04	
5011.04	12878.05	22347.70	
5026.84	12898.80	22383.75	
5048.97	12927.79	22434.12	
5077.44	12964.97	22498.72	

$m = 10$			
$P/P_c = 0$			
$n$	$f_1$	$f_2$	$f_3$
1	563.17	4188.57	7245.89
2	1196.55	6123.37	10597.00
3	2195.92	8410.40	14562.79
4	3600.27	10830.29	18756.15
5	5414.29	13310.62	23052.99

$P/P_c = 0.5$			
$f_1$	$f_2$	$f_3$	
400.58	4169.22	7234.85	
1077.53	6100.93	10584.18	
2088.67	8382.92	14547.01	
3498.39	10796.81	18736.89	
5315.33	13270.66	23029.97	

TABLE IV

EFFECT OF EXTERNAL UNIFORM PRESSURE ON  
FREQUENCIES (CYCLES/SEC.) IN BUCKLING  
MODE COMPARISON OF THEORIES

Parameters:  $h/2a = 0.01$ ,  $l/2a = 0.2$   
Buckling Mode:  $n = 1$ ,  $m = 9$   
Buckling Pressure:  $P_c = 5083.855$  p.s.i.  
(Flügge's Theory)  
 $P_c = 5071.793$  p.s.i.  
(Timoshenko's Theory)

Flügge's Theory

$P/P_c$	Including Axial Inertia			Neglecting Axial Inertia
	$f_1$	$f_2$	$f_3$	$f_1$
0	517.04	3936.83	6807.24	519.78
0.2	462.47	3929.78	6803.23	464.91
0.4	400.52	3922.72	6799.21	402.62
0.6	327.03	3915.64	6795.19	328.74
0.8	231.25	3908.55	6791.18	232.46
1.0	---	---	---	---

Timoshenko's Theory

$P/P_c$	$f_1$	$f_2$	$f_3$	$f_1$
0	517.05	3937.01	6807.29	519.82
0.2	462.47	3933.98	6807.90	464.94
0.4	400.51	3930.95	6808.52	402.65
0.6	327.02	3927.92	6809.14	328.76
0.8	231.24	3924.90	6809.75	232.47
1.0	---	---	---	---

TABLE V  
EFFECT OF EXTERNAL UNIFORM PRESSURE ON DYNAMIC RESPONSE FOR UNIT IMPULSE

Flügge's Theory

Time = 0.0006 sec.  $P_c = 5071.793$  p.s.i.

Displacements, Strains, Stresses, Given in Inch Units

$P/P_c$	$u \times 10^{12}$	$v \times 10^5$	$w \times 10^2$	$\epsilon_x \times 10^5$	$\epsilon_\phi \times 10^4$	$\gamma_{x\phi} \times 10^{13}$	$\sigma_x$	$\epsilon_\phi$	$\tau_{x\phi} \times 10^6$
0	-2.7277	0.0000	2.9461	-3.3372	2.7508	0.0000	1968.3	8903.5	0.0000
0.25	0.4485	0.0000	3.5206	-2.0180	2.8794	0.0000	2558.3	9449.1	0.0000
0.50	4.3863	0.0000	4.2052	-0.2079	2.9856	0.0000	3282.7	10053.0	0.0000
0.75	9.5507	0.0000	5.0398	2.140	3.0685	0.0000	4174.5	10597.0	0.0000
0	0.5760	4.0157	-0.0656	-0.1681	-0.0582	-2.3409	-122.3	-215.5	-2.6336
0.25	0.5523	4.2870	-0.0646	-0.2117	-0.0576	-2.3987	-136.2	-218.2	-2.6985
0.50	0.5073	4.4458	-0.0589	-0.1895	-0.0559	-2.3412	-128.0	-213.5	-2.6338
0.75	0.7580	4.4566	-0.0486	-0.1261	-0.0552	-2.1625	-105.8	-203.9	-2.4329
0	-6.9778	0.0000	2.9403	-2.6418	2.8352	0.0000	2298.0	9271.6	0.0000
0.25	-3.8182	0.0000	3.5164	-1.2752	2.9730	0.0000	2914.2	9890.4	0.0000
0.50	0.299	0.0000	4.2035	0.5278	3.0853	0.0000	3649.1	10472.0	0.0000
0.75	5.5291	0.0000	5.0327	0.2847	3.1696	0.0000	4527.0	11018.0	0.0000
0	1.2938	1.0068	-0.0457	0.5808	-0.0562	-2.5181	189.7	46.37	-2.8329
0.25	1.2645	1.2954	-0.0449	0.5879	-0.0457	-2.617	193.3	50.72	-2.9446
0.50	1.2255	1.4828	-0.0398	0.5382	-0.0033	-2.566	198.2	56.22	-2.8862
0.75	1.1860	1.5337	-0.0299	0.6123	-0.0018	-2.349	204.6	62.75	-2.6430

Without In-Plane Inertia With In-Plane Inertia

TABLE VI  
DYNAMIC RESPONSE FOR UNIT IMPULSE WITH AND WITHOUT IN-PLANE INERTIA  
Flügge's Theory

Time = 0.0006 sec.  $P/P_c = 0.5$

Displacements, Strains, Stresses, Given in Inch Units  
Including In-Plane Inertia

$\phi$	$u \times 10^{12}$	$v \times 10^5$	$w \times 10^2$	$\epsilon_x \times 10^5$	$\epsilon_\phi \times 10^4$	$\gamma_{x\phi} \times 10^{12}$	$\sigma_x$	$\sigma_\phi$	$\tau_{x\phi} \times 10^5$
0	4.3863	0.0000	4.2052	-0.2079	2.9856	0.0000	3288.70	10053.00	0.0000
$\pi/4$	-1.3593	-1.0792	0.2489	-0.5523	-0.0021	1.1629	-188.76	-69.21	1.3083
$\pi/2$	0.5073	4.4468	-0.0589	-0.1895	-0.0569	-0.2341	-128.00	-213.45	-0.2634
$3\pi/4$	0.3238	-1.5013	-0.0361	0.1045	-0.0392	0.1412	-8.82	-120.53	-0.1589
$\pi$	0.5995	0.0000	0.0180	0.2459	-0.0362	0.0000	42.27	-94.49	0.0000
Neglecting In-Plane Inertia									
0	0.2987	0.0000	4.2035	0.5278	3.0853	0.0000	3649.10	10472.00	0.0000
$\pi/4$	2.7424	4.5379	0.2693	1.2245	-0.00451	0.5581	408.19	122.53	0.6279
$\pi/2$	1.2295	1.4828	-0.0398	0.5982	-0.00328	-0.2566	198.11	56.22	-0.2886
$3\pi/4$	1.3112	-1.2071	-0.01681	0.6377	-0.00178	0.1667	213.23	65.74	-0.1875
$\pi$	1.5129	0.0000	0.03737	0.7256	0.00408	0.0000	249.47	95.39	0.0000

TABLE VII  
EFFECT OF EXTERNAL UNIFORM PRESSURE ON DYNAMIC RESPONSE FOR UNIT IMPULSE  
Comparison of Theories with In-Plane Inertia Included

Time = 0.0006 sec.

Displacements, Stresses, Strains Given in Inch Units

P/P <sub>c</sub>	u × 10 <sup>12</sup>	v × 10 <sup>5</sup>	w × 10 <sup>2</sup>	ε <sub>x</sub> × 10 <sup>5</sup>	ε <sub>φ</sub> × 10 <sup>4</sup>	γ <sub>xφ</sub> × 10 <sup>13</sup>	σ <sub>x</sub>	σ <sub>φ</sub>	τ <sub>xφ</sub> × 10 <sup>6</sup>
0	-2.7277	0.0000	2.9461	-3.3372	2.7508	0.0000	1968.3	8908.5	0.0000
0.25	0.4485	0.0000	3.5206	-2.0180	2.8794	0.0000	2558.3	9491.0	0.0000
0.50	4.3863	0.0000	4.2052	-0.2079	2.9856	0.0000	3288.7	10053.0	0.0000
0.75	9.5507	0.0000	5.0308	2.140	3.0685	0.0000	4174.5	10597.0	0.0000
0	0.5760	4.0157	-0.0656	-0.1681	-0.0582	-2.3409	-122.3	-215.5	-2.6336
0.25	0.5523	4.2870	-0.0646	-0.2117	-0.0576	-2.3987	-136.2	-218.2	-2.6985
0.50	0.5073	4.4458	-0.0589	-0.1895	-0.0569	-2.3412	-128.0	-213.5	-2.6338
0.75	0.7580	4.4566	-0.0486	-0.1261	-0.0562	-2.1625	-105.8	-203.9	-2.4329
0	-4.7460	0.0000	2.9456	-2.7139	2.7469	0.0000	2174.2	8965.3	0.0000
0.25	-1.2307	0.0000	3.5196	-1.2115	2.8661	0.0000	2815.6	9536.8	0.0000
0.50	3.0350	0.0000	4.2042	0.6924	2.9604	0.0000	3564.1	10069.0	0.0000
0.75	8.6714	0.0000	5.0300	3.1742	3.0282	0.0000	4478.0	10577.0	0.0000
0	0.2610	4.0601	-0.0656	-0.3017	-0.0559	-2.4608	-164.8	-222.8	-2.768
0.25	0.3678	4.3612	-0.0645	-0.2685	-0.0554	-1.9987	-152.9	-217.1	-2.249
0.50	0.3178	4.5464	-0.0589	-0.2625	-0.0551	-1.4416	-150.5	-215.4	-1.622
0.75	0.5896	4.5793	-0.0485	-0.1828	-0.0548	-0.7995	-123.4	-205.6	-0.899



TABLE VIII  
DYNAMIC RESPONSE FOR UNIT IMPULSE WITH IN-PLANE INERTIA

Comparison of Theories

Time = 0.0006 sec.  $P/P_c = 0.5$

Displacements, Strains, Stresses Given in Inch Units

Flügge's Theory

$\phi$	$u \times 10^{12}$	$v \times 10^5$	$w \times 10^2$	$\epsilon_x \times 10^5$	$\epsilon_\phi \times 10^4$	$\gamma_{x\phi} \times 10^{12}$	$\sigma_x$	$\sigma_\phi$	$\tau_{x\phi} \times 10^5$
0	4.3863	0.0000	4.2052	-0.2079	2.9856	0.0000	3288.70	10053.00	0.0000
$\pi/4$	-1.3593	-1.0792	0.2489	-0.5523	-0.0021	1.1629	-188.76	-69.21	1.3083
$\pi/2$	0.5073	4.4458	-0.0589	-0.1895	-0.0569	-0.2341	128.00	-213.45	-0.2634
$3\pi/4$	0.3238	-1.5013	-0.0361	-0.1045	-0.0392	0.1412	-8.82	-120.53	-0.1589
$\pi$	0.5995	0.0000	0.0180	0.2459	-0.0362	0.0000	42.27	-94.49	0.0000

Timoshenko's Theory

$\phi$	$u \times 10^{12}$	$v \times 10^5$	$w \times 10^2$	$\epsilon_x \times 10^5$	$\epsilon_\phi \times 10^4$	$\gamma_{x\phi} \times 10^{12}$	$\sigma_x$	$\sigma_\phi$	$\tau_{x\phi} \times 10^5$
0	3.0350	0.0000	4.2042	0.6924	2.904	0.0000	3564.1	10069.00	0.0000
$\pi/4$	-1.3883	-1.1953	0.2485	-0.4348	-0.0118	1.4390	-169.02	-115.69	1.6189
$\pi/2$	0.3178	4.5464	-0.0589	-0.2625	-0.051	-0.1442	-150.53	-215.36	-0.1622
$3\pi/4$	0.2017	-1.5087	-0.0361	0.0513	-0.0400	0.0441	-27.73	-129.34	0.0496
$\pi$	0.549	0.0000	0.0180	0.2142	-0.0371	0.0000	30.52	-101.20	0.0000

TABLE IX  
EFFECT OF EXTERNAL UNIFORM PRESSURE AND LOADING AREA ON DYNAMIC RESPONSE FOR UNIT IMPULSE  
Flügge's Theory with In-Plane Inertia Included

Time = 0.0006 sec.  $\phi = 0.0$

Displacements, Strains, Stresses Given in Inch Units

P/F <sub>c</sub>	u × 10 <sup>12</sup>	v × 10 <sup>5</sup>	w × 10 <sup>2</sup>	$\epsilon_x \times 10^5$	$\epsilon_\phi \times 10^4$	$\gamma_{x\phi} \times 10^{13}$	$\sigma_x$	$\sigma_\phi$	$\tau_{x\phi} \times 10^6$
0	-2.7277	0.0000	2.9461	-3.3372	2.7508	0.0000	1968.3	8908.5	0.0000
0.40	2.8774	0.0000	3.9164	-0.9363	2.9459	0.0000	2998.1	9837.2	0.0000
0.60	6.3306	0.0000	4.5165	0.6686	3.0216	0.0000	3623.7	10273.0	0.0000
0.80	10.5790	0.0000	5.21620	2.6315	3.0823	0.0000	4355.7	10699.0	0.0000
0	-5.0438	0.0000	10.3530	-8.1653	9.0096	0.0000	7380	29489	0.0000
0.40	11.8610	0.0000	13.9770	-1.3521	10.0576	0.0000	10858	33792	0.0000
0.60	22.596	0.0000	16.2100	3.4277	10.5435	0.0000	13018	35970	0.0000
0.80	35.860	0.0000	18.802	9.2771	11.0011	0.0000	15507	38172	0.0000
$\epsilon_1, \epsilon_2$	u × 10 <sup>12</sup>	v × 10 <sup>5</sup>	w × 10 <sup>2</sup>	$\epsilon_x \times 10^5$	$\epsilon_\phi \times 10^4$	$\gamma_{x\phi} \times 10^{13}$	$\sigma_x$	$\sigma_\phi$	$\tau_{x\phi} \times 10$
2,2	6.3306	0.0000	4.5165	0.6686	3.0216	0.0000	3623.7	10273.0	0.0000
4,4	22.5960	0.0000	16.2100	3.4277	10.5435	0.0000	13018.0	35970.0	0.0000
8,8	69.471	0.0000	44.794	25.4101	27.2613	0.0000	39245	94865	0.0000
16,16	-92.041	0.0000	53.917	-43.092	46.237	0.0000	37437	151200	0.0000

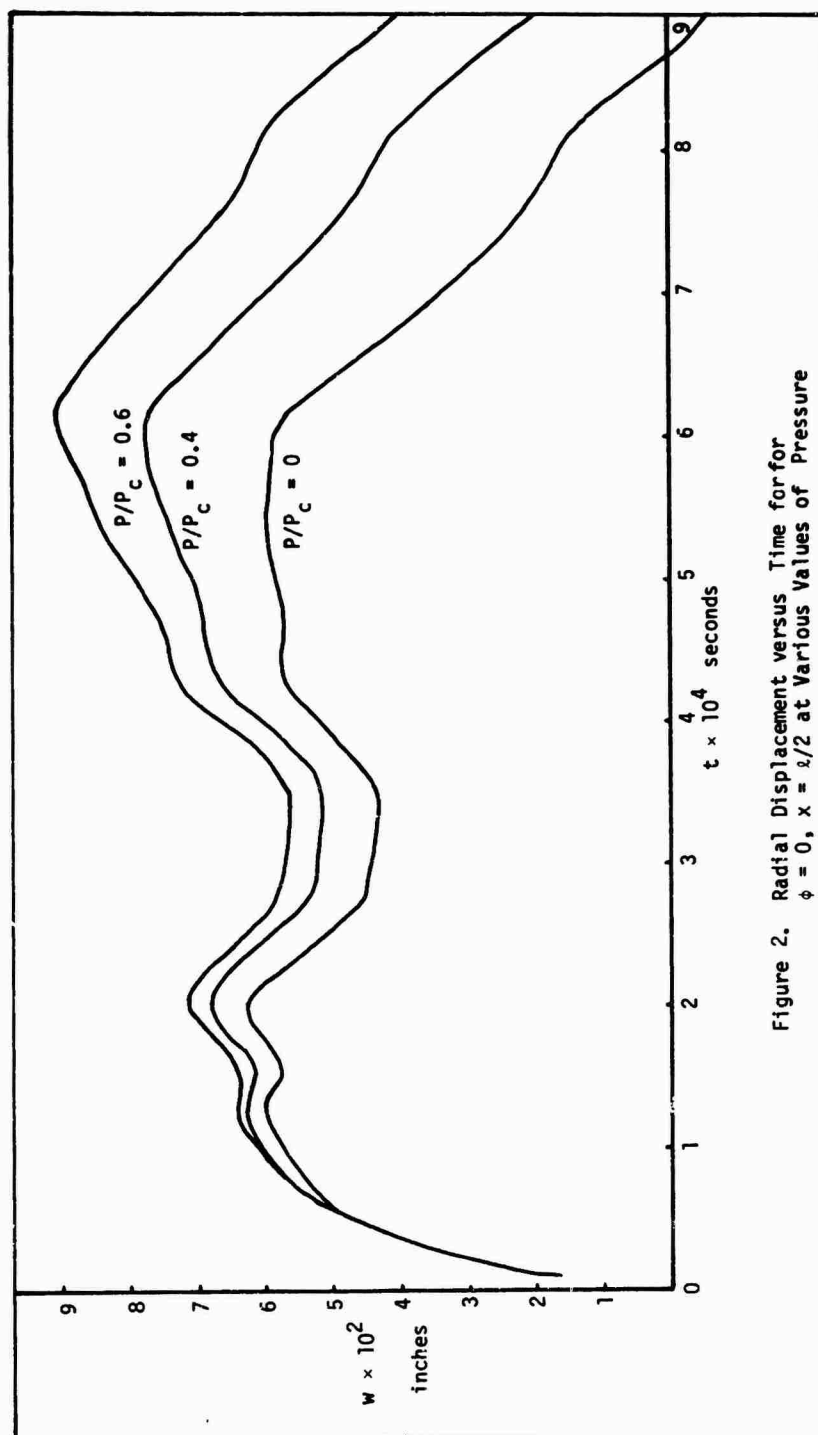
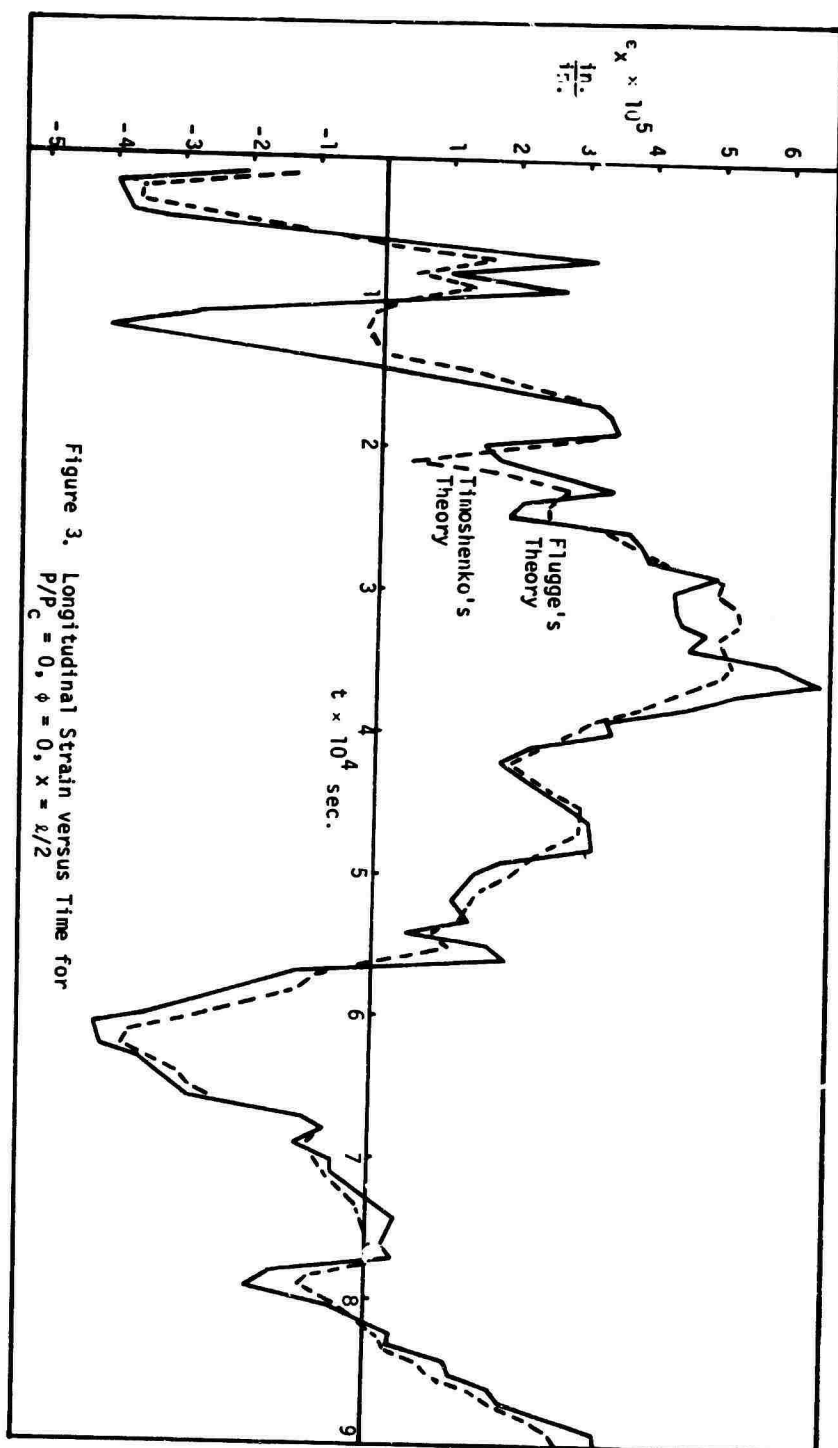


Figure 2. Radial Displacement versus Time for for  $\phi = 0$ ,  $x = 1/2$  at Various Values of Pressure



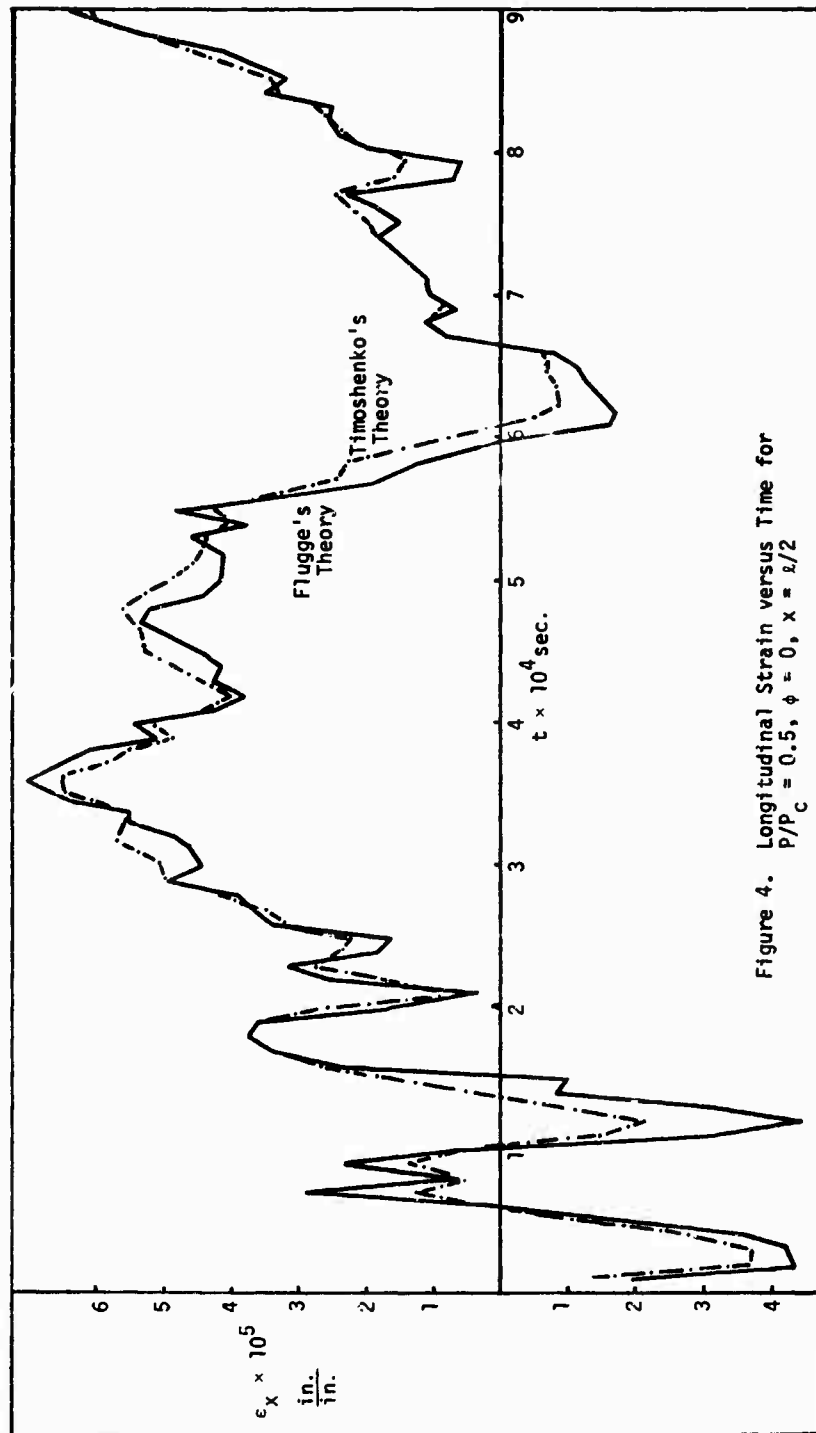


Figure 4. Longitudinal Strain versus Time for  $P/P_C = 0.5$ ,  $\phi = 0$ ,  $x = l/2$

## Conclusions

External uniform pressures of large magnitude and small variations of impulsive area widths greatly affect the dynamic response of cylindrical isotropic shells subjected to a localized impulsive loading.

For free vibrations pressures of large magnitude reduce the lower frequencies substantially while the higher frequencies are not appreciably affected. Uniform pressures in the neighborhood of 50 percent of the buckling pressure can reduce the fundamental frequencies by 30 percent, while the higher frequencies normally the membrane mode frequencies of the  $n, m$  mode will have no appreciable change.

Comparison of frequencies with the Flugge and Timoshenko theories show good agreement for  $n = 1, m = 9$ , Table IV; however for low order bending modes ( $n = 2, m = 1$ ) there may indeed be a moderate difference in the frequencies.

For forced vibrations as illustrated by a localized unit impulse, the following conclusions can be made:

a. Large external uniform pressures have predominantly large effects on longitudinal displacements and strains. Consequently the longitudinal stresses,  $\sigma_x$  will be more sensitive to change while the circumferential strains and stresses will increase moderately.

b. Shearing stresses also decrease as demonstrated in Table VII.

c. Radial displacements and response times will have considerable increases as shown in Figure 2.

d. Increasing the width of loading can produce large changes in the displacements and stresses as shown in Table IX.

e. Comparison of the theories, with or without in-plane inertias indicates that good agreement exists between the radial and circumferential displacements, while the greatest discrepancy occurs in longitudinal displacements and strains.

## References

- [1] Liao, E.N.K., and Kessel, P.G., "Dynamic Response of Cylindrical Shells With Initial Stress and Subjected to General Three-Dimensional Surface Loads," *Journal of Applied Mechanics*, Vol. 38, No. 4, 1971, pp. 978-986.
- [2] Flugge, W., *Stresses in Shells*, Springer-Verlag, Berlin, Germany, 1960.
- [3] Greenspon, J.E., "Vibrations of a Thick-Walled Cylindrical Shell - Comparison of the Exact Theory with Approximate Theories," *Journal of the Acoustical Society of America*, Vol. 32, No. 5, May 1960, pp. 571-578.

## Acknowledgements

This research was performed under the sponsorship of the Office of Naval Research. Computations were done at the University of Massachusetts Research Computer Center, Amherst, Massachusetts.

ON DEFINING TIME DOMAINS FOR  
RADIATION DAMPING AND ADDED MASS EFFECTS  
IN FLUID-STRUCTURAL INTERACTION

Alfred V. Clark, Jr.  
Naval Research Laboratory  
Washington, D.C. 20375

A study is made of the behavior of an oscillator composed of a rigid sphere immersed in an acoustic fluid of infinite extent, and coupled to a fixed base by an elastic spring. The sphere is impulsively excited and its subsequent motion calculated. For high-frequency oscillators, it is found that radiation damping by the fluid determines the form of motion for all times. For low-frequency oscillators, added mass effects dominate the solution for times on the order of a period of the oscillator. The assumption of radiation damping is shown to approximate the exact solution for low-frequency oscillators at early-times, but underestimates peak response.

INTRODUCTION

In the study of fluid-structural interaction problems, attempts are often made to approximate fluid effects due to structural motion by "radiation damping" or "added mass." In general, the statement is made that radiation damping is valid for "high-frequency, early-time" phenomena, and added-mass (or accession to inertia) for "low-frequency, late-time" phenomena. For vibration problems, where transient effects can be ignored, one can use the ratio of structural to acoustic wavelengths to determine whether high- or low-frequency effects are dominant.

For underwater shock phenomena, "early time" is often described as being much less than the time necessary for a shockwave to transit the body, so that the time scale is based on geometric considerations. However, it can be shown that there are cases for which radiation damping influences the motion of the structure for times much later than early-times.

To obtain estimates of the relative importance of radiation damping for various time (or frequency) regions, a study has been made of the response of a simple single-degree-of-freedom oscillator submerged in an infinite acoustic medium, and subjected to an impulsive excitation. It can be shown that the loading due to structural motion through the fluid, i.e., the "radiation loading" can be represented by the convolution of the oscillator acceleration with a "hydrodynamic function." This hydrodynamic function represents the load on the oscillator when given a step-velocity change, so that it is a generalized impulse response.

For an arbitrary body, it is difficult to

find the exact form of this function, so various schemes for approximating it have been proposed; these schemes take advantage of the early- and late-time behavior of the function, and attempt to approximate its behavior at intermediate times. Since the presence of the convolution integral in the equation of motion of the oscillator increases its complexity, it is desirable to know when it is permissible to use radiation damping and added mass theories in underwater shock problems.

By examining the equation of motion in dimensionless form, it can be shown that a relevant parameter is the dimensionless time (or frequency) ratio  $\epsilon$ , defined to be the ratio of the period of the oscillator to the time for an acoustic wave to pass around the body perimeter. If  $\epsilon \ll 1$ ; i.e., for a high-frequency oscillator (by this definition), radiation damping will be the dominant mechanism in determining structural motion for all times of interest. For  $\epsilon \gg 1$ , low-frequency oscillators, added mass effects will be dominant for times which are of the order of magnitude of oscillator period.

This paper considers the case of a rigid, oscillating sphere, since it is possible to solve for the hydrodynamic function exactly, and examine its effect on oscillator motion. It is shown that there is no "boundary layer" in time for which radiation damping is dominant, and is to be matched with added-mass effects occurring at a later time. Rather, in those cases for which added mass effects are dominant, these effects are present at all times; for cases in which radiation damping is dominant, it will be dominant at all times. The frequency ratio  $\epsilon$  is the factor which determines the character of the solution; it is shown that indiscriminate use of early-time radiation damping in conjunction

with low-frequency oscillators or late-time added mass with high-frequency oscillators can lead to erroneous results.

#### EQUATIONS OF MOTION AND INTERACTION

Consider a rigid sphere submerged in an acoustic medium and connected to a rigid base by an elastic spring as shown in Fig. 1. It is assumed that the acoustic impedance seen by the

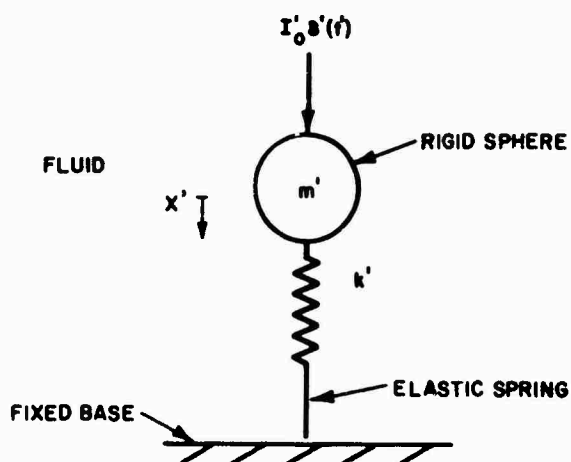


Fig. 1. Rigid Sphere Immersed in Acoustic Medium and Connected to Fixed Base by Elastic Spring

sphere is that of an infinite medium. The sphere is initially at rest and is given an impulse at  $t' = 0^*$ . The resulting motion of the sphere is determined from the equation

$$m' \ddot{x}'(t') + k' x'(t') = + F'_f(t') + I'_0 \delta'(t') \quad (1)$$

where  $m'$  = mass of sphere  
 $x'$  = displacement of sphere  
 $k'$  = stiffness of spring  
 $F'_f$  = fluid force on sphere  
 $I'_0$  = impulse  
 $\delta'$  = Dirac delta function.

Obviously, we need the value of  $F'_f$ , to specify the problem completely.

The fluid force,  $F'_f$ , arises due to the sphere's motion through the fluid. Let  $\sigma'$  denote the surface of the body, and  $y'$  denote displacement of the body along its outward normal. If  $y' = \varphi(\sigma') x'(t')$  with  $\varphi$  a dis-

\*We use primes to denote dimensional quantities; unprimed quantities are dimensionless.

placement pattern and  $x'$  a generalized coordinate, the fluid force can be related to body motion by the following equation [1]:

$$F'_f(t') = - \int_{\sigma'}^{\infty} \lambda'(t' - \tau') \ddot{x}'(\tau') d\tau' \quad (2)$$

It can be verified by direct substitution that the impulse response function,  $\lambda'$ , is proportional to the fluid force acting on the body when the body is given a step-velocity change in displacement pattern  $\varphi(\sigma')$ ; i.e., when  $\dot{y}'(\sigma', t') = \theta' \delta'(t') \varphi(\sigma')$ . Except for simple geometries, we do not have exact expressions for  $\lambda'(t')$ ; however, it is possible to generate approximations which will give early-time radiation and late-time added mass behavior.

For the rigid, oscillating sphere, we can calculate  $\lambda'$  by first determining the pressure acting over its surface due to a step velocity change. When the sphere is given the velocity  $\dot{y}'(\sigma', t') = \theta' \delta'(t') \varphi(\sigma')$ , the pressure over its surface can be computed from [1]

$$P'(\sigma', t') = \int_{\tau'=0}^{\infty} z'(\sigma', t' - \tau') \ddot{x}'(\tau') d\tau' \quad (3)$$

For the sphere, let  $\dot{y}'(\sigma', t') = \frac{\theta'}{V_0} \delta'(t') \cos \theta$

where  $\theta$  is the angle between the outward normal and the  $x'$ -direction in Fig. 2.

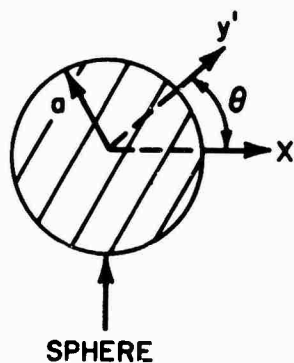


Fig. 2. Defines Angle  $\theta$

Then the associated pressure  $P'_\theta(\sigma', t')$  is

$$P'_\theta(\sigma', t') = \int_{\tau'=0}^{\infty} z'(\sigma', t' - \tau') \frac{\theta'}{V_0} \delta'(\tau') d\tau' \quad (4)$$



which shows that

$$z'(\sigma', t') = P'_0(\sigma', t') / \dot{V}'_0$$

The surface pressures for the sphere given a velocity step have been calculated to be

$$P'_0(\sigma', t') = \rho c \dot{V}'_0 e^{-w'_1 t'} \cos(w'_1 t') (\cos \theta) \quad (5)$$

where  $w'_1 = c/a$ ,  $c$  = sound speed in fluid, and  $a$  is the sphere radius [2].

The force associated with this pressure is computed from

$$F'_f(t') = - \oint_{\sigma'} P'(\sigma', t') \cos \theta d\sigma' \quad (6)$$

where the integration is performed over the sphere surface; from equations (2), (3), and (5), it is found that

$$\lambda'(t') = \oint_{\sigma'} z'(\sigma', t') \cos \theta d\sigma'$$

for the oscillating sphere. Consequently,

$$\lambda'(t') = \frac{4\pi a^2}{3} \rho c e^{-w'_1 t'} \cos w'_1 t' H(t') \quad (7)$$

with  $H(t')$  the Heaviside step function.

Substituting this result into equation (2), taking the Laplace transform of (2) for zero initial conditions, and rearranging leads to:

$$\left[ (s')^2 + 2w'_1 s' + 2w_1^2 \right] \bar{F}'_f(s') = \frac{-\rho c A}{3} (s')^2 (s' + w'_1) \bar{x}'(s') \quad (8)$$

with  $A$  = the area of the sphere.

This can be inverted to give the differential equation

$$\ddot{F}'_f(t') + 2w_1 \dot{F}'_f(t') + 2w_1^2 F'_f(t') = \frac{-\rho c A}{3} \left( \ddot{x}'(t') + w'_1 \dot{x}'(t') \right) \quad (9)$$

provided that appropriate initial conditions vanish. We can guarantee this by letting our system respond at  $t' = 0$ , a short time after the application of the impulse.

Equation (9) is the interaction equation which relates fluid force to oscillator motion. Combined with (1), it completely defines the problem, giving rise to a 4th order set of equations.

It is convenient to cast the problem in dimensionless form; to this end, we set

$$\begin{aligned} w'_0 &= \sqrt{k'/m'}, \text{ natural frequency in vacuo} \\ t &= w'_0 t' \\ x &= x'/a \\ m'_w &= \rho a A / 3 \\ I_0 &= I'_0 / (m' a w'_0) \end{aligned}$$

$$F = F'_f / (m' a (w'_0)^2)$$

$$\epsilon = w'_1 / w'_0$$

$$\dot{x} = dx/dt$$

$$m = m'_w / m'$$

The system of equations (1) and (9) assume the dimensionless form

$$\ddot{x}(t) + x(t) - F(t) = I_0 \delta(t) \quad (10)$$

$$\begin{aligned} \ddot{F}(t) + 2\epsilon \dot{F}(t) + 2\epsilon^2 F(t) = \\ -m\epsilon \left[ \ddot{x} + \epsilon \dot{x} \right] \end{aligned} \quad (11)$$

Note the quantity  $m\epsilon$  is a measure of the coupling between the fluid and the sphere; this quantity has several physical interpretations

Writing

$$m\epsilon = \left( \frac{\rho c A}{3} \right) / (m' w'_0) = R$$

shows that  $R$  is the ratio of two impedance-like terms. The denominator represents the impedance of the sphere-spring system in vacuo, whereas the numerator is the early-time impedance of a piston with surface area equal to  $1/3$  of the sphere surface. Hence,  $R$  is the ratio of the "fluid impedance" to the "oscillator impedance in vacuo." For simplicity, we let  $m \sim 0(1)^*$  in this paper.

Since  $w'_1$  is the frequency (and decay constant) for  $\lambda'(t')$ , we have another interpretation of  $R$ . The quantity  $\epsilon$  measures how fast  $\lambda'(t')$  is oscillating (and decaying) relative to the sphere-spring oscillator. When  $\epsilon$  is small, then  $w'_1 \ll w'_0$  and we have a "high-frequency oscillator."  $\lambda'(t')$  remains essentially constant (a Heaviside step-function), while the oscillator executes many vibrations. For large  $\epsilon$ , we have a low-frequency oscillator;  $\lambda'(t')$  oscillates (and decays) rapidly, while the oscillator is slowly responding.

In the literature, it is sometimes stated that the submerged body moving through the fluid radiates plane-waves for "early-times," or that the fluid can be represented as an added-mass for "late-times." It is proposed to deduce from the equations of motion and interaction for the sphere what the effect these phenomena have upon oscillator motion. Since the parameter  $\epsilon$  is a measure both of frequency and fluid-oscillator coupling in the interaction equation (11), it is natural to consider what happens to this equation (and the equation of motion (10)) when  $\epsilon$  becomes asymptotically small or large. That is, we look at the behavior of the equations for high- and low-frequency oscillators. We will find the exact solution for oscillator displacement  $x$  by taking the Laplace transform of the coupled set of equations (10) and (11) then rearranging to obtain an equation for  $x$ ; this will have the form  $x = N(s)/D(s)$ , with  $x$  the Laplace transform

\*The notation  $m \sim 0(1)$  means that  $(m)$  is of the order of magnitude of unity.

of  $x$ . We use the residue theorem to solve for  $x$ ; to do so, we must find the roots of the denominator  $D(s)$ . We will discover that the location of the roots is easily estimated for  $\epsilon \gg 1$  and  $\epsilon \ll 1$ ; i.e., for low- and high-frequency oscillators. One set of roots will be of order of magnitude unity; the other set will be of order  $\epsilon$ . The first set of roots correspond to vibrations on the time scale of the oscillator period in vacuo. The second set of roots correspond to motion on what we call the "intermediate-time" scale,  $t' \sim 0(a/c)$ . We will show that the residues associated with this latter set of roots become vanishingly small for low- and high-frequency oscillators. In the asymptotic analysis section, we show why we should expect this behavior. Furthermore, we show that using radiation damping to predict the response of low-frequency systems is only valid for early-times, and that maximum oscillator excursions occur (for  $\epsilon \gg 1$ ) at late-times. The early-time damping theory will be shown to underpredict peak oscillator displacement by a factor proportional to  $1/\epsilon$ , for  $\epsilon \gg 1$ .

#### EXACT SOLUTION FOR OSCILLATING SPHERE

Returning to the system of equations (10) and (11), taking the Laplace transform for zero initial conditions, and combining the two transformed equations results in

$$\bar{x}(s) = \frac{I_0 [(s + \epsilon)^2 + \epsilon^2]}{[(s^2 + 1)(s^2 + 2\epsilon s + 2\epsilon^2) + s^2(m)(s + \epsilon)]} \quad (12)$$

Here  $s = s'/w'_0$ ,  $s'$  being the (dimensional) Laplace transform variable, and

$$\bar{x}(s) = \int_{t=0}^{\infty} e^{-st} x(t) dt \quad (13)$$

We rewrite our equation on  $\bar{x}$  as

$$\bar{x}(s) = \frac{I_0 [(s + \epsilon)^2 + \epsilon^2]}{(s - s_1)(s - s_2)(s - s_3)(s - s_4)} \quad (14)$$

where  $s_1, s_2$  etc., are roots of the denominator in (12).

Now late-times are those for which  $t' \gg a/c$ ; recall that our dimensionless time  $t$  is given by  $w'_0 t'$ . For low-frequency oscillators, late times will correspond to  $t \sim 0(1)$ , since  $w'_0 \ll a/c$ ; that is, late-times correspond to times on the order of magnitude of the oscillator period. Thus, for low-frequency oscillators at late times, we set  $\epsilon \gg 1$  and  $s \sim 0(1)$  in (12); the denominator in (12) will then be approximated by

$$2\epsilon^2 (s^2 + 1) + s^2 \epsilon^2 (m) \approx 0 \quad (15)$$

which gives us the roots

$$s_{3,4} = \pm i \left[ \frac{2}{2 + m} \right]^{1/2} \quad (16)$$

This gives us an undamped sinusoidal vibration for low-frequencies at late-times. The ratio of this submerged frequency to the in vacuo frequency is:

$$\frac{w'_{sub}}{w'_0} = \left[ \frac{2}{2 + m} \right]^{1/2}, \text{ which shows how the}$$

"added mass" effect lowers the frequency.

Now let us consider the low-frequency case at intermediate times; we have  $t' \sim 0(a/c)$ , so that  $t \sim 0(w'_0 a/c)$ , or  $t \sim 0(1/\epsilon)$ . For motion to occur on the intermediate time scale, we require that  $s \sim 0(\epsilon)$ . The denominator becomes, approximately,

$$s^4 + \epsilon s^3 (2 + m) + \epsilon^2 s^2 (2 + m) \approx 0 \quad (17)$$

which has roots

$$s_{1,2} = -\frac{\epsilon}{2} \left[ (2 + m) \pm \{(2 + m)^2 - 4(2 + m)\}^{1/2} \right] \quad (18)$$

If the mass of displaced water,  $m'_w$ , is greater than  $2m'$ , then  $s_{1,2}$  will be real; this gives exponentially decaying solutions to the equation of motion at intermediate-times. If  $m'_w < 2m'$ , then the sphere will experience damped vibration for intermediate-times.

Consider the high-frequency case  $\epsilon \ll 1$ , and let us look at intermediate-time solutions;  $s \sim 0(\epsilon)$  or,  $s \ll 1$ . The denominator reduces to\*

$$s^2 + 2\epsilon s + 2\epsilon^2 \approx 0 \text{ or } s_{3,4} = -\epsilon \pm i\epsilon; \quad (19)$$

we see that intermediate-time solutions correspond to lightly-damped, slow oscillations. For early-times,  $t' \ll a/c$ ; in the case of high-frequency oscillators,  $w'_0 \gg a/c$ . Thus, early-times for high-frequency oscillators are those for which  $t \sim 0(1)$ . Motion occurring on this time-scale will be associated with roots for which  $s \sim 0(1)$ . For  $\epsilon \ll 1$  and  $s \sim 0(1)$ , we have:

$$s^2 + \epsilon m s + 1 \approx 0 \quad (20)$$

which has roots

$$s_{1,2} = -\frac{\epsilon}{2} \left[ m \pm \{m^2 - 4\}^{1/2} \right] \quad (21)$$

Depending on the sign of the discriminant, we can have underdamped, critically damped, or over-damped solutions. However, since we have stipulated that  $\epsilon \ll 1$ , it will take a large mass ratio  $m$  to give us an overdamped solution, even for early-times.

Roots for the specific case of  $m = 2.5$  are given in Table A. The early time roots for  $\epsilon \ll 1$  are given as  $s_1$  and  $s_2$ , as are intermediate-time roots for  $\epsilon \gg 1$ ; intermediate and late-time roots for  $\epsilon \ll 1$  and  $\epsilon \gg 1$  are  $s_3$  and  $s_4$ . These are in good agreement with the asymptotic

\* We assume  $\epsilon m \ll 1$ ,  $\epsilon^2 m \ll 1$

roots listed above.

For the high-frequency cases ( $\epsilon = .01, .10$ ) we have a solution in the form of decaying sinusoids.

$$\begin{aligned} X(t) &= X_e(t) + X_i(t) \\ &= \frac{I_0}{b_1} e^{a_1 t} [Q_1 \sin b_1 t + Q_2 \cos b_1 t] \\ &\quad + \frac{I_0}{b_3} e^{a_3 t} [Q_3 \sin b_3 t + Q_4 \cos b_3 t] \end{aligned} \quad (22)$$

where we have set

$$\begin{aligned} s_1 &= a_1 + ib_1 & s_2 &= a_1 - ib_1 \\ s_3 &= a_3 + ib_3 & s_4 &= a_3 - ib_3 \end{aligned}$$

and the constants  $Q_1$  through  $Q_4$  are defined in Table B. Note that  $a_1$  and  $a_3$  are negative. Here  $X_e(t)$  is the early-time solution corresponding to roots  $s_1, s_2$ ;  $X_i(t)$  is the intermediate-time solution.

For the intermediate- ( $\epsilon = 1.0$ ) and low-frequency cases, we have

$$\begin{aligned} X(t) &= X_i(t) + X_l(t) \\ &= \frac{I_0[\alpha_1^2 + \epsilon^2] e^{a_1 t}}{(a_1 - a_2)(A_1^2 + b_3^2)} \\ &\quad + \frac{I_0[\alpha_2^2 + \epsilon^2] e^{a_2 t}}{(a_2 - a_1)(A_2^2 + b_3^2)} \\ &\quad + \frac{I_0}{b_3} e^{a_3 t} [g \sin b_3 t + h \cos b_3 t] \end{aligned} \quad (23)$$

The coefficients are defined in Table C;  $X_i$  is the intermediate-time solution, and  $X_l$  is the late-time solution.

For the high-frequency oscillator, we can show that:

$$\begin{aligned} a_1 &= -\frac{\epsilon}{2} m & a_3 &= -\epsilon \\ b_1 &= 1 & b_3 &= \epsilon \\ Q_1/b_1 &= 1 & Q_2 &= Q_3 = Q_4 = 0 \end{aligned} \quad (24)$$

We see from (21) that the conditions on  $a_1$  and  $b_1$  are fulfilled. To show e.g. that  $Q_4$  vanishes, consider that Table B gives  $Q_4$  as

$$Q_4 = [2(a_3 + \epsilon)b_3 H_1 + A_1 J_1 (\epsilon^2 - b_3^2 + (a_3 + \epsilon)^2)]/M_1 \quad (25)$$

Since  $a_3 = -\epsilon$  and  $b_3 = \epsilon$  (as shown by (19)), we see that  $Q_4$  vanishes; similar results hold for  $Q_2$  and  $Q_3$ . It can also be verified that  $Q_1/b_1 = 1$ , reducing (22) to the high-frequency,

early-time solution

$$X = I_0 e^{-m\epsilon t/2} \sin t H(t-0^+) = \lambda_e$$

A plot of (22) is shown in Fig. 3 for  $\epsilon = .01$  and  $I_0 = 1$ ; it is seen that  $X$  does indeed have the form above.

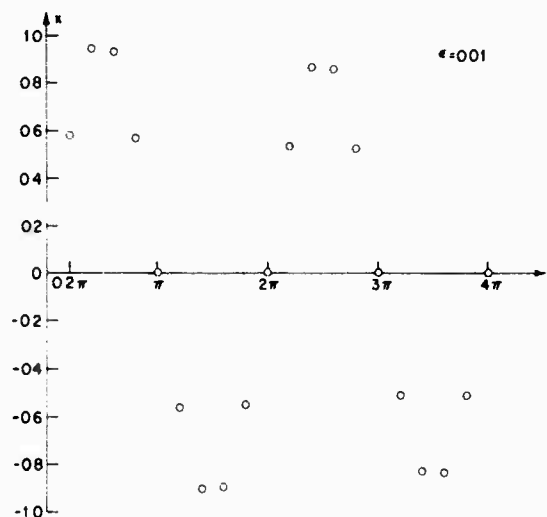


Fig. 3. High-Frequency Oscillator Response

In the instance of the low-frequency oscillator, we wish (23) to reduce to the added

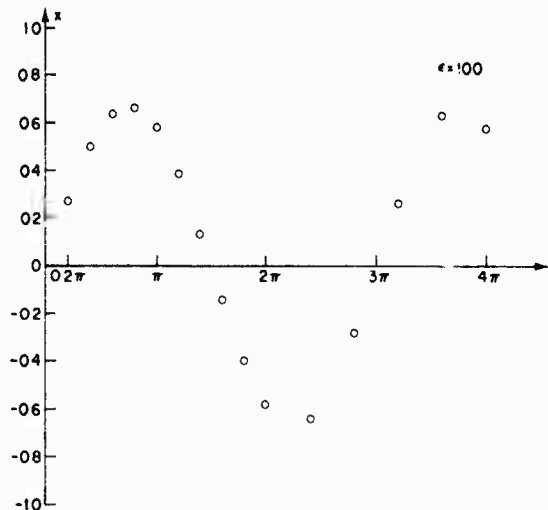


Fig. 4. Low-Frequency Oscillator Response

mass, late-time solution given by  $I_0 b \sin b t - H(t=0)$ . Now the roots given in (17) show that  $a$  becomes vanishingly small, and  $b^2$  equals  $(2/(2+m))$  for  $\epsilon \gg 1$ . Using these results, we find that the coefficients multiplying the exponentials  $e^{at}$  and  $e^{bt}$  in (23) are  $O(1/\epsilon)$ ; the intermediate-time solution then becomes vanishingly small as  $\epsilon$  becomes large. Furthermore, it can be demonstrated that  $h \rightarrow 0$ , so that the late-time solution depends only upon  $(I_0/b) g \sin b t$ . For the specific case of  $m = 2.5$ , we have  $b^2 = 4/9$ ; also,  $g = 9/20.25$  as  $\epsilon \gg 1$  or  $g = b^2$  so that  $(I_0 g)/b = I_0 b_0$ , and we have reduced our general solution (23) to the low-frequency, late-time form. The behavior of (23) is shown in Fig. 4 for  $\epsilon = 100$  and  $I_0 = 1$ . In Fig. 5, we show  $X_i$  and  $X_e$  for  $\epsilon = 10$  over the time domain for which they are the same order of magnitude; this clearly indicates that our solution is dominated by late-time, added-mass effects.

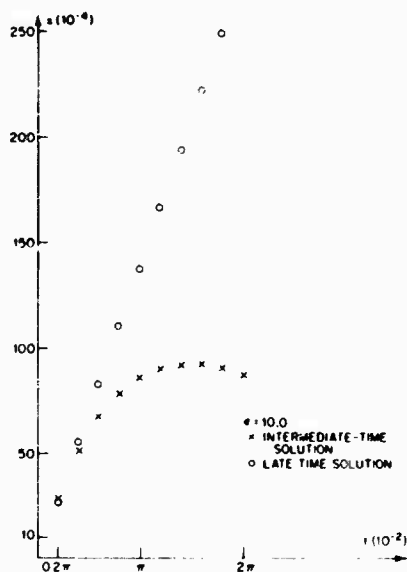


Fig. 5. Intermediate- and Late-Time Solutions for Low-Frequency Oscillator

It is interesting to compare the exact solution for  $\epsilon \gg 1$  with approximate solutions generated by assuming early-time radiation damping. In this case, our interaction equation (11) reduces to  $F(t) = -m \epsilon \dot{X}(t)$ , giving an equation of motion of the form

$$\ddot{X}(t) + m \epsilon \dot{X}(t) + X(t) = I_0 \delta(t) \quad (26)$$

For large  $\epsilon$ , the solution to this is given (approximately) by  $X = I_0 (1 - e^{-m \epsilon t})/(m \epsilon)$ . In Fig. 6, we show the exact solution  $X_e$  (from (23)), and  $X_i$  plotted for early-times. Note that, although good agreement exists between the two for early-times, these times are much shorter than the time necessary for the oscillator to reach its peak excursion. Now  $X_e$  has an upper bound given by  $I_0/m \epsilon$ , whereas

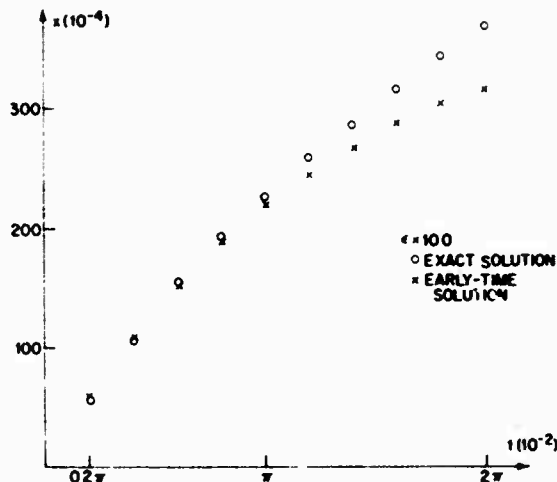


Fig. 6. Early-time and Exact Solutions for Low-Frequency Oscillator

the maximum oscillator excursion, from the exact solution, is given by  $I_0 b$ . Hence, if we were to try to predict peak oscillator displacements using radiation damping, we would underestimate the peak by a factor of  $1/bm \epsilon$  for  $\epsilon \gg 1$ .

#### ASYMPTOTIC ANALYSIS

We previously noted how the poles of our expression for  $\bar{X}(s)$  could be found by assuming motion on time scales  $t \sim O(1)$  and  $t \sim O(1/\epsilon)$ . Note that, although the denominator in (12) is a quartic, this assumption allowed us to simplify the determination of roots of the denominator to the problem of finding roots of a quadratic (see e.g. equations (15), (17), (19), and (20)). We could have further reduced our labor in finding the exact solution had we known that residues associated with poles for which  $s \sim O(\epsilon)$  would become vanishingly small. We will use some ideas from perturbation theory to show why our system of equations (10) and (11), (which give rise to (12)) exhibits this behavior.

We will consider the behavior of the coupled system of equations (10) and (11) for various time scales. We make the assumption that, for each time scale, all the time derivatives of  $F$  are the same order of magnitude; a similar assumption is made concerning derivatives of  $X$ . We then solve the coupled system (for each time scale) and examine the character of the solution. If it is a physically meaningful solution, our assumptions above are valid; physically impossible solutions imply that our assumptions are invalid. In the former case, we have derived a set of equations which govern the behavior of the system for that particular time scale. In

the latter case, our system of equations is discarded as inapplicable. We will use a scale factor  $\hat{s}$ , defined as follows: We let  $\hat{t} = \hat{s}t$ , with  $\hat{t} \sim 0(1)$  and  $\tau = \hat{s}'t'$ ; thus  $\hat{s}$  determines the order of magnitude of (dimensionless) time we are considering. We will discover that the magnitude of  $\hat{s}$  for which we derive meaningful solutions corresponds to the magnitude of the roots of the denominator in equation (12).

### Low-Frequency Oscillators

#### Case 1. Late-times

Considering the low-frequency case first, we look at times much greater than the time for a sound wave to travel around the body. For  $\epsilon \gg 1$ , this corresponds to a time scale  $t \sim 0(1)$ ; i.e., we consider times on the order of a few periods of vibration of the oscillator. Looking at the interaction equation (11), we assume all derivatives of  $F$  with respect to  $t$  are the same order of magnitude, as are all derivatives of  $x$ ; i.e.,  $F \sim 0(F)$  and  $\ddot{x} \sim 0(\ddot{x})$ . Since  $\epsilon \gg 1$ , this allows us to simplify the interaction equation to read  $F \approx -m \ddot{x}$ . Recalling that  $F(t) = -\int_0^t \lambda(t-\tau) \ddot{x}(\tau) d\tau$  and that the added mass  $m'$  is  $(1/2)m'$  for the sphere, we see that  $\lambda(t) \approx (m'/m)$  for low-frequency oscillators on this time scale. We have recovered our low-frequency, late-time approximation on time scale  $t \sim 0(1)$ .

Inserting this form of  $F$  into the equation of motion gives

$$(2+m) \ddot{x}(t) + 2 \dot{x}(t) = 2 I_0 \delta(t)$$

for  $t \sim 0(1)$ ; this has a solution  $X_l = I_0 b \sin bt H(t-0^+)$  with  $b^2 = 2/(2+m)$ . We use the notation  $X_l$  to denote the solution to our equation of motion on the late-time scale. Note that  $X_l$  begins at  $t = 0^+$  to allow satisfaction of the initial conditions.

For times other than late-times, we define a new time variable  $\hat{t} = \hat{s}t$ , where  $\hat{s}$  is a dimensionless scale factor. Substituting this into the interaction equation, we have

$$\hat{s}^2 \frac{d^2 F}{d\hat{t}^2} + 2\epsilon \hat{s} \frac{dF}{d\hat{t}} + 2\epsilon^2 F = -m \epsilon \hat{s}^2 \left[ \hat{s} \frac{d^3 x}{d\hat{t}^3} + \epsilon \frac{d^2 x}{d\hat{t}^2} \right] \quad (27)$$

We will examine the behavior of this equation for various orders of magnitude of  $\hat{s}$ .

#### Case 2. Early-times

Defining early-times as those for which radiation-damping is the dominant fluid mechanism, so that  $-F' = (\rho c A/3) \ddot{x}'(t)$ , requires that  $\lambda' = (\rho c A/3) H(t')$  for early-times. We see that  $\lambda'(t')$  will have this asymptotic form when  $t' \ll a/c$ , or when our dimensionless time  $t$  is of order  $1/\hat{s}$  with  $\hat{s} \gg \epsilon$ . Our interaction equation (27) then has the approximate form

$$\frac{d^2 F}{d\hat{t}^2} = -m \epsilon \hat{s} \frac{d^3 x}{d\hat{t}^3}$$

which states, as expected, that  $F = -m \epsilon \dot{x}$  on this time scale.

Substituting this into our equation of motion (10) gives

$$\hat{s}^2 \frac{d^2 x}{d\hat{t}^2} + m \epsilon \hat{s} \frac{dx}{d\hat{t}} + x = I_0 \delta(t) \quad (28)$$

and, assuming all derivatives are the same order of magnitude and recalling that  $\hat{s} \gg \epsilon$ , we can rewrite (28) in the form

$$\hat{s}^2 \frac{d^2 x}{d\hat{t}^2} + m \epsilon \hat{s} \frac{dx}{d\hat{t}} \approx I_0 \delta(\hat{t})$$

The solution is given by  $X_e = (I_0/\alpha)(1-e^{-\alpha \hat{t}})$  with  $\alpha = m \epsilon$ ; this physically impossible solution corresponds to the solution of (26) and we have shown its behavior in Fig. 6. Since our solution describes a physically unreasonable displacement of the sphere, our coupled set of equations will not admit a solution which varies on the early time scale. We conclude that, although radiation-damping is the dominant fluid mechanism at early-times, these times are too short to significantly affect the oscillator motion. Furthermore, we cannot attempt to "match" this early-time solution to a late-time solution, since the early-time solution approaches the value  $X_e = I_0/\alpha$ .

#### Case 3. Intermediate times

This motivates a search for a solution where time derivatives are the same order of magnitude for intermediate times; i.e., when  $t \sim 0(1/\epsilon)$ , or, in terms of dimensional time,  $\tau \sim 0(a/c)$ .

We take  $\hat{t} = \hat{s}t$ , where now  $\hat{s} \sim 0(\epsilon)$ . Recall that our late-time solution  $X_l$  was given by  $I_0 b \sin bt$ , which will be non-zero even for  $t \sim 0(1/\epsilon)$ ; we must account for  $X_l$  and its derivatives in (10) and (27). Accordingly, we set  $X = X_l + X_i$ , where  $X_i$  will be the solution for intermediate times, and will vanish for late-times, as we will subsequently show. Combining (27) and (10) gives the fourth-order differential equation

$$\hat{s}^4 \frac{d^4 x}{d\hat{t}^4} + (2+m) \epsilon \hat{s}^3 \frac{d^3 x}{d\hat{t}^3} + (2+m) \epsilon^2 \hat{s}^2 \frac{d^2 x}{d\hat{t}^2} +$$

$$\hat{s}^2 \frac{d^2 x}{d\hat{t}^2} + 2\epsilon \hat{s} \frac{dx}{d\hat{t}} + 2\epsilon^2 x =$$

$$I_0 \left( \hat{s}^2 \frac{d^2 \delta}{d\hat{t}^2} + 2 \epsilon \hat{s} \frac{d\delta}{d\hat{t}} + 2\epsilon^2 \delta(t) \right); \quad (29)$$

with the choice  $X = X_l + X_i$ , we reduce this to a simpler form

$$\hat{s}^4 \frac{d^2 X_1}{d\hat{t}^2} + (2+m) \epsilon \hat{s}^3 \frac{d^3 X_1}{d\hat{t}^3} + (2+m) \epsilon^2 \hat{s}^2 \frac{d^4 X_1}{d\hat{t}^4} \approx$$

(29a)

$$I_0 \left( \hat{s}^2 \frac{d^2 \delta}{d\hat{t}^2} + 2 \epsilon \hat{s} \frac{d\delta}{d\hat{t}} + 2 \epsilon^2 \delta \right)$$

This has a solution  $X_1 = (I_0/\epsilon) [a_1 e^{-P_1 t} +$

$$+ a_2 e^{-P_2 t}] H(t-0^+)$$

where  $P_1$  and  $P_2$  are roots of the quadratic

$$P^2 + (2+m) \epsilon P + (2+m) \epsilon^2 = 0; \quad (30)$$

which is the same as equation (17).

It can be shown that the solution corresponding to  $P^2 = 0$  vanishes identically. Note that  $X_1 \rightarrow 0$  as  $t \sim 0(1)$ . Since  $X_1$  does not decay exponentially as intermediate times are approached, we cannot define a region in time where  $X_1$  and  $X_e$  are to be matched. Furthermore,  $X_1$  and  $X_e$  are the same order of magnitude for  $t \sim 0(1/\epsilon)$ , so that no "boundary layer" in time exists; Fig. 5 compares  $X_1$  and  $X_e$  over intermediate-times for  $\epsilon = 10$ .

The constant  $a_1$  and  $a_2$  are  $O(1)$  so that  $X_1$  is  $O(I_0/\epsilon)$  and becomes vanishingly small for low-frequency oscillators,  $\epsilon \gg 1$ . Our solution reduces to the modified impulse response  $I_0 \sin bt$ ; the intermediate-time solution, which arises due to the complicated fluid-structural interaction on time scale  $t \sim 0(1/\epsilon)$ , can be neglected.

#### High-Frequency Oscillators

##### Case 1. Early-times

The high-frequency oscillator corresponds to  $\epsilon \ll 1$ , or  $\omega_1 \ll \omega_0$ . Setting  $\hat{t} = \hat{s}t$  for early-times again gives the interaction equation (27).

With  $\hat{s} \sim 0(1)$  and  $\epsilon \ll 1$ , (27) reduces to

$$F = -m \epsilon \hat{s} \frac{dX}{d\hat{t}} \quad (31)$$

This shows that the fluid force on the sphere is due to radiation damping at early-times for the high-frequency oscillator. Using (31) in the equation of motion, we have

$$\frac{d^2 X}{d\hat{t}^2} + m \epsilon \frac{dX}{d\hat{t}} + X = I_0 \delta(\hat{t}) \quad (32)$$

with solution  $X = I_0 e^{-(m\epsilon/2)\hat{t}} \sin \hat{t} H(\hat{t}-0^+)$ . The characteristic equation for (32) is the same as equation (20).

##### Case 2. Intermediate-times

For intermediate-times, we take  $\hat{t} = \hat{s}t$  where now  $\hat{s} \sim 0(\epsilon)$ ; we also let  $X = X_e + X_1$ ,

where  $X_1$  is unknown as yet. For this time scale, it is straightforward to verify that all terms in the interaction equation must be retained, provided we made the assumption that all derivatives of  $F$  (and all derivatives of  $X_1$ ) are the same order of magnitude. Combining the interaction and motion equations leads to (29). This can be simplified by recalling that  $X = X_e + X_1$ , and that  $X_e$  satisfied the differential equation (32). Using this fact allows us to reduce (29) to the form

$$\hat{s}^2 \frac{d^2 X_1}{d\hat{t}^2} + 2 \epsilon \hat{s} \frac{dX_1}{d\hat{t}} + 2 \epsilon^2 X_1 \approx 0 \quad (\epsilon^3) \quad (33)$$

Note that the characteristic equation for (33) is the same as (19). From the above, we conclude  $X_1 \sim 0(\epsilon)$  so that  $X_1 \rightarrow 0$  for  $\epsilon \ll 1$ .

##### Case 3. Late-times

There is no late-time, added mass solution for high-frequency oscillators. This can easily be verified by looking at time scale  $t \sim 0(1/\hat{s})$  with  $\hat{s} \ll \epsilon$ ; on this time scale,  $X_e$  and its derivatives vanish due to the exponential term  $e^{-(m/2)\hat{s}t}$ . Then the interaction equation reduces to the added-mass form

$$F = -\frac{1}{2} m \frac{d^2 X_1}{d\hat{t}^2}$$

where  $X_1$  is the late-time solution.

We assume  $X_1$  varies on the late-time scale so that all its derivatives are the same order of magnitude. The equation of motion becomes

$$\hat{s}^2 (1+m/2) \frac{d^2 X_1}{d\hat{t}^2} + X_1 + \hat{s}^2 \frac{d^2 X_e}{d\hat{t}^2} + X_e = I_0 \delta(\hat{t}) \quad (34)$$

and since  $X_e$  satisfied the early-time equation (32), we have

$$X_1 \approx (m/2) \epsilon \hat{s} \frac{dX_e}{d\hat{t}} + 0 \left( \hat{s}^2 \frac{d^2 X_e}{d\hat{t}^2} \right) \quad (35)$$

We conclude that  $X_1 \sim 0(\hat{s})$ ; for  $\hat{s} \ll \epsilon$ , we see that  $X_1 \approx 0$ .

Then we are left with only our early-time solution; we conclude that although radiation-damping is the dominant fluid mechanism for early-times only, its effect determines the form of solution for much longer times.

Recapitulating the above results;

1) For late-times at low-frequencies ( $\hat{s} \sim 0(1)$ ,  $\epsilon \gg 1$ ), added-mass effects are dominant in the interaction equation;  $t \sim 0(1)$ , or late-times, correspond to times comparable to a period of the oscillator.

2) For early-times at high-frequencies ( $\hat{s} \sim 0(1)$ ,  $\epsilon \ll 1$ ), radiation damping is dominant in the

interaction equation, and, since  $t \sim O(1)$ , early-times are comparable to a period of the oscillator.

3) For intermediate-times at high- and low-frequencies, it is necessary to set  $\hat{s} \sim O(\epsilon)$ , and  $t \sim O(1/\epsilon)$ . All terms are retained in the interaction equation, so that radiation damping is not dominant for low-frequency oscillators at intermediate-times, and added-mass effects are not dominant for high-frequency oscillators at intermediate-times.

4) Although radiation damping is the dominant fluid mechanism for early-times, we found that coupling the early-time interaction equation with the early-time form of the equation of motion led to a physically impossible solution for low-frequency oscillators. The late-time added-mass dominated form of the coupled equations was found to be  $O(\hat{s}^2)$  for high frequency oscillators; we had  $\hat{s} \ll \epsilon \ll 1$  in this case.

5) For the low-frequency oscillator, the dominant solution occurs on the late-time scale when added-mass theory is valid. It is erroneous to attempt to use radiation-damping to account for fluid effects for this oscillator. There is no boundary layer in time.

6) For high-frequency oscillators, the motion is accurately treated by assuming radiation-damping as the dominant fluid mechanism; even though this is strictly true only for early-times, its effect on the oscillator is felt for much longer times.

#### CONCLUSION

We have shown that the effect of the fluid can be calculated by convolving the hydrodynamic function with the acceleration of the submerged oscillator. This convolution can be approximated by radiation-damping for early-times, defined by  $t' \ll a/c$ , or times much less than a transit time; for late-times, if the oscillator is low-frequency, then added-mass effects prevail.

For a given mass ratio, we use the value of dimensionless parameter  $\epsilon = c/(a\omega_0)$  to estimate whether our oscillator is high- or low-frequency. We found that, by appropriately scaling the dimensionless time and keeping in mind the magnitude of  $\epsilon$ , we were able to couple our interaction equation and motion equation to give meaningful results. In this way, we discovered that we cannot use the early-time radiation-damped form of the interaction equation in conjunction with the motion equation for  $\epsilon \gg 1$ , low-frequency oscillators. The correct form was shown to be the intermediate-time form of the interaction equation, in which no simplification was possible. The same result was shown to be true for late-times when we considered high-frequency oscillators. We defined intermediate-times as those for which  $t' \sim O(a/c)$ , the time for a wave to transit the body.

It was demonstrated that the intermediate-time solution, derived from the coupling of the full, unsimplified form of the interaction equation with the equation of motion, became vanishingly small for both high- and low-frequency oscillators. This left us with the early-time, radiation damped solution for  $\epsilon \ll 1$ , showing that radiation damping made its effect felt long after early-times for high-frequencies. For  $\epsilon \gg 1$ , the late-time added-mass solution is dominant over virtually all times; if we wish to find maximum oscillator excursions (for maximum stresses, etc.), it is sufficient to use added-mass. The use of radiation-damping in conjunction with low-frequency oscillators, though accurate for early-times, led to underestimates of peak oscillator response by a factor of  $1/\epsilon$ . We also showed that the exact solution for our sphere model reduced appropriately to high- and low-frequency solutions predicted by our asymptotic analysis.

#### REFERENCES

1. Clark, A.V., A Study of Fluid-Structure Interactions and Decoupling Approximations, Naval Research Laboratory Report No. 7590, Dec. 21, 1973.
2. Junger, M.C. and Thompson, W., J. Acoust. Soc. Am., 38, 978-986, 1965.
3. Mnev, Ye. N. and Pertsev, A. K., Hydroelasticity of Shells, trans. by FTD, Wright-Patterson AFB, FTD-MT-24-119-71.
4. Cole, J.D., Perturbation Methods in Applied Mathematics, Blaisdell Publ. Co., Waltham, Mass. 1968.
5. Burke, W.L., Phys. Rev., Vol. 2 No. 4, 1501-1505, 1970.

#### ACKNOWLEDGEMENT

This research was sponsored by the Defense Nuclear Agency under Subtask V99 QAX NB002, Work Unit 14, Work Unit Title "Exposed Submarine Appendages."

# APPENDIX

## Tables of Constants Used in Solutions

TABLE I  
Roots of Quartic  
( $m = 2.5$ )

$\epsilon = .01$	: $s_{1,2} = -.0125 \pm .9998i$ $s_{3,4} = -.0100 \pm .0100i$
$\epsilon = .10$	: $s_{1,2} = -.1250 \pm .9792i$ $s_{3,4} = -.1000 \pm .1026i$
$\epsilon = 1.0$	: $s_1 = -2.000, s_2 = 2.4620$ $s_{3,4} = 0.0191 \pm .6370i$
$\epsilon = 10.0$	: $s_1 = -15.0371, s_2 = -29.9630$ $s_{3,4} = -.0000 \pm .6671i$
$\epsilon = 100.0$	: $s_1 = -150.0037, s_2 = -299.963$ $s_{3,4} = -.000 \pm .6671i$

TABLE III  
Constants for Intermediate-  
and Low-frequency Solutions

$s_1 = a_1$	$s_2 = a_2$
$s_3 = a_3 + ib_3$	$s_4 = a_3 - ib_3$
$H_{12} = A_1 A_2 - b_3^2$	
$A_{12} = A_1 + A_2$	
$g = (F_3 H_{12} - G_3 b_3 A_{12}) / (A_1^2 + b_3^2)(A_2^2 + b_3^2)$	
$h = (G_3 H_{12} + b_3 A_1 F_3) / (A_1^2 + b_3^2)(A_2^2 + b_3^2)$	

(For definitions of  $A_1, A_2$ , etc., see Table II)

TABLE II  
Constants for High-frequency Solution

$s_1 = a_1 + ib_1$	$s_2 = a_1 - ib_1$
$s_3 = a_3 + ib_3$	$s_4 = a_3 - ib_3$
$\alpha_1 = a_1 + \epsilon$	
$\alpha_3 = a_3 + \epsilon$	
$A_1 = a_1 - a_3$	
$A_3 = a_3 - a_1$	
$B_1 = b_1 + b_3$	
$B_3 = b_1 + b_3$	
$\beta_1 = b_3 - b_1$	
$\beta_3 = b_1 - b_3$	
$F_1 = \alpha_1^2 + \epsilon^2 - b_1^2$	
$F_3 = \alpha_3^2 + \epsilon^2 - b_3^2$	
$G_1 = 2\alpha_1 b_1$	
$G_3 = 2\alpha_3 b_3$	
$H_1 = A_1^2 - B_1 \beta_1$	
$H_3 = A_3^2 - B_3 \beta_3$	
$J_1 = B_1 + \beta_1$	
$J_3 = B_3 + \beta_3$	
$M_1 = (A_1^2 + \beta_1^2)(A_1^2 + B_1^2)$	
$M_3 = (A_3^2 + \beta_3^2)(A_3^2 + B_3^2)$	
$Q_1 = (F_1 H_3 - A_3 G_1 J_3) / M_3$	
$Q_3 = (G_1 H_3 + F_1 A_3 J_3) / M_3$	
$Q_2 = (F_3 H_1 - A_1 G_3 J_1) / M_1$	
$Q_4 = (G_3 H_1 + F_3 A_1 J_1) / M_1$	



# ENVIRONMENTS AND MEASUREMENTS

## HARPOON MISSILE FLIGHT ENVIRONMENTAL MEASUREMENT PROGRAM

V. S. Noonan, J. L. Gubser, R. D. Harmening  
McDonnell Douglas Astronautics Company—East  
St. Louis, Mo.

This paper presents a summary of acoustic and vibration measurements made during the Design Phase flights of the Harpoon missile. The data is presented in the form of power spectral density and shock spectrum plots.

### INTRODUCTION

The Harpoon is an anti-ship missile capable of being launched from various aircraft and surface ships. The main features of the missile are shown in Figure 1. With the award of the Harpoon Missile Program to McDonnell Douglas Astronautics

Company-East, an inflight dynamics data measurement program was implemented to evaluate the acoustic and vibration predictions made for the missile and to serve as a data base for future tactical missile designs. This paper presents a summary of the flight data obtained during the Design Phase of the program.

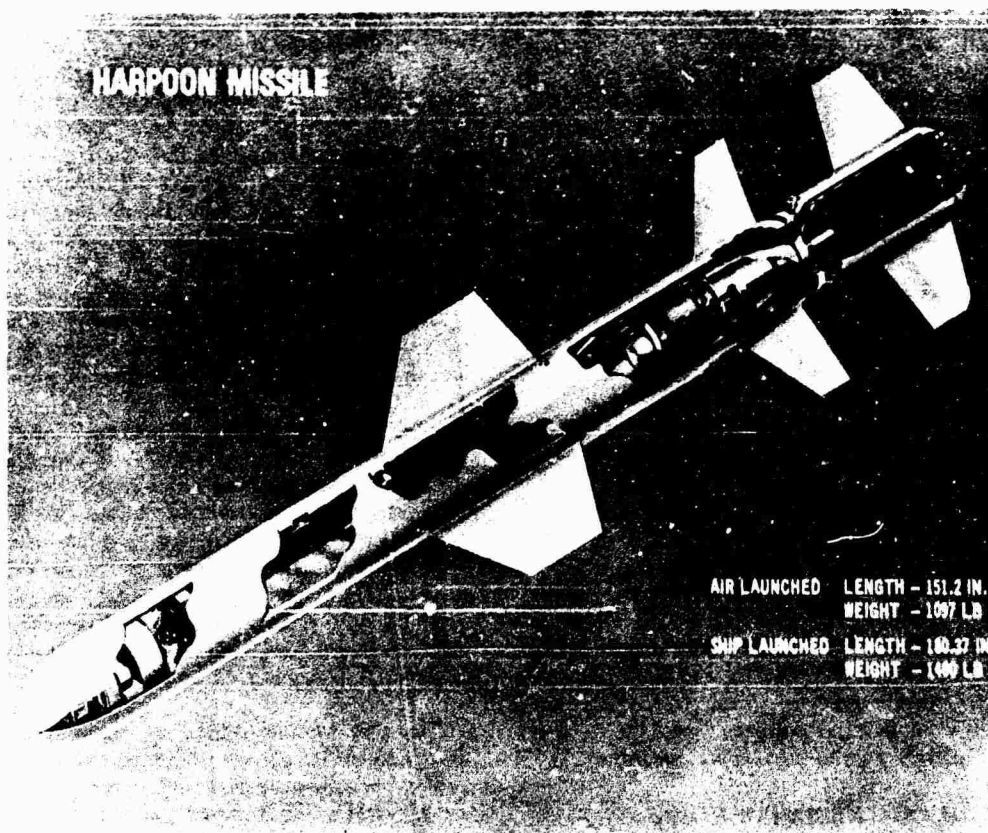


FIGURE 1 HARPOON MISSILE

The objective of the Design Phase of the Harpoon program was to prove the adequacy of the overall missile system concept and to verify the compatibility of the missile with aircraft and surface ship launch platforms. To accomplish these objectives required several types of vehicles. The first vehicles flown in the program were Aerodynamic Test Vehicles (ATV) and Blast Test Vehicles (BTV) which were of boilerplate construction. The ATV's were air launched from a P-3 aircraft while the BTV's were launched from an ASROC launcher located at a shore site (Naval Missile Center, Point Mugu, California) or on a DE-1052 ship. After successful boilerplate flights Control Test Vehicles (CTV) and Guidance Test Vehicles (GTV) were flown. These vehicles were used to verify the performance of individual and overall missile systems. The CTV's and GTV's had no warhead and were essentially identical with one exception. The GTV's had a functional seeker while the CTV's utilized a dummy seeker which was dynamically similar to the real seeker. The air launched and surface launched CTV's and GTV's utilized a turbo-jet engine during cruise flight and the surface launched vehicles used a solid propellant booster. CTV's and GTV's were launched from P-3 aircraft and from an ASROC launcher located at a shore site or on a DE-1052 ship.

Internal and external acoustic and vibration measurements were made on ATV's, BTV's, CTV's and GTV's. Data presented in this paper is in the form of power spectral density and shock spectrum plots. The data provides a good cross section of dynamic environments resulting from P-3 aircraft captive carry, solid propellant boost flight, turbojet engine flight, high and low altitude drops, maximum aerodynamic pressures and transient conditions resulting from aircraft launch, booster ignition and separation and turbojet engine ignition.

#### DATA MEASUREMENT SYSTEMS

Acoustic and vibration measurements were made onboard and offboard of the Harpoon missile using piezoelectric type sensors. The offboard acoustic and vibration sensor systems had a 10 to 8000 Hz and 10 to 2000 Hz bandwidth respectively. The onboard acoustic and vibration sensor systems had a 10 to 2000 Hz bandwidth which was dictated by the missile telemetry system. Onboard acoustic and vibration data were measured continuously using IRIG channels 15, 17 and 19. During the ATV captive flight tests, data was "hard wired" to the P-3. For BTV, CTV and GTV flights, the data was telemetered to a ground station for recording.

#### SPECTRAL ANALYSIS TECHNIQUE

Data were obtained for each flight and recorded on

magnetic tape. The resulting time histories were reviewed for peak amplitude values and used to select data intervals for subsequent PSD and shock spectrum analysis. Upon review of the time histories the data were classified as either stationary or non-stationary for spectral analyses. Stationary data were analyzed by the use of power spectral density analyses and transient data were analyzed by shock spectrum techniques. Whenever possible, sample lengths and bandwidths were chosen to yield maximum frequency resolution and sufficient degrees of freedom for statistical confidence in amplitude levels.

Some difficulties were experienced in interpretation of the power spectral density data due to low signal to noise (S/N) ratios. The lowest possible maximum amplitude setting for the vibration sensor systems was 5.0 g's peak. Most of the vibration levels measured in the forward portion of the missile were less than 1.0 g peak for steady flight conditions. Therefore most of the steady state data was below 20% of full scale. The vibration measurement systems showed a nominal noise floor of approximately 7% of full scale. The combination of the low signal level and the nominal noise level results in a S/N of 3 or less.

A S/N ratio of approximately 1.5 results in only about 10 dB of spectral resolution. If the portion of the spectrum above 300 Hz is of lower amplitude than the low frequency portion of the spectrum, this low S/N will result in masking the spectrum by the noise floor leaving telemetry cross talk harmonics at 400, 800, 1200, 1600 and 2000 Hz as the predominate peaks. This effect can be seen in some of the PSD plots presented later. When the S/N increased to approximately 2.5 the spectral resolution improved to 25 or 30 dB, but the telemetry noise at 400 Hz still is visible. For good resolution in power spectral density analyses, a S/N of at least 4 is desirable.

PSD analyses were performed on a Time/Data 100 Time-Series analyzer by the Pacific Missile Range. The system uses a Fast Fourier Transform technique. The analysis bandwidth used on the Time/Data 100 is a direct function of the digitizing rate used to process the flight analog data. For the onboard data, with a 2KHz frequency response, the narrowest analysis bandwidth possible was 10 Hz. For offboard data, with an 8 KHz response, the narrowest analysis bandwidth possible was 20 Hz.

The plot format utilized by the Pacific Missile Range for PSD analysis presented spectral values in reference to a pseudo peak unit squared per Hz rather than a RMS unit squared per Hz. The amplitude values used were based on a sinusoidal peak unit (i.e., 1.4 times the rms); thus, all PSD amplitudes were

plotted a factor of two greater than the usual format. To prevent confusion, the plots presented in this paper are copies of the originals with the scales changed to reflect the spectral values based on rms rather than peak values.

#### OFFBOARD MEASUREMENTS

Measurements offboard of the missile were made during the BTv, CTv and GTv flight tests.

During air launches of the CTv's and GTv's the vibration environment inputted to the Harpoon Data Processor (HDP), mounted in the P-3, was measured. The measurement was made at the interface of the HDP and aircraft structure. The HDP was mounted inside the fuselage structure away from the missile. Thus, all vibration inputs to the HDP were P-3 generated. Figures 2 and 3 present PSD plots of the longitudinal and vertical (referenced to aircraft) HDP vibration inputs. A dynamic analysis identified the PSD peaks at 15, 25, 65, 135, 205 and 275 Hz as local

resonances of the HDP mounting structure.

During launches from the shore based ASROC launcher, acoustic measurements were made in the live and empty adjacent cells and at various ground level locations in front of the launcher. During ship launches from the ASROC launcher acoustic measurements were made in the live and empty adjacent cells and at several deck locations. Locations of the ground and deck sensors are shown in Figure 4 and 5.

A summary of the maximum overall sound pressure levels measured offboard during shore and ship launches is shown in Figure 6. Data from 5 shore launches and 5 ship launches is represented in the table. The data measured in the live cell during shore launches was similar to that obtained during ship launches. This was also the case for the adjacent cell measurements. The live cell measurements are somewhat questionable due to the heat generated during missile booster ignition system, in effect, saturated the acoustic sensor system.

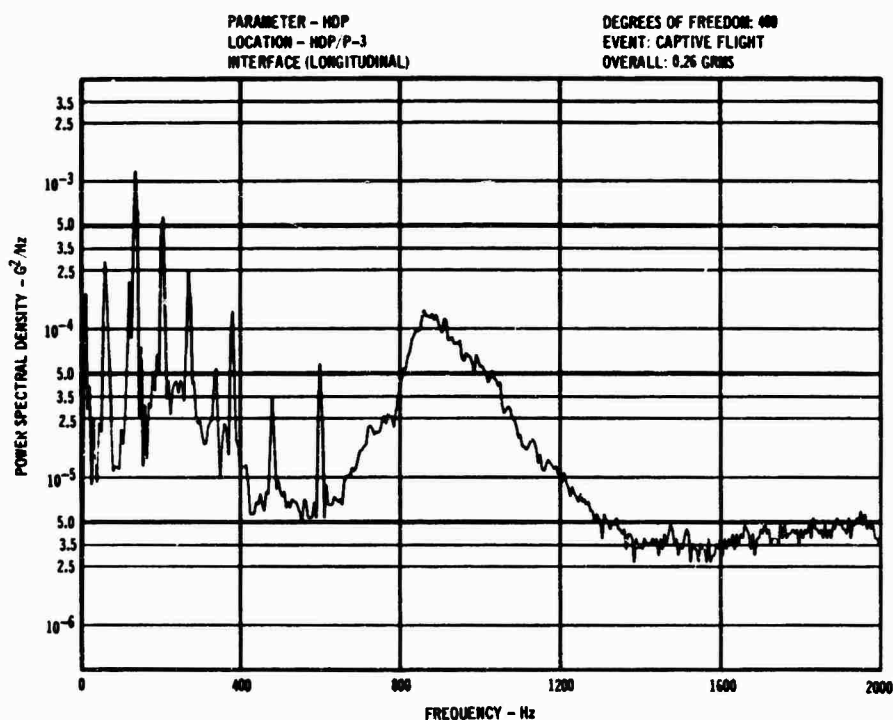


FIGURE 2 POWER SPECTRAL DENSITY

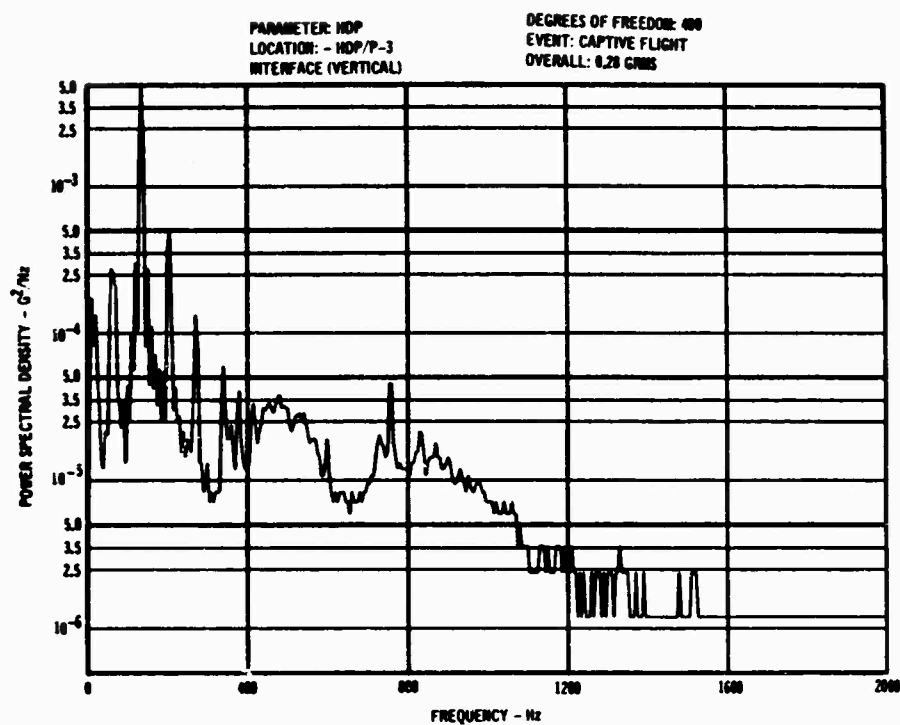


FIGURE 3 POWER SPECTRAL DENSITY

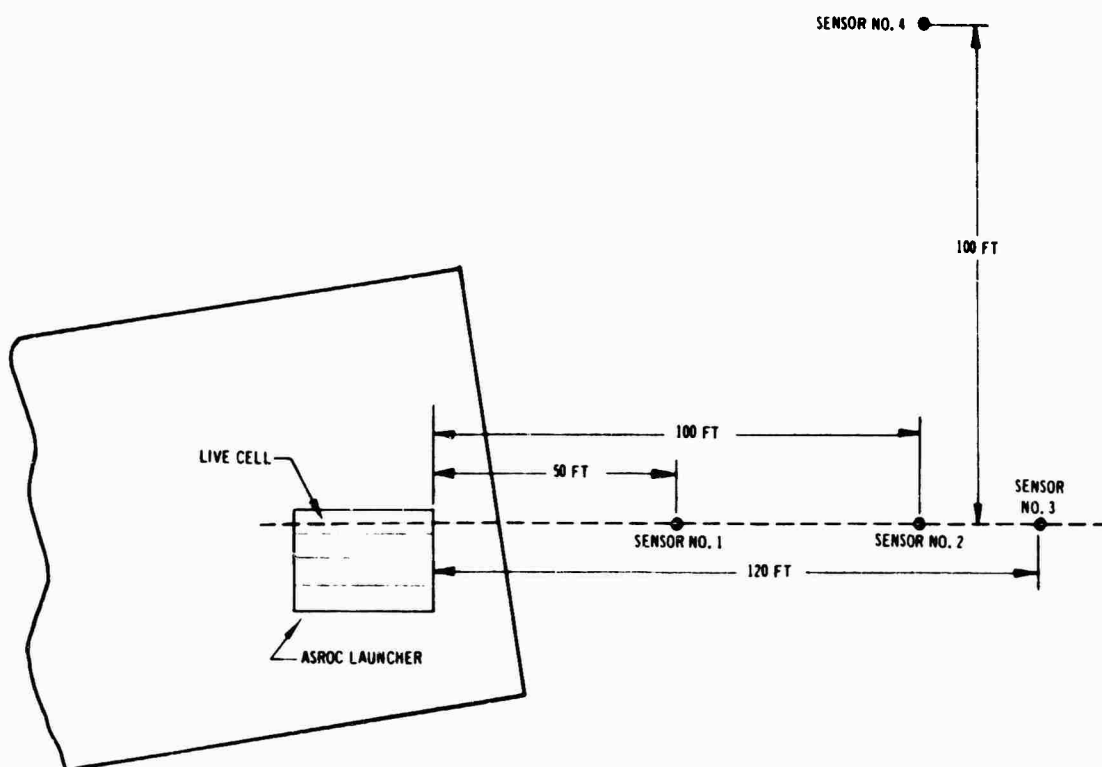
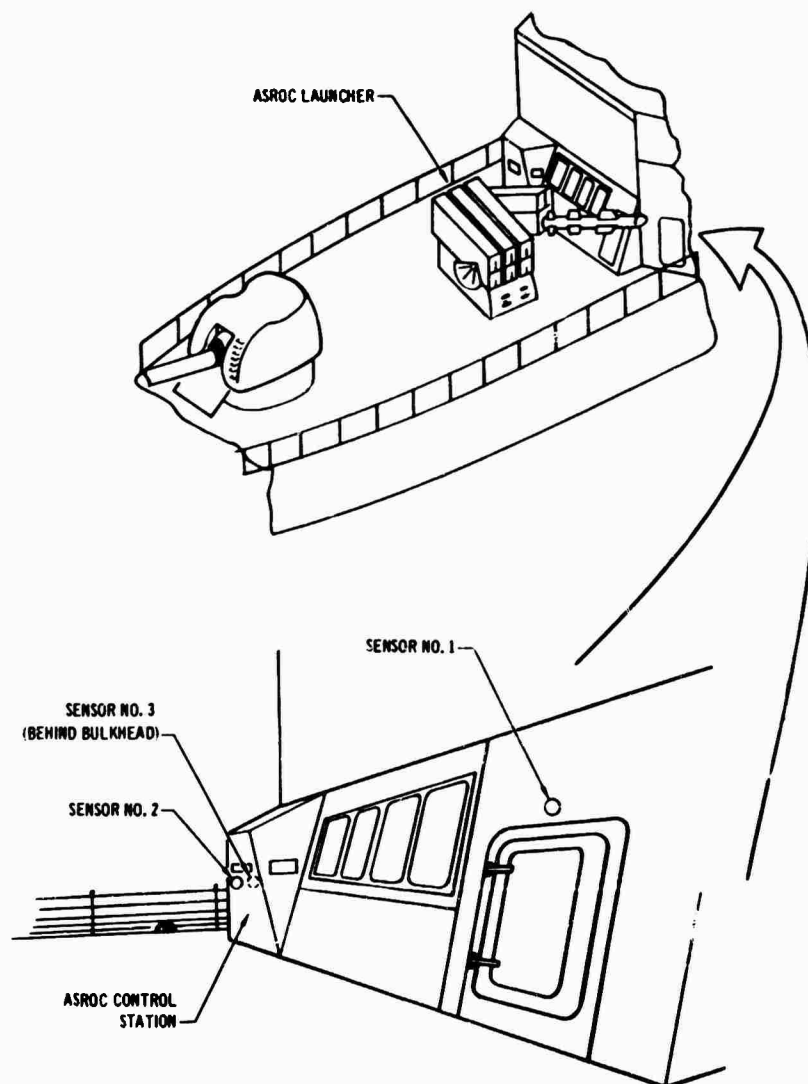


FIGURE 4 OFFBOARD ACOUSTIC SENSOR LOCATIONS - SHORE LAUNCHES



**FIGURE 5 - OFFBOARD ACOUSTIC SENSOR LOCATIONS - SHIP LAUNCHES**

OFFBOARD ACOUSTIC SENSOR LOCATION	MAXIMUM OVERALL SOUND PRESSURE LEVEL*
LIVE CELL	170 dB
ADJACENT CELL	146 dB
GROUND SENSOR (SHORE LAUNCHES)	
SENSOR NO. 1	155 dB
SENSOR NO. 2	150 dB
SENSOR NO. 3	148 dB
SENSOR NO. 4	140 dB
DECK SENSORS (SHIP LAUNCHES)	
SENSOR NO. 1	160 dB
SENSOR NO. 2	158 dB
SENSOR NO. 3	134 dB

\* REFERENCED TO 0.0002 DYNES CM<sup>2</sup>

**FIGURE 6 - SUMMARY OF MAXIMUM OFFBOARD ACOUSTIC LEVELS - SHORE AND SHIP LAUNCHES**

## ON-BOARD MEASUREMENTS — ATV'S

The objective of the ATV's was to evaluate the inflight proximity effects of the Harpoon and P-3 aircraft and to demonstrate safe captive carriage and release from the aircraft. The ATV was a boilerplate structure which simulated the external geometry, weight, center-of-gravity, and inertias (pitch and yaw) of the Harpoon missile.

One ATV was utilized for captive flight acoustic

measurements. Six flush mounted microphones were located at various points on the missile shown in Figure 7. As the ATV's were boilerplate no vibration measurements were made. All data were collected and "hard-wired" to a frequency modulated tape recorder located in the aircraft. A total of six ATV/P-3 captive carriage flights were flown with the aircraft performing various specified maneuvers. In general, the tests were conducted for various speeds and altitudes, turns, near stall, side slip and dive conditions.

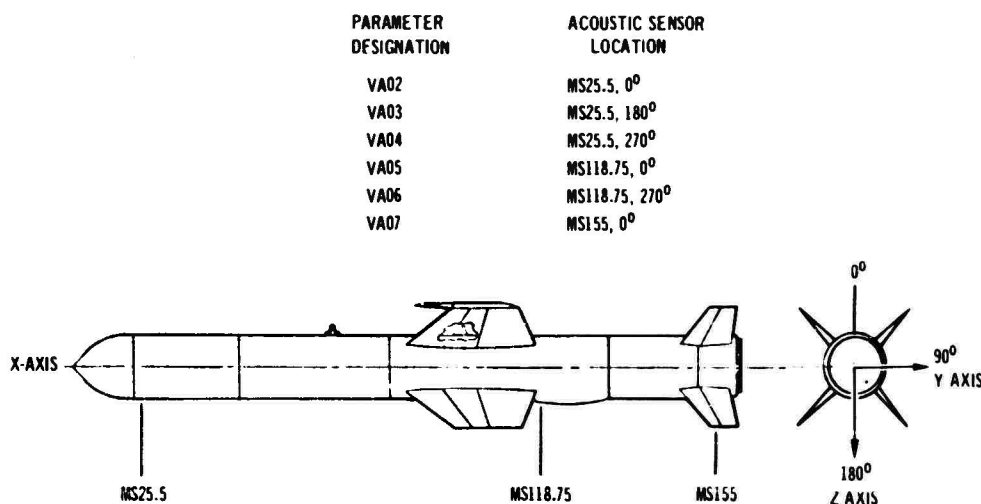


FIGURE 7 — EXTERNAL ACOUSTIC SENSOR LOCATIONS — ATV

A table of the maximum acoustic overall sound pressure levels for the various maneuvers and locations is presented in Figure 8. Review of the sound pressure levels shows the highest level to be 155 dB which was measured during a low altitude dive. Acoustic levels tend to be 1 to 5 dB higher on the top (0°) of the missile as compared to the same station but on the side or bottom of the missile. This effect was due to turbulence from the missile/rack interface. Also, the levels toward the rear of the vehicle tend to be higher due to turbulence.

Review of the CTV and GTV acoustic data also showed the aft measurements to have a higher frequency content than the forward measurements.

## ON-BOARD MEASUREMENTS — BTV'S

The objective of the BTV's was to evaluate booster ignition, performance and separation during surface launched Harpoon flights. Three BTV's were shore

launched from an ASROC launcher and one from a ship based ASROC launcher. The BTV's were boilerplate construction having the same geometry, mass center-of-gravity, and inertias as the Harpoon missile but having alive booster.

The BTV's were instrumented to investigate the external acoustic environment and the longitudinal vibration levels imparted to the missile by the booster at the booster/missile interface during booster operation and separation. The external acoustic environment at stations M.S. 25.5 (Parameter VA10) and M.S. 155.4 (Parameter VA11) on the missile were monitored during the flights of two vehicles. Both measurements were at top vertical center. The booster/missile interface vibration levels were monitored by two accelerometer systems; one with a high peak acceleration level to investigate the booster ignition and separation shocks and one with a low peak acceleration to investigate the booster burn vibration. Vibration measurements were made on two BTVs.

OPERATION NO. 8963																			
EVENT	UNITS	TAKE OFF	MACH 0.50	MAX SPEED	NEAR STALL	100° N TRN	100° L TRN	2G WUT	MAX G L TRN	MAX G R TRN	L SIDE SLIP	R SIDE SLIP	L RPO	R RPO	MAX SPEED	DIVE 20°	DIVE 10°	DIVE 10°	NEAR STALL
SPEED			358 KT	360 KT	120 KT	250 KT	248 KT	250 KT	200 KT		190 KT	190 KT	300 KT	300 KT	365 KT	340 KT	200 KT	340 KT	114 KT
ALTITUDE			10 K-FT	10K-FT	10 K-FT	10 K-FT	10 K-FT	15 K-FT	200 KT		20 K-FT	20 K-FT	20 K-FT	20 K-FT	20 K-FT	20 K-FT	20 K-FT	9 K-FT	1000 FT
PICKUP																			
VA 02	dB	141	143	-	140	141	141	146	143	143	143	143	143	143	-	146	-	143	143
VA 03		141	141	-	140	140	140	143	143	143	141	141	141	141	-	143	-	141	141
VA 04		140	140	-	140	140	140	140	141	141	140	140	140	140	-	140	-	140	141
VA 05		140	146	-	141	143	143	150	144	144	144	144	146	146	-	150	-	140	140
VA 06		143	143	-	140	141	141	146	143	143	143	143	143	143	-	147	-	143	146
VA 07	dB	143	147	-	141	143	143	151	144	144	144	144	147	147	-	153	-	140	150
OPERATION NO. 9546																			
VA 02	dB	141	143	144	140	140	140	144	141	141	140	140	143	143	141	144	142	-	146
VA 03		141	141	141	140	140	140	143	140	140	140	140	141	141	140	141	140	-	141
VA 04		141	140	140	140	140	140	140	140	140	140	140	140	140	140	140	140	-	142
VA 05		143	150	150	140	143	143	151	143	143	147	147	151	151	146	151	150	-	151
VA 06		140	141	141	140	140	140	143	140	140	140	140	143	143	141	142	141	-	141
VA 07	dB	143	150	150	141	143	143	150	143	143	146	145	150	150	144	151	150	-	150
OPERATION NO. 8969																			
VA 02	dB	142	142	142	140	141	-	145	140	140	140	140	142	142	142	141	144	143	145
VA 03		142	140	140	140	140	-	142	140	140	140	140	140	140	140	140	140	140	140
VA 04		140	140	140	140	140	-	140	140	140	140	140	140	140	140	140	140	140	140
VA 05		142	147	146	140	145	-	151	142	142	146	146	146	146	146	141	147	147	150
VA 06		142	142	142	140	141	-	144	140	140	140	140	141	141	141	140	143	143	140
VA 07	dB	142	146	144	140	143	-	151	142	142	142	144	144	144	144	142	147	147	149
OPERATION NO. 0153																			
VA 02	dB	137	135	137	127	-	-	-	-	-	-	-	-	-	137	136	138	137	126
VA 03		136	126	129	126	-	-	-	-	-	-	-	-	-	127	127	129	127	126
VA 04		130	131	135	127	-	-	-	-	-	-	-	-	-	135	135	137	132	127
VA 05		142	147	150	141	-	-	-	-	-	-	-	-	-	144	149	151	150	141
VA 06		140	140	140	140	-	-	-	-	-	-	-	-	-	140	142	142	140	141
VA 07	dB	142	145	148	141	-	-	-	-	-	-	-	-	-	142	147	150	147	142
OPERATION NO. 9678																			
EVENT	UNITS	TAKE OFF	MACH 0.50	MAX SPEED	NEAR STALL	100° N TRN	100° L TRN	2G WUT	MAX G L TRN	MAX G R TRN	L SIDE SLIP	R SIDE SLIP	LRPO	RRPO	MAX SPEED	DIVE 20°	DIVE 10°	DIVE 10°	NEAR STALL
SPEED			352 KT	362 KT	130 KT	250 KT	240 KT	350 KT	200 KT	210 KT	250 KT	250 KT	300 KT	300 KT	369 KT	340 KT	350 KT	345 KT	112 KT
ALTITUDE			10 K-FT	10 K-FT	10 K-FT	10 K-FT	10 K-FT	12 K-FT			10 K-FT	10 K-FT	10 K-FT	10 K-FT	11 K-FT	20 K-FT	20 K-FT	2500 FT	1000 FT
PICKUP																			
VA 02	dB	135	135	136	132	134	134	139	135	135	137	137	139	138	130	136	140	142	140
VA 03		134	134.5	134	132	132	132	137	135	135	136	136	137	137	137	135	137	138	137
VA 04		137	137	137	134	134	134	140	139	139	139	139	140	139	139	132	140	141	138
VA 05		148	149	149	146	146	146	151	149	149	149	149	151	151	151	149	152	153	149
VA 06		148	149	148	148	148	148	152.5	152	152	153	153.5	153.5	153	153	153	154	154.5	153
VA 07		140	150	149	148	148	148	152.5	152	152	152	153	153	152.5	153	153	154	154.5	152

WUT - WING UP TURN  
RPO - ROLLING PULL-OUT

FIGURE 8 - SUMMARY OF MAXIMUM MISSILE EXTERNAL ACOUSTIC LEVELS - ATV

The maximum overall sound pressure levels measured during boost flight were 143 dB at the front of the missile and 144 dB at the rear. Figures 9 and 10 present PSD's of the BTV boost acoustic measurements. Due to the short duration of boost flight the DEGREES-OF-FREEDOM are small thus statistically compromising the amplitude accuracy of the data.

Review of booster/missile interface vibration data indicated lower than expected shock levels due to booster ignition and separation. The high level accelerometer (full scale 350g 0-pk) showed no data above the nominal noise floor (approximately -g 0-pk). The low level accelerometer (full scale 20g 0-pk) appeared to just saturate at both booster ignition and separation. The levels during boost flight were near the nominal noise floor (approximately 2g 0-pk) and were too low to yield any spectral data. The level of the vibration data while the missile was still within the launcher cell was approx. 8g 0-pk.

#### ON-BOARD MEASUREMENTS-CTV'S & GTV'S

The Control Test Vehicle (CTV) and the Guidance Test Vehicle (GTV) flights were conducted to evaluate the overall performance of the prototype Harpoon Weapon System. Both vibration and acoustic environments were measured throughout the missile flights to investigate aircraft captive carry, boost and cruise levels. A total of 15 CTV and GTV flights were made, of which 6 were surface launches and 9 were air releases. The surface launches were performed from ASROC launchers which were either ship or shore based. The air released flights were conducted from a P-3 aircraft. The CTV and GTV were structurally representative of the production Harpoon but with the warhead replaced by a test and evaluation section which contained telemetry components. The CTV's and GTV's were equivalent except for the absence of an operational seeker on the CTV. The CTV was fitted with a dynamic model of the seeker to provide complete dynamic similarity.

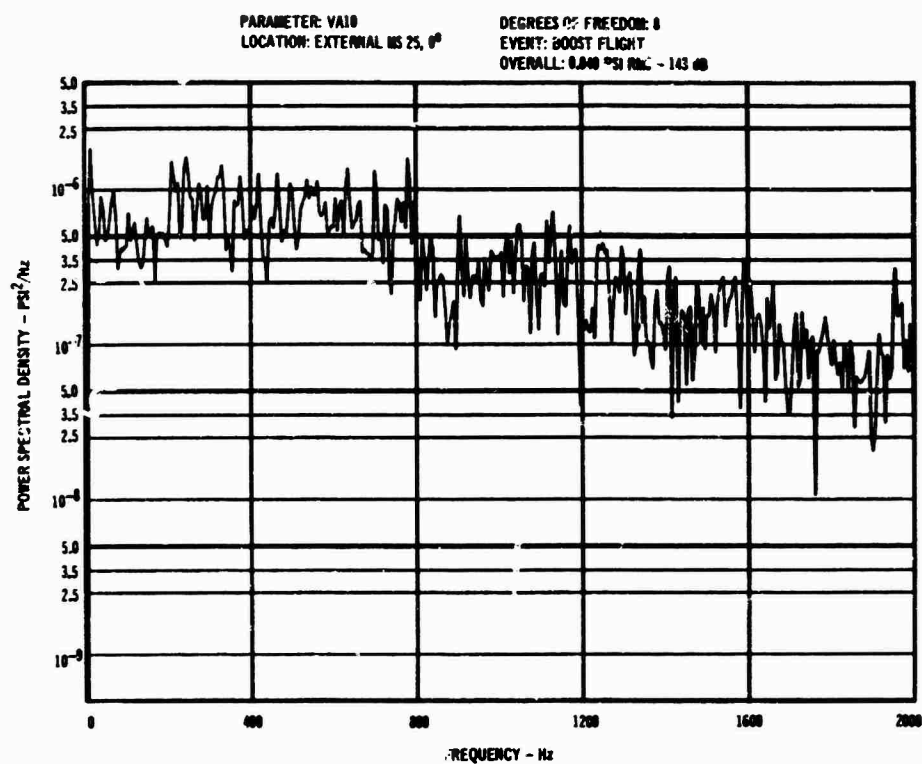


FIGURE 9 POWER SPECTRAL DENSITY

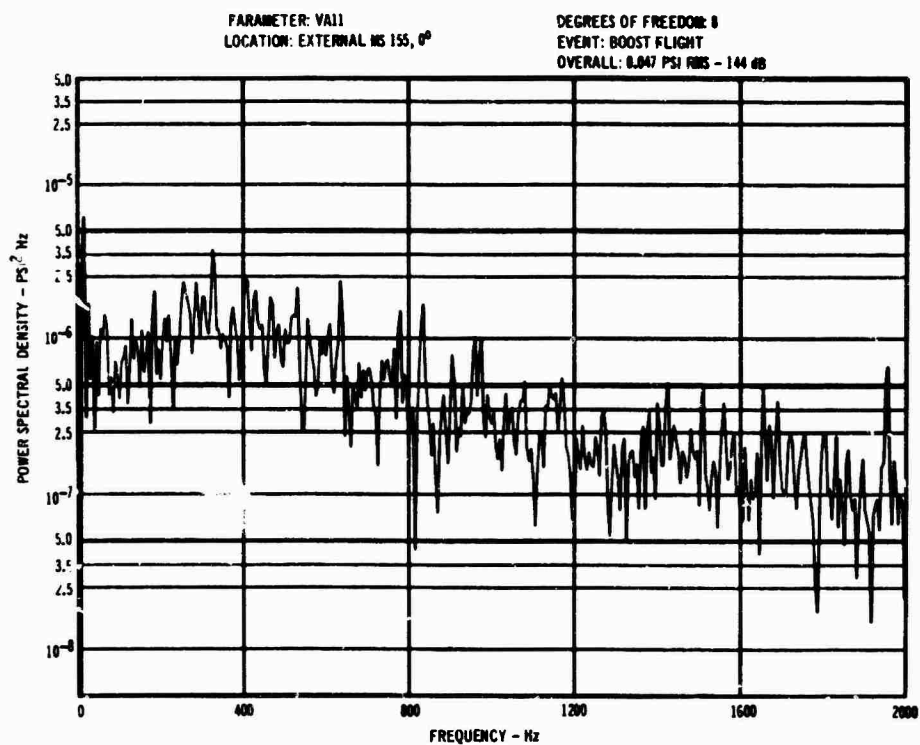


FIGURE 10 - POWER SPECTRAL DENSITY



between the CTV and GTV. The only configuration difference between flights was due to the type of launch. Surface launch missiles were fitted with a booster and booster separation system which allowed the missile to achieve sufficient velocity for turbo-jet engine start. After booster separation there was no significant configuration difference between surface launch and air release missiles.

Measurements were made to determine the vibration levels inputted to the Missile Guidance Unit (MGU), seeker, turbo-jet engine, missile/booster interface control actuators and forward aircraft

hook. All of these items are mounted directly to missile primary structure. The vibration sensors were located at the interface of the item and the missile primary structure. Acoustic levels were measured both internal and external to the missile. Only three continuous channels were available during each flight, thus making it necessary to change the measurements for different flights to obtain data at various locations in 3 axes. Figure 11 shows sensor locations. Dynamic data were recorded during all phases of the missile flight. A total 32 vibration measurements, 4 internal acoustic and 3 external acoustic measurements were made.

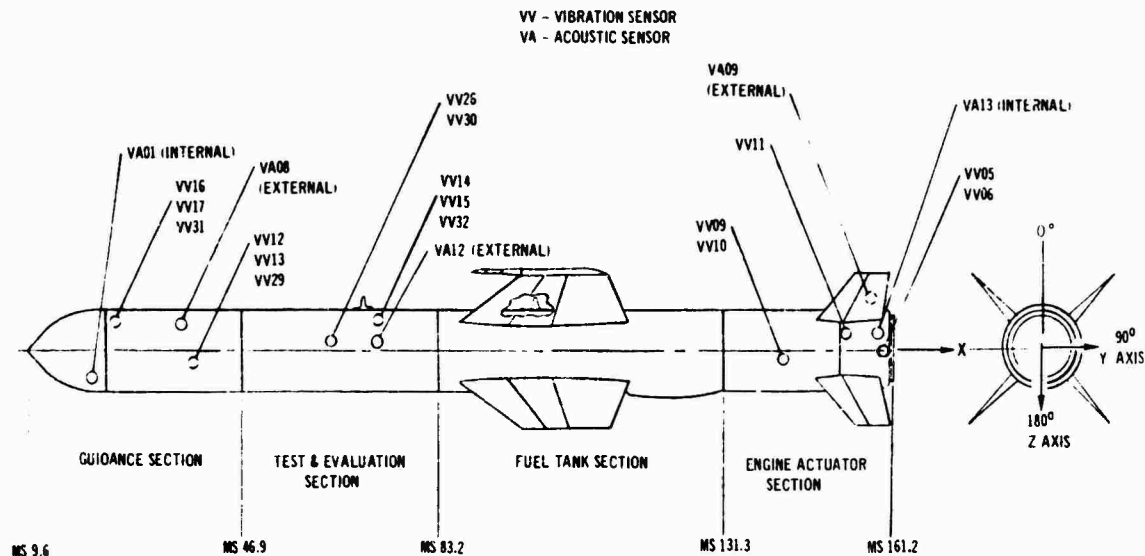


FIGURE 11 - ACOUSTIC AND VIBRATION SENSOR LOCATION - CTV AND GTV

PSD analyses were performed for selected time intervals. Except for those intervals occurring during boost flight it was possible to use durations of sufficient magnitude to yield PSD's with an adequate number of degrees-of-freedom. The duration of boost flight was too short to accomplish this but PSD analyses were still performed to yield frequency information.

Figures 12 and 13 illustrate the external acoustic environment measured during P-3 captive flight. The measured data indicates that the external acoustic level was 138 dB at the forward missile station and 145.5 dB at the aft missile station. Figure 14 is the internal acoustic level measured at the aft missile station during captive carry. A reduction in noise level of approximately 8 dB is realized through the missile structure.

The vibration spectra for the P-3 captive carry are shown in Figures 15 through 18. These plots are typical for all of the captive carry flights for which

data was obtained. In general, the vibration is low level with the amplitude of the high frequencies increasing for the sensors located in the aft sections of the missile. The data is consistent since the turbulent boundary layer does increase along the missile and this is the primary source of the high frequency vibrations. P-3 propeller frequencies of 15 and 65 Hz are also evident in much of the vibration data. The high amplitude spikes occurring at 400, 800, 1200, 1600 and 2000 Hz are the telemetry harmonics previously discussed.

Operating of the missile turbo jet engine had a pronounced effect on the vibration levels throughout the missile. The engine was started while the missile was still captive to the aircraft. Figures 19 through 21 show the captive vibration environment at the seeker, MGU and engine after the engine has achieved 100% rpm. The first axial bending mode frequency at approximately 200 Hz is evident. The engine operating frequency at approximately 670 Hz is very evident.

PARAMETER: VAOB  
LOCATION: EXTERNAL NS 36, 0°

DEGREES OF FREEDOM: 200  
EVENT: CAPTIVE FLIGHT  
OVERALL: 0.823 PSI RMS - 138 dB

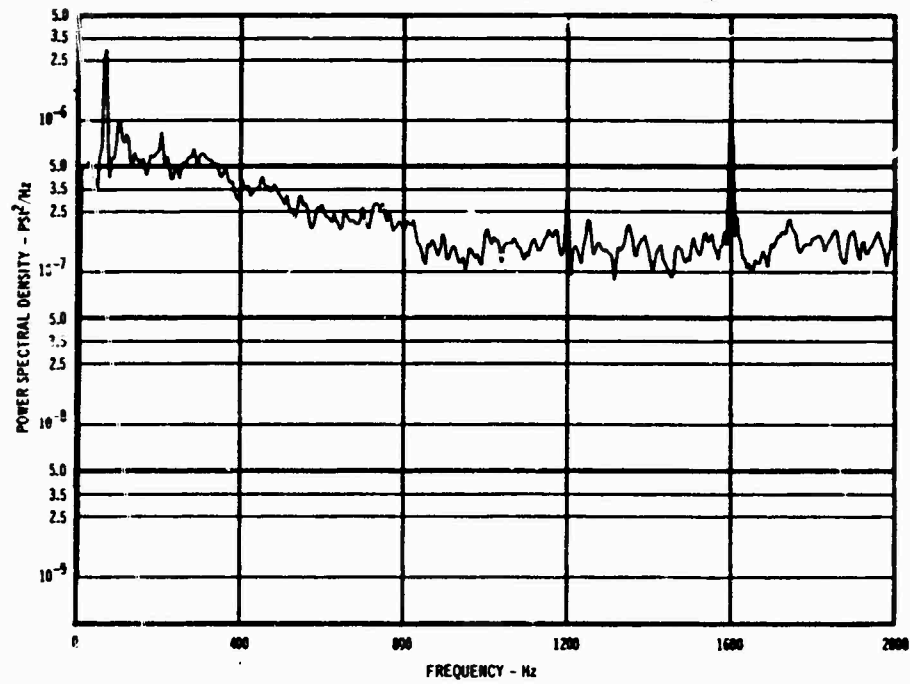


FIGURE 12 - POWER SPECTRAL DENSITY

PARAMETER: VAOB  
LOCATION: EXTERNAL NS 155, 0°

DEGREES OF FREEDOM: 200  
EVENT: CAPTIVE FLIGHT  
OVERALL: 0.055 PSI RMS - 145.5 dB

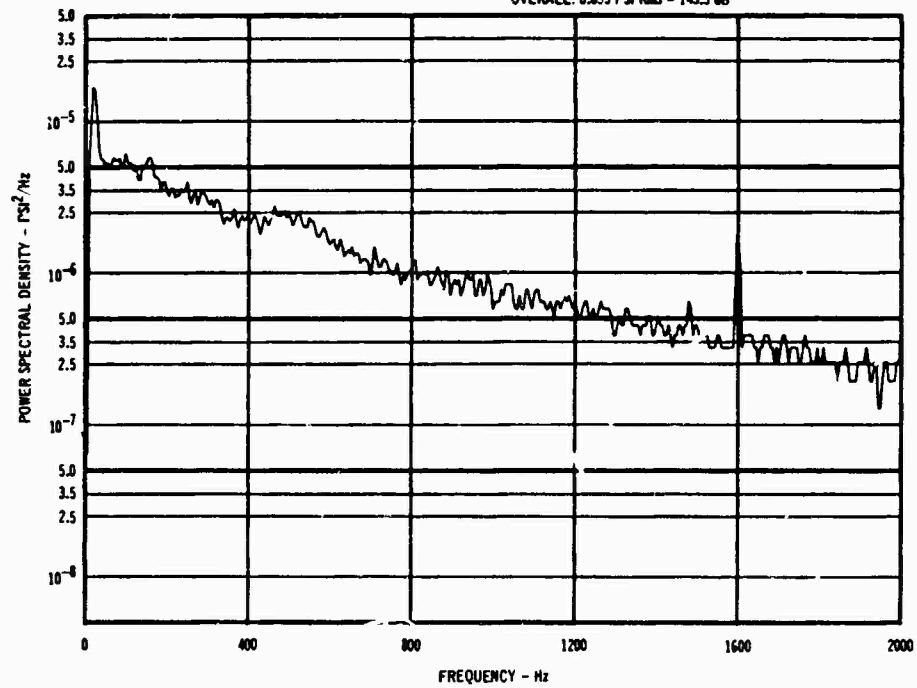


FIGURE 13 - POWER SPECTRAL DENSITY

PARAMETER: VAJ3  
LOCATION: INTERNAL-ACTUATOR

DEGREES OF FREEDOM: 262  
EVENT: CAPTIVE FLIGHT  
OVERALL: 0.089 PSI RMS - 130 dB

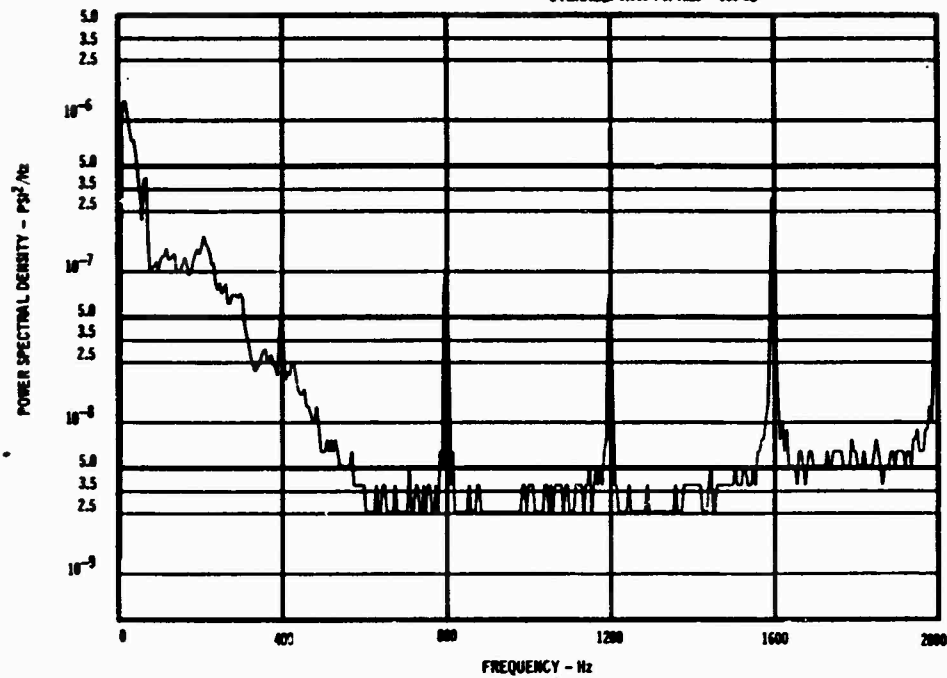


FIGURE 14 POWER SPECTRAL DENSITY

PARAMETER: VV31  
LOCATION: SEEKER - Z AXIS

DEGREES OF FREEDOM: 100  
EVENT: CAPTIVE FLIGHT  
OVERALL: 0.32 G RMS

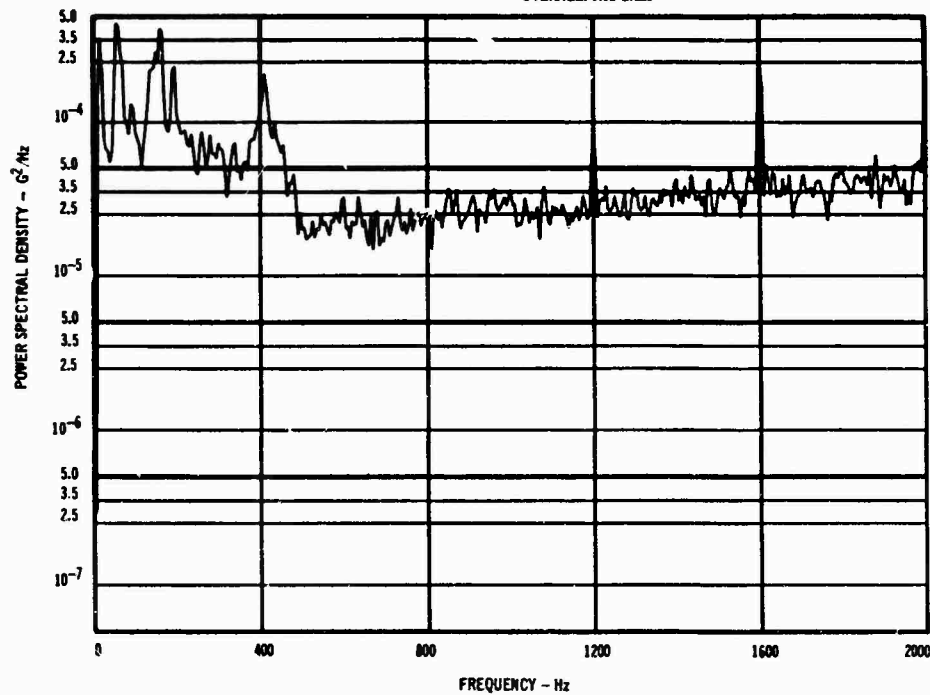


FIGURE 15 POWER SPECTRAL DENSITY

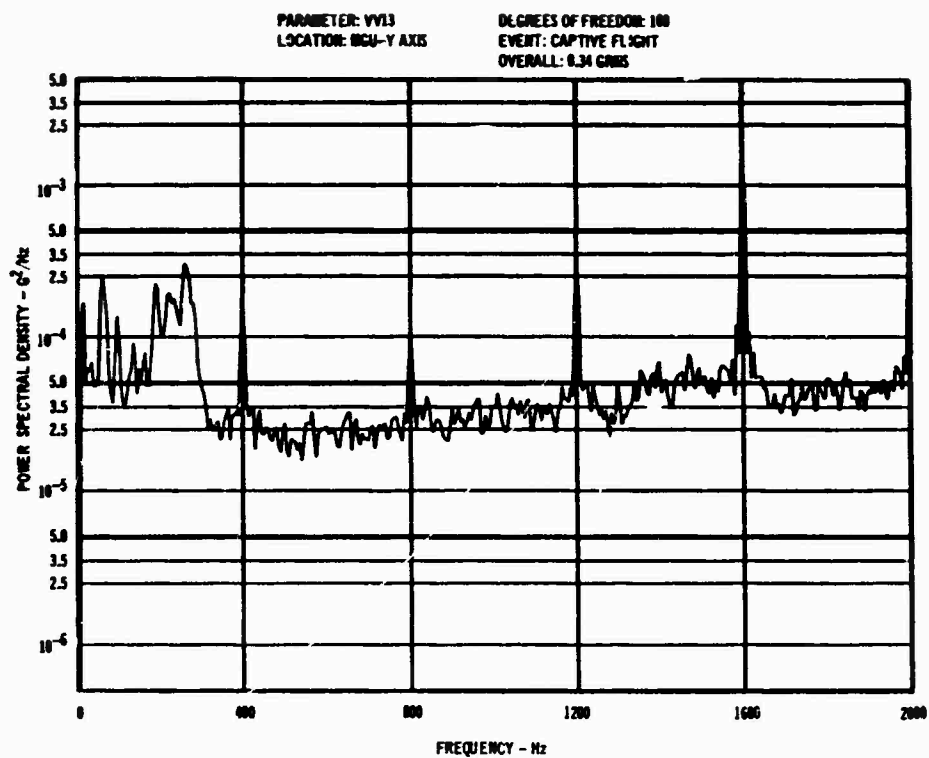


FIGURE 16 POWER SPECTRAL DENSITY

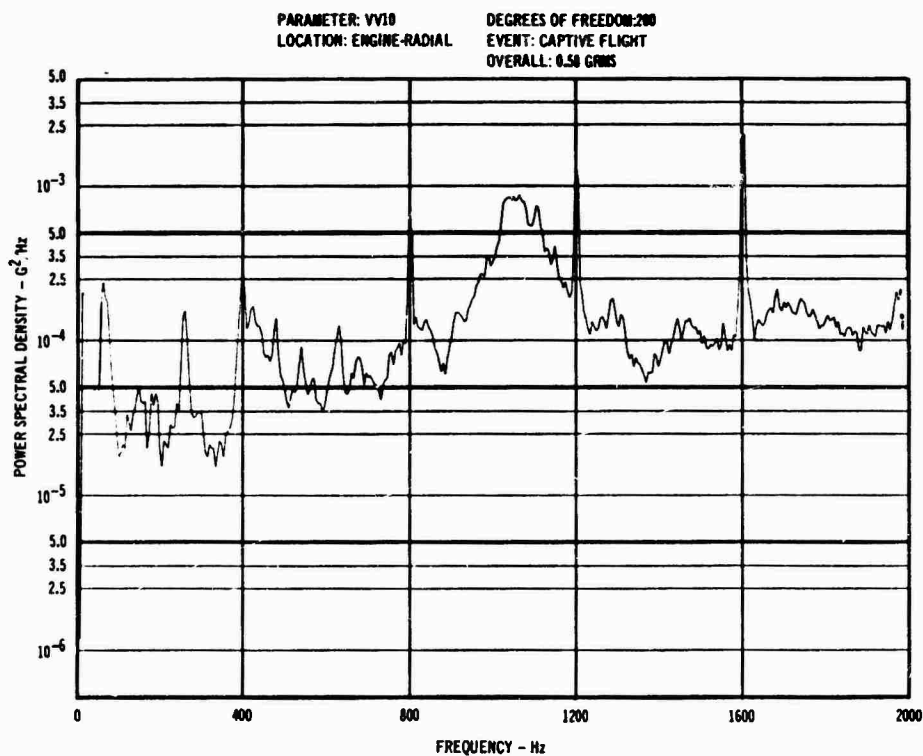


FIGURE 17 POWER SPECTRAL DENSITY

PARAMETER: VY11  
LOCATION: ACTUATOR-RADIAL

DEGREES OF FREEDOM: 200  
EVENT: CAPTIVE FLIGHT  
OVERALL: 0.71 GRMS

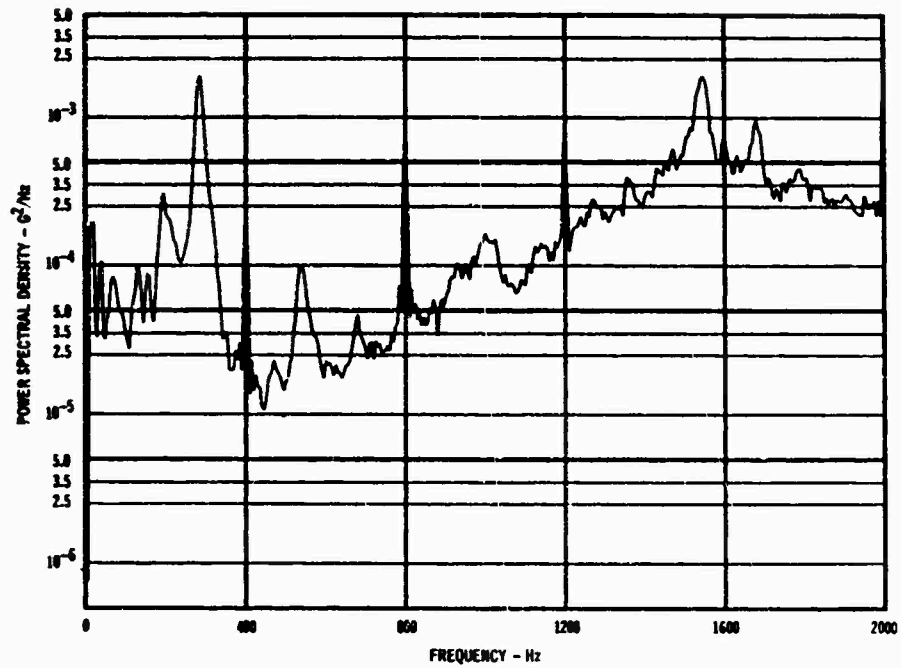


FIGURE 18 POWER SPECTRAL DENSITY

PARAMETER: VY31  
LOCATION: SEEKER-Z AXIS

DEGREES OF FREEDOM: 100  
EVENT: CAPTIVE 190% ENGINE RPM  
OVERALL: 0.72 GRMS

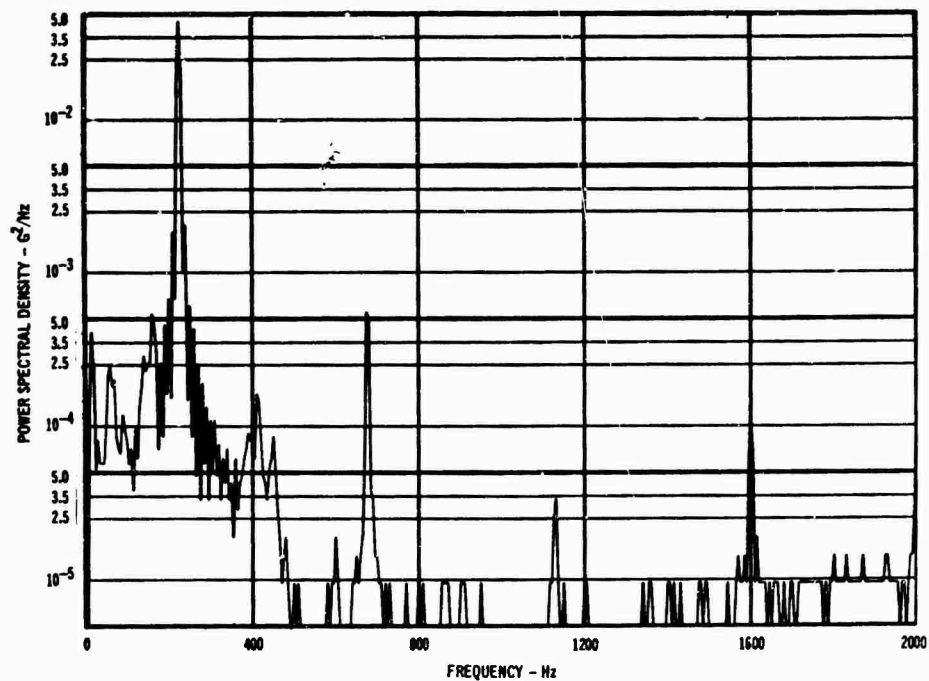


FIGURE 19 POWER SPECTRAL DENSITY

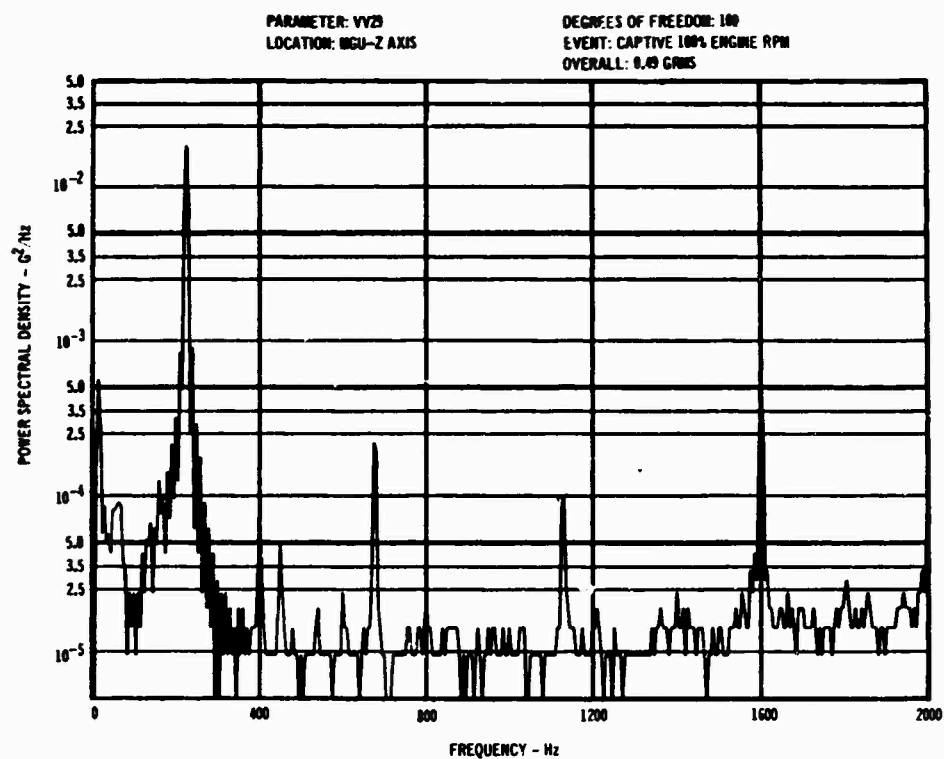


FIGURE 20 POWER SPECTRAL DENSITY

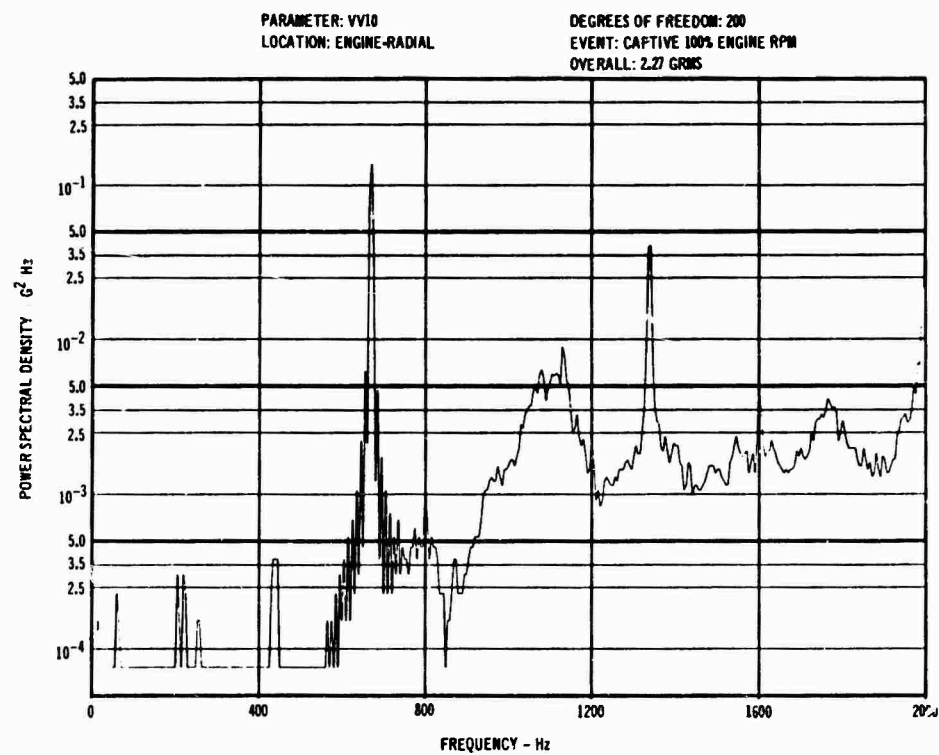


FIGURE 21 POWER SPECTRAL DENSITY

Vibration resulting from booster burning was much lower than expected. Figures 22 through 24 are spectra of the longitudinal vibration and Figures 25 and 26 are spectra of the lateral vibration during the boost phase. All vibration for this phase show less than 1 grms with the maximum level shown in Figure 24 which was a x-axis sensor located on primary missile structure at the missile/booster interface.

Missile cruise-flight starts with release from the aircraft or separation from the booster. Once this occurs the acoustic and vibration data becomes essentially stationary. Any changes in vibration levels during cruise can normally be associated with some change in turbojet engine performance. External acoustic levels are very low as shown in Figure 27. However, the internal acoustic level in the aft section of the missile is primarily influenced by engine noise and is higher. This internal acoustic spectrum shown in Figure 28 indicates that an overall level of 147 dB can be expected as a result of the engine noise. Vibration levels during cruise flight are shown in Figures 29 through 40. The measured levels show approximately 1 grms in the forward section of the missile and 3 grms in the aft section. The engine

frequency of approximately 670 Hz and its 1st harmonic are evident throughout the missile and can usually be seen in all the frequency spectra regardless of the direction being measured. A first axial (220 Hz) missile mode that developed during the cruise flight can be seen in Figure 29 measured at the forward end of the missile and in Figure 40 measured at the aft end of the missile.

Shock spectrum analyses were performed on some of the transient events. Figures 41 and 42 show the shock spectra at the seeker and turbojet engine for the booster ignition transient. Comparing Figures 41 and 42 gives an indication of the shock attenuation that can be attained along the longitudinal axis of the missile. Figure 43 through 45 are the shock spectrum for booster separation and Figures 46 through 48 are for turbojet engine start. These figures again show the shock response in the forward and aft sections of the missile. Figures 43 and 46 show the cross-axis response at the seeker to these events. In general, shock levels for the major transient events are much lower than expected and may be due to the filter action measurement systems which rolled off at 24 dB above 2 KHz.

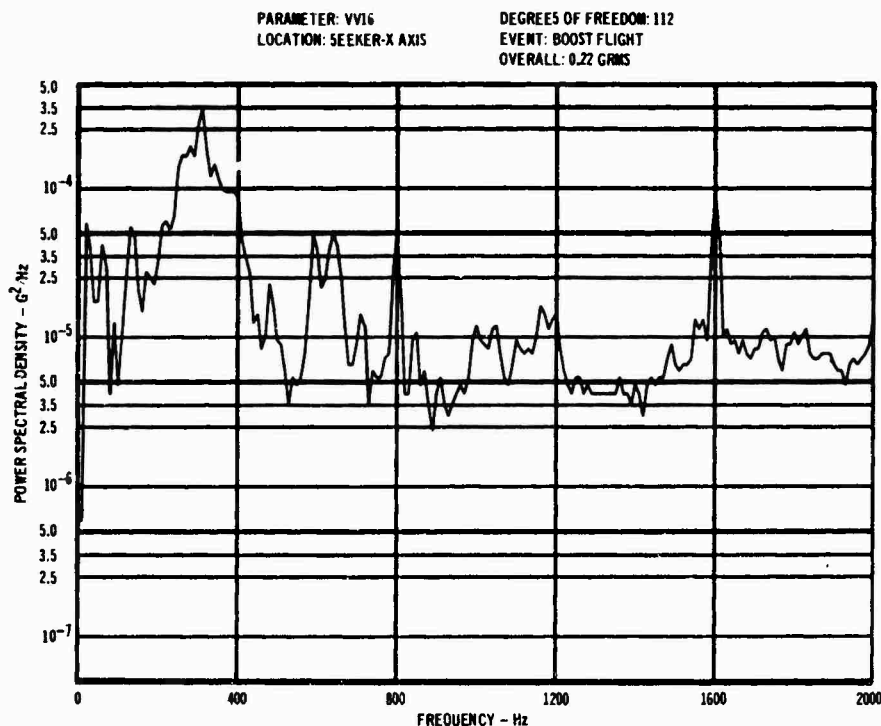


FIGURE 22 POWER SPECTRAL DENSITY

PARAMETER: VV06  
LOCATION: ENGINE - X AXIS

DEGREES OF FREEDOM: 30  
EVENT: BOOST FLIGHT  
OVERALL: 0.53 GRMS

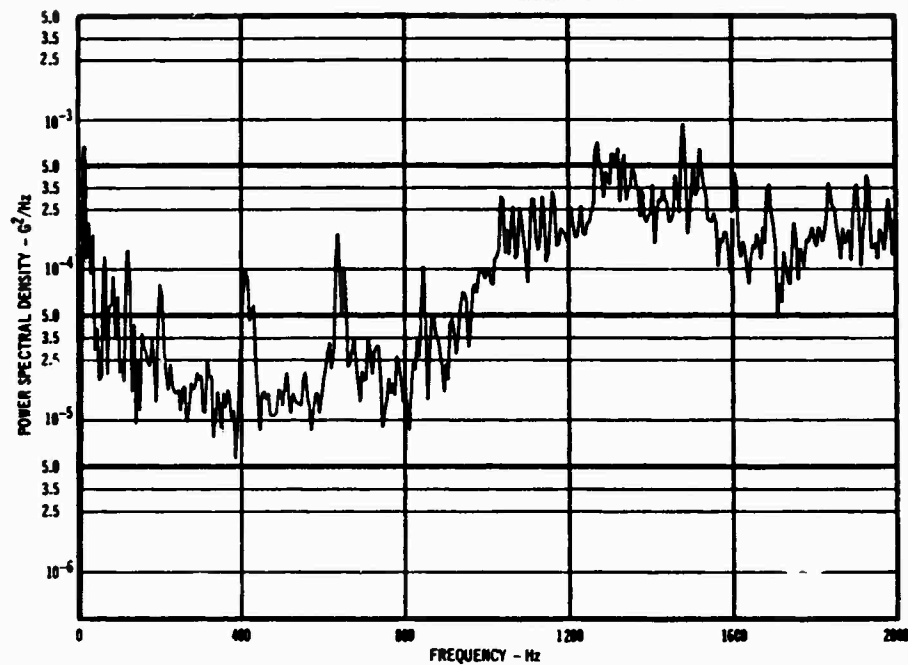


FIGURE 23 POWER SPECTRAL DENSITY

PARAMETER: VV06  
LOCATION: MISSILE BOOSTER  
INTERFACE X-AXIS

DEGREES OF FREEDOM: 112  
EVENT: BOOSTER FLIGHT  
OVERALL: 0.72 GRMS

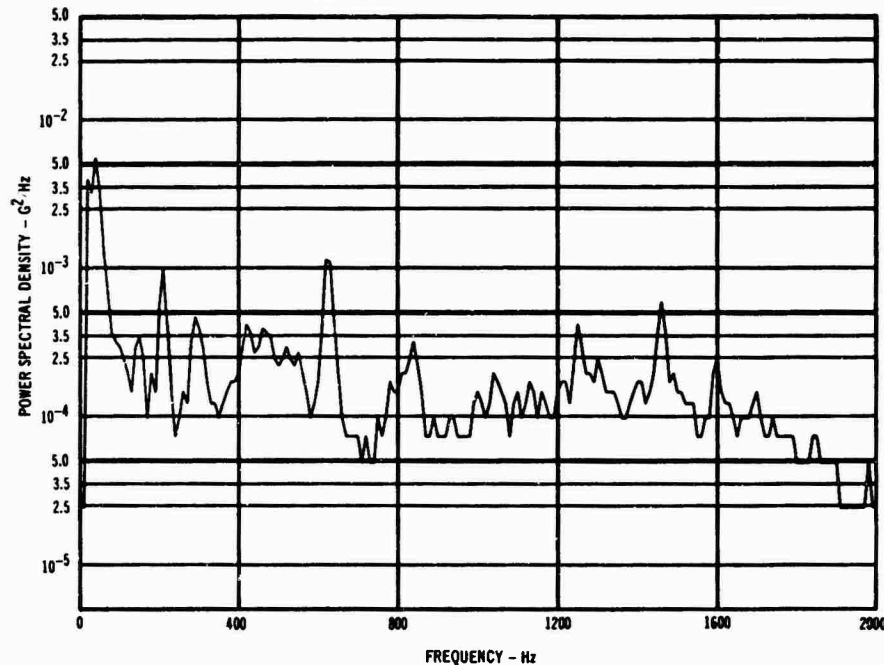


FIGURE 24 POWER SPECTRAL DENSITY



PARAMETER: VV13      DEGREES OF FREEDOM: 30  
 LOCATION: INGU-Y AXIS      EVENT: BOOST FLIGHT  
 OVERALL: 0.17 GRMS

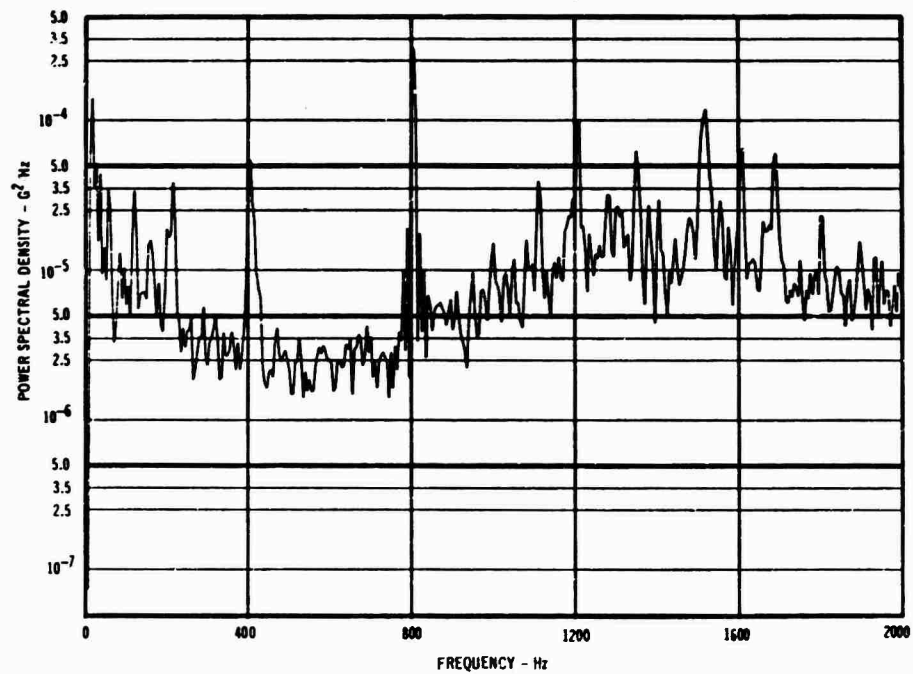


FIGURE 25 POWER SPECTRAL DENSITY

PARAMETER: VV17      DEGREES OF FREEDOM: 30  
 LOCATION: SEEKER - Y AXIS      EVENT: BOOST FLIGHT  
 OVERALL: 0.18 GRMS

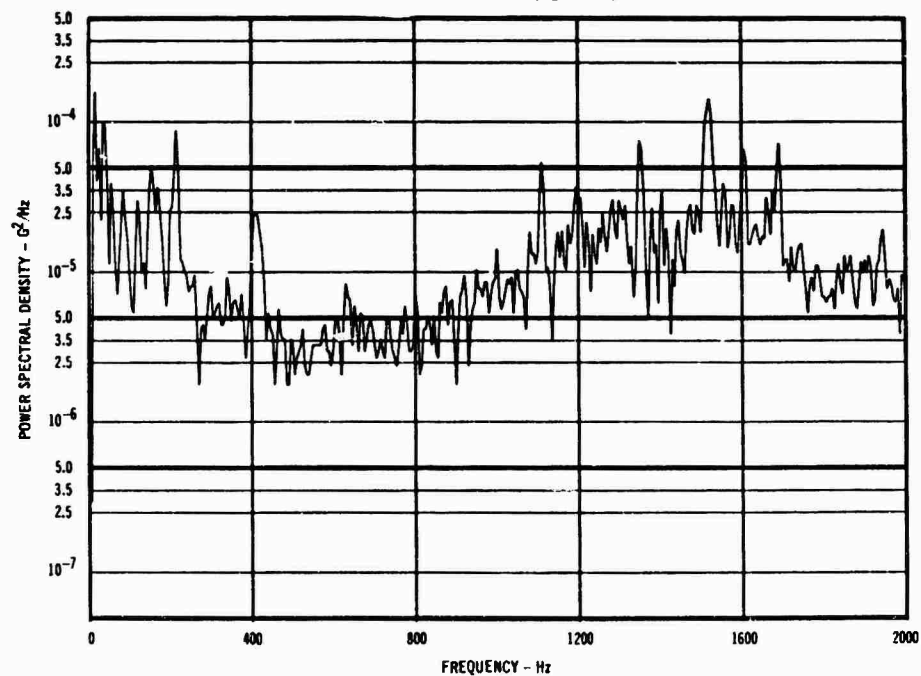


FIGURE 26 POWER SPECTRAL DENSITY

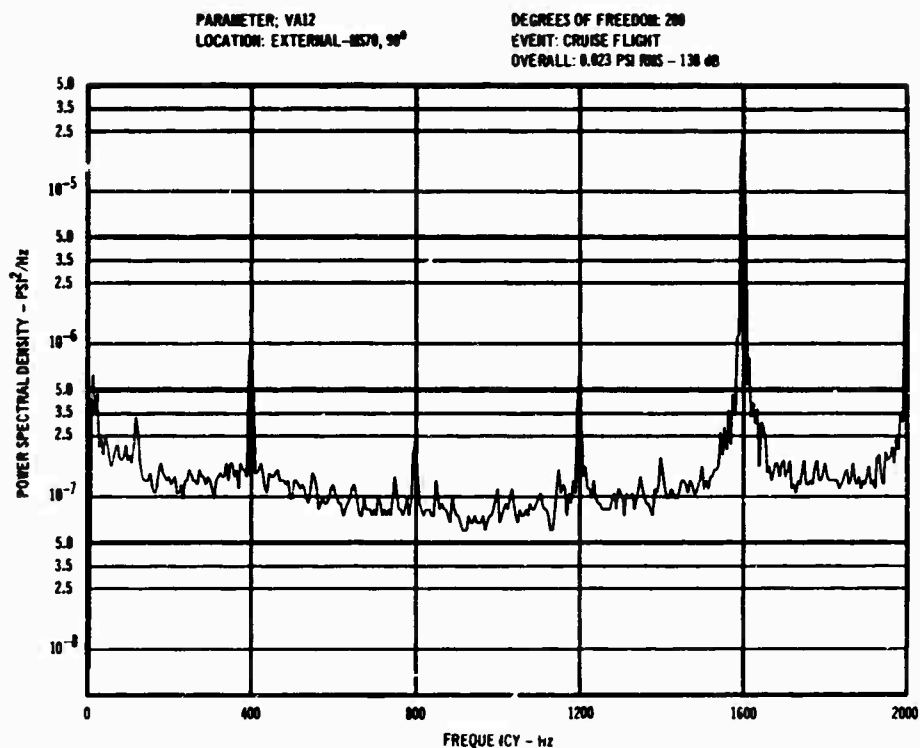


FIGURE 27 POWER SPECTRAL DENSITY

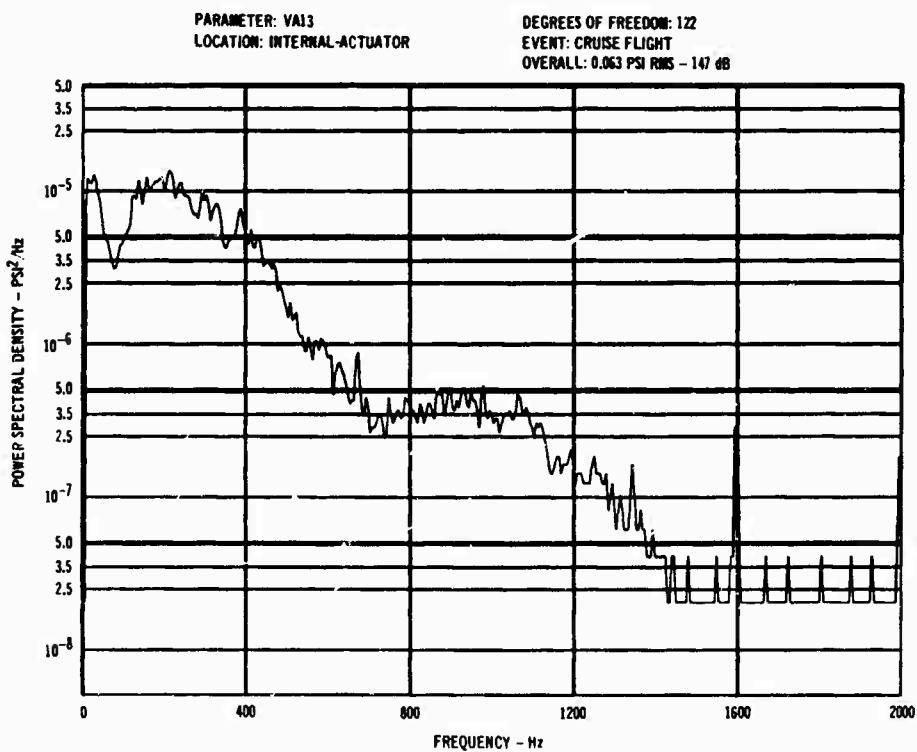


FIGURE 28 POWER SPECTRAL DENSITY

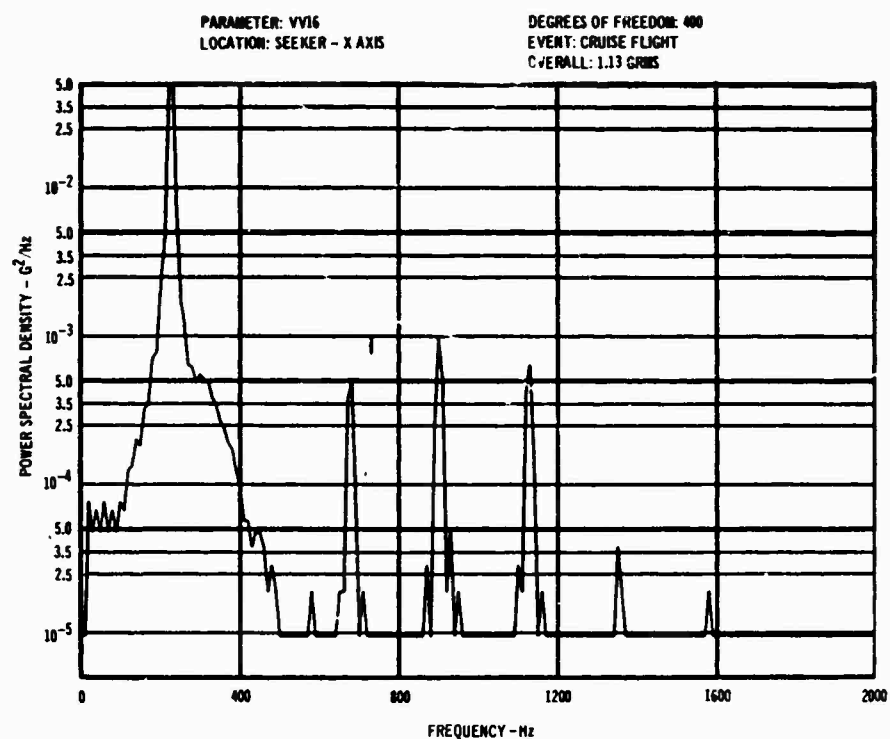


FIGURE 29 POWER SPECTRAL DENSITY

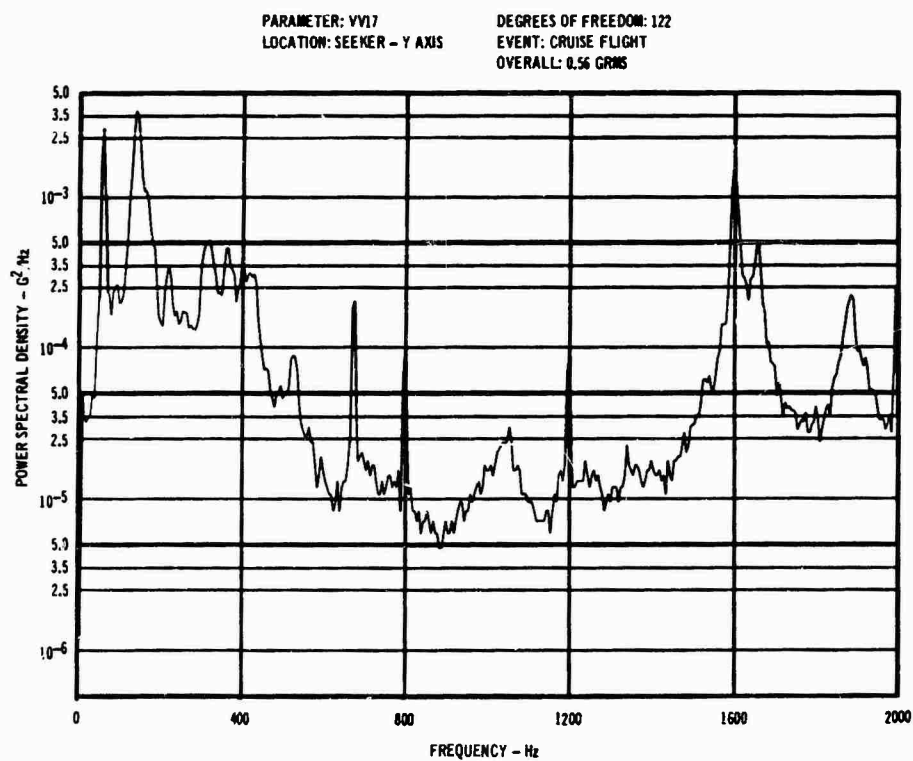


FIGURE 30 POWER SPECTRAL DENSITY

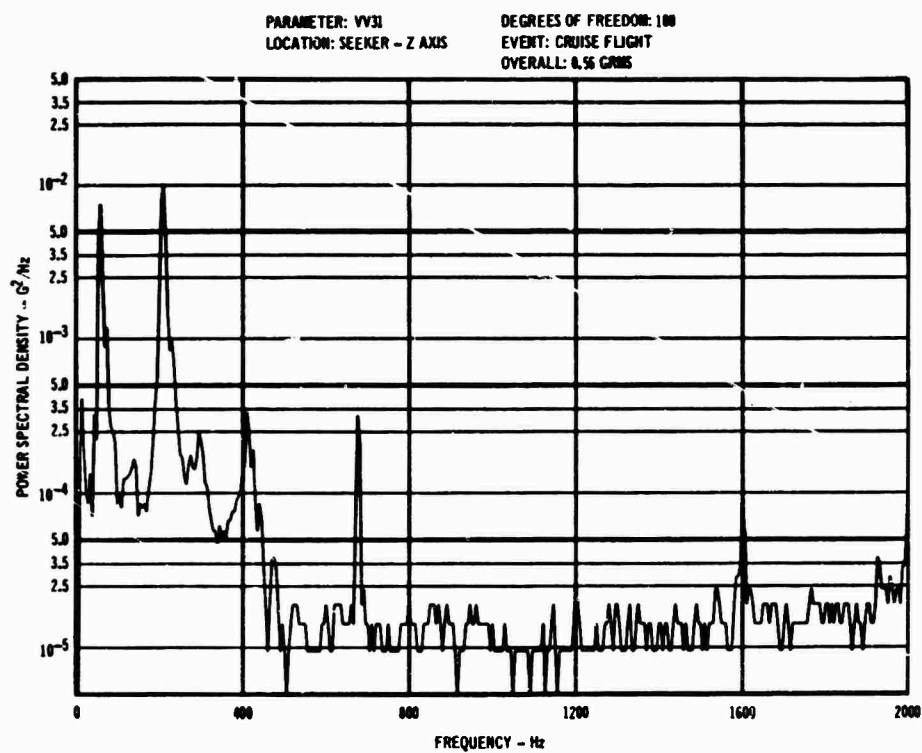


FIGURE 31 POWER SPECTRAL DENSITY

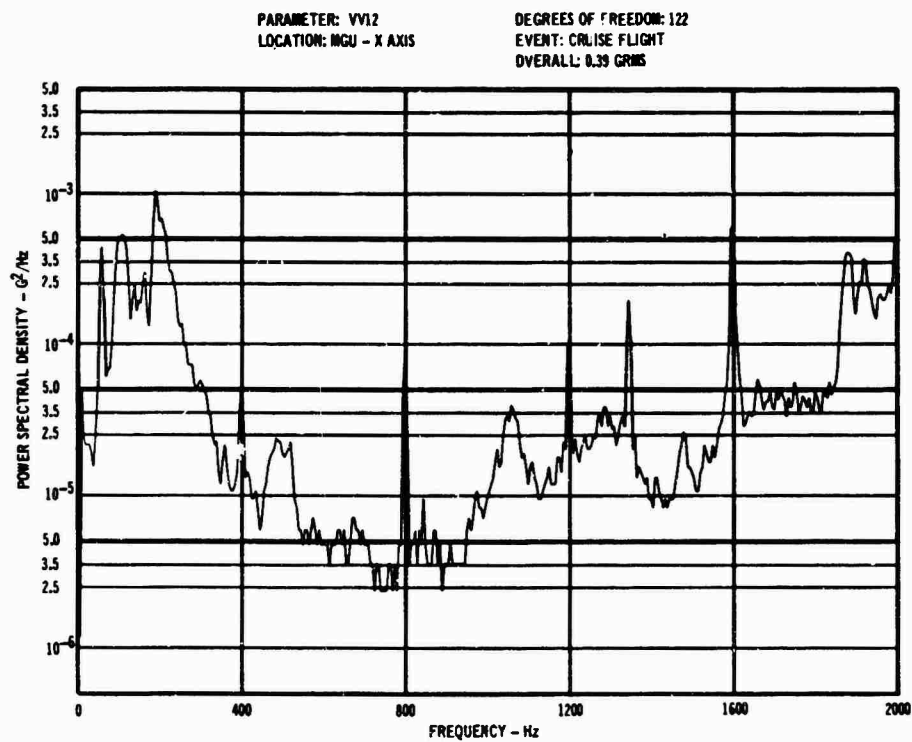


FIGURE 32 POWER SPECTRAL DENSITY

PARAMETER: VV13  
LOCATION: MGU - Y AXIS

DEGREES OF FREEDOM: 100  
EVENT: CRUISE FLIGHT  
OVERALL: 0.41 GRMS

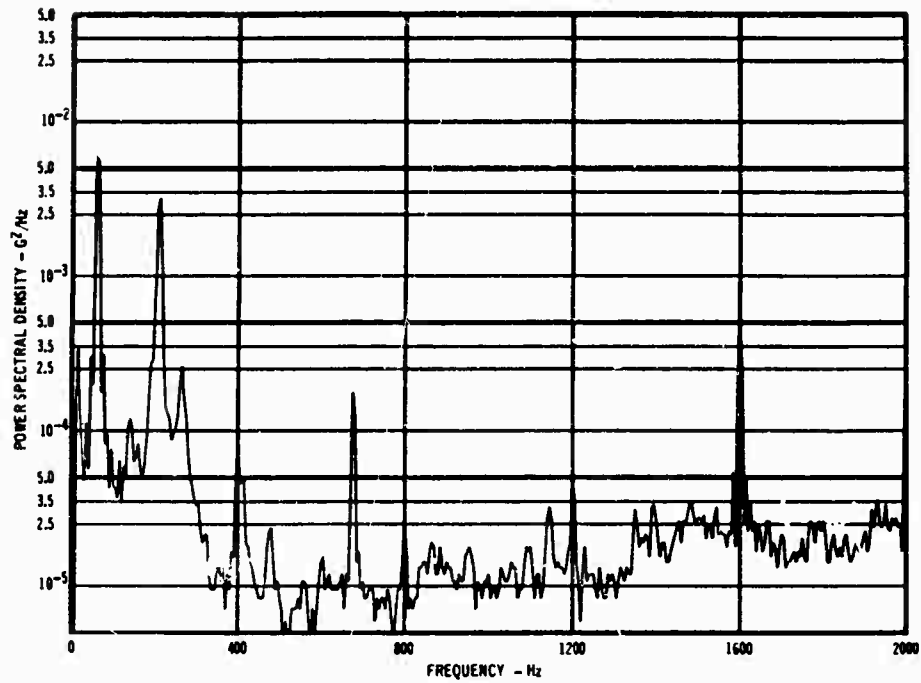


FIGURE 33 POWER SPECTRAL DENSITY

PARAMETER: VV29  
LOCATION: MGU - Z AXIS

DEGREES OF FREEDOM: 100  
EVENT: CRUISE FLIGHT  
OVERALL: 0.59 GRMS

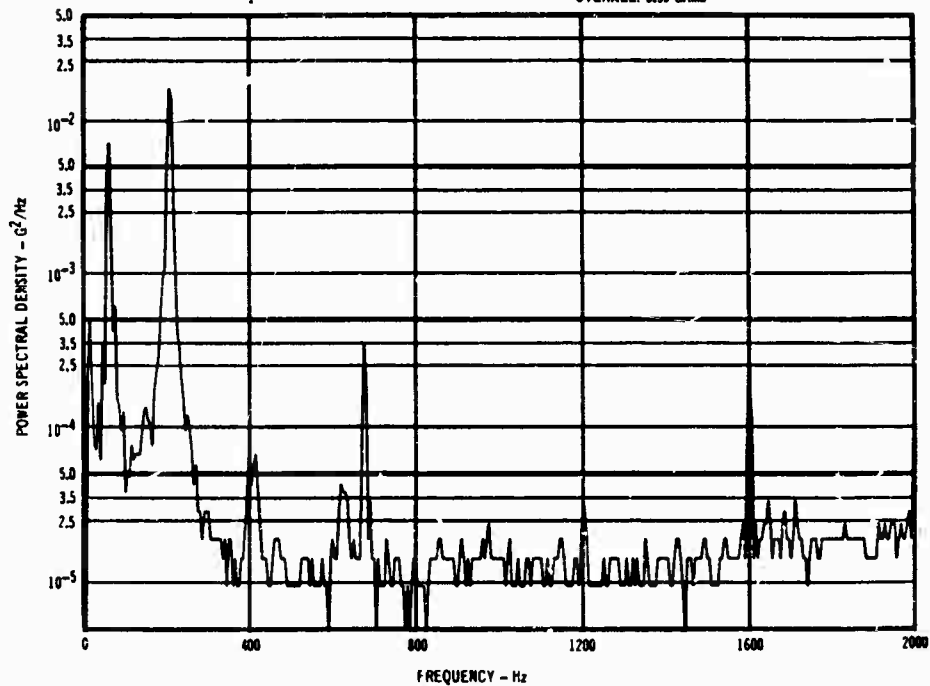


FIGURE 34 POWER SPECTRAL DENSITY

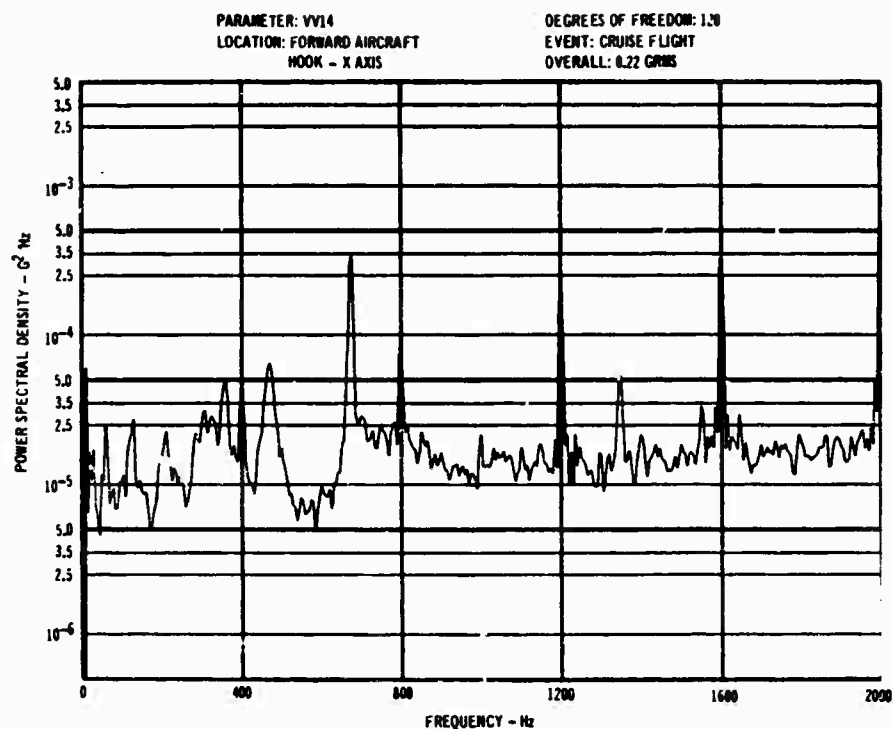


FIGURE 35 POWER SPECTRAL DENSITY

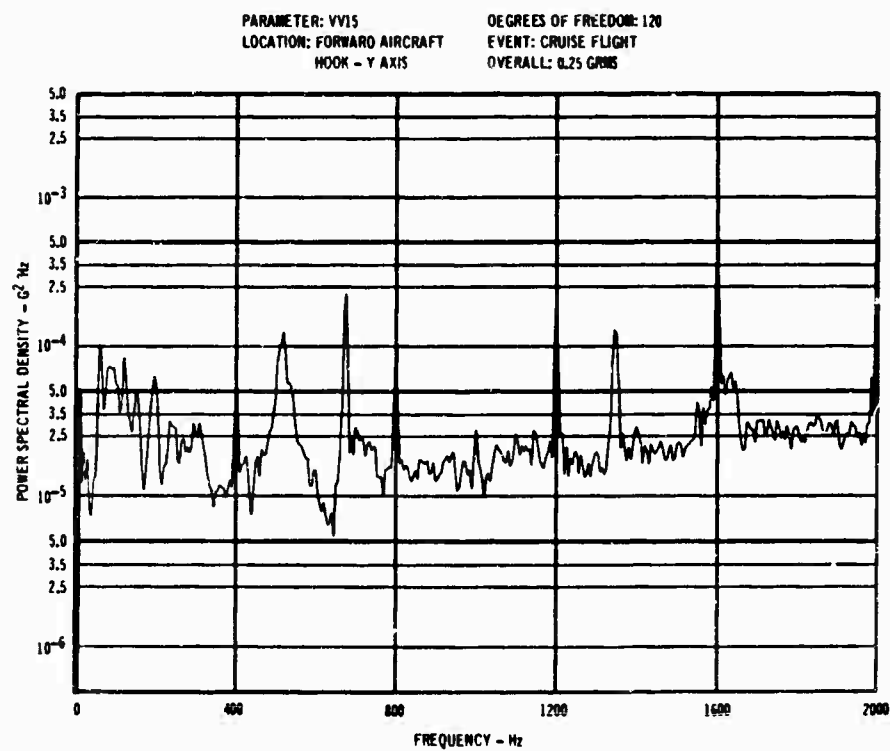


FIGURE 36 POWER SPECTRAL DENSITY

PARAMETER: VV09  
LOCATION: ENGINE - X AXIS

DEGREES OF FREEDOM: 200  
EVENT: CRUISE FLIGHT  
OVERALL: 1.85 GRMS

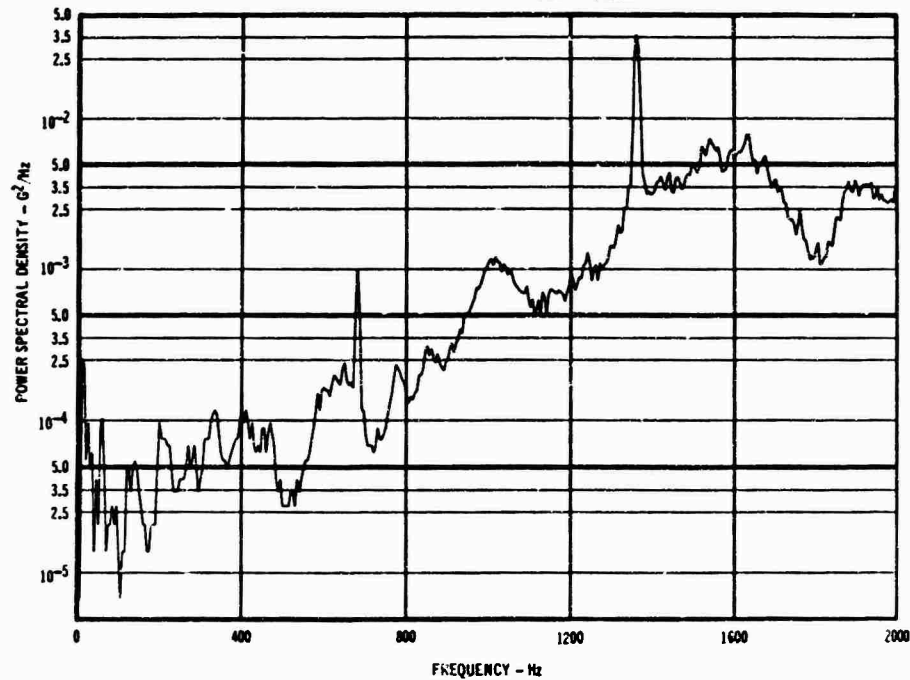


FIGURE 37 POWER SPECTRAL DENSITY

PARAMETER: VV10  
LOCATION: ENGINE - RADIAL

DEGREES OF FREEDOM: 200  
EVENT: CRUISE FLIGHT  
OVERALL: 3.61 GRMS

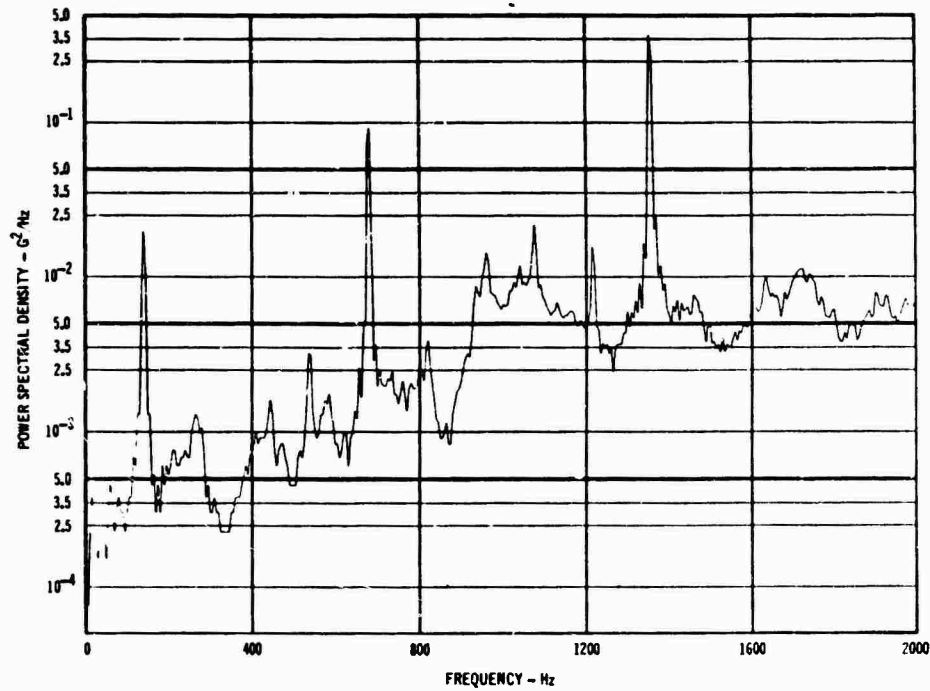


FIGURE 38 POWER SPECTRAL DENSITY

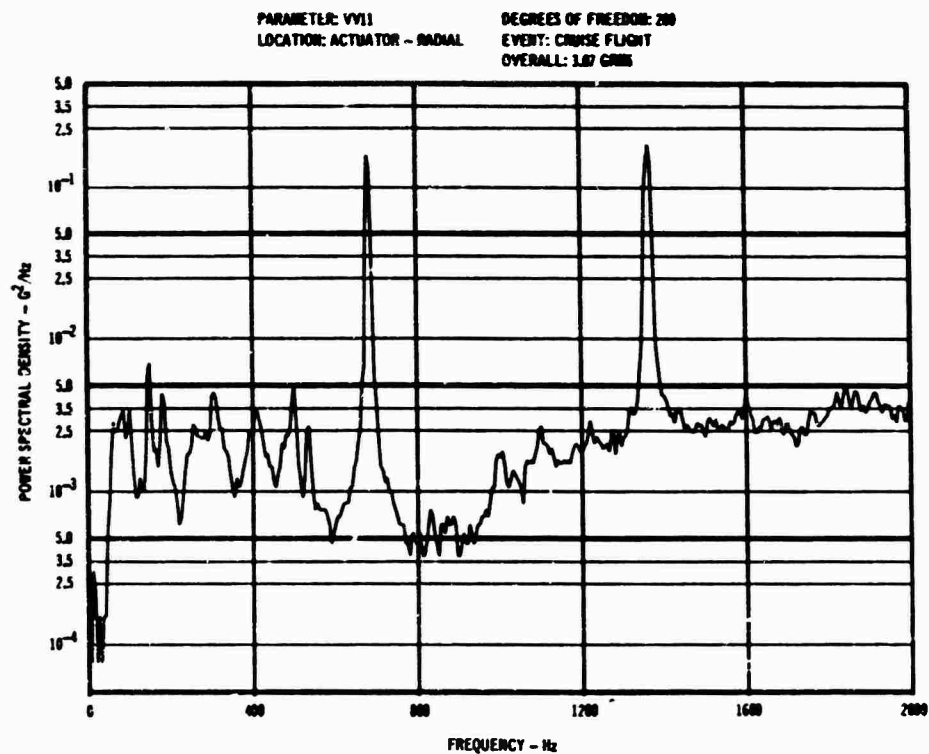


FIGURE 39 POWER SPECTRAL DENSITY

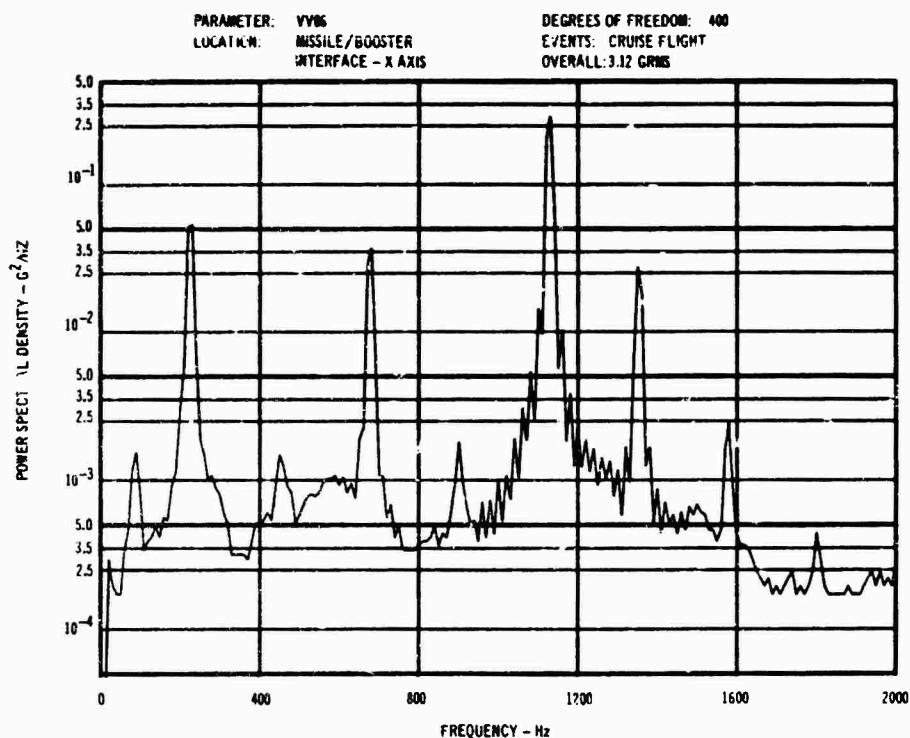


FIGURE 40 POWER SPECTRAL DENSITY



PARAMETER: VV31      EVENT: BOOSTER IGNITION  
LOCATION: SEEKER - Z AXIS      DAMPING: 5%

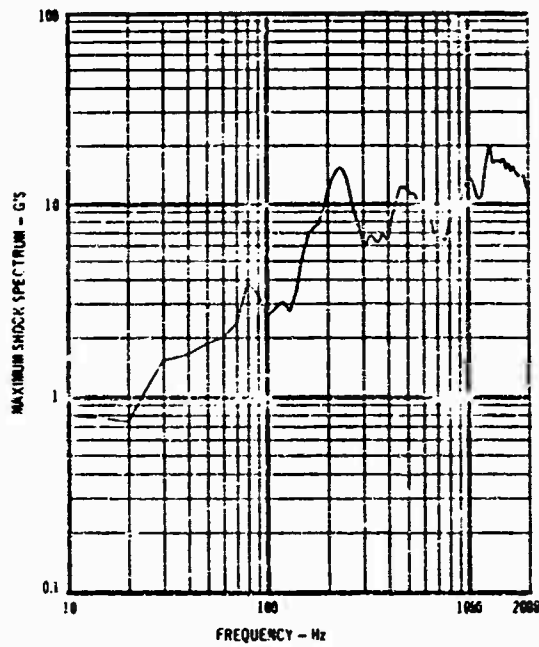


FIGURE 41 - SHOCK SPECTRUM

PARAMETER: VV09      EVENT: BOOSTER IGNITION  
LOCATION: ENGINE - X AXIS      DAMPING: 5%

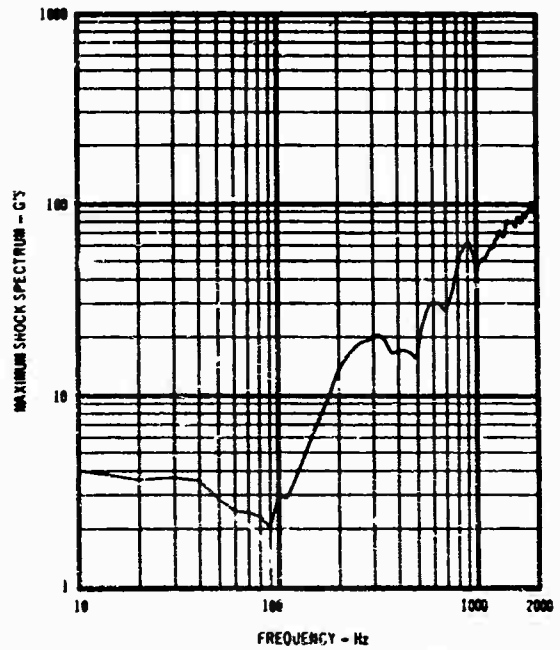


FIGURE 42 - SHOCK SPECTRUM

PARAMETER: VV31      EVENT: BOOSTER SEPARATION  
LOCATION: SEEKER - Z AXIS      DAMPING: 5%

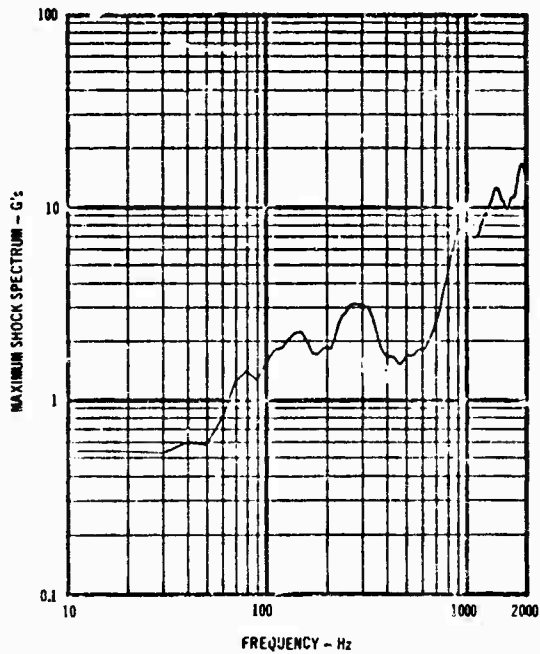


FIGURE 43 SHOCK SPECTRUM

PARAMETER: VV15      EVENT: BOOSTER SEPARATION  
LOCATION: SEEKER - X AXIS      DAMPING: 5%

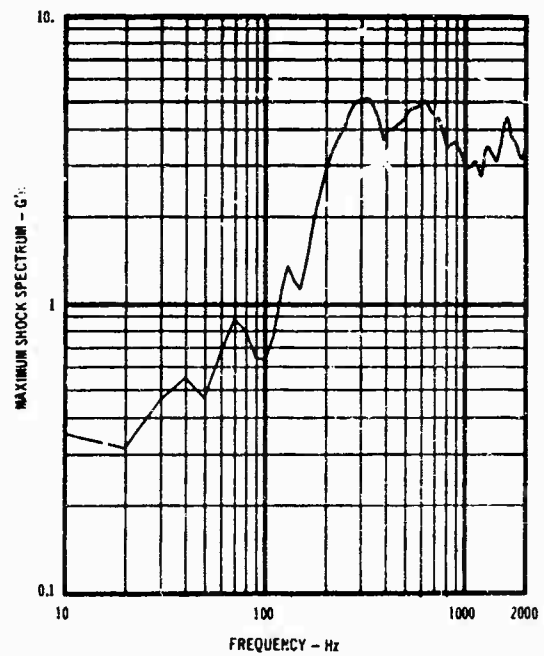


FIGURE 44 SHOCK SPECTRUM

PARAMETER: VV11  
 LOCATION: ACTUATOR-RADIAL  
 EVENTS: BOOSTER SEPARATION  
 DAMPING: 5%

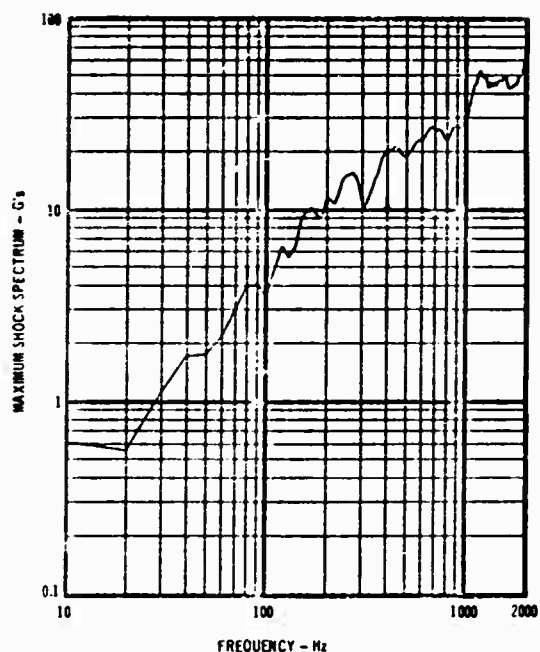


FIGURE 45 SHOCK SPECTRUM

PARAMETER: VV31  
 LOCATION: SEEKER-Z AXIS  
 EVENTS: TURBO JET ENGINE START  
 DAMPING: 5%

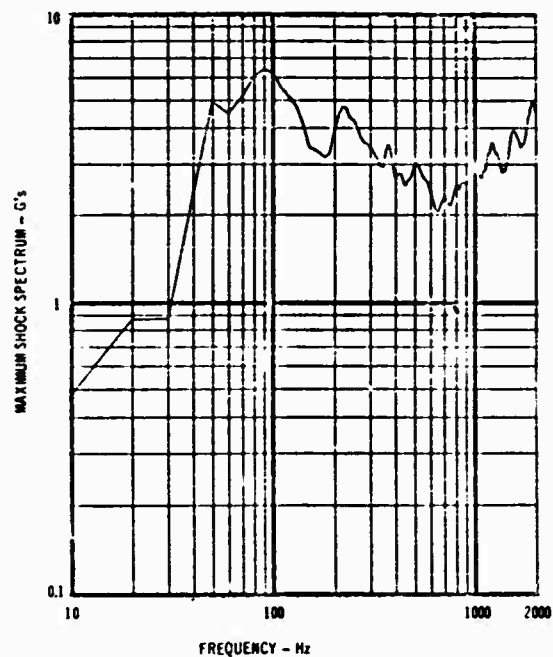


FIGURE 46 SHOCK SPECTRUM

PARAMETER: VV16  
 LOCATION: SEEKER-X AXIS  
 EVENT: TURBO JET ENGINE START  
 DAMPING: 5%

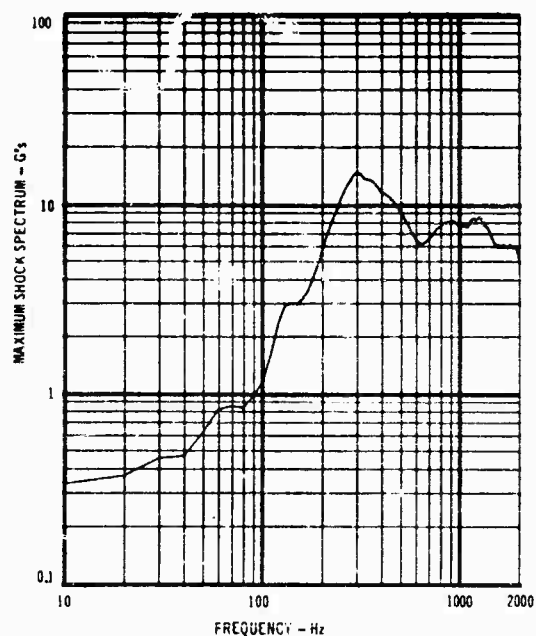


FIGURE 47 SHOCK SPECTRUM

PARAMETER: VV11  
 LOCATION: ACTUATOR-RADIAL  
 EVENT: TURBO JET ENGINE START  
 DAMPING: 5%

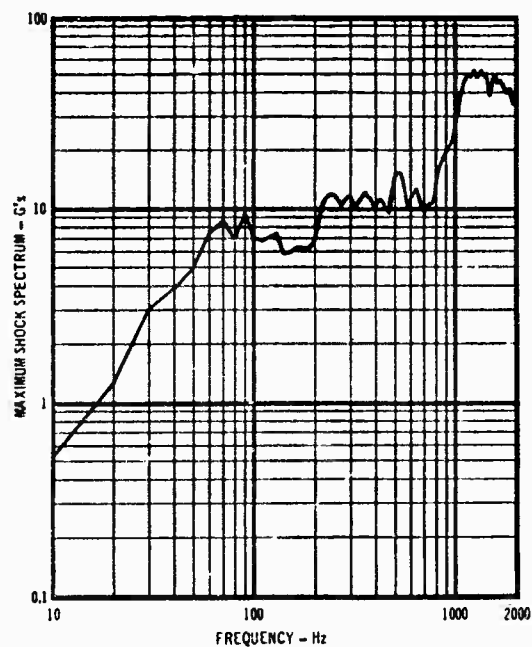


FIGURE 48 SHOCK SPECTRUM

## CONCLUSIONS

In general, good acoustic and vibration data was obtained for all flights during the Design Phase of the Harpoon Missile Program. This data will be used to update weapon system development phase environmental requirements and, if necessary, to support design changes. The extensive dynamic data provides a good basis for establishing dynamic

environments for future tactical missile programs. The Harpoon missile vibration and acoustic data provides information for turbo-jet engine and solid booster motor operation, high and low altitude flight, maximum dynamic pressure flight and P-3 captive flight. The data provides good coverage of all missile sections for all of the various flight conditions.

NARROW BAND TIME HISTORY ANALYSIS OF  
TRANSPORT AIRCRAFT VIBRATION DATA

Roger E. Thaller and Jerome Pearson  
Air Force Flight Dynamics Laboratory  
Wright-Patterson AFB, Ohio

The requirement to transport fragile aerospace payloads in large aircraft has created the need to accurately define the cargo deck vibration environments of such aircraft as the C-135, the C-141, and the C-5A. To determine the probability of occurrence of damaging accelerations during cargo aircraft operations, a special method was developed for analyzing and displaying the data, which may be non-Gaussian. The method was applied to low-frequency cargo deck vibrations in order to develop vibration test qualification curves for a large, flexible spacecraft. The results allow the probabilities of given levels of acceleration in separate frequency bands to be computed and provide a measure of how these probabilities may differ from the Gaussian case.

#### INTRODUCTION

In recent years the availability of large transport aircraft has allowed the transporting by air of many large, fragile aerospace payloads. Some of these payloads, such as spacecraft and launch vehicles carried horizontally, are sensitive to low levels of vibration at frequencies lower than 10 Hertz. The measurement of cargo deck vibration environments has a long history (REF. 1-4), but most of these studies have dealt with the frequency range above 5 or 10 Hz. Vibration data are ample in the higher frequency ranges up to 2000 Hz but are nearly non-existent below 5 Hz.

Faced with this lack of data and the need to transport payloads with known high responses to 0.5 to 2 Hz excitation, the Air Force Space and Missiles System Organization (SAMSO) requested that the Air Force Flight Dynamics Laboratory perform the necessary flight tests to measure low-frequency responses of a large aircraft cargo deck and to provide a measure of the risk of given levels of acceleration occurring during operations. The magnitude of the accelerations of concern is such that if they occur only once, the payload will be damaged. It was known that large cargo aircraft have elastic modes with frequencies as low as 0.73 Hz (5), and it was desired to measure responses at least

this low in frequency.

#### FLIGHT TESTS

The flight vibration tests were designed to provide a maximum amount of information on the probability of occurrence of different levels of acceleration with a minimum of instrumentation, with no modification to the aircraft, and with few test flights. In order to accomplish this, 12 low-frequency accelerometers were mounted in pairs at six locations on the cargo deck as shown in Figure 1. The accelerometers were attached to aluminum blocks mounted on the permanent cargo tie-down rails at the sides of the cargo deck. Since vertical accelerations were considered likely to be the highest, all six locations included a vertical accelerometer. The forward and aft locations included lateral accelerometers and the center locations included longitudinal accelerometers. By combining the signals from pairs of these accelerometers in real time, roll, pitch, and yaw angular accelerations were also derived. It was felt that this amount of information would be sufficient to define the vibratory environment of the cargo deck.

The data of interest were chiefly the accelerations below 10 Hz. Past studies of cargo deck accelerations were limited

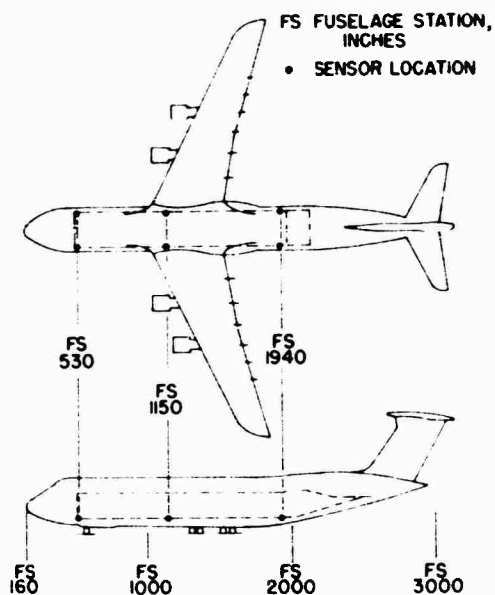


Figure 1 Transducer Locations

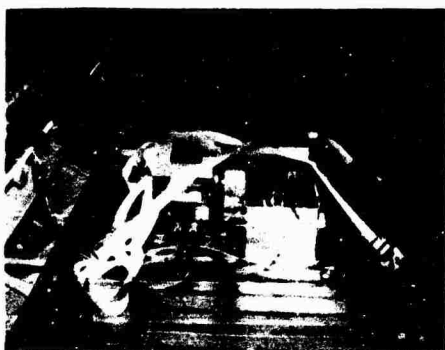


Figure 2 Instrumentation Package in Aircraft

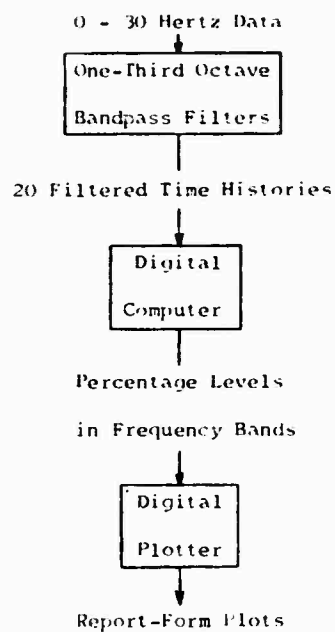


Figure 3 Flow Chart of Special Analysis

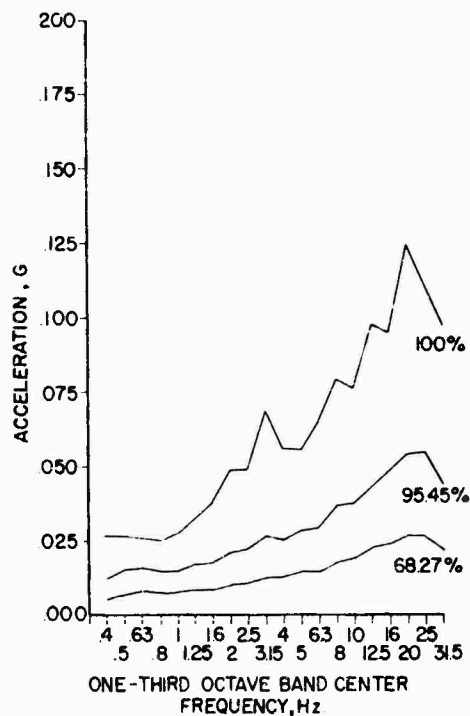


Figure 4 Results of Specialized Analysis Performed on Gaussian Data

mainly to frequencies above 5 Hz, and the results at the lower frequencies had large errors. The data were low-pass filtered at 30 Hz in order to eliminate the higher frequency and higher g signals which commonly occur in aircraft flight. The accelerometers chosen had capability to DC; however, the signals were high-pass filtered at 0.2 Hz in order to prevent amplification of any DC offset in the amplifiers. The frequency range of the data was then 0.2 to 30 Hz.

The 12 channels of data were amplified and recorded in flight by a compact instrument package shown in Figure 2, which contained the amplifiers, power supply, and a tape recorder. The amplifiers were equipped with automatic gain controls which adjusted the amplifier gain in 10 dB steps over a 70 dB range to ensure that the signals were recorded with proper amplitude. The automatic gain change was triggered when the signal level was out of the amplifier range for more than 0.4 seconds. Most flight conditions of interest, including taxi, takeoff, cruise, flight in turbulence, and descent, could thus be recorded without advance knowledge of the vibration levels. For the landing data, however, the amplifiers were locked into a precalculated gain step in order to avoid clipping the response at the instant of runway impact.

The test flights were intended to cover a range of variables that could affect the accelerations experienced in various flight conditions. Although only one aircraft was used, the gross weights during the flight tests ranged from 455,000 pounds to 673,000 pounds, several different pilots flew the aircraft, 27 takeoffs and landings were made on different runways, and four hours of cruising time were recorded in conditions ranging from smooth air to terrain following at low altitude, which simulates heavy turbulence.

#### DATA ANALYSIS

The data tapes were analyzed by the procedure shown in Figure 3. The initial survey of the results indicated that the conditions of climb, cruise in smooth air, and descent were not important in terms of the cargo deck accelerations produced. The conditions of landing, high-speed taxi, and low altitude terrain avoidance, which simulated flight in heavy turbulence, produced the highest accelerations and were chosen for detailed analysis.

Because it was desired to know the vibration environment as a function of frequency, the accelerometer data were

immediately divided into twenty one-third octave bands with center frequencies of 0.4 Hz to 31.5 Hz. In order to use the standard one-third octave band filters which are available with center frequencies of 3.15 Hz and higher, the recorded data were played back at eight times the recording speed. The 0.4 Hz data were thus filtered by the 3.15 Hz filter, and similarly for the other bands. Each of these 20 filtered time histories for each accelerometer was then analyzed statistically. Each time history was sampled at a high rate compared to the signal frequency and an acceleration histogram was constructed from the absolute values of acceleration. To completely describe each filtered time history, the histogram and its statistical parameters such as mean, variance, and peak value should be plotted. Then the character of the data could be assessed completely. However, this would require 20 plots for each of 12 sensors for each flight condition — a prohibitively large number.

The method chosen to display these data more compactly was to plot just three values for each frequency band — the highest acceleration observed, the acceleration level below which 95.45% of the data fell, and the level below which 68.27% of the data fell. A sample of data plotted in this fashion is shown in Figure 4 for a Gaussian random signal. The reason for choosing these particular percentage levels is that they correspond to  $2\sigma$  and  $\sigma$  of a Gaussian distribution. As a result, these two curves should be in the ratio of 2:1 for Gaussian data. The peak value curve will be a function of the testing time in terms of the frequency — that is, the number of cycles of data measured. Theoretically, an infinitely long testing time will give an infinite peak value and an exact 2:1 ratio between the 95.45% and 68.27% curves. For practical testing times and for physically realizable accelerations, this ratio is still very close to 2:1, but the peak value curve usually falls between  $3\sigma$  and  $6\sigma(6)$ .

When this method of analyzing and displaying the data is applied to a time signal whose character is unknown, it is possible to see very quickly how closely the data meet this test of being Gaussian, and to make some estimate of the probability of occurrence of any given level of acceleration. These acceleration probabilities can be used to determine the probability of damage to a particular payload. If the payload is unable to withstand the environment, these results can then be used to design isolation mounts for the required attenuation.

## TEST RESULTS

Some representative data from the flight tests during landing and during low-level terrain following have been assembled for illustration. Figure 5 shows vertical accelerations at the right rear cargo deck for 27 landings. This composite plot was made of all the landings in the test program, and includes three runways, several pilots, and a range of gross weights. The result is a composite of the typical landing acceleration. Figure 6 shows the lateral acceleration at the left rear cargo deck and Figure 7 the longitudinal acceleration at the left center cargo deck for all the landings. These results show a ratio of about 2:1 between the 95.45% and 68.27% levels, and indicate that the data are not very different from Gaussian excitation for most frequency bands. There appears to be sinusoidal excitation superimposed at discrete frequencies, apparently corresponding to airframe resonances.

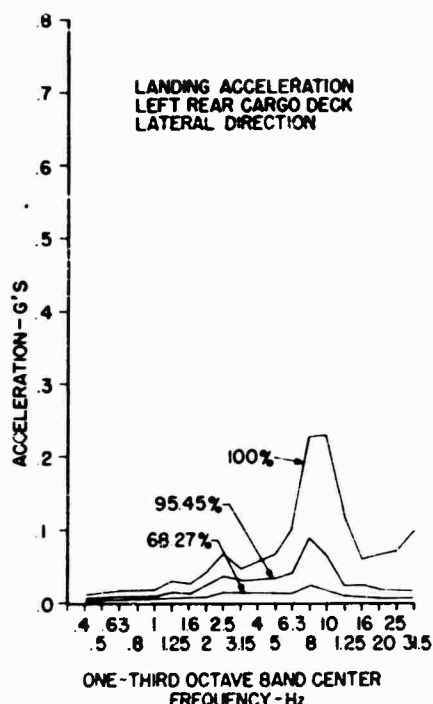


Figure 6 Lateral Landing Accelerations

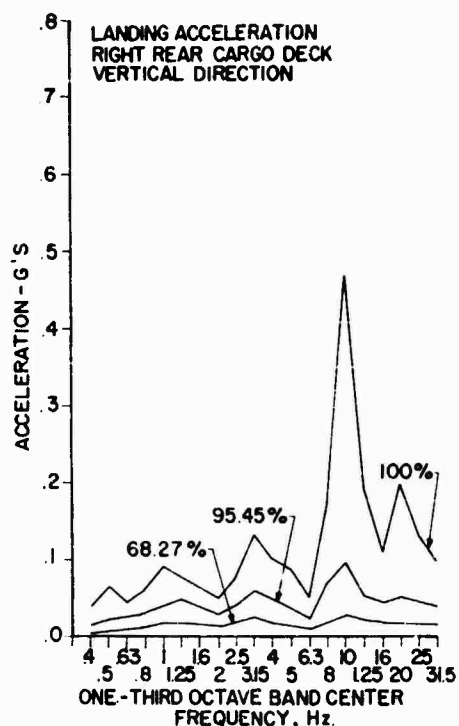


Figure 5 Vertical Landing Accelerations

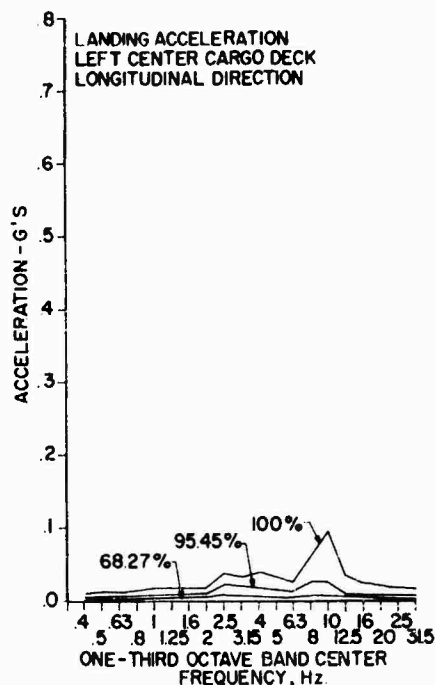


Figure 7 Longitudinal Landing Accelerations

A typical time history of landing accelerations in the three orthogonal directions is shown in Figure 8. The highest value of acceleration recorded occurred in the 10 Hz frequency band. Angular acceleration measurements showed it to be a roll mode which causes large vertical accelerations at the sides of the cargo deck in the gear-fixed modes of landing and taxiing.

It was hoped that some data would be obtained from flight in clear air turbulence during the test program, but only very light turbulence was recorded in several hours of flight. In order to obtain a measure of the response accelerations to be expected during turbulence, data were taken during low-level terrain avoidance. In this flight condition, the aircraft flies at a fixed height of 1000 feet above the ground. A terrain-avoidance radar corrects the flight path in response to changes in ground elevation ahead of the aircraft. The result is a high level of vibration which is similar to flight in very rough air. The responses recorded in this flight condition were used as an indication of those expected during flight in severe turbulence.

A summary of vertical accelerations at the right rear cargo deck over 14 minutes of terrain following is shown in Figure 9; Figure 10 and Figure 11 show corresponding values for lateral accelerations at the left rear cargo deck and longitudinal accelerations at the left center cargo deck, respectively. Since all these data were taken during the equivalent of heavy turbulence, these curves should be used in conjunction with an estimate of the risk of encountering heavy turbulence during expected flight profiles in deriving vibration test criteria. A short time history of the three orthogonal accelerations during terrain following is shown in Figure 12. Measurements were made during high-speed taxiing, in addition to landing and terrain following. These results and the results of the derived angular accelerations are described completely in a limited distribution report (7).

#### CONCLUSIONS

The results of this flight test program and analysis are summarized by the plots of maximum vibration amplitude versus frequency in Figure 13. In this figure, a vibration test curve from previous data (8, 9) is shown as a dashed line. The maximum accelerations observed in this program have been converted to equivalent double amplitudes and plotted as open circles. By applying an appro-

priate safety factor to account for the short testing times, a vibration test curve can be drawn using these plots.

The data were found to be approximately Gaussian with sinusoidal excitation superimposed at discrete frequencies which apparently correspond to airframe resonances. Assuming the data are Gaussian, the 68.27% level corresponds to  $\sigma$ , and the probability of occurrence of higher values of acceleration can be computed from this value and from the testing times given in this paper. A different test curve could then be developed using a particular criterion for the probability of failure. This method could be refined to apply to specific locations on the cargo deck by using the complete data available in Reference 7.

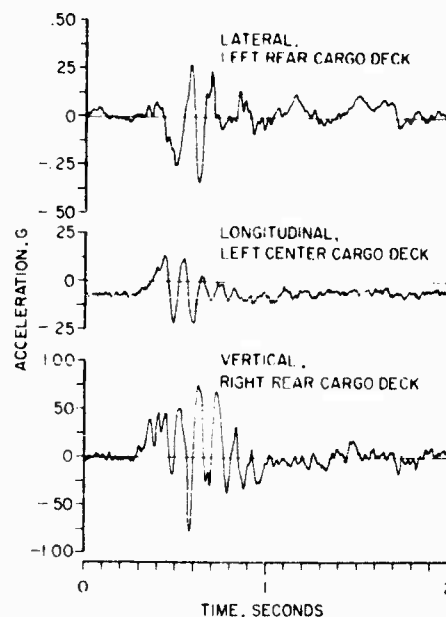


Figure 8 Landing Acceleration Time Histories



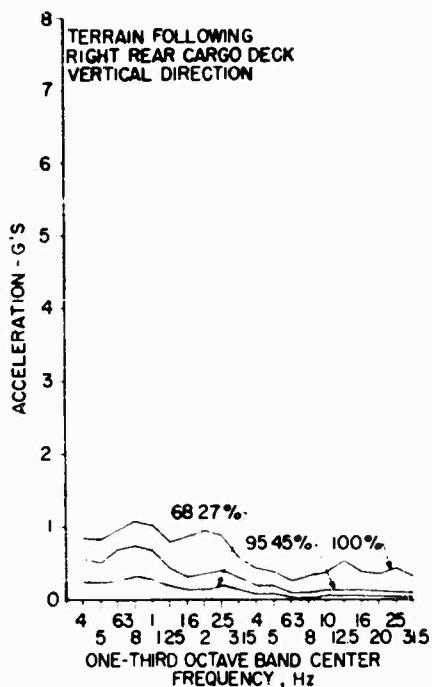


Figure 9 Terrain-Following  
Vertical Acceleration

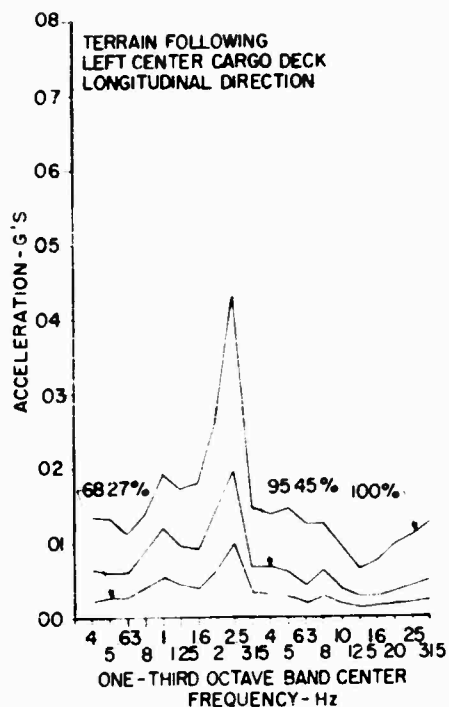


Figure 11 Terrain-Following  
Longitudinal Acceleration

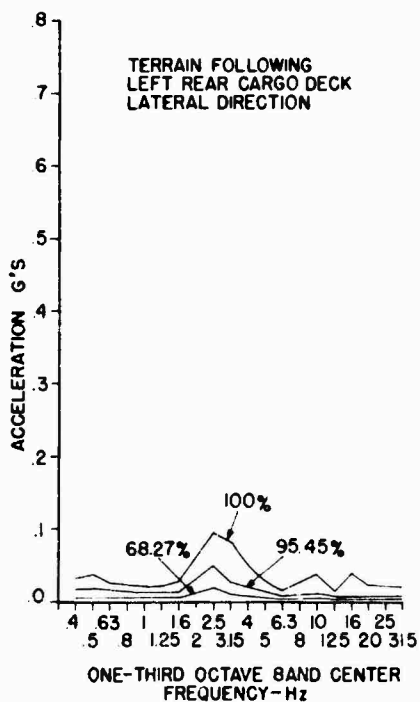


Figure 10 Terrain-Following  
Lateral Acceleration

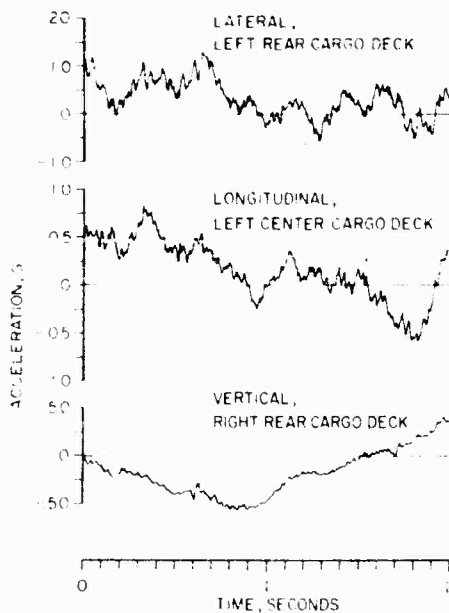


Figure 12 Terrain-Following  
Acceleration Time Histories

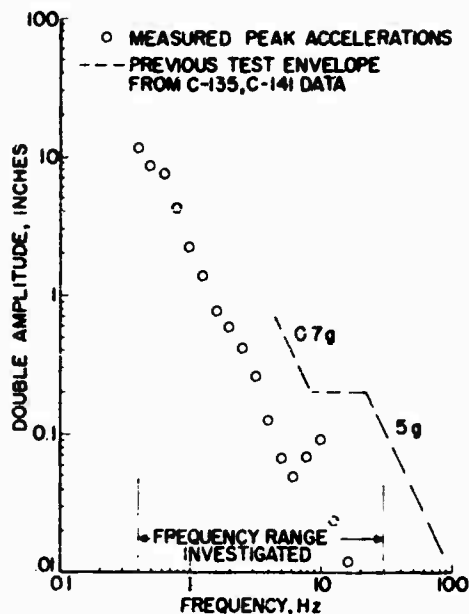


Figure 13 Recommended Vibration Test Envelope

#### REFERENCES

1. Magrath, H.A., Rogers, O.R., and Grimes, C.K.: Shock and Vibration Handbook, (Harris, C.M. and Crede, C.E., Eds.), Vol. 3, Chapter 47, McGraw-Hill, New York, 1961.
2. Ostrem, F.E.: "A Survey of the Transportation Shock and Vibration Input to Cargo." Shock and Vibration Bulletin, Part 1, January 1972, pp. 137-142.
3. Foley, J.F., M.B. Gens, and C.F. Magnuson: "Current Predictive Models of the Dynamic Environment of Transportation." Proceedings of the Institute of the Environmental Sciences 18th Annual Technical Meeting, May 1972, pp. 162-171.
4. Magnuson, C.F.: "Dynamic Environment Study of Turbojet Cargo Aircraft." Proceedings of the Institute of the Environmental Sciences 18th Annual Technical Meeting, May 1972, pp. 420-425.
5. Anon., "C-5A Final Flutter Analysis, Vol. IV - Vibration Analysis." Lockheed-Georgia Company Report LG1US61-2-4, October 1968.
6. Bendat, J.S., Enochson, Klein, & Piersol: "The Application of Statistics to the Flight Vehicle Vibration Problem." Air Force Aeronautical Systems Division Report ASD TR 61-123, December 1961.
7. Pearson, J., Thaller, R.E., and Bayer, A.C.: "Test Report on C-5A Cargo Deck Vibration Measurements." Air Force Flight Dynamics Laboratory Test Report AFFDL/FYS/73-12, 1973.
8. Lunney, E.J., and Crede, C.E.: "The Establishment of Vibration and Shock Tests for Airborne Electronics." Wright Air Development Center Report WADC TR 57-75, 1957.
9. Harley, R.A.: "Impromptu Vibration Data Acquisition With the EL 1-31 Recorder." Institute of Environmental Sciences 13th Annual Technical Meeting Proceedings, Volume 1, April 1967, pp. 83-93.

## DISCUSSION

Mr. Senn (Army Test & Evaluation Command): You mentioned and your pictures showed that your data were taken on the floor of the aircraft with no load.

Mr. Thaller: No, in fact the plane was loaded and had a variety of loads. Our test occurred during actual use of the aircraft. We couldn't put any accelerometers along the center longitudinal axis of the CSA cargo deck because it was actually in use at the time.

Voice: In line with the last question did you find any difference in the response of the payload deck, or the cargo deck, as a function of the payload or cargo weight? Was it significant enough to warrant setting up different test levels for different weight payloads?

Mr. Thaller: This was a quick reaction for SAMSO to obtain this data and to give them what they want. I have just written up a plan for exactly that project. We are going to do an analysis of variance and other statistical techniques to find out any dependence upon cargo loading.

Mr. Van Ert (Aerospace Corporation): Were any operations performed on this 1/3 octave band data to put it in the terms of the last chart you showed which inferred a sinusoidal type of test mode? Your data is 1/3 octave band data which infers there is a bandwidth and then your final slide shows double amplitude as a function of frequency which infers to many people that a sine wave test would be appropriate. Have you somehow arrived at some process to equate sinusoidal and random data?

Mr. Thaller: No, the actual data was always in "g's" and this was just a convenient way of plotting it.

Mr. Van Ert: Then it wouldn't be convenient for me to sinusoidally sweep to those amplitudes. What I should do is have a 1/3 octave band data raised to that double amplitude to that "g" level.

Mr. Thaller: We have sent SAMSO time histories of the most severe accelerations and they are going to use them in a simulation program.

Mr. Van Ert: I would expect it might possibly be used in the design of an isolation system rather than sinusoidal testing?

Mr. Thaller: I'm not really aware of what they are going to do since I didn't really get into that phase of it.

PRELIMINARY MEASUREMENT AND ANALYSIS OF THE VIBRATION ENVIRONMENT  
OF COMMON MOTOR CARRIERS

W.N. Sharpe Jr., T.J. Kusza, F.W. Sherman and J.G. Goff  
School of Packaging  
Michigan State University  
East Lansing, Michigan 48824

INTRODUCTION

It is often difficult to separate product damage due to handling from damage due to vibration. Handling mechanical damage usually produces immediate failure when the product is dropped, whereas the fatigue failure caused by vibration may be immediate or delayed. Successful design and testing of a package requires that both environments be considered. Packages are routinely subjected to drop tests in which the drop heights are supposedly representative of the expected handling environment. The ASTM vibration test for shipping containers (D999) requires bouncing of the package for one hour on a constant displacement shaker at 1.1 G (frequency and amplitude unspecified). This test is admittedly not representative of the dynamic environment; as such, it is not the optimal test specification.

An example of vibration damage is a laser that after shipping had a very short life. A sine-sweep test uncovered a resonant frequency of the long thin laser tube of 15 Hz, which is in the range of truck vibrations. Stiffening of the package to reduce the vibration input to the tube cured the problem. It is very unlikely that the laser manufacturer would subject his product to a bounce test for one hour. But he would be willing to subject it to a vibration test representative of the expected environment and thus cure the problem before his produce reached the customer.

Naturally, realistic testing cannot be performed if the environment is not known; it is the purpose of this work to measure the dynamic environment of common motor carriers for use in package testing.

BACKGROUND

Ostrem (1) published a survey recently (1972) of the transportation shock and vibration input to cargo. This survey was compiled from measurements by other researchers and contains data on trucks, railcars, ships and aircraft. The vibration data is presented as probability of occurrence of acceleration plotted versus

frequency. The data on trucks comes from four sources:

- a) Foley (2) reported on the vibration environment of a 15 ton radioactive fuel cask shipped cross-country on a flatbed tractor-trailer.
- b) Data (3) on a rebuilt tractor-trailer combination was collected and showed that rebuilding substantially reduces the vibration levels.
- c) Foley (4) also reported on a flatbed truck subjected to rough roads.
- d) Schlue and Phelps (5) reported the vibration levels experienced in an air-ride van carrying spacecrafts across the country.

Foley (6) wrote a description and summary of vibration data that is particularly oriented toward packaging.

A main point here is that none of these measurements have been made in commercial shipper's trucks under ordinary conditions.

MEASUREMENTS AND ANALYSIS

Accelerations were measured on four runs of tractor-trailers operated by a local trucking firm. Two runs were used for equipment checkout. Run 3 was a 40 mile run primarily over expressway with a 45 foot trailer carrying a mixed cargo of 28,000 pounds. Run 4, over 60 miles of mostly two-lane road was with a 40 foot trailer carrying 6000 pounds of foam cups. Run 5 was a "peddle run" around the city with a 30 foot trailer and an initial load of 6200 pounds. Run 6 was over expressway with a 40 foot trailer loaded with 9200 pounds of auto parts.

Accelerations were measured in the vertical direction on the floor at the front, middle and rear of the trailer. Piezoresistive accelerometers with a frequency response of from DC to 200 Hz were mounted at the rear of

the trailer. Piezoelectric accelerometers with a frequency response of 2 to 5000 Hz were used at the front and middle locations. Lateral accelerations were measured at the floor and ceiling in the rear location using piezoresistive accelerometers identical to those used for the rear vertical acceleration. It should be noted that these accelerometers recorded all inputs to the vehicle floor and sidewalls including those transients caused by bouncing packages. Such inputs were, however, modified by the structural elements of the floor and sidewall located between the source of the disturbance and the accelerometer.

Acceleration data were recorded on two INTERMED four-track cassette tape recorders with one track on each recorder used for voice commentary and synchronization. Piezoresistive and piezoelectric accelerometers were used. The frequency response of the recording system was DC to 3db-down at 400 Hz. A separate reproducer is required with this recording system.

Standard kinds of analyses were made. An IBM 1800 computer was used to compute probabilities and a SAICOR real time analyzer was used for the bulk of the analysis.

## RESULTS AND DISCUSSIONS

The results presented and the discussions of them are pointed toward the purpose of this research; namely, the measurement of the dynamic environment for use in package testing.

Figure 1 is a plot of the rear vertical acceleration over the entire Run 3. It shows that the distribution is sharper than would be recorded for Gaussian randomness; the moment of kurtosis is 4.3. The standard deviation is 0.46 G, and there is some departure from symmetry for the higher accelerations. Although not Gaussian, the data are similar enough to justify using the simpler Gaussian approach to planning and analysis of tests.

A VIBRAN plot of probability of acceleration versus frequency was obtained for a portion of Run 3 at 55 mph using a filter and the probability program--see Figure 2. The same bandwidth and center frequencies as in Ostrem's report (1) were used. Comparison with the data in that report shows generally lower accelerations were measured in commercial trucks.

The basic character of the truck vibration is shown in the PSD plot of Figure 3. There are several fairly sharp peaks indicating harmonics in the 0-50 Hz range, a sharp peak at approximately 70 Hz, and narrow-band random vibration in the 120-200 Hz range. This general picture appears for all the runs with variation of the levels and frequencies.

The effect of speed is seen in Figure 3 to be slight elevation of the PSD levels with

little change in shape of the plot. RMS values (2-400 Hz) were measured to be 0.52 G at 45 mph, 0.54 G at 50 mph, 0.55 G at 55 mph, and 0.68 G at 60 mph. RMS and PSD measurements were made on data for steady speeds over concrete expressway. There is no significant change with speed, i.e. there are no new frequencies introduced as speed is increased. It seems reasonable then to take a PSD plot of a high-speed run as representative of the most severe dynamic environment.

Figure 4 shows that the vertical acceleration is largest at the rear position in the trailer for Run 3. Furthermore, the lower frequency harmonics are present only on the rear signal which implies that they are generated by the tires and suspension system. This was also true for Run 6, but the RMS values of the vertical accelerations of Run 4 were nearly equal for all three positions in the trailer. Other results (3) have shown that the forward position has higher vertical acceleration. For realistic vibration data, one should record vertical accelerations in at least the fore and aft positions of the truck.

Lateral accelerations were found to be much smaller than the vertical as evidenced by Figure 5. This is plotted on a smaller frequency scale because the lateral data contained little information over 100 Hz. Note that the shapes of the PSD plots are quite similar demonstrating the strong influence of the vibration input through the rear suspension. One need only record the vertical accelerations to document the most severe vibrations.

Figure 6 compares the rear vertical vibration for the three over-the-road runs. The general shape and levels are roughly similar. This is encouraging because it leads one to think that, in spite of the tremendous number of variables in trucks, cargo, roads, etc., there may be sufficient similarity in the vertical acceleration PSDs to make a composite PSD useful.

It may be premature with the limited amount of data we have, but a composite PSD for high-speed trailer vibrations based on our results would appear as in Figure 7. Possibly the inclusion of more data would fill in the region between 30 and 65 Hz. Foley (6) has compiled a composite derived from data on 7 truck types with 5 load ranges. It is very interesting to note that his low frequency PSD level is exactly the same ( $1.5 \times 10^{-2} \text{ G}^2/\text{Hz}$ ) as ours. This fact lends support to the argument that a composite can be developed that is representative of many truck types and conditions.

A truck, in the course of its run, will experience several transients from intersections, railroad crossings, pavement cracks, etc. These show up on the floor of the truck

as an increase in the level of low frequency components, not as a sharp pulse. In other words, the acceleration signal as seen on a strip-chart recorder builds up as a nearly pure sinusoid at low frequency which then dies out. Figure 8 is a plot of wave analyses taken in the "capture" mode with the real time analyzer. Each analysis is for one second of data. The truck drove onto a bridge at 60 mph. The wave analysis taken while the trailer is "ringing" in response to the transient input shows the greatest increase in an acceleration level at very low frequencies. It does not appear necessary to test a package separately for vibration transients; the drop test which is much more severe is adequate. In fact, the largest peak G for a transient for any run was 5 G; most peaks were around 2 G.

An interesting characteristic of trailer vibration can be seen in Figure 9. It presents wave analyses of the "peddle run" truck as it started and accelerated to 40 mph. The basic shape of the frequency distribution is established as soon as the truck begins to move; increasing the speed merely raises the level of vibrations.

#### CLOSING

These preliminary results show that the data can be acquired and managed into a useful form without too much difficulty. These results plus those of Foley (6) disclose that the vertical accelerations are most severe and therefore are the only ones needed. This is important if one is contemplating recording enough sample vibrations to generate a statistically reliable picture.

The package test one would aim for would be the kind where an electrohydraulic shaker was programmed to reproduce truck floor vibrations at a large table. If the goods were shipped in stacks of five, then a stack of five would have to be tested to examine the effect of stacking. If the programmed vibrations were representative, this should be a good test.

Even if one has adequate data about truck floor vibration in hand, the question of how to compile this into a simple usable form is a difficult one. Simply enveloping the PSD data is selecting the worst possible case and may be overly severe. It is likely that some type of testing at various PSD levels for specified periods of time would be better.

#### REFERENCES

1. Ostrem, F.F., "A Survey of the Transportation Shock and Vibration Input to Cargo," The Shock and Vibration Bulletin, Vol. 42, Part 1, pp. 137-151, 1972.
2. Foley, J.T., "The Environment Experienced by Cargo on a Flatbed Tractor-Trailer Combination," Sandia Corporation Research Report SC-RR-66-677, 1966.
3. Anonymous, "Data Package of 182 Documents from AEC/DOD Environmental Data Bank," Sandia Laboratories, 1967.
4. Foley, J.T., "Normal and Abnormal Environment Experienced by Cargo on a Flatbed Truck," Sandia Corporation Development Report SC-DR-67-3003, 1967.
5. Schlue, J.T. and Phelps, W.D., "A New Look at Transportation Vibration Statistics," The Shock and Vibration Bulletin, Vol. 37, Part 7, pp. 19-37, 1968.
6. Foley, J.T., "Transportation Shock and Vibration Description for Package Designers," Sandia Laboratories SC-M-72-0076, 1972.

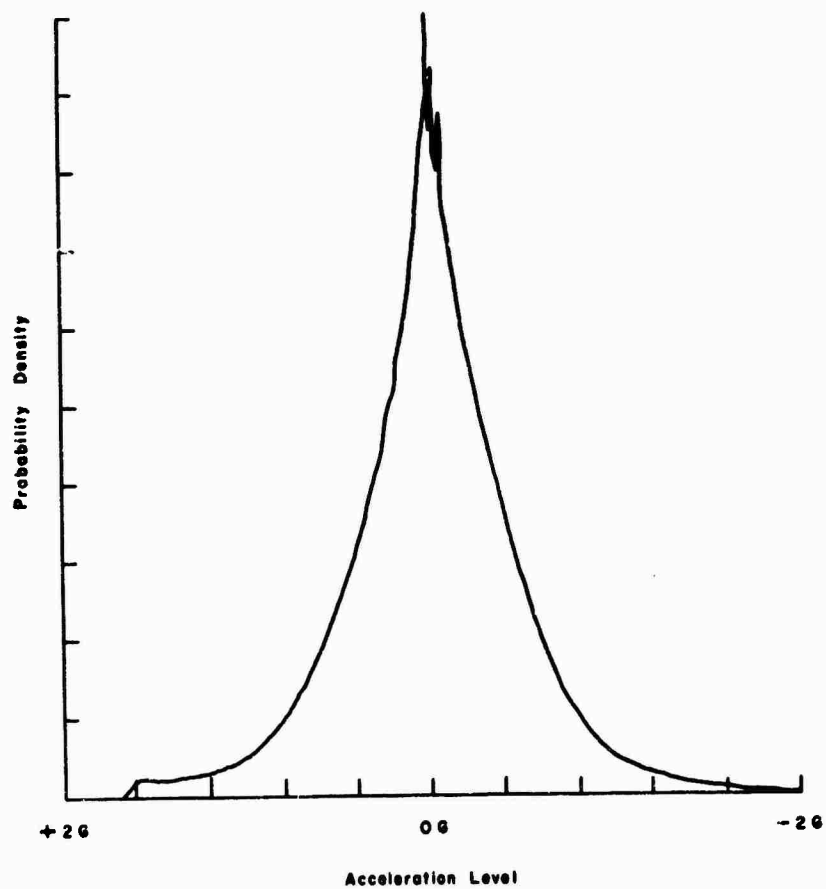


Figure 1. Probability density  
plot of rear vertical  
acceleration of Run 3.

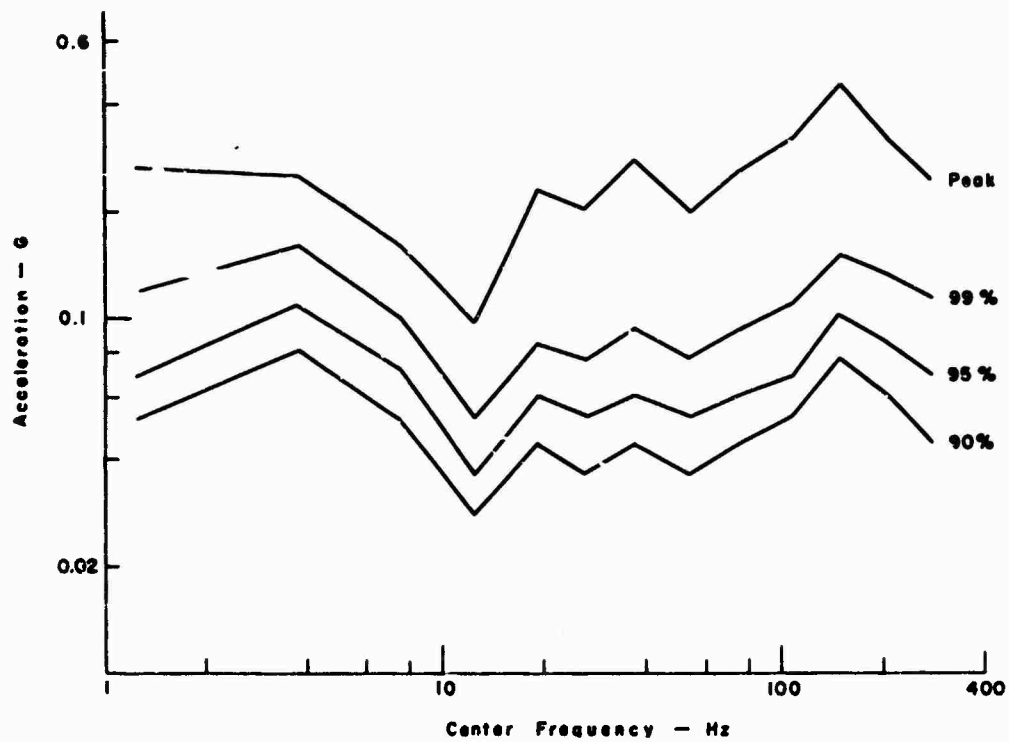


Figure 2. VIBRAN plot of rear vertical acceleration of Run 3 at 55 mph.



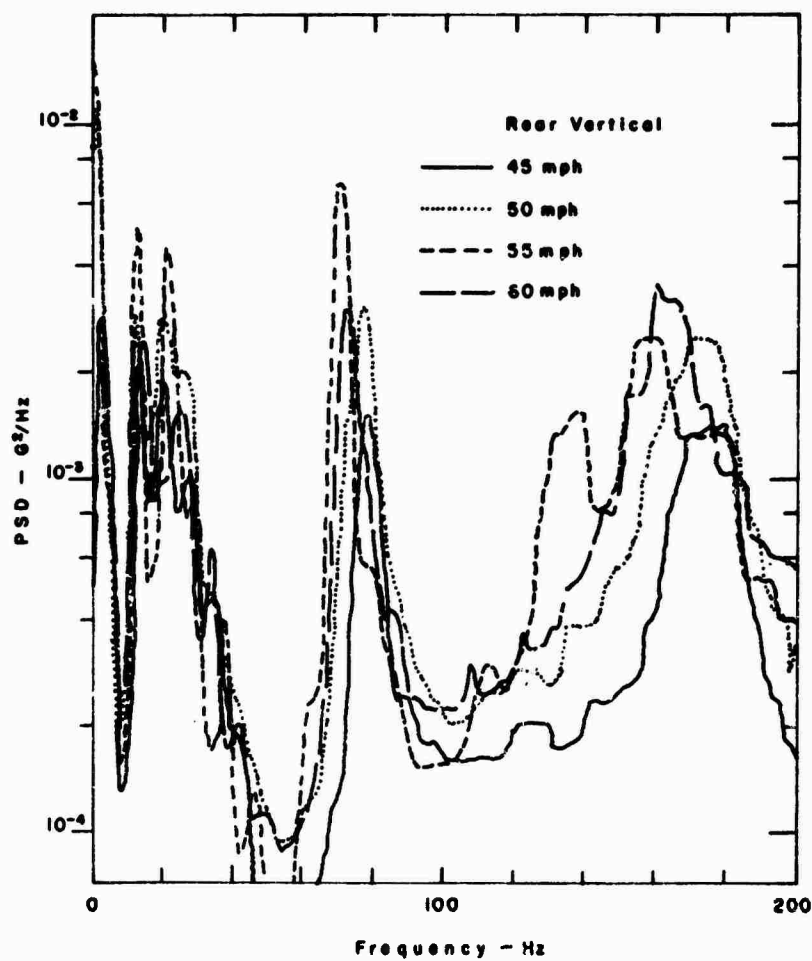


Figure 3. Effect of speed on the rear vertical acceleration of Run 3.

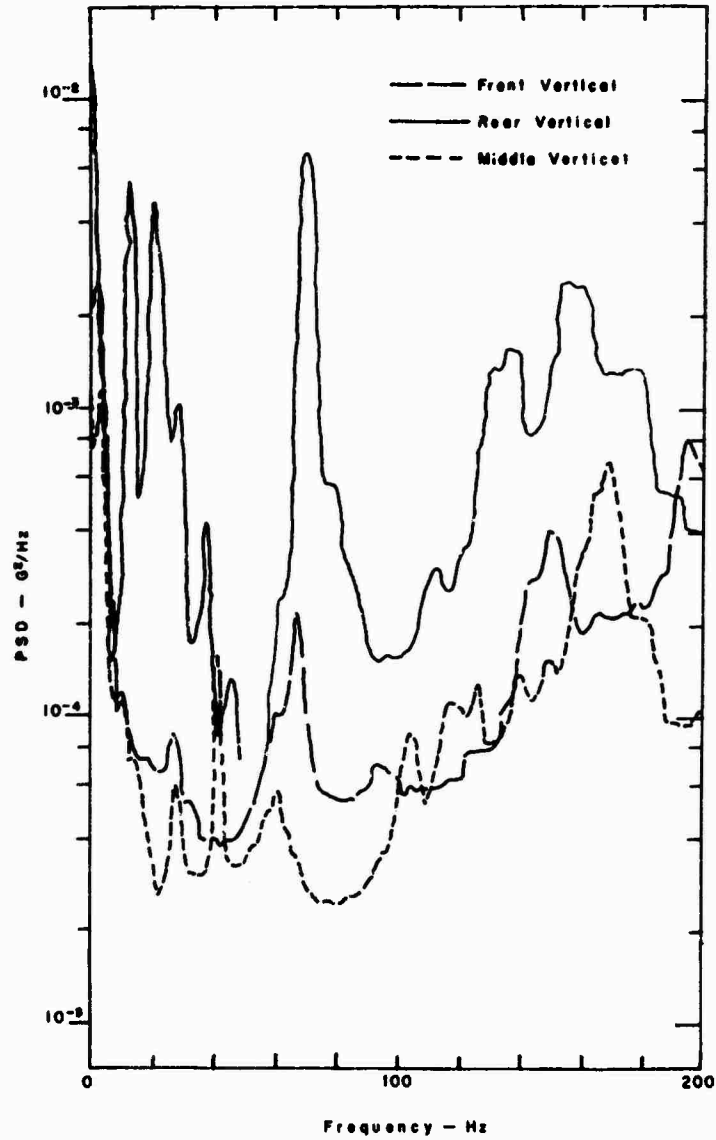


Figure 4. Effect of accelerometer location on the vertical acceleration of Run 3.

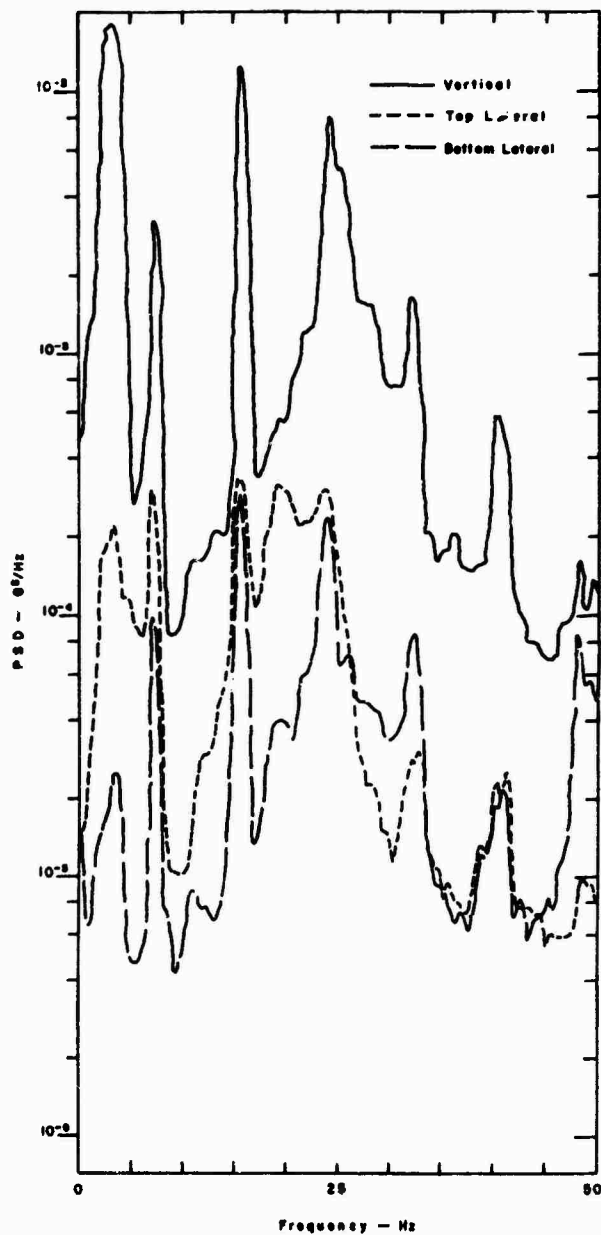


Figure 5. Comparison of vertical and lateral accelerations for Run 3.

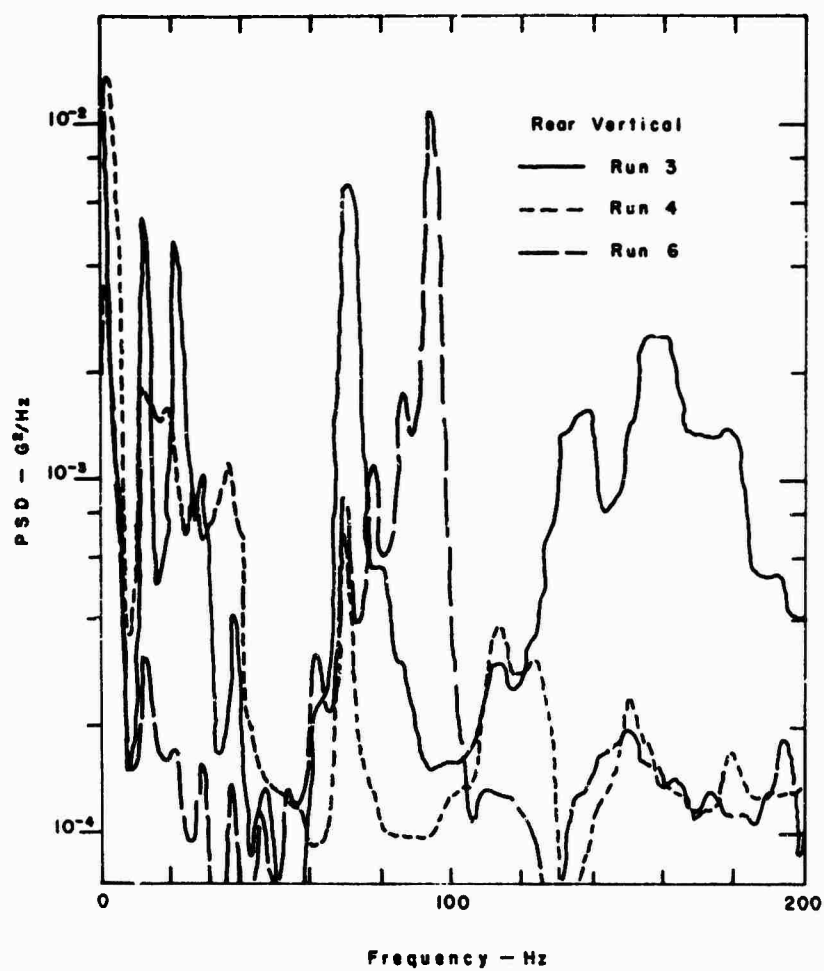


Figure 6. Rear vertical acceleration for 3 runs.

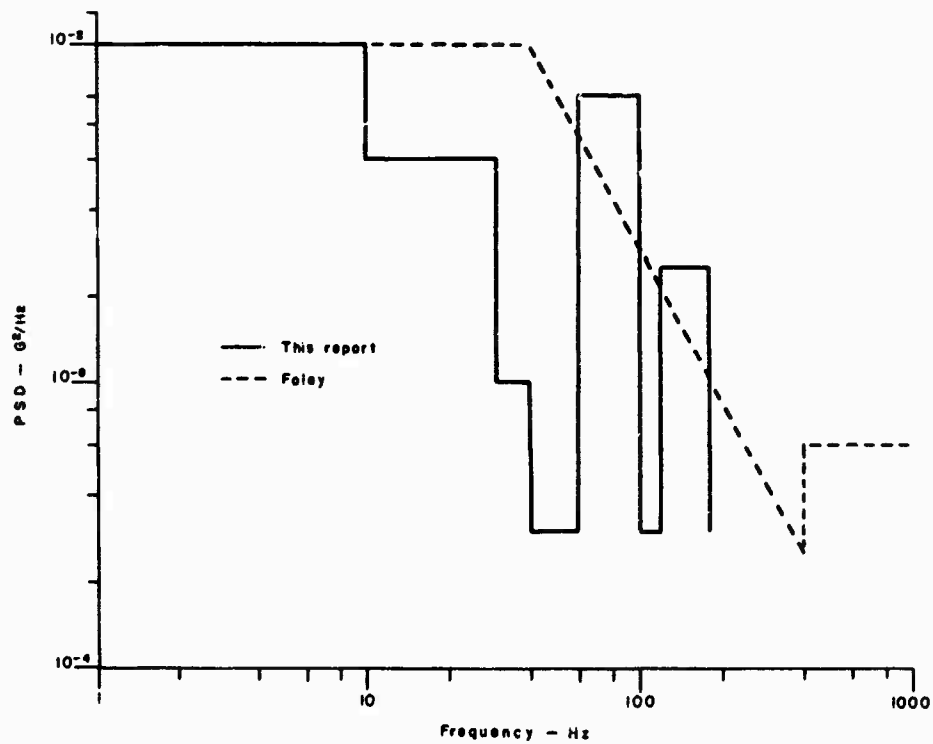


Figure 7. Composite PSDs for vertical acceleration.

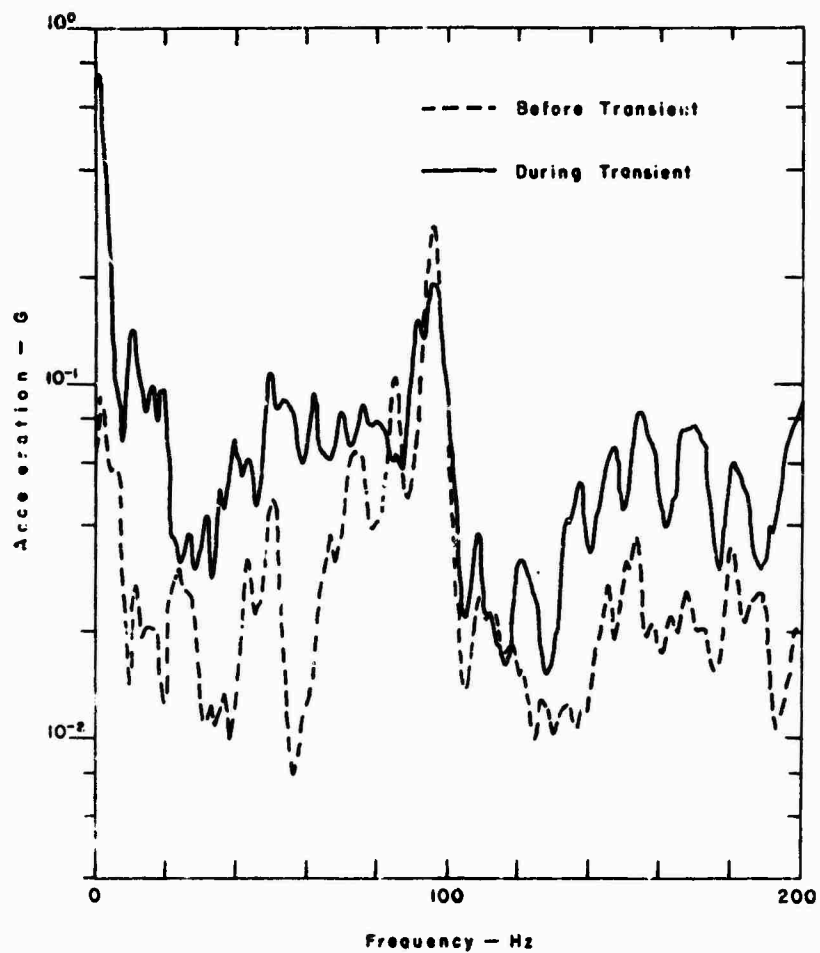


Figure 8. Wave analyses before and after the truck of Run 6 drove onto a bridge at 60 mph.

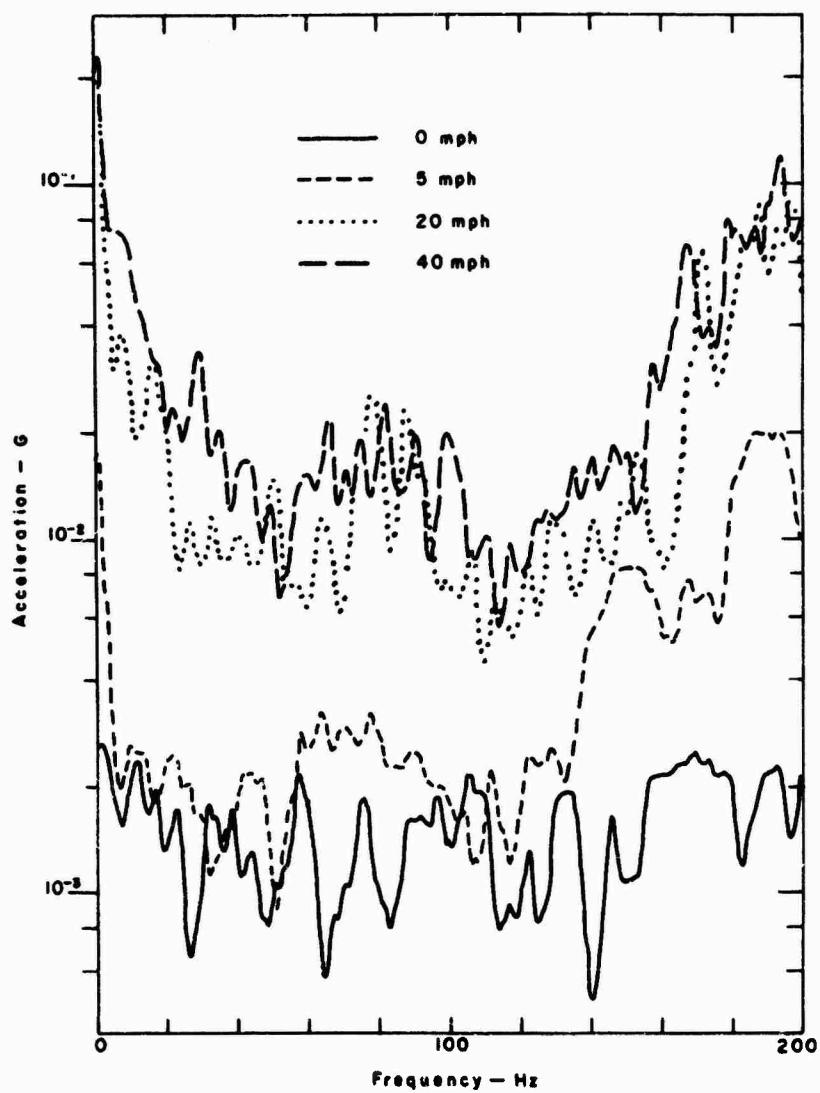


Figure 9. Wave analyses of "peddle run" as the truck accelerates.

## DISCUSSION

Mr. Storay (Army Missile Command): Do you have any plans in the future to scale up the levels and scale down the time for laboratory testing?

Mr. Sharpe: No, we aren't that far along yet. In terms of the problem of packaging it is necessary to have a suitable failure criterion, depending on the product. I think that type of time scaling would have to go along with the particular type of product.

Mr. Gertel (Kinetic Systems): I was curious if you had considered trying a similar series of measurements on a package tester to see how this compares with some of your actual measured observations?

Mr. Sharpe: What package tester?

Mr. Gertel: The bounce tester, so called or that family of testing devices.

Mr. Sharpe: Are you referring to the ASTM type test?

Mr. Gertel: Yes.

Mr. Sharpe: We did a quick and preliminary look at that and that generated a spectrum in the package that consists of a series of sharp lines, dependent upon particular type of package. We haven't gone into a thorough investigation of that but it is a completely different type of spectra that you obtain.

Mr. Condouris (Army Electronics Command): Did you examine any of the packages that were transported to see if they were damaged. If they had been damaged were they properly packaged?

Mr. Sharpe: No.

Mr. Condouris: We ran some tests on helicopters with Army electronic gear packaged in their proper container, either wooden cases or cardboard boxes, and we found that very little vibration which came through from the helicopter deck got into the actual electronics; if the package were properly protected we felt that there would be no need for a vibration test, so I was curious if you had data of this kind?

Mr. Sharpe: No, the thrust of this work is to obtain environmental data so we could test packaged cargo in the laboratory.



## THE DYNAMIC ENVIRONMENT OF LANDING CRAFT\*

Mark B. Gens  
Sandia Laboratories  
Albuquerque, New Mexico 87115

Measurements were made of the dynamic environment found on the cargo decks of several amphibious vehicles and assault boats employed by the Navy and Marine Corps for assault landings. The work was done in cooperation with the Naval Weapons Evaluation Facility, Kirtland Air Force Base, New Mexico, the Naval Amphibious Base, Coronado, San Diego, California and the Marine Corps Landing Force Development Center, Camp Pendleton, California. The vessels measured were LVTP7, LCA2, LCM8 and LCU.

The reduced data show relatively low magnitudes, but high incidence of discrete, intermittent and narrow-band random excitation. The LVTP7 exhibited the highest amplitudes both during land and water operation.

### INTRODUCTION

Supplies for ground troops during an invasion from the sea may be brought in by helicopter or by small craft from the fleet standing off the coast. The dynamic environment encountered during such transfer is a part of the overall environment to which tactical weapons may be exposed. The helicopter environment has been reported previously [1,2,3]. This document is a report on the landing craft environment.

A study of the landing craft environment was carried out with the cooperation of the Naval Ordnance System Command (NAVORDSYSCOM), Washington, D. C., and the Naval Weapons Evaluation Facility (NWEF), Kirtland Air Force Base, New Mexico.

### MEASUREMENT OF THE DYNAMIC ENVIRONMENT

#### General

Measurements were made on two types of vessels. The LVTP and LCA are amphibious craft. Both the LCM and LCU, although very different in configuration and in size, are capable of beaching.

\*This work was supported by the U. S. Atomic Energy Commission.

### Instruments

Measurements were made by means of the ELI 31 recorder [4] with piezoelectric and piezoresistive accelerometers. The instrumentation (Table I) was configured in advance because of the necessity of rapid setup and take-down to avoid interference with the assault exercise. Even though restricted by the length of the available cables, accelerometer placement at the forward and aft areas of the cargo deck

TABLE I  
Instrumentation for Landing Craft

Channel	Instrument Type	Axis	Calibration (g)
1	PE	L	2.0
2	PE	T	2.0
3	PE	V	2.0
4	PR	L	10.0
5	PR	T	10.0
6	PR	V	10.0
7	PE	L	20.0
8	PE	T	20.0
9	PE	V	20.0
10	PR	L	2.0
11	PR	T	2.0
12	PR	V	2.0

was possible in all cases except on the LCU.

One limitation became apparent when data were reduced. The recorder had developed a malfunction which appeared in the data as a high number of spurious peaks in the frequency band between 180 and 240 Hz. Wherever this spurious data completely masked real data, the values in that frequency band were deleted.

#### Data Reduction

The data were reduced in the following steps:

1. A real-time oscillograph record
2. Amplitude spectral density plots
3. Vibran records
4. VAIL summaries [5]

Examination of the oscillograph records revealed that the amphibious vehicles were dominant in amplitude over all of the landing craft; therefore, a decision was made to reduce a complete cross section of data for these vehicles and only typical events for the others.

#### DYNAMIC ENVIRONMENT OF LANDING CRAFT

The dynamic environment of transport has been described as complex [6]. It consists of broadband random excitation distributed in a Gaussian manner, as well as some discrete elements which may be either superimposed upon the broadband base or intermixed with it. All of these elements are found in the dynamic environment of landing craft.

The dynamic environment of landing craft may be characterized as basically broadband Gaussian in nature, with, in many cases, discrete components superimposed on it. When the discrete components are independent of the basic continuous excitation, they are found in the top 1 percent of the peaks. These independent peaks may occupy as much as 80 percent or as little as 1 percent of the amplitude range. At times discrete components are intermixed with the continuous components to the extent that they may not be identified separately even though their presence is detectable. Although this discussion is devoted largely to the basic broadband excitation, the presence of discrete elements (as shown on arrowheads on the appropriate frequency band) are pointed out from time to time.

Examination of the VIBRAN records for each event and many of the VAIL summaries revealed major differences

between the forward and aft positions. On the amphibious vehicles (LVTP7 and LCA2) the records for the forward accelerometers were generally Gaussian random in distribution while those from the aft position were dominated by discrete, often intermittent, excitation. The records for the assault boats (LCM8 and LCU) were reversed. The aft records were largely Gaussian random while the forward records showed a preponderance of discrete excitation. In all cases, the Gaussian random excitation was detected near the engines. This suggests that the vehicle structure tends to damp out the steady state excitation and that the discrete measurements were the result of external excitation from the tracks, bow slap, etc.

#### DYNAMIC ENVIRONMENT OF AMPHIBIOUS VEHICLES

Two types of amphibious vehicles were encountered. One, the LVTP7, is representative of a group of vehicles which may be characterized as floating armored personnel carriers. These vehicles are propelled on land by tracks and in water by hydrojet. The other amphibious vehicle, the LCA2, is primarily a boat which has the capability of moving on land by use of tracks and in water propulsion by hydrojet. Little data are available from the LCA2 since it broke a track during the approach to the ocean. Because the data obtained indicated values lower than those of the other amphibious vehicle and because the LCA2 is not in general use, it was decided not to pursue the study of this vehicle further.

#### LVTP7 (Figure 1)

Transducer placement in the LVTP7 included triaxial piezoelectric accelerometers near the forward bulkhead and aft, near the ramp hinge, as well as a triaxial cluster mounted approximately amidships.

The LVTP7 exhibits two levels of vibration. The amplitudes measured during progression on land fall in a higher order of magnitude than those measured in the water.

Measurement began as the LVTP7 moved across a concrete area. The vehicle continued down a concrete ramp and entered a calm, land-locked bay. After crossing the bay, the vehicle ascended a sandy beach, crossed an area of loose sand, descended to the shoreline, and entered the surf of the Pacific Ocean. It continued out through the surf, turned, and returned to its

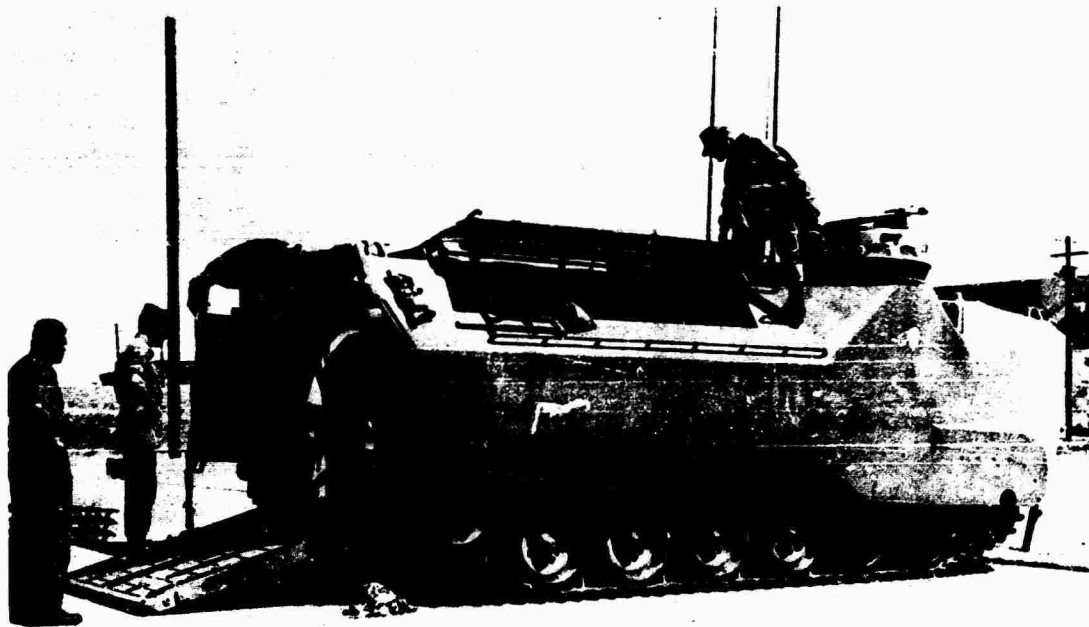


Fig. 1 - LVTP7 Amphibious vehicle

base by following the same route in reverse. The final record was made as the vehicle turned on the concrete pavement before shutting down.

The data for the LVTP7 were reduced in amplitude spectral density format by use of program MACRAN and in a peak amplitude distribution form by use of program VIBRAN. The VIBRAN records were combined by program VAIL to give summaries of the land events and the water events separately, as well as a composite of all events.

The broadband base vibration results for the land events are summarized in Figure 2. Levels shown are higher than any associated with other types of landing craft or with the LVTP7 during water events. Axis domination in this vehicle is distributed typically. The lower frequencies, up to 180 Hz, are dominated by the vertical axis. Except in the 500- to 1000-Hz bands and above 1400 Hz, the frequencies above 240 Hz are generally governed by the transverse axis. The highest amplitudes are found in the 500- to 700-Hz frequency band and in the longitudinal axis.

Comparison of the land event data obtained from the forward and the aft accelerometer groups reveals differences in the amplitudes and axis dominance. Figures 3a and 3b are derived from the VAIL summaries for each position. In

the forward position (Figure 3a) the vertical axis dominates up to 1000 Hz; at higher frequencies it drops below both the longitudinal and transverse axis. At the aft end of the deck (Figure 3b), however, the vertical axis is dominant only to 350 Hz and then again above 1000 Hz. In the forward

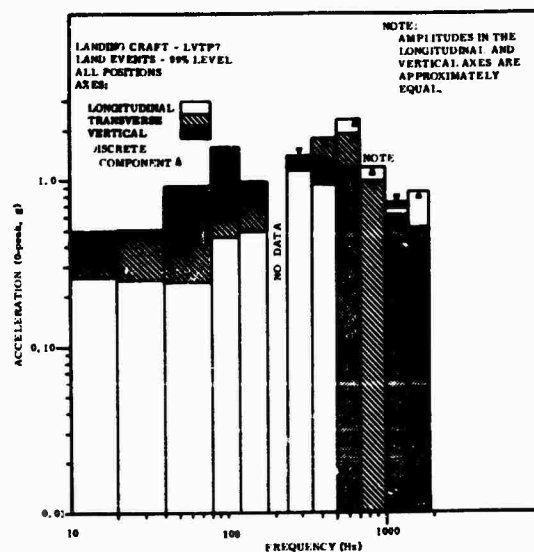


Fig. 2 - LVTP7 Land Events, Continuous Excitation Summary

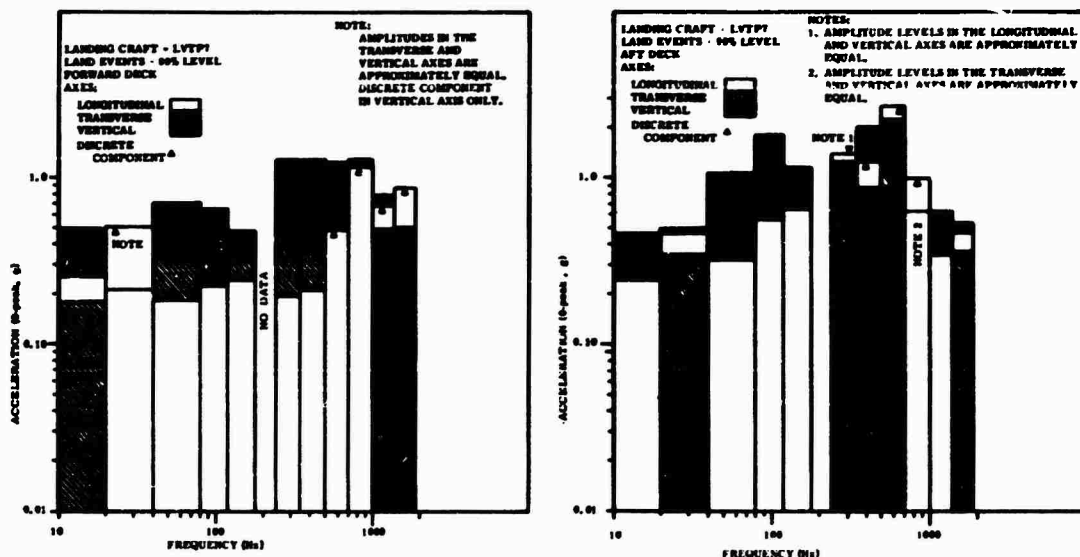


Fig. 3 - LVTP7 Land Events, Excitation Forward and Aft

end the highest amplitudes are in the vertical between 240 and 1000 Hz; in the aft end the longitudinal axis shows the highest amplitudes in a relatively narrow band between 500 and 700 Hz. In the same band, the transverse axis shows higher amplitude than is shown on any of the vertical records.

Comparisons between the forward and aft records by axis are shown in Figures 4a, 4b, and 4c. Generally, the highest amplitudes are found at the aft. In the longitudinal and transverse axes, except for the higher frequencies (>700 Hz), the higher amplitudes are shown in the aft records. In the vertical axis, although the high amplitudes occur at the aft in the middle frequencies, they are almost always shown in the forward records at the high and low frequencies. The exception is between 1400 and 1900 Hz, where the aft record shows high amplitudes.

The general characteristics of the dynamic environment of the LVTP7 during water events are much the same as those during the land events. Figure 5 is a summary of the water events. The outstanding difference between the two types of events is the amplitude of overall dynamic excitation. In all instances, the data recorded in the water are lower in amplitude than those recorded on land. Again, the excitation on the forward deck generally is

lower in amplitude than that of the after deck (see Figures 6a and 6b).

Figures 7a, 7b, and 7c show the relationship between the forward and aft records by axis. Once again there is a striking similarity in the shapes and in the portion of the vehicle which gives the highest amplitudes. There are some minor differences; however, in those frequency bands where the two records reverse dominance, there is little difference in amplitude.

Inspection of the VAIL summaries indicates the presence of a discrete component mingled with the broadband Gaussian random excitation in the 500- to 700-Hz frequency band. This phenomenon is particularly apparent in the aft position in records of the land events. The plots of the power spectral density reveal the presence of a "spike" in the 500- to 700-Hz area in almost every instance, both forward and aft and on land or in water. This confirms the presence of a discrete element which seems to be a narrow-band, randomly distributed excitation. Since it is not possible to separate the discrete component from the broadband random background, its presence has been shown by an arrowhead on the graph.

In summary, the dynamic environment measured on the LVTP7 showed higher amplitude than those of any other vessel.

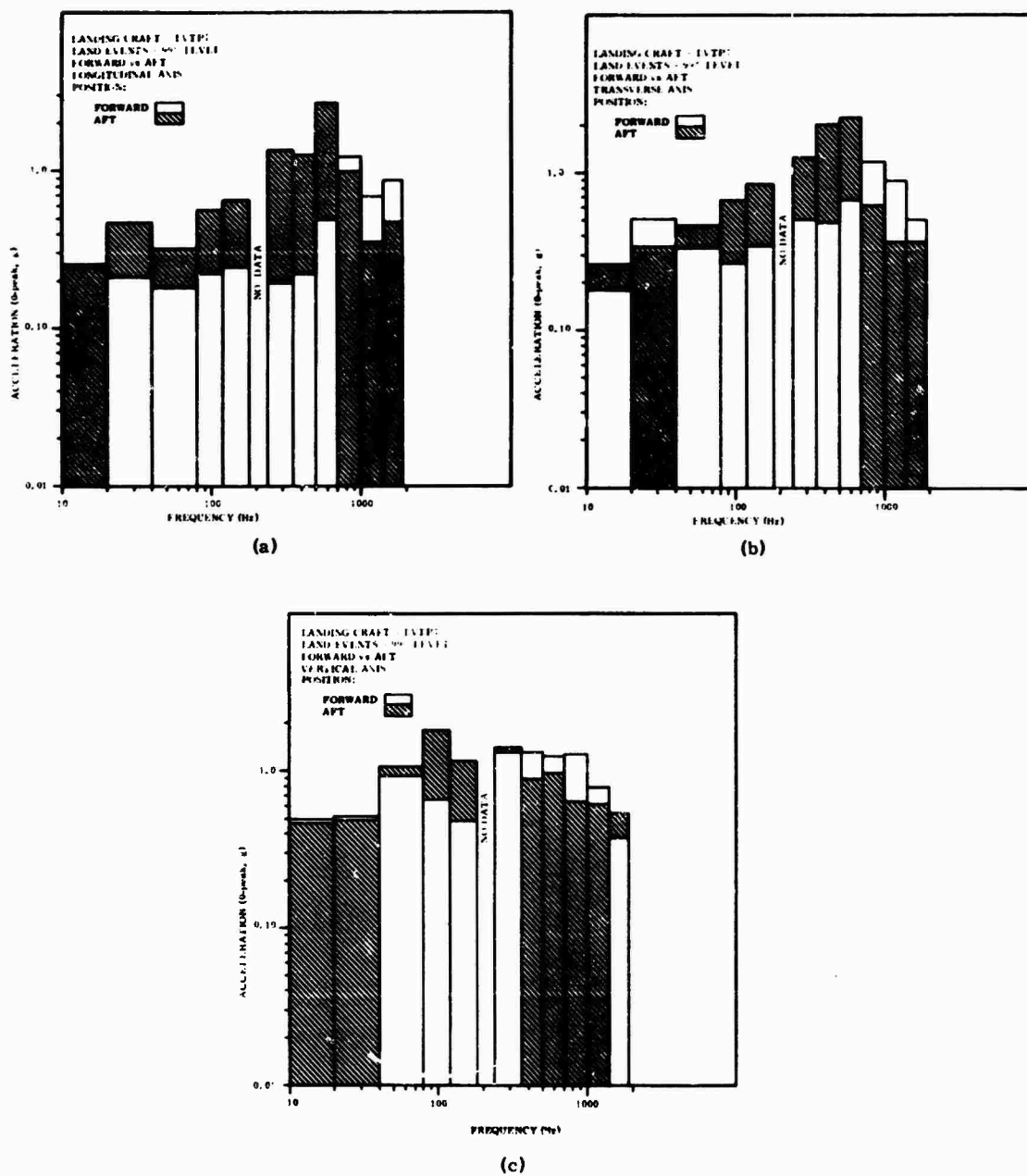


Fig. 4 - LVTP7 Land Events, Comparison Between Forward and Aft Records

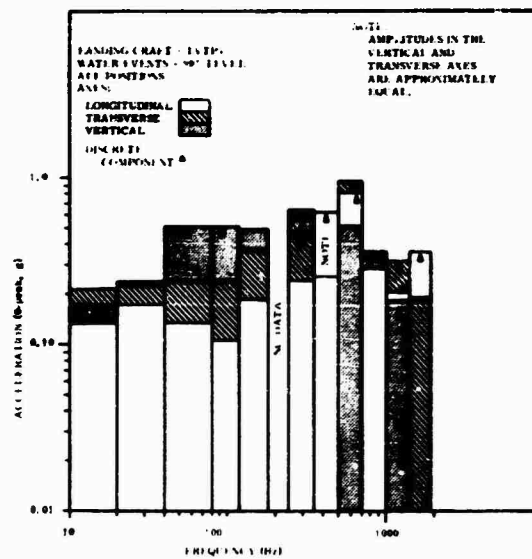


Fig. 5 - LVTP7 Water Events, Continuous Excitation Summary

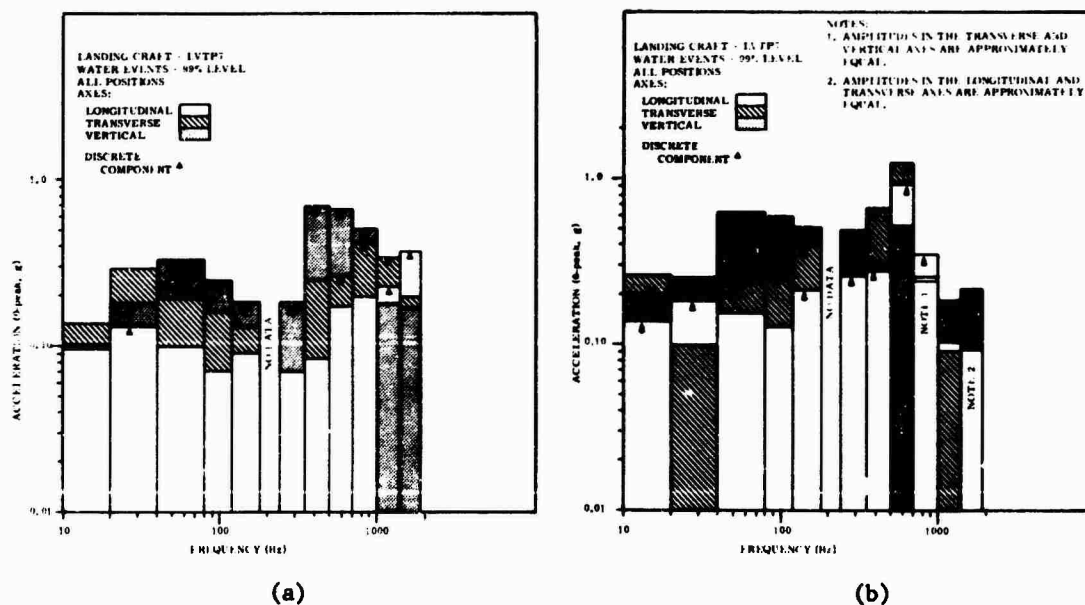
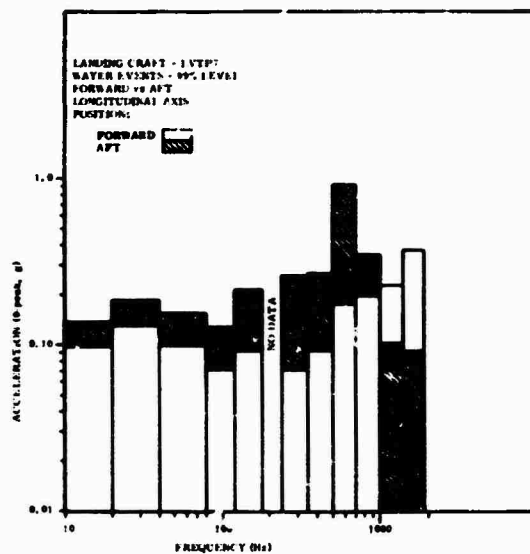
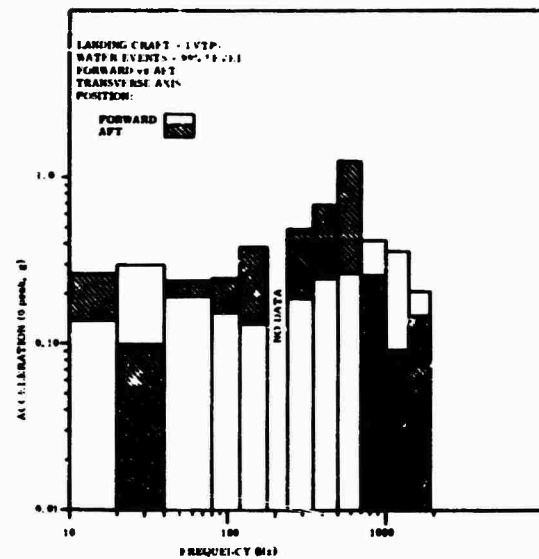


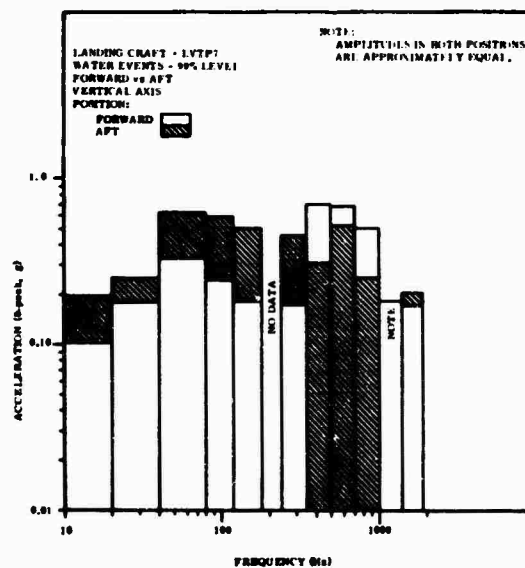
Fig. 6 - LVTP7 Water Events, Excitation Forward and Aft



(a)



(b)



(c)

Fig. 7 - LVTP7 Water Events, Comparison Between Forward and Aft Records

The land events gave higher readings than the water events, and the aft position showed higher amplitudes than the forward position. The highest reading, 2.7g, was recorded in the 500- to 700-Hz band in the aft position during land events. The complex character of the excitation is more evident in records from the water events than from the land events.

## LCA2

Measurement of the dynamic environment of the LCA2 was accomplished by use of the same instrumentation as for the LVTP7. The triaxial clusters of piezoelectric accelerometers were located aft in the vicinity of the ramp hinge and forward near the bulkhead. The piezoresistive instruments were placed amidship on the plate directly above the engines.

At the time of boarding, the vessel was located on the beach, parallel to the surf line and above the coastal ridge. The ridge was about 5 feet above the high tide level. The plan was to drive along the ridge until reaching a convenient place to descend to the beach, cross the beach, enter the surf, and run out several hundred yards into the ocean. The route would then be reversed, with the vessel returning to the same position. The only portion of the program which was accomplished was raising the ramp, backing to position, and starting toward the point of descent. The track broke at this point; therefore, measurement of the entire trip had to be abandoned.

The data shown in Figure 8 were derived from the three records available. The vertical axis is generally dominant below 350 Hz, except in the 20- to 40-Hz band, where the transverse axis is slightly higher. In the frequencies higher than 350 Hz the transverse and longitudinal axes essentially alternate in dominance. The presence of discrete components is apparent only in the transverse axis in the 700- to 1000-Hz band. This appears to be a contribution from the forward set of accelerometers. Figures 9a and 9b show the forward and aft measurements. Comparison of the two plots shows that, in general, the higher amplitudes are found in the records taken from the aft deck. This is especially true below 700 Hz. Comparisons by axis (Figures 10a, 10b, 10c) show that only in the transverse axis is the forward record frequently higher than the aft, and then in only one-third of the frequency bands.

The presence of discrete components may be detected by inspection of the VAIL summaries. Even though it seems, in the overall summaries, that narrow-band random excitation is present in many frequency bands in all axes, it

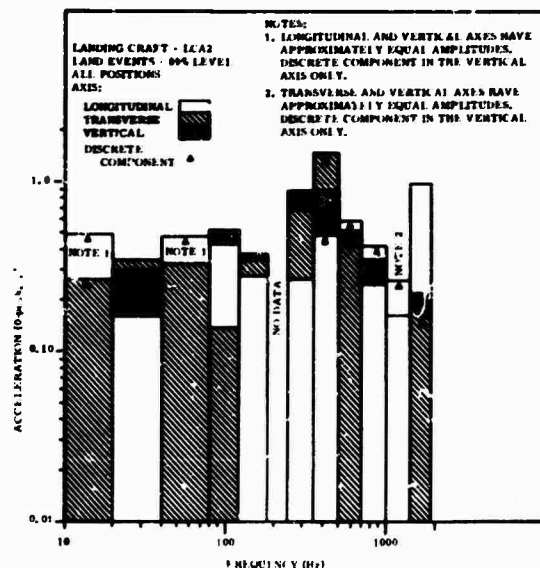


Fig. 8 - LCA2 Land Events, Continuous Excitation Summary

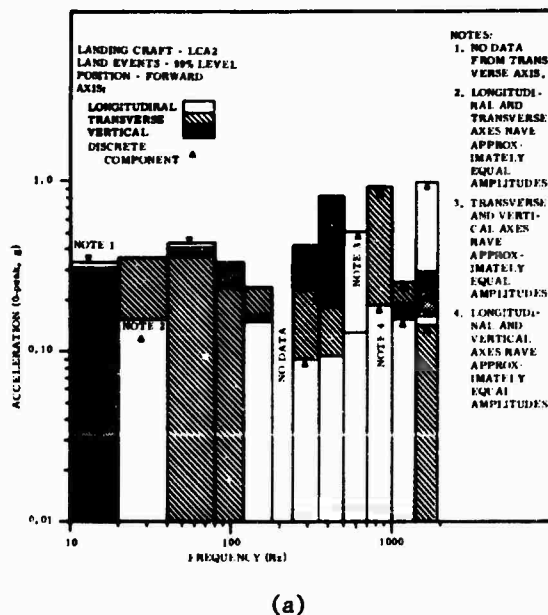
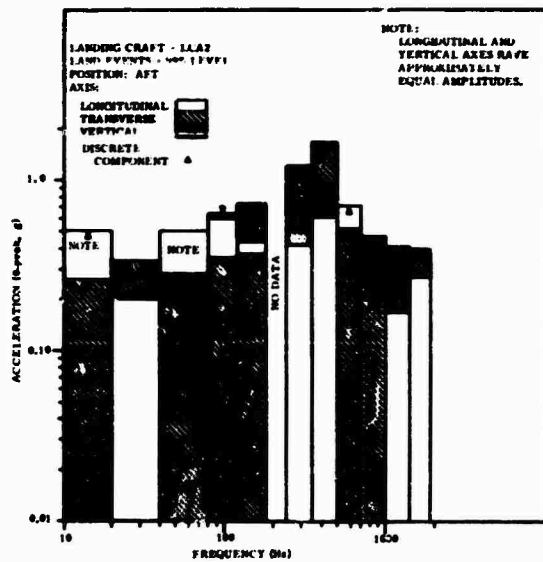


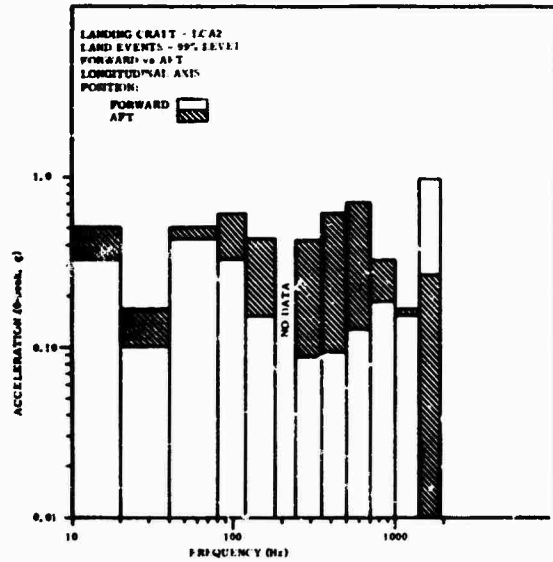
Fig. 9 - LCA2 Land Events, Excitation Forward and Aft





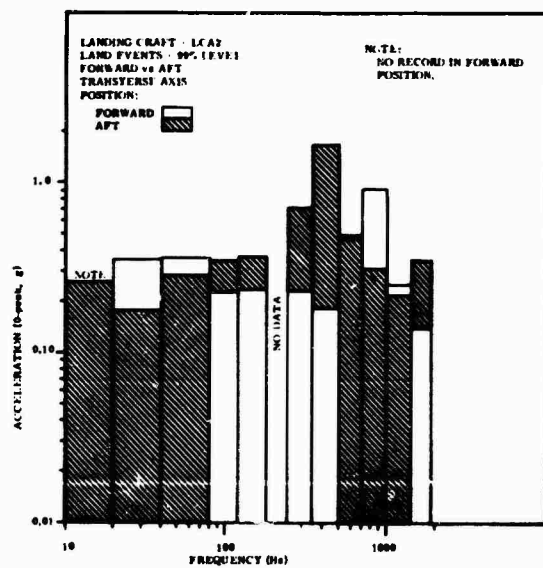
(b)

Fig. 9 - (Cont.)



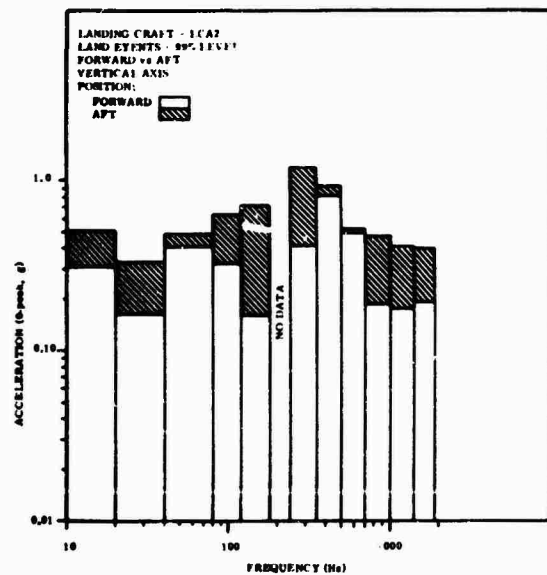
(a)

Fig. 10 - LCA2 Land Events, Comparison Between Forward and Aft Records



(b)

Fig. 10 - (Cont.)



(c)

Fig. 10 - (Cont.)

may be seen that this effect is found largely in the record of the forward accelerometers. Little evidence of intermixed discrete excitation is shown in the records from the aft accelerometers.

#### DYNAMIC ENVIRONMENT OF ASSAULT BOATS

Assault boats are small vessels which may be used to carry troops, vehicles, and supplies from the fleet to the beach. They are characterized by a shallow draft, a bow ramp, and an ability both to run up on the beach and to back off from it. The types in current use are landing craft mechanized (LCM6 and LCM8) and landing craft utility (LCU).

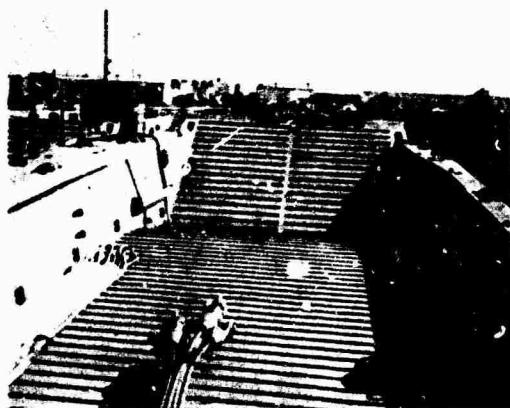
The LCM6 and LCM8, called "Mike" boats, differ in minor details, but are used in the same manner. The engines and command facilities are located in the aft section. Figures 11a and 11b are views looking forward to the ramp

and aft to the quarter deck. The LCU, which is larger than either of the Mike boats, is configured with the engines below aft and the command facilities contained in a superstructure located at the aft portion of the starboard side.

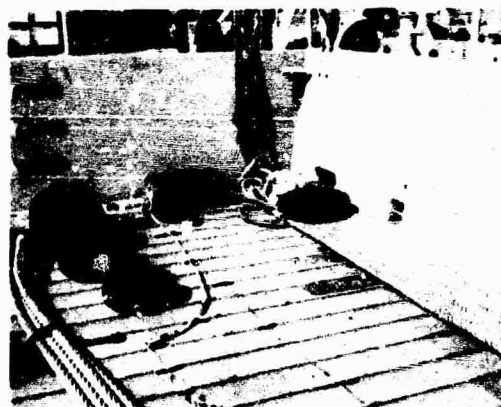
#### LCM8

The measurements were made on the Mike 8 during a run for the beach that was part of an assault exercise being conducted by COMPHIBPAC. The boat was aboard the LPD (USS Dubuque) at the time of instrumentation. Because the cargo (trucks) had not been loaded when the boat was available to install the instruments, the accelerometers were placed on the gunwale rather than on the cargo floor. Figure 12 is a diagram of the final configuration.

The measurements were made during the trip from the dock ship to the beach. The actions included a period



(a)



(b)

Fig. 11 - LCM8 Assault Boat

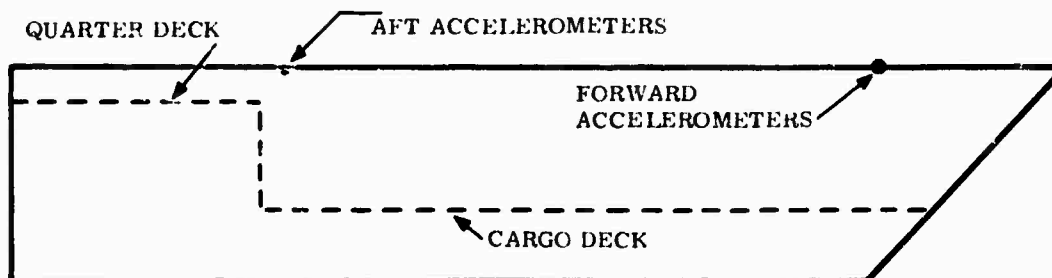


Fig. 12 - Test Configuration of the LCM8 (no scale)

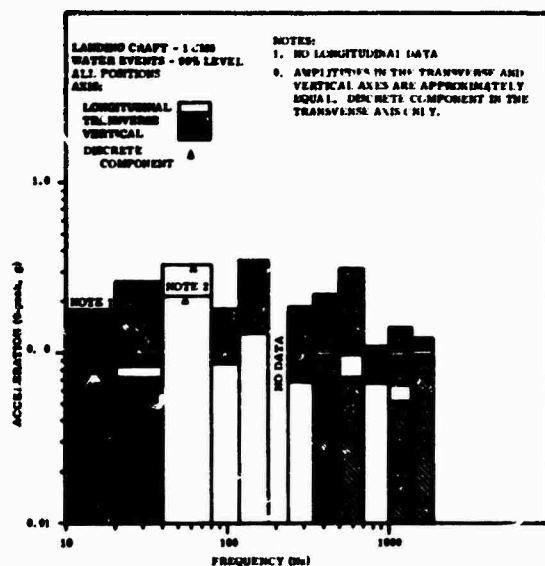
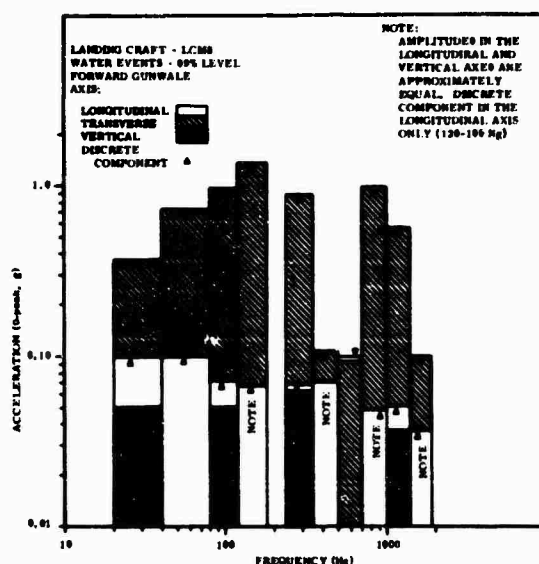


Fig. 13 - LCM8, Continuous Excitation Summary

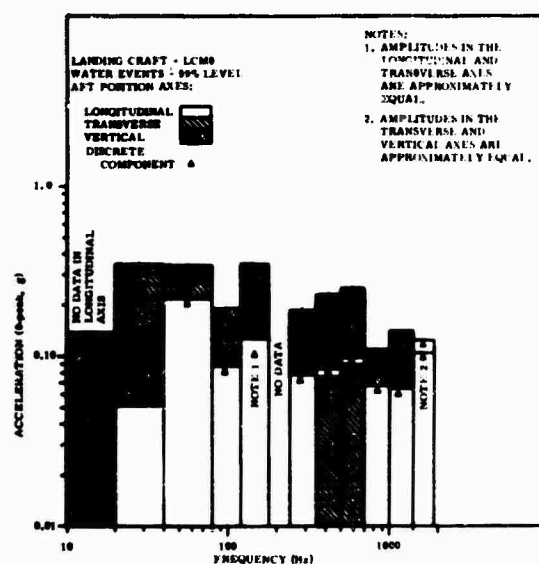
of circling with the other boats until the signal was given to run straight for the beach. Measurements were made during the pre-run maneuvers, during the run for the beach, and when the beach was reached.

When the data were reduced, it became apparent that the records taken from the forward accelerometers were quite different from those from the aft cluster. Although some events and some frequency bands seem to have a Gaussian-like distribution, the number of peaks counted during a 5-second interval are too few to represent a steady-state excitation. It would appear that the environment measured in the bow of the LCM8 is an intermittent series of discrete excitations.

A representation of the overall vibration of the LCM8, shown in Figure 13, was developed from the VAIL summaries. Comparison of Figure 13 with Figure 14 shows that the peak values of the former are much lower than those in Figure 14a. This result is caused by the operation of program VAIL, which tends to average the values it combines. Since there were so many more peaks recorded in the aft position (Figure 14b), the few high peaks recorded in the forward position were averaged out.



(a)



(b)

Fig. 14 - LCM8 Excitation, Forward and Aft

Generally, the amplitudes given for the aft position (Figure 14b) should be considered to represent the steady-state accelerations, whereas those in the forward record (Figure 14a) are the discrete, intermittent excitations. Figure 14b is a representation of the data taken from the accelerometers located in the aft portion of gunwale in the cargo area. The longitudinal axis, in general, shows the lowest amplitudes and the vertical axis the highest. The amplitudes are low, never exceeding 0.4g. Analysis of the nature of the excitation shows that in the longitudinal and vertical axes there is evidence of the influence of discrete or narrow-band random excitation in every frequency band above 40 Hz. This excitation is mixed with broadband Gaussian random excitation. The excitation in the transverse axis appears to be only broadband random with a near-Gaussian distribution.

One occurrence as the LCMB was approaching the beach showed an interesting comparison between the excitation in the forward and aft positions. There was a sand ridge far enough out that

the craft had not yet reduced speed for beaching. As the boat struck the ridge, the impact was great enough to cause one member of the group to lose his footing and fall to the deck. The acceleration time histories and response spectra derived from this event are shown in Figure 15 for the aft position.

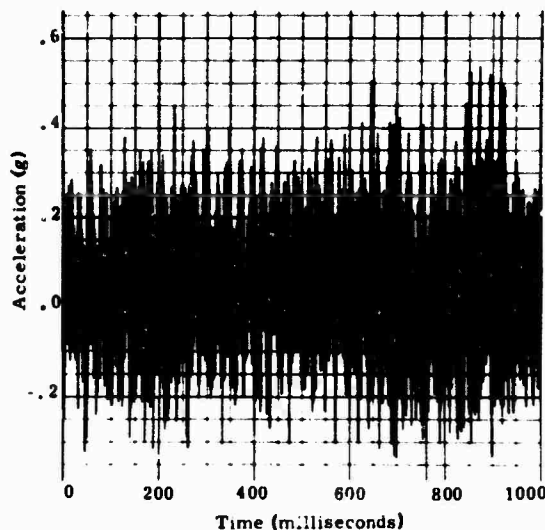
In the longitudinal and vertical axes, the response is greatest at 45 Hz in the forward position, but the aft shows greatest response at 170 Hz. In the transverse axis, however, the forward response is different in shape, peaking at 200 Hz, and the aft response is essentially flat across the entire spectrum at 0.8g. The highest response is 1.25g at 170 Hz in the vertical axis in the aft position.

Comparison between the records in the forward and aft positions (Figure 16) shows great dominance of the forward excitation in the transverse axis. Since this does not represent a large number of peaks, and is intermittent discrete rather than steady-state excitation, comparison is, perhaps, not logical. The high amplitudes of the

#### ACCELERATION vs TIME

Test No. R423160 Acceleration Ch 4 Time Interval 00.53.13 to 00.53.14 LCMB, Hitting the beach.

Aft Gunwhale  
Axis L. P.E. 2g pk to pk.  
Data Compression Tolerance = 0.000 g  
Delta V = 1.6v ft/sec



#### SHOCK SPECTRA

Aft Gunwhale  
Axis L. P.E. 2g pk to pk.  
+ Damping = .030  
0 Damping = .050

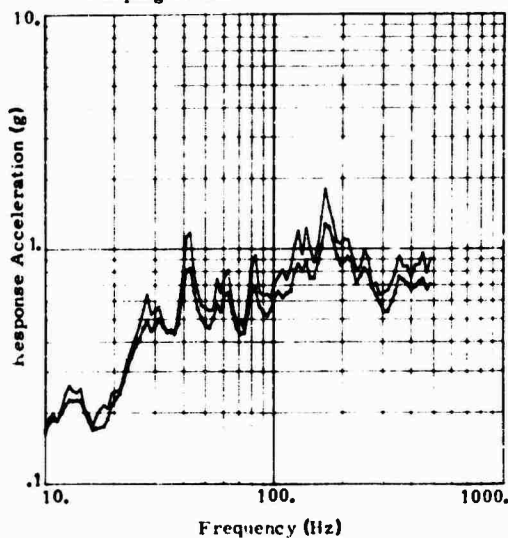
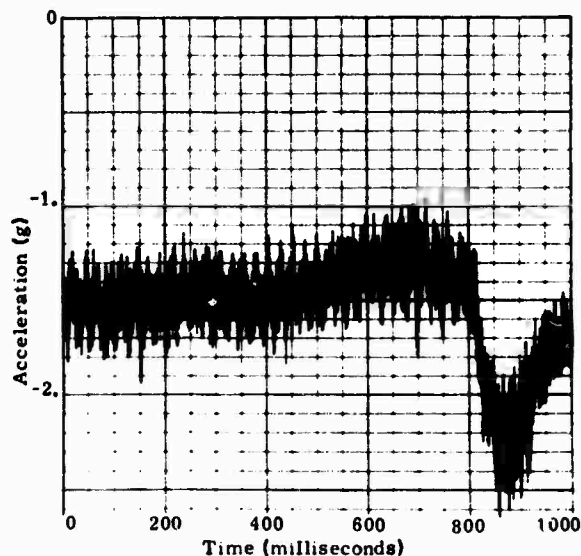


Fig. 15 - LCMB Hitting the Beach  
Response Spectra

# ACCELERATION vs TIME

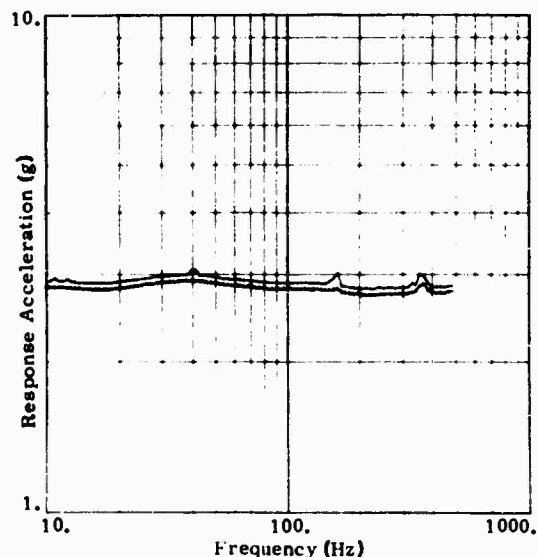
Test No. R423160 Acceleration Ch 5 Time Interval 00.53.13 to 00.53.14 LCM8. Hitting the beach.

Aft Gunwhale  
Axis T. P.E. 2g pk to pk.  
Data Compression Tolerance = 0.000 g  
Delta V = -49.44 ft/sec



# SHOCK SPECTRA

Aft Gunwhale  
Axis T. P.E. 2g pk to pk.  
+ Damping = .030  
0 Damping = .050

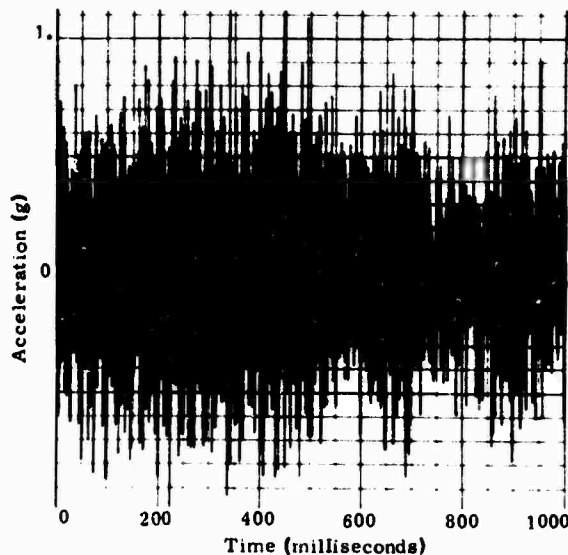


(b)

# ACCELERATION vs TIME

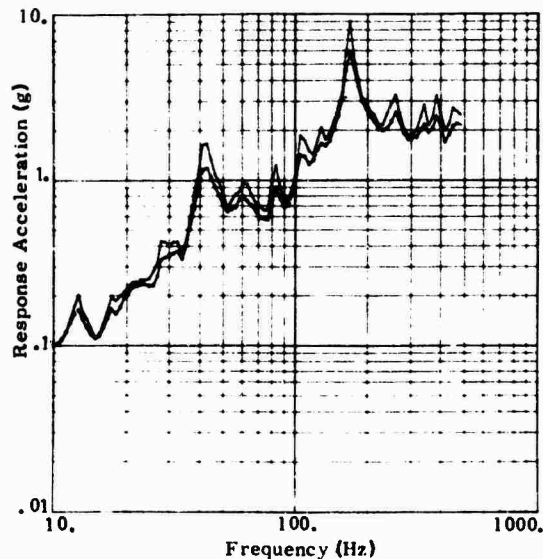
Test No. R423160 Acceleration Ch 6 Time Interval 00.53.13 to 00.53.14 LCM8. Hitting the beach.

Aft Gunwhale  
Axis V. P.E. 2g pk to pk.  
Data Compression Tolerance = 0.000 g  
Delta V = .84 ft/sec



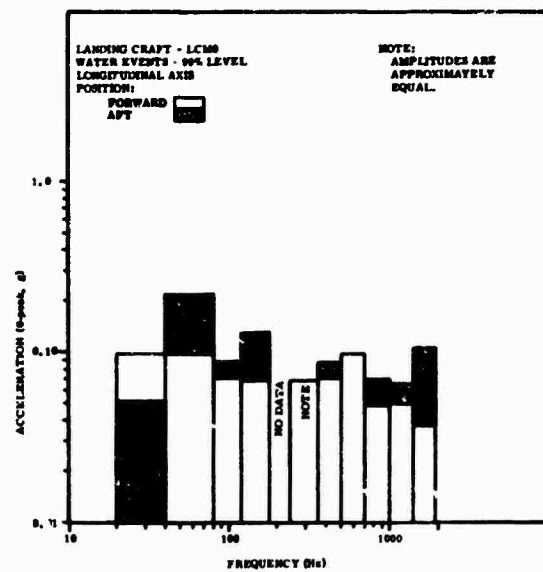
# SHOCK SPECTRA

Aft Gunwhale  
Axis V. P.E. 2g pk to pk.  
+ Damping = .030  
0 Damping = .050

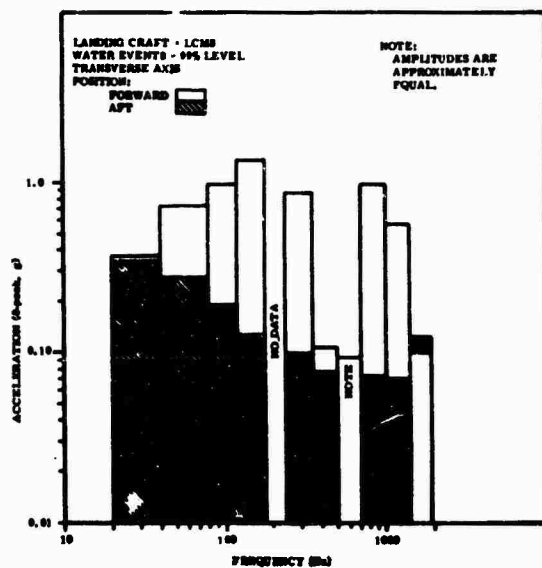


(c)

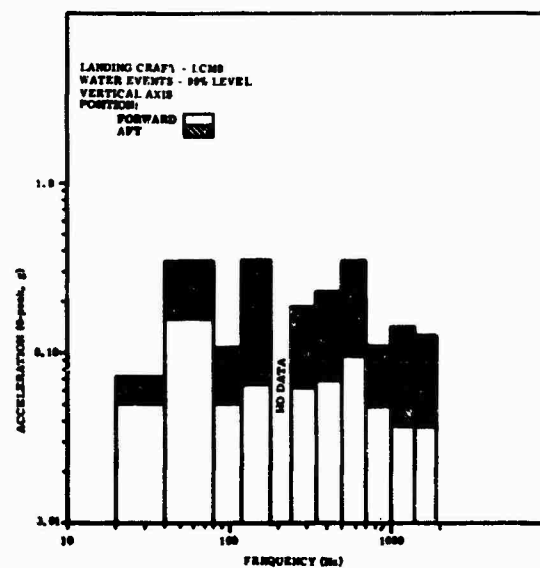
Fig. 15 - (Cont.)



(a)



(b)



(c)

Fig. 16 - LCM8, Comparison Between Forward and Aft Records

excitation in the bow, however, should be noted. The steady-state excitation with Gaussian random distribution measured in the aft position dominates the other two axes.

The characteristic excitation found at the bow of the LCM8 is largely intermittent. Farther aft, near the engines, there is a broadband random base which is Gaussian in distribution, but with a generous mixture of narrow-band random excitation. The amplitudes are low.

#### LCU

The measurements were made on the LCU during a trip on San Diego Bay. The boat ran up the bay for a period, then beached at normal speed, backed off, and returned to its berth at the Coronado Amphibious Base. Because of the size of the LCU, it was not possible to instrument both forward and aft. One triaxial cluster was located about 10 yards forward of midships on a tiedown cleat at centerline. The others were placed aft between the engines. The measurements were taken during a run at flank speed, beaching, backing off, and full back.

Figure 17 is a composite derived from all of the records taken on the LCU. While the amplitudes in the vertical axis generally dominate, the highest values, up to 0.35g, are found in the transverse axis between 20 and 80 Hz. High amplitudes in the longitudinal axis appear above 1000 Hz. Otherwise, the longitudinal axis frequently shows the lowest values.

The summaries for the forward and midships positions are shown in Figures 18a and 18b. A comparison reveals that the amplitudes are approximately equal below 80 Hz; however, above that point the record for the midships position, near the engines, generally dominates. It also shows the prominence of the transverse axes in the lower frequencies. The vertical axis generally dominates in the middle frequencies up to 1000 Hz, and the longitudinal axis emerges above that point.

Figures 19a, 19b, and 19c provide a comparison between the forward and midships records, with peak amplitude in each axis considered. The record for midships dominates in all axes and frequencies except in the 700- to 1000-Hz frequency band in the vertical axis.

In general, the characteristics discussed under the LCM8 appear in the data from the LCU, although not so

vividly. Records of individual events show that in the forward position the unusual peak distribution across the spectrum appears, but only when normal or slow speeds are being used. During the high-speed events, flank speed and nearly full back, the peak distribution is more like the normal situation, which is exhibited consistently by the measurements made near the engines. The large number of peaks produced during the high-speed events dominates the record to the extent that the VAIL summaries do not exhibit this characteristic. It seems reasonable to conclude that under normal speed conditions the excitation on the forward cargo deck of the LCU is largely discrete and intermittent in nature, but at high speeds becomes more continuous and largely Gaussian random.

The VAIL composite records for the forward accelerometers show the presence of narrow-band random excitation only in the vertical axis between 500 and 1400 Hz; at the midship station, however, the characteristics of the narrow-band excitation are present in all axes. In the longitudinal direction, there are few indications, and only between 350 and 1000 Hz. In the transverse axis, again, there are few, and only between 240 and 700 Hz in the 40- to 80-Hz band. In the vertical axis, such phenomena are seen in all frequency bands except the lowest. Comparisons of the number of peaks reported in all positions show the most continuous condition to be in the midship position. For instance, in the longitudinal record from the forward position 16,057 peaks are shown in the highest frequency band, whereas 57,235 appear in the same band of the longitudinal axis in the midship position.

The excitation measured in the LCU was very similar to that measured in the LCM8. Forward there was a great deal of intermittent discrete excitation, whereas the midship position exhibited a dominative broadband, near-Gaussian excitation with some narrow-band excitation intermixed. The amplitudes were generally lower in the LCU.

#### SUMMARY

A summary of the land events measured (Figure 20) is based on the VAIL summaries. A comparison of Figure 20 with Figure 2 shows that, although there is little difference between the LVTP7 and the LCA2, the LVTP7 is the dominant vehicle. The vertical axis dominates up to 350 Hz. The other two axes have amplitudes which are slightly higher above that frequency; however, in the

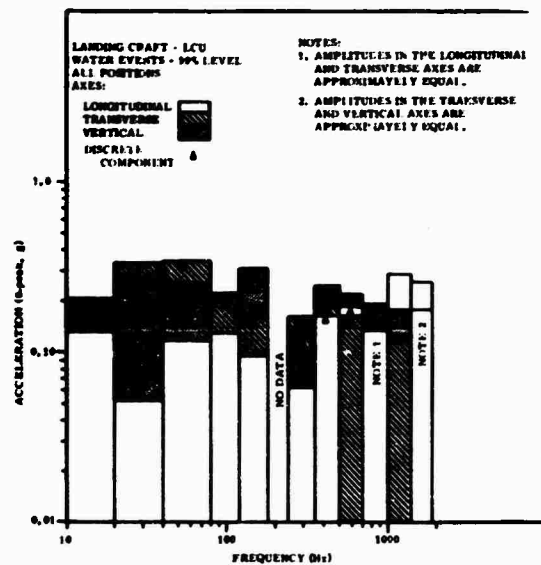
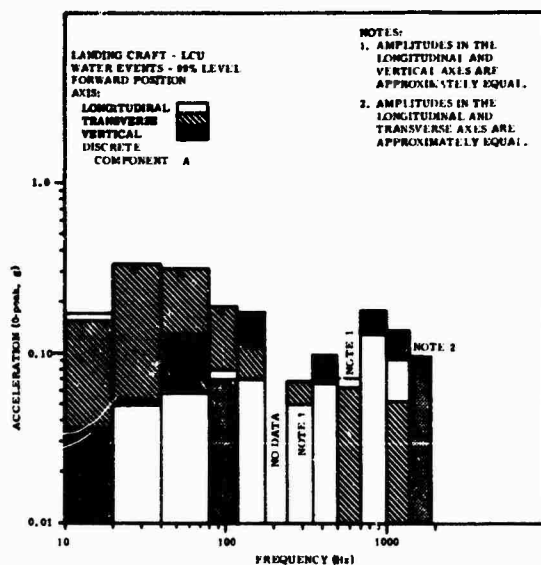
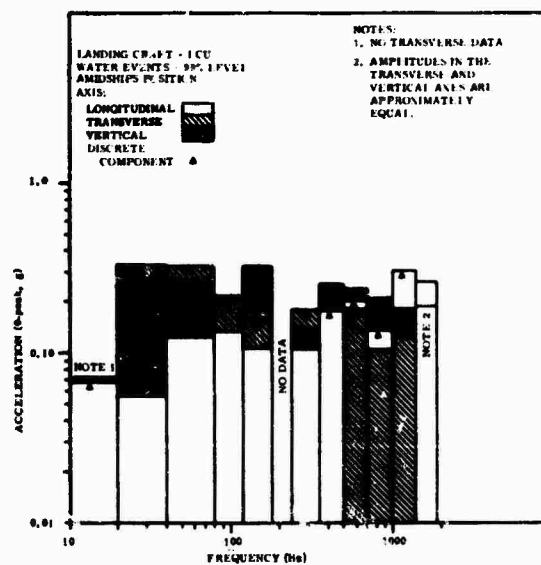


Fig. 17 - LCU Assault Boat, Continuous Excitation Summary



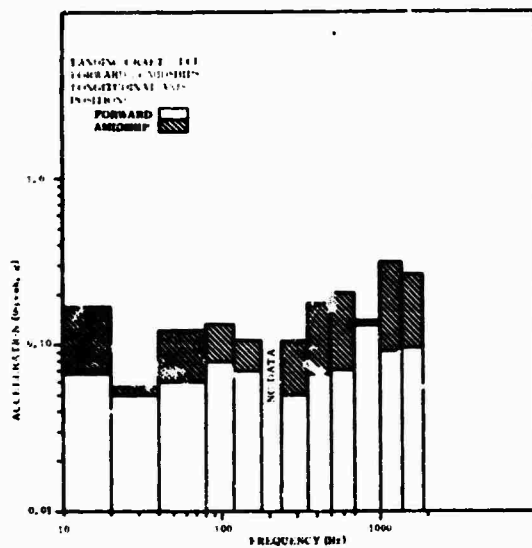
(a)



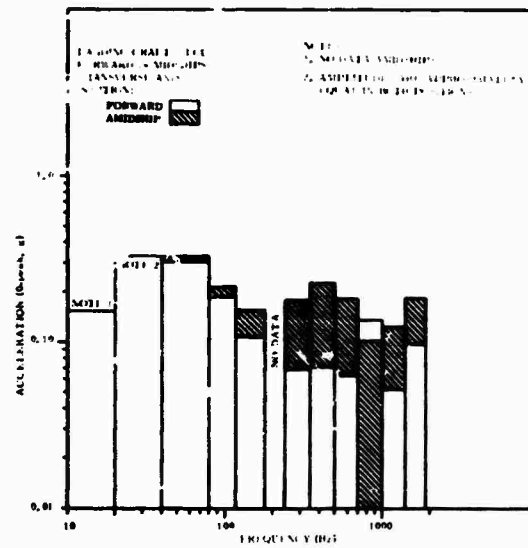
(b)

Fig. 18 - LCU Excitation, Forward and Amidships

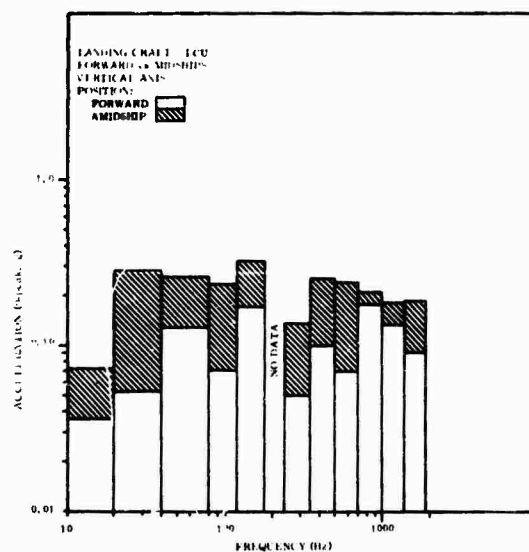




(a)



(b)



(c)

Fig. 19 - LCU, Comparison Between Forward and Amidships

700- to 1000-Hz band, the longitudinal and vertical axes are approximately of equal amplitude. A comparison between the records of the LVTP7 and the LCA2 (Figure 21) shows that only in two frequency bands in the records of the longitudinal axis does the LCA2 show higher amplitudes than the LVTP7.

The summary of water events (Figure 22) exhibits acceleration amplitudes that are lower than those measured during the land events. The transverse axis predominates in six of the frequency bands, whereas the vertical predominates in only four. Examination of the records of the various vehicles shows that the LVTP7 exhibited generally higher amplitudes during the water events than did the LCU or LCMS. However, this dominance is not complete. Only in the vertical axis above 20 Hz is the LVTP7 completely dominant. These data are shown in Figure 23.

The virtually complete ascendancy of the record of land events over the water events is depicted in Figure 24. Only in the low-frequency band of the transverse axis does the amplitude of the accelerations measured during the water events rise above those measured on land.

#### CONCLUSIONS

The following general conclusions may be made:

1. The LVTP7 has excitations of higher amplitude than any of the other assault or amphibious vessels measured.
2. In all cases, the excitation is basically broadband with a Gaussian random distribution in the vicinity of the engines, but shows much more influence of discrete and often intermittent excitation at a distance from them.

#### REFERENCES

- [1] M. B. Gens, "A Preliminary Observation of the Dynamic Environment of Helicopters," 1968 Proceedings, 14th Annual Technical Meeting, Institute of Environmental Sciences, St. Louis, Mo., April 1968, pp 423-432.
- [2] M. B. Gens, "The Dynamic Environment of Selected Military Helicopters," 42nd Shock and Vibration Bulletin, U. S. Naval Research Laboratories, Washington, November 1971.
- [3] M. B. Gens, "Dynamic Environment of Helicopters - Complete Data," SC-M-71-0604, Sandia Laboratories, Albuquerque, N. M., November 1971.
- [4] F. R. Gustke, "Eli-31 Portable Environmental Sampler," SC-TM-65-567, Sandia Laboratories, Albuquerque, N. M., February 1966.
- [5] L. A. Faw, "Program VAIL (User's Manual)," SC-M-71-0709, Sandia Laboratories, Albuquerque, N. M., November 1971.
- [6] J. T. Foley, M. B. Gens, and C. F. Magnuson, "Current Predictive Models of the Dynamic Environment of Transportation," Proceedings, 18th Annual Technical Meeting, Institute of Environmental Sciences, New York, May 1972.
- [7] M. B. Gens, "Dynamic Environment Vehicles and Vessels Associated with Assault Landings," SLA-73-0172, Sandia Laboratories, Albuquerque, N. M., June 1973.

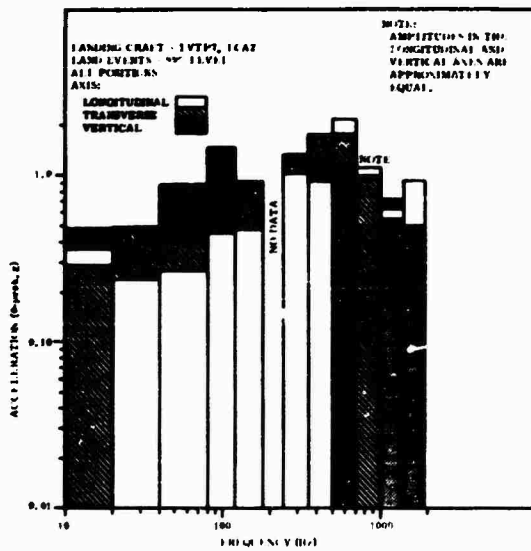


Fig. 20 - LVTP7 and LCA2 Land Events Summary

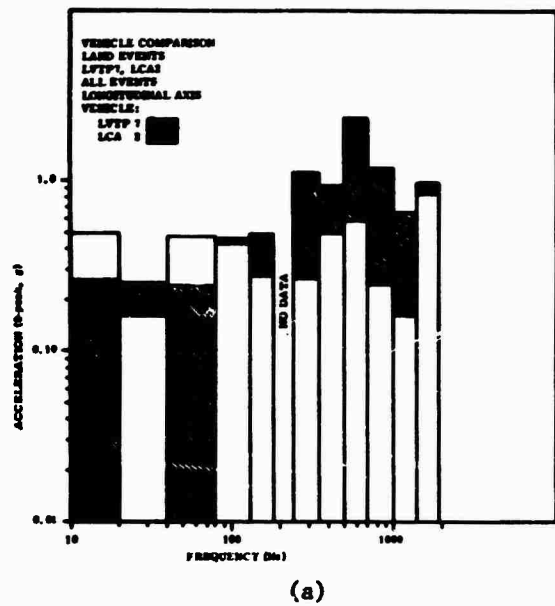


Fig. 21 - Land Events, Comparison Between LVTP7 and LCA2

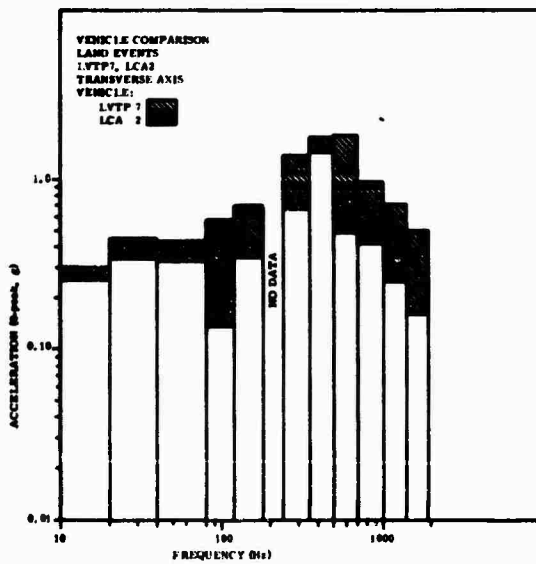


Fig. 21 - (Cont.)

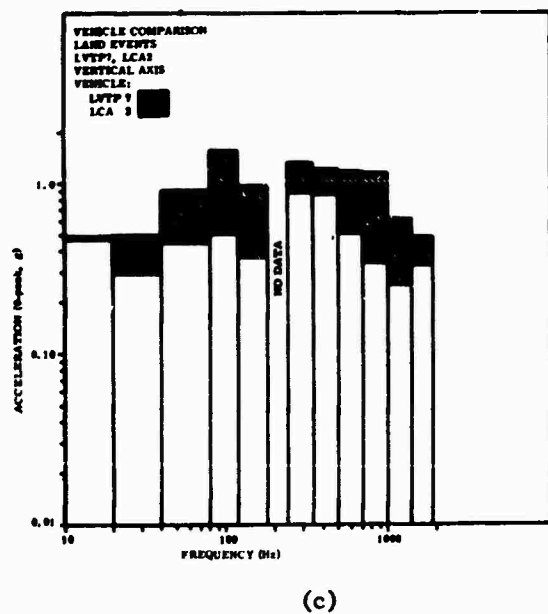


Fig. 21 - (Cont.)

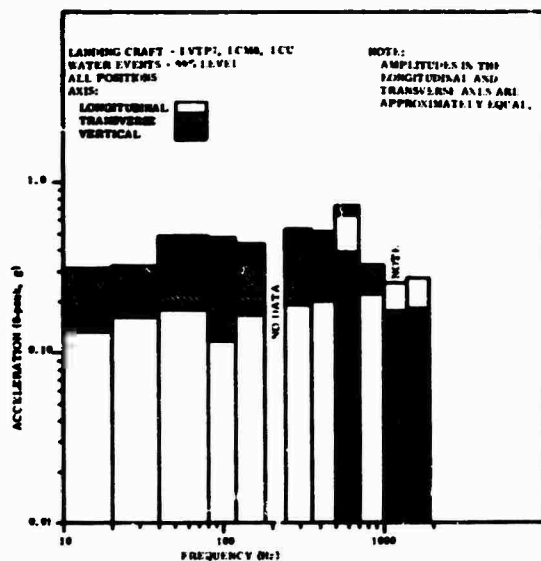
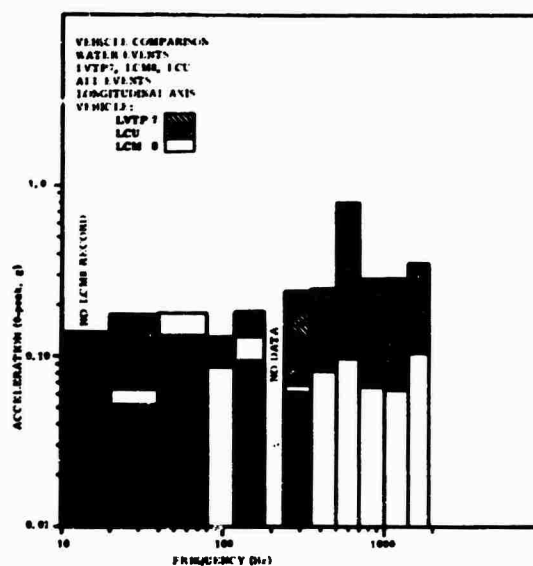
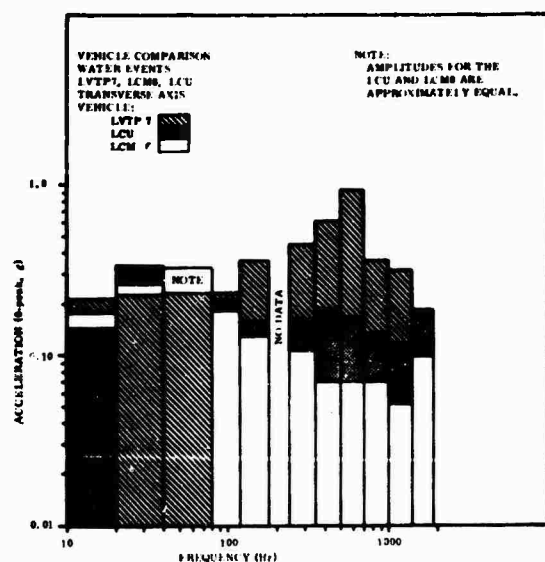


Fig. 22 - LVTP7, LCM8, and LCU Water Events, Summary



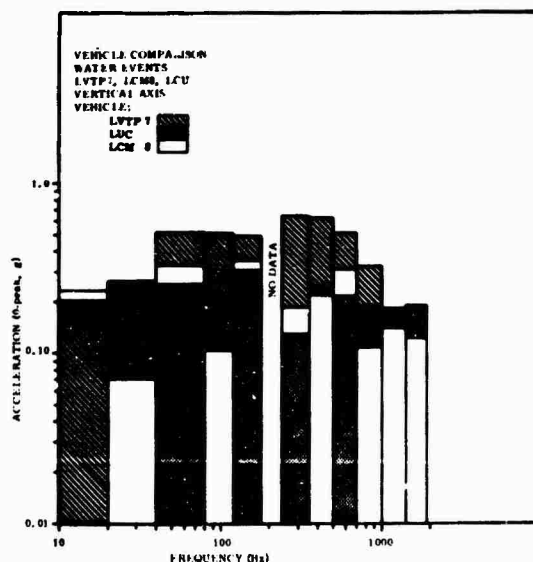
(a)

Fig. 23 - Water Events, Comparison of LVTP7, LCU, and LCM8



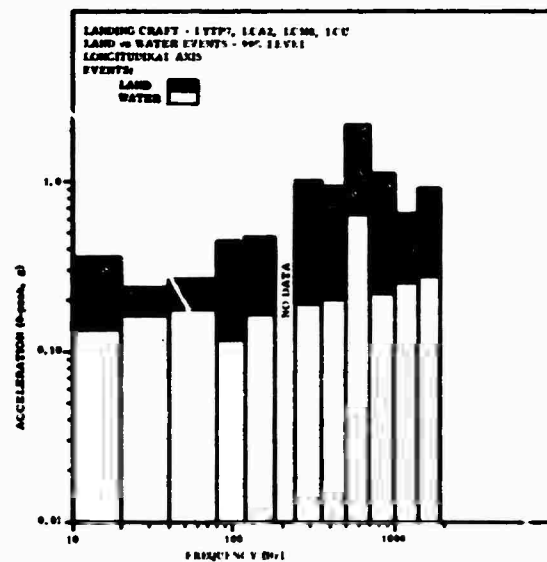
(b)

Fig. 23 - (Cont.)

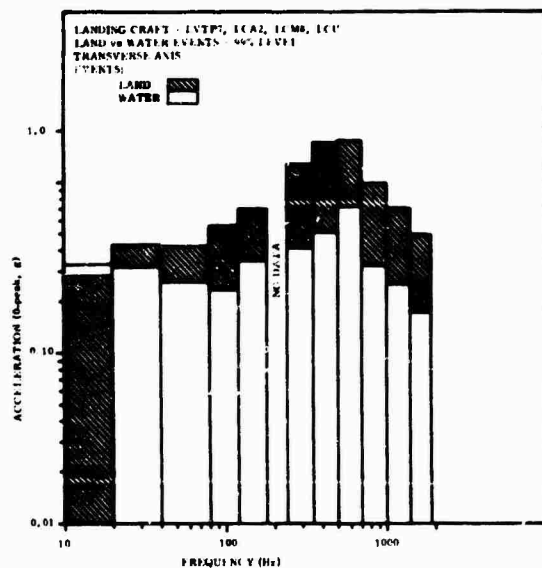


(c)

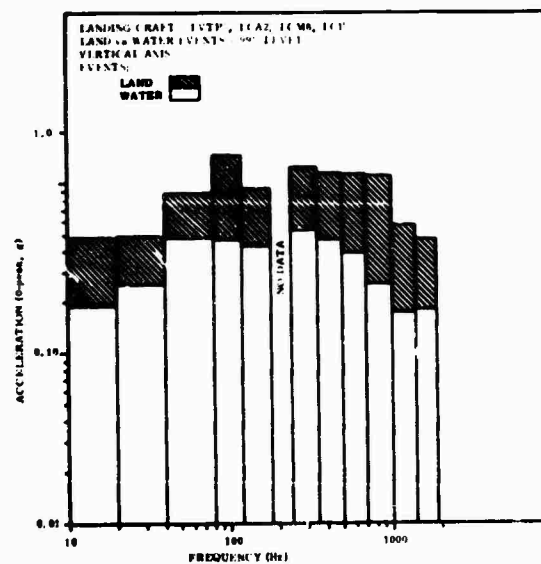
Fig. 23 - (Cont.)



(a)



(b)



(c)

Fig. 24 - Comparison Between Land and Water Events

## A RESONANCE-TYPE BACK-TO-BACK CALIBRATOR FOR ACCELEROMETERS

J.A. Macinante, N.H. Clark and B.H. Cresswell  
CSIRO Division of Applied Physics, National Standards Laboratory,  
Sydney, NSW 2008, Australia.

When a comparison calibration is made with a test and a reference accelerometer assembled on the table of an electromagnetic vibrator, significant error can result if the comparison is made at frequencies where appreciable transverse motion of the vibrator occurs. A new method is described in which lateral motion is restrained by using annular spring diaphragms to support the two accelerometers and constrain their motion to a rectilinear path. The amplitude of the calibrating motion is amplified by driving the system at resonance. By varying the thickness, material and outer clamping diameter of the diaphragms a large number of calibrating frequencies is provided. In the prototype calibrator described, these frequencies are in the range 98-520 Hz, and the calibrating motion has less than one per cent total harmonic distortion and less than one per cent transverse acceleration for displacements up to 0.25 mm peak-to-peak. The corresponding values of peak acceleration are  $47 \text{ ms}^{-2}$  (98 Hz) and  $1330 \text{ ms}^{-2}$  (520 Hz).

### INTRODUCTION

In comparison methods, the test accelerometer is calibrated by comparison with a reference accelerometer that has been calibrated in terms of the relevant national standards of measurement. Laboratories concerned with vibration measurement mostly use comparison methods, while absolute calibrations are normally performed only by laboratories maintaining primary measurement capability [1].

The two accelerometers to be compared may be assembled back-to-back on a fixture as in Fig.1(a), or the comparison may be made with the two accelerometers side-by-side on the vibrator table if suitable precautions are taken [2]. In recent years increasing use is being made of the type of reference accelerometer designed so that the test accelerometer can be attached directly to the reference accelerometer as in Fig.1(b). Descriptions of reference accelerometers of this type and discussion of their absolute calibration and the technique of their use can be found in Ref.[3] Parts 1 and 2. Procedures and techniques of comparison calibration, and precautions necessary to ensure valid comparison of accelerometers, are discussed in Ref.[3].

Ideally, a calibrator should generate rectilinear simple harmonic motion and the two

accelerometers should be subjected to the same amplitude of this motion. Departures from this ideal that give trouble in practice are distortion and non-rectilinearity of the motion. Such defects in the calibrating motion may cause errors because they can produce different contributions to the outputs of the two accelerometers.

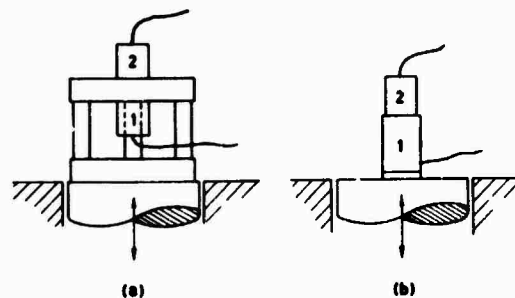


FIGURE 1 Back-to-Back Assemblies

In practice the calibration may be confined to frequency ranges in which the vibrator behaves satisfactorily, if such ranges have been identified in a prior investigation of the performance of the calibrator under the

same conditions of loading and use as in the calibration. Alternatively the quality of the vibratory motion may be monitored during the actual calibration. For example, in the comparison calibrator described in Ref. [3] Part 3, the input motion is determined by a set of three reference accelerometers which are arranged and operated to indicate non-rectilinearity of the motion.

Some laboratories have constructed vibrators designed specifically as vibration input generators; for example, Dimoff [4] used an air bearing to constrain the motion of an electrodynamic vibration standard. More recently there has been commercial development of vibrators designed for use as calibrators. In the present paper, a different approach is

described in which no unusual quality is demanded of the vibrator. Instead, the motion derived from an ordinary vibrator is constrained laterally and amplified axially by a resonance fixture interposed between the vibrator and the back-to-back accelerometers.

In Australia as elsewhere, establishments concerned with vibration measurement maintain reference accelerometers which they use to check the calibration of their 'working' accelerometers. The new calibrator will be used to compare these reference accelerometers in the low frequency range (100-500 Hz) with a reference accelerometer that has been calibrated at the National Standards Laboratory by the interferometric methods developed by Goldberg [5,6,7].

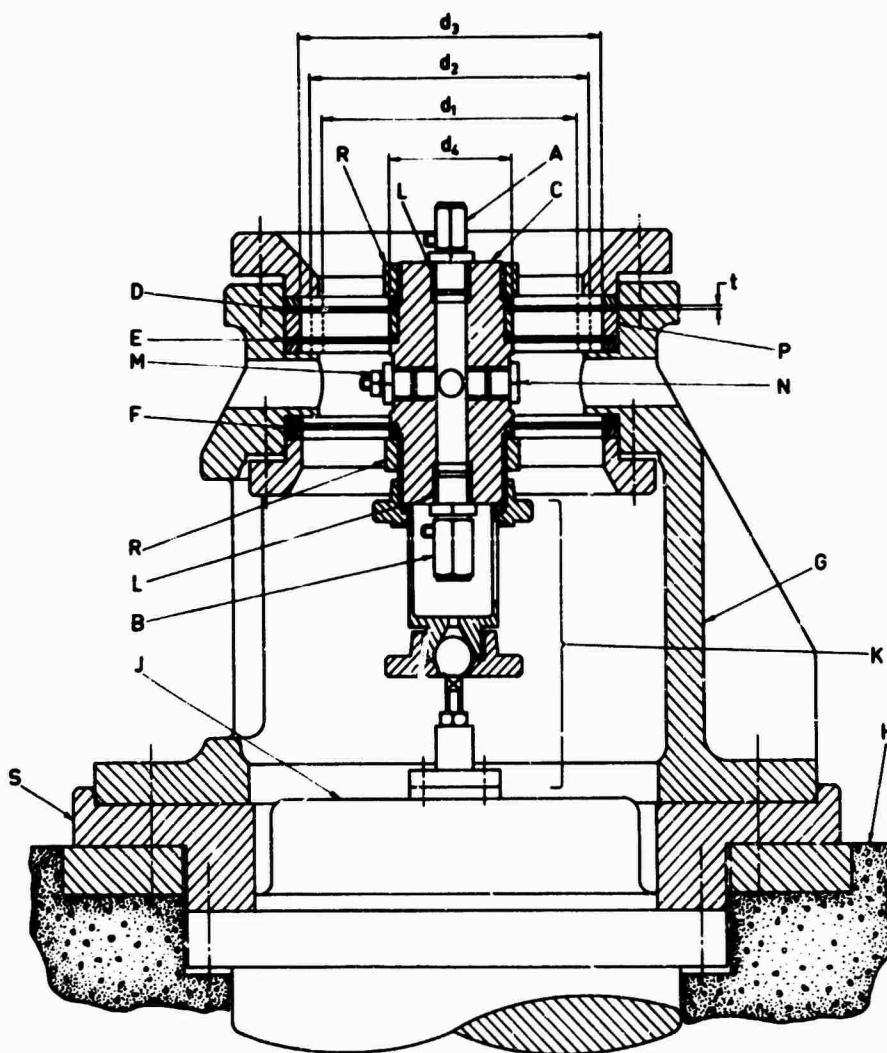


FIGURE 2 Cross Sectional View of Calibrator

#### BASIC DESIGN OF CALIBRATOR

Referring to the cross sectional diagram in Fig.2, the test accelerometer A and reference accelerometer B are fixed at opposite ends of the capsule C with their sensitive axes coaxial with the capsule. The capsule is supported on three annular spring diaphragms D, E and F that are clamped around their outer edges in a housing G fixed on a concrete block H in which the vibrator J is fixed. The inner edges of the diaphragms are clamped to the capsule, which is connected through the driving assembly K to the moving system of the vibrator.

In principle only two diaphragms are necessary, one near each end of the capsule: the third is incorporated so that when the upper diaphragm and clamping rings are removed and others substituted to change the resonance frequency, as explained later, the lowest diaphragm holds the capsule in position.

The frequency of the input signal to the vibrator is adjusted to the fundamental axial resonance frequency of the system and, with the vibration amplitude set at the required level, the electrical outputs of the accelerometers (or accelerometer, amplifier, readout systems) are compared. This is repeated at other frequencies as required.

#### DESCRIPTION OF THE CALIBRATOR

Fig.3 is a photograph of the calibrator and Fig.4 shows a typical assembly of the moving system.

##### *Capsule*

The capsule is of aluminium 100 mm long, 60 mm diameter and mass 1.1 kg. The accelerometers to be compared are screwed into adaptors L threaded to suit different makes of accelerometer. The test accelerometer is at the immediately accessible upper end of the



FIGURE 3 The Back-to-Back Calibrator



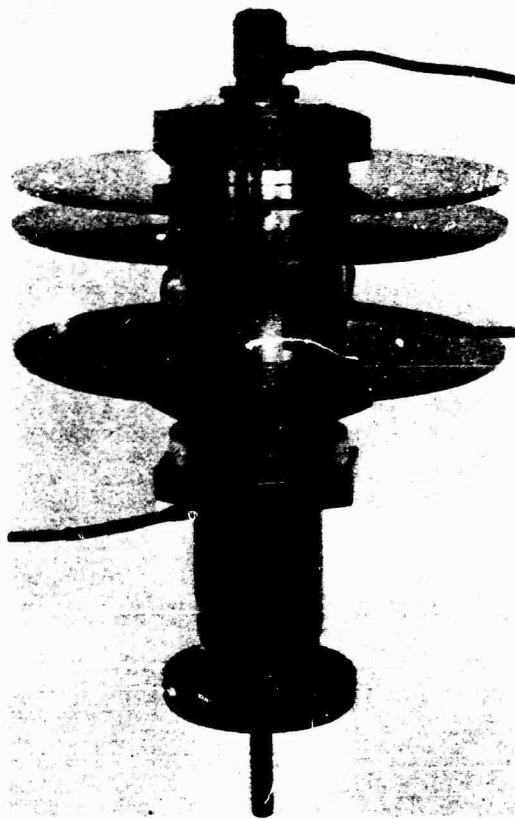


FIGURE 4 Typical Assembly of the Moving System

capsule. The reference accelerometer, which normally remains undisturbed while various test accelerometers are compared with it, is at the lower end. Additional positions are provided in the sides of the capsule for accelerometers M to monitor lateral motion, or targets N for use with optical proximity probes for checking lateral motion.

For the prototype calibrator two capsules were designed, one of aluminium and one ceramic. The advantages of using a ceramic material such as aluminium oxide for vibration tables have been stated in Ref. [3] Part 3. Because of the high stiffness, low density and damping properties of this material, the frequency at which wave motion becomes significant is above the usual range of calibration frequencies. This material has the further advantage that it is an electrical insulator, hence the two accelerometers are electrically insulated from one another and from ground except where connections are deliberately introduced. The development of the prototype and assessment of its mechanical performance described in the present paper have been carried out with the aluminium capsule. The calculated axial resonance frequency of the aluminium capsule, about 25 kHz, is well above

the operating frequency range of the calibrator.

#### *Driving Assembly*

The lower end of the capsule is connected to the moving system of an electrodynamic vibrator of peak force rating 140 N by the driving assembly K, which is designed to clear the reference accelerometer and its cable, and to permit adjustments for alignment and centring.

#### *Spring Diaphragms and Clamping Rings*

Two sets of diaphragms have been provided, one set made of stainless steel and the other of phosphor bronze. Each set comprises twelve diaphragms: four values of thickness ( $t_1 = 0.7$  mm,  $t_2 = 0.9$  mm,  $t_3 = 1.2$  mm and  $t_4 = 1.6$  mm) for each of the three diaphragms.

The effective outer clamping diameter of the upper pair of diaphragms, D and E, is changed by using different sets of the clamping rings P. Three sets of outer rings provide values of  $d_1 = 107$  mm,  $d_2 = 117$  mm,  $d_3 = 127$  mm. For the lowest diaphragm F, the outer clamping diameter is always  $d_3 = 127$  mm. The effective inner clamping diameter ( $d_4$ ) of all diaphragms is 50 mm.

When tightening the hexagonal nut R at one or other end of the capsule to load the inner clamping rings, a special fixture is used so that, when the external torque (55 Nm) is applied, the reaction is transferred directly to the housing, and the capsule is not strained in torsion.

To ensure uniformity of clamping on the outer clamping rings the screws holding the upper and lower flanges are uniformly tightened to a specified torque (30 Nm).

#### *Housing*

The shape of the cast iron housing G is best seen in Fig.3. The three large openings in the sides are for access to the driving assembly. Four smaller holes, two of which can be seen in the photograph, align with the cross holes in the capsule. These provide access for the proximity probes mentioned earlier, and are used as exits for the cables of transverse monitoring accelerometers.

The housing is located on an adaptor plate S designed so that, when the drive is disconnected and the housing removed for access to the reference accelerometer or the lowest diaphragm, the system can be reassembled without loss of alignment.

The calibrator is supported on the concrete block H of mass 160 kg resting on vibration isolators.

#### *RANGE AND PERFORMANCE OF CALIBRATOR*

A series of tests has been made to evaluate the range of the calibrator and the quality of the calibrating motion. Ideally the

calibrating motion should be undistorted rectilinear simple harmonic motion. For practical purposes the aim has been to determine the range in which distortion and transverse motion are within acceptable limits.

#### Frequency Range

The 192 basic combinations available are shown in Table 1. Additional combinations could be made by not choosing the same material and thickness for the upper two diaphragms.

accelerometer mounted on the calibrator, using an XY recorder calibrated for frequency against a frequency counter. The resonance frequency was read from these response records.

A representative sequence of 12 resonance responses recorded in a succession of settings is illustrated in Fig.5. The sharpness of resonance is indicated by  $Q = 40$ , calculated directly from the higher frequency records. The value of  $Q$  would appear less if calculated

TABLE 1  
Basic Combinations of Diaphragm Material,  
Thickness and Clamping Diameter.

Lowest Diaphragm		Upper Pair of Diaphragms		
Material	Thickness	Material	Clamping Diameter	Thickness
SS*	$t_1$	SS	$d_1$	$t_1 \ t_2 \ t_3 \ t_4$
			$d_2$	$t_1 \ t_2 \ t_3 \ t_4$
			$d_3$	$t_1 \ t_2 \ t_3 \ t_4$
SS	$t_2$	SS	12 combinations as above	
SS	$t_3$	SS	12 combinations	
SS	$t_4$	SS	12 combinations	
PB†	$t_1 \ t_2 \ t_3 \ t_4$	PB	48 combinations as above	
SS	$t_1 \ t_2 \ t_3 \ t_4$	PB	48 combinations	
PB	$t_1 \ t_2 \ t_3 \ t_4$	SS	48 combinations	

\*SS stainless steel

†PB phosphor bronze

For the experimental evaluation of the calibration frequency range, the calibrator was set up and operated at a selection of about half of the first 96 combinations listed in the table; that is, using the same material for the upper pair of diaphragms as for the lowest diaphragm.

At each setting the input frequency to the driving vibrator was swept through a suitable range and a record made of the output of an

from the lower frequency records, due to the influence of the 5 Hz bandwidth of the detector.

The numerical values of the 50 resonance frequencies observed in these tests are plotted in Fig.6. It can be seen from the spread of the test results, which represent about a quarter of the basic combinations shown in Table 1, that a resonance frequency for calibration purposes could be provided in the vicinity of any required frequency in the range

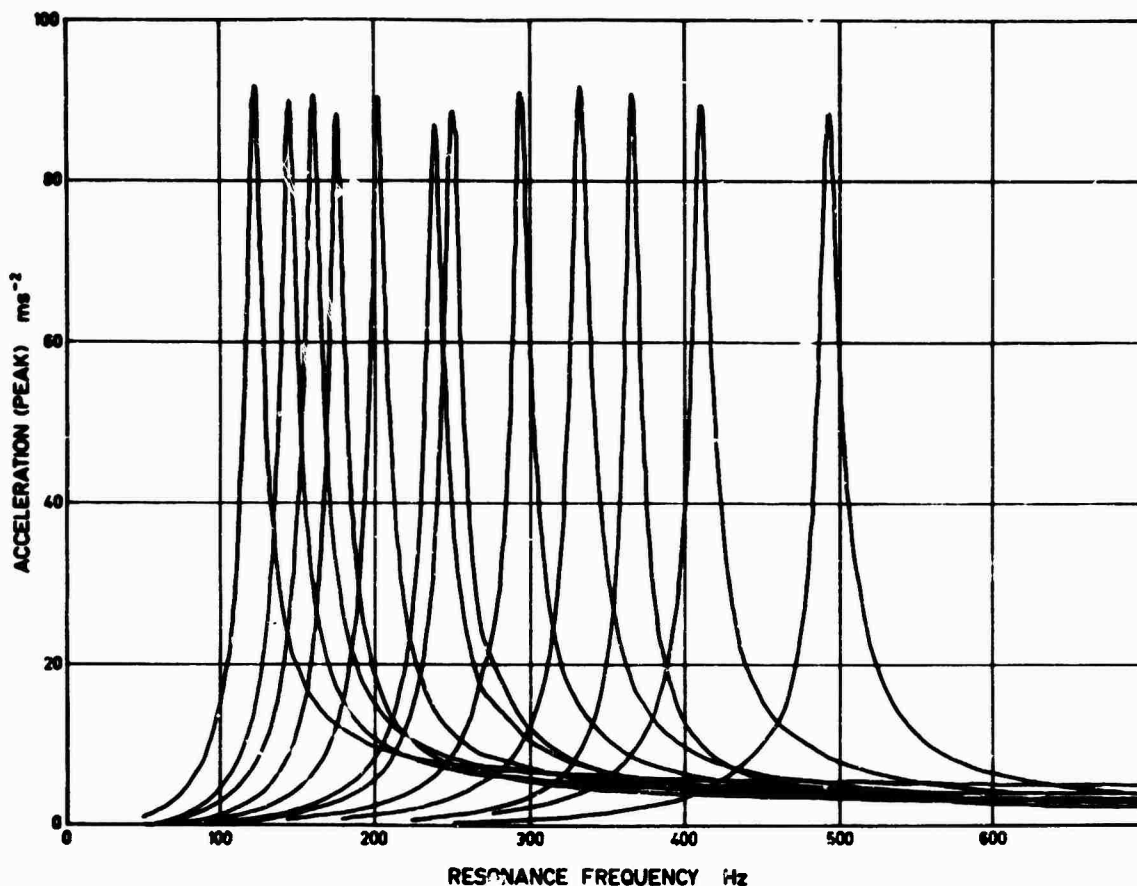


FIGURE 5 Typical Resonance Response Records

98-520 Hz.

If a particular precise value of the frequency is required, a combination can be chosen having a resonance frequency slightly higher, and mass added to the capsule to lower the frequency to the desired value. For example, in an observation at a resonance frequency of 260 Hz, addition of a 200 gram mass reduced the resonance frequency to 250 Hz; addition of 500 gram reduced the resonance frequency from 260 to 230 Hz.

#### Distortion

Distortion in the form of harmonics of the calibrating frequency may arise from distortion

of the electric signal applied to the vibrator or from non-linear stiffness of the mechanical system. The input signal distortion is readily measured and has been found to be negligible.

Distortion attributable to the mechanical system has been investigated by driving the calibrator at a fixed amplitude and analysing the signal from an accelerometer mounted on the top face of the capsule. The analysis was made with a heterodyne analyser, sweeping over a wide range using a 5 Hz bandwidth. With the set-up used, distortion components could be measured down to 0.1 per cent with a resolution of 0.05 per cent.

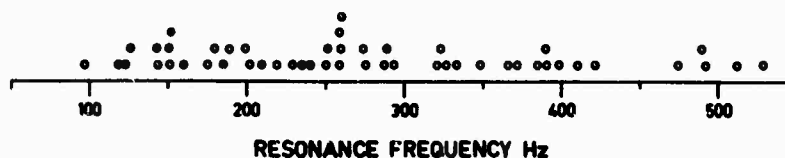


FIGURE 6 Observed Resonance Frequencies

These tests showed that the total harmonic distortion was less than one per cent if the displacement was limited to a maximum value of 0.25 mm peak-to-peak.

One manifestation of the mechanical non-linearity has been a decrease in resonance frequency with increase in displacement amplitude. In an experiment made with an improved method of clamping the diaphragms, the resonance frequency increased with increased amplitude, which is in accord with the theory for centre-loaded diaphragms with perfect clamping [8].

Tests with matched accelerometers, one at each end of the capsule, indicated no phase or amplitude difference within the limits of the frequency range of the calibrator.

Another form of distortion of the acceleration signal results from external vibration. With the calibrator installed in the manner described earlier there has been no distortion attributable to site vibration.

#### Acceleration Range

The acceleration range is determined by the acceptable displacement amplitude, because the distortion resulting from the non-linear stiffness of the system becomes more serious with increasing displacement. With the calibrator in its present form and the displacement limited to 0.25 mm peak-to-peak, the maximum acceleration (peak) is  $47 \text{ ms}^{-2}$  at 98 Hz and  $1330 \text{ ms}^{-2}$  at 520 Hz.

#### Transverse Motion

The transverse motion was measured using a fibre-optics proximity probe to determine the displacement of the capsule relative to the probe. The reference faces on the capsule were polished brass targets N fitted as shown in Figs. 2 and 4. Observations were made with two targets having their faces vertical and mutually perpendicular. The probe was supported independently of the calibrator in such a way that it functioned as an inertial reference for the purpose of these measurements.

The probe was calibrated at each frequency against the accelerometer used to measure the axial motion. The calibration procedure was to mount the probe so that it measured the vertical displacement of the accelerometer whilst simultaneously the accelerometer output and the frequency were observed. This was repeated at several amplitudes to check system linearity. The displacement probe was then re-positioned to measure the transverse motion.

These observations showed that the transverse displacement of the capsule throughout the frequency range of 98-520 Hz was less than one per cent of the axial displacement.

#### CONCLUDING REMARKS

The performance tests of the calibrator described in this paper indicate that unwanted transverse motion can be constrained by using annular spring diaphragms. The use of such diaphragms makes it possible to design the system for operation at a resonance frequency in a useful range for calibration purposes, and the incorporation of means of varying the stiffness properties of the set of diaphragms makes other resonance frequencies available.

If one per cent total harmonic distortion and one per cent transverse acceleration are considered to be acceptable, the range of the calibrator in its present form is determined by a displacement limitation of 0.25 mm peak-to-peak in the range 98-520 Hz. The corresponding limit of peak acceleration is  $47\text{--}1330 \text{ ms}^{-2}$  (or  $5\text{--}136 \text{ g}$ , where  $\text{g}$  = acceleration due to gravity).

A further development now in progress will provide for a set of diaphragms of increased thickness ( $t = 3.2 \text{ mm}$ ) and improved clamping. This is expected to raise the frequency range to about 1 kHz, which is probably the practical limit for this particular design.

A smaller and simpler version of the calibrator is being developed for use at test sites to provide for comparison calibrations at two or three frequencies.

#### REFERENCES

1. American National Standards Institute Inc., American National Standard for the Selection of Calibrations and Tests for Electrical Transducers used for Measuring Shock and Vibration, ANSI S2.11-1969, (Section 4, Calibration Methods).
2. American Standards Association, American Standard Methods for the Calibration of Shock and Vibration Pickups, S2.2-1959, (Section 5, Calibration by Comparison with Calibrated Pickup).
3. Instrument Society of America, 22nd Annual ISA Conference Proceedings, Vol. 22, 1967, Paper M18-3-MEST 1ND-67, in five parts:  
Part 1; pp.2-8, R.R. Bouche, "Vibration Standards for performing comparison calibrations".  
Part 2; pp.9-17, R. Chernoff, "Comparison calibration techniques for vibration transducers".  
Part 3; pp.18-20, S. Edelman, "The National Bureau of Standards comparison calibrator for vibration".

- Part 4; pp.21-25, R.S. Musa,  
'Comparison calibration of rectilinear  
vibration and shock pickups".
- Part 5; pp.26-42, K. Unholz, 'Vibration  
transducer calibration using the  
comparator method".
4. T. Dimoff, "Electrodynamic Vibration  
Standard with a Ceramic Moving  
Element", J. Acoust. Soc. Amer.,  
Vol. 40, No. 3, pp.671-676, 1966.
  5. J.L. Goldberg, "New Method for the  
Accurate Standardization of  
Mechanical Oscillation of Small  
Amplitude", J. Acoust. Soc. Amer.,  
Vol. 36, No. 10, pp.1922-25, 1964.
  6. J.L. Goldberg, "Method of Measuring  
Vibratory Displacement in Terms of a  
Light Wavelength", Shock and Vib.  
Bull., Vol. 37, Pt. 2, pp.13-16, 1968.
  7. J.L. Goldberg, "An Interferometric  
Method for the Standardization of  
Oscillatory Displacement", Metrologia,  
Vol. 7, No. 3, pp.87-103, July 1971.
  8. D.C. Chiang and S.S.H. Chen,  
"Large Amplitude Vibration of a  
Circular Plate with Concentric  
Rigid Mass", Am. Soc. Mech. Engrs.-  
Trans. Ser. E - J. Appl. Mech.,  
Vol. 39, No. 2, pp. 577-83,  
June 1972.

# A NEW TRANSVERSE CALIBRATOR FOR ACCELEROMETERS

J.A. Macinante, N.H. Clark and B.H. Cresswell  
CSIRO Division of Applied Physics, National Standards Laboratory,  
Sydney, NSW 2008, Australia.

The transverse sensitivity characteristics of the test accelerometer are determined by mounting the accelerometer with its sensitive axis vertical, on a horizontal surface which is caused to oscillate with simple harmonic motion of constant acceleration amplitude  $A$  in any direction  $\theta$  in the horizontal plane. In the prototype calibrator described, the horizontal surface is the free end of a vertical cantilever beam that is driven in transverse flexural vibration by two small electrodynamic vibrators arranged and operated in such a way that by varying the relative amplitudes of the driving forces any desired direction  $\theta$  can be set. The acceleration vector  $\vec{A}(\theta)$  is determined by measuring its two orthogonal horizontal components with a pair of monitoring accelerometers attached to the beam adjacent to the test accelerometer. The procedure is described for determining the relationship between the transverse sensitivity ratio (TSR) and  $\theta$ , and hence evaluating the two quantities of most practical significance: the maximum TSR, and the orientation of the accelerometer for minimum TSR. Examples are given of typical transverse calibrations at 100 Hz and  $A = 200 \text{ ms}^{-2}$ , with  $\theta$  stepped through 10 degree intervals. Sources of error are discussed and uncertainties estimated.

## NOMENCLATURE

$A$  = amplitude of transverse acceleration ( $\text{ms}^{-2}$ )  
 $f$  = frequency of transverse vibration (Hz)  
 $\theta$  = direction of vibration in xy plane (deg)  
TSR = transverse sensitivity ratio  
 $Z$  = identification of test accelerometer  
 $E_Z$  = output of test accelerometer (V)  
 $S_Z$  = axial sensitivity of test accelerometer, along axis  $Oz$  ( $\text{Vm}^{-1} \text{s}^2$ )  
 $Cz$  = sensitive axis of test accelerometer, normal to mounting surface (see Fig.1)  
 $\theta(\text{TSRmin})$  = value of  $\theta$  for which TSR is minimum (deg)

$X, Y$  = identifications of transverse monitoring accelerometers

$Ox, Oy$  = co-ordinate directions in horizontal plane (see Fig.1)

$E_X, E_Y$  = outputs of  $X$  and  $Y$  accelerometers respectively (V)

$S_X, S_Y$  = axial sensitivities of  $X$  and  $Y$  accelerometers respectively ( $\text{Vm}^{-1} \text{s}^2$ )

Other symbols are defined in context as required

## INTRODUCTION

Accelerometers are in widespread use for the measurement of the mechanical vibration of vehicles, structures, machinery and many other test objects. In the most common type, a piezo-electric element having a seismic mass attached to one end, has its other end fixed to the body of the accelerometer which is attached to the

object whose vibration is to be measured. The assembly is designed to have an axis of symmetry normal to its base, and is intended to measure vibratory acceleration applied in the direction of that axis, which is referred to as the sensitive axis of the accelerometer.

If an accelerometer is being used to measure vibration in the direction of its sensitive axis while it is also being subjected to acceleration having components normal to that axis (i.e. transverse acceleration) it is desirable that the transverse acceleration should not contribute to the electrical output of the accelerometer. This is unfortunately an ideal which is not usually attained in practice. Minor inaccuracies involved in the processes of manufacturing and assembling the various components of the accelerometer, and some non-uniformity and asymmetry of the properties of the materials used, cause the transverse sensitivity of most accelerometers to be in the range from less than one to about ten per cent of the axial sensitivity. Neglect of this factor in vibration measurement may result in significant error, therefore it is essential to determine the transverse sensitivity characteristics of accelerometers.

The specific objects of transverse calibration are to determine:

- (i) the maximum transverse sensitivity ratio, denoted by  $TSR_{max}$ ,
- (ii) the transverse angular direction on the accelerometer that corresponds to the minimum transverse response denoted by  $\theta(TSR_{min})$ .

In a simplified conceptual model of an accelerometer which assumes that the transverse response is attributable to a simple lack of coincidence of the sensitive axis  $Oz$ , as defined, and some axis  $Oz'$  along which the sensitivity is a maximum (see Fig.1), the direction of  $TSR_{max}$  lies in a plane containing these two axes, and  $\theta(TSR_{min})$  is normal to this plane.

When an accelerometer is to be used to measure vibration in a specified direction,  $TSR_{max}$  is a measure of the greatest output likely to arise from vibrations in other directions. If the direction of a particular source of transverse acceleration is known, then knowledge of  $\theta(TSR_{min})$  will allow the accelerometer to be oriented so that the contribution from transverse components is greatly reduced. In the simplified model, for example, aligning  $\theta(TSR_{min})$  within  $\pm 6$  deg of the direction of the transverse acceleration will reduce the effect by a factor of about 10, and a  $\pm 2$  deg alignment will reduce it by a factor of about 30, with respect to the maximum possible if no alignment precautions are taken.

This paper describes a new and simple method of transverse calibration. Although the paper refers to piezoelectric accelerometers, obviously the principle is applicable to the

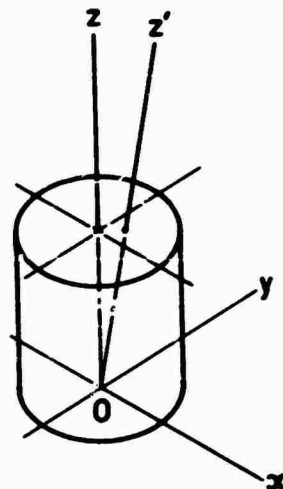


FIGURE 1 Definition of Sensitive Axis

transverse calibration of vibration transducers in general.

#### PRESENT METHODS OF TRANSVERSE CALIBRATION

The transverse sensitivity ratio TSR is defined as  $E_1/E_2$ , where  $E_1$  is the output of a pickup when oriented with its sensitive axis transverse to the direction of the input motion, and  $E_2$  is the output when the sensitive axis is aligned in the direction of the same input motion [1]. The transverse sensitivity calibration is performed by applying a transverse sinusoidal motion at a single frequency below 500 Hz where it is known that the transverse excitation is at least 100 times that in the direction of the sensitive axis [2]. Because the transverse sensitivity is known to vary considerably with the direction of oscillation in the transverse plane, the accelerometer is rotated about its sensitive axis through 360 deg in increments of 45 deg or less to determine the maximum transverse response.

Rockwell and Ramboz [3] have described transverse calibration methods which account for the vector components of test accelerometer output due to motion in other than the desired direction. Ramboz [4] described a development in which the full polar plot of transverse sensitivity is derived from observations at only four values of  $\theta$ . Finley [5] described a comparison method using a reference accelerometer whose transverse sensitivity had been carefully pre-determined. The comparison was made at eight angular settings about the accelerometer axis using an octagonal fixture as shown in Fig.2(a). In Ref. [6] a mechanically driven apparatus is described which provides for rotation of an accelerometer about its sensitive axis while it is being vibrated transversely.

In the method described in this paper,

physical resetting of the accelerometer about its sensitive axis is not necessary; instead the accelerometer remains attached to a horizontal surface in the xy plane throughout as shown in Fig.2(b) and the surface itself is caused to oscillate parallel to any direction  $\theta$  in the plane.

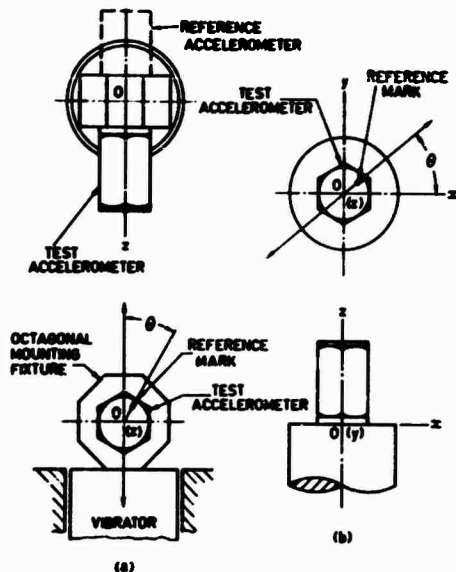


FIGURE 2 Basic Difference Between  
(a) Existing Method and  
(b) New Method

#### PRINCIPLE OF THE NEW TRANSVERSE CALIBRATOR

The new method makes use of the fact that two rectilinear coplanar sinusoidal motions of the same frequency, acting in phase along mutually perpendicular directions, have as their resultant a rectilinear motion acting in a direction which is determined by the relative amplitudes of the two input components and which can be varied by adjusting the relative amplitudes. Referring again to Fig.2(b) the input components acting along  $Ox$  and  $Oy$  are adjusted to produce motion along a line at any required angle  $\theta$  in the xy plane.

This is implemented in the new calibrator in the manner shown schematically in Fig.3. A vertical cantilever beam of circular or annular cross section is clamped near its lower end. The test accelerometer is attached to the upper end of the beam with its sensitive axis  $Oz$  coaxial with the beam. The beam is driven in transverse vibration by two small electrodynamic vibrators having their axes mutually perpendicular and in a horizontal plane a short distance above the clamp. The vibrators are operated in phase from a single oscillator which is adjusted to the transverse resonance frequency of the system. By varying the relative amplitudes of the two driving forces the test accelerometer can be subjected to transverse

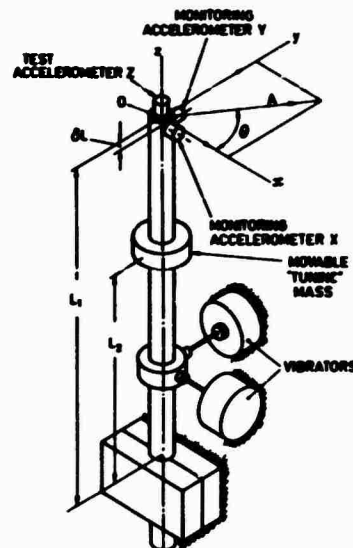


FIGURE 3 Schematic Diagram of  
New Transverse Calibrator

vibration in any direction in the plane xy of its mounting face.

The TSR is determined by measuring the output ( $E_z$ ) of the test accelerometer when a transverse acceleration of known amplitude  $A$  is applied at successive values of  $\theta$ . The acceleration vector  $\vec{A}(\theta)$  is determined from its orthogonal horizontal components, which are measured with a pair of monitoring accelerometers X and Y attached to flat surfaces ground on the beam near the test accelerometer. The outputs  $E_x$  and  $E_y$  of these accelerometers are connected to an oscilloscope so that an analogue of the transverse motion is displayed as a Lissajous figure.

#### DESCRIPTION OF NEW TRANSVERSE CALIBRATOR

In the prototype calibrator illustrated in Figs. 3 and 4 the cantilever beam is a 25 mm diameter steel bar of total length 0.7 m. The beam is clamped near its lower end in a housing which also supports the two vibrators and is bolted to a vertical face of a heavy concrete block. For clarity the photograph shows the calibrator removed from the concrete block.

The vibrators, which are of a commercially available type with a peak force rating 8.5 N, have their axes in a horizontal plane 0.1 m above the upper face of the clamp. The signals to the two vibrators are obtained through a two-channel amplifier (see Fig.5) from a common oscillator operated at the frequency of resonance of the beam. Each channel has an amplitude control and a  $\pm 90$  deg variable phase-shift control. The latter is necessary to compensate for the effects of small variations in the transverse mechanical stiffness of the system as the direction of vibration is altered; these variations cause differing phase shifts in the two component directions, giving rise to



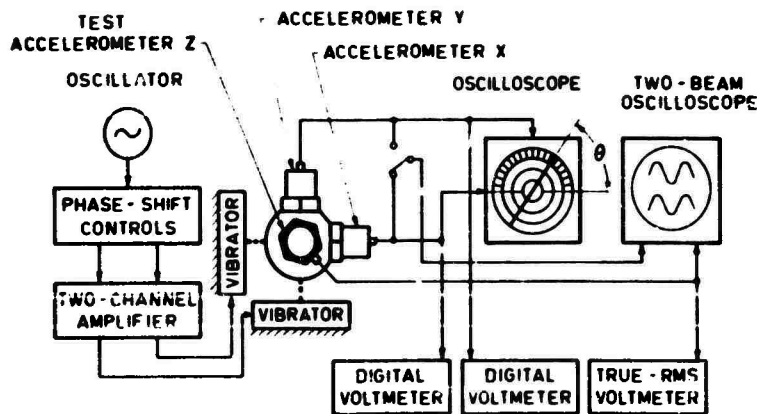


FIGURE 5 Block Diagram of System

excitation of the X and Y accelerometers themselves and of their offset  $\delta L$  from the xy plane (Fig.3) are discussed in a later section.

The outputs  $E_x$  and  $E_y$  of the two monitoring accelerometers are applied to the 'X' and 'Y' plates respectively of an oscilloscope, thus A and  $\theta$  can be measured by using the circles and lines of a polar scale fitted over the oscilloscope screen (Fig.5).

With the test and monitoring accelerometers in position, the resonance frequency can be adjusted to near the desired value by varying the clamping position of the bar. For fine adjustment a small 'tuning' mass in the form of a collar can be clamped at any position ( $L_1$ , Fig.3) between the driving collar and the monitoring accelerometers.

With the system as illustrated and the resonance frequency adjusted to 100 Hz the free length of the beam, ( $L_1$ ), is approximately 0.4 m.

#### CALIBRATION TECHNIQUES

With the test accelerometer in place, its orientation with respect to  $Ox$  (Fig.2(b)) is noted, making use of a suitable mark or feature on the accelerometer and using a protractor which fits over the top of the bar. The drive is applied, and while observing the oscilloscope screen the phase and amplitude of the driving signals are adjusted to produce on the screen a straight line of length representing the desired acceleration amplitude A and inclined nominally at the direction  $\theta$  as read from the polar scale.

The output  $E_z$  of the test accelerometer and the output  $E_x$  of the monitoring accelerometer X are displayed on a two-beam oscilloscope (Fig.5), from which is obtained the phase of  $E_z$  with reference to the positive direction of the applied transverse acceleration. When  $\theta$  is in the vicinity of 90 deg or 270 deg, and output  $E_x$  is consequently very small, output  $E_y$  may be substituted. The outputs  $E_x, E_y$  and  $E_z$  are also read from digital voltmeters. This

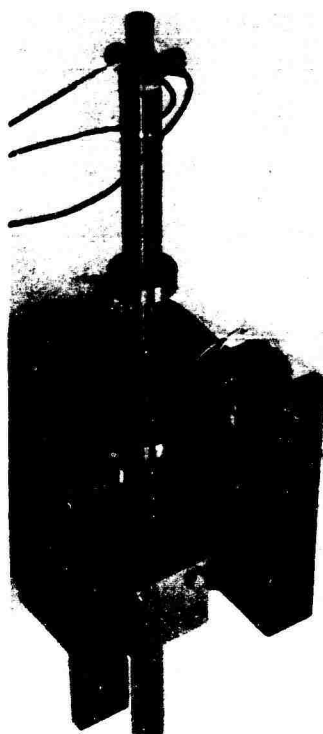


FIGURE 4 Prototype Calibrator  
Removed from Supporting Block

elliptic rather than rectilinear motion in the transverse plane.

The test accelerometer Z is mounted on the upper end surface of the beam with its sensitive axis coaxial with the beam. Also at the upper end are four flat ground surfaces, orthogonal to each other and to the flat end of the beam, on two of which are attached the monitoring accelerometers X and Y. These measure the transverse acceleration components  $A \cos \theta$  and  $A \sin \theta$  respectively. The effects of transverse

is repeated for say 10 deg increments of  $\theta$ , and finally corresponding values of TSR and  $\theta$  are calculated using the following equations:

$$\text{TSR} = E_z/S_z A \quad (1)$$

$$\theta = \arctan \frac{(E_y/S_y)}{(E_x/S_x)} \quad (2)$$

$$\text{where } A = \{(E_x/S_x)^2 + (E_y/S_y)^2\}^{1/2} \quad (3)$$

and  $S_x$ ,  $S_y$  and  $S_z$  are the axial sensitivities of the three accelerometers.

The convention adopted for Eq.(1) is that the sign of TSR is + or - when  $E_z$  is in-phase or anti-phase respectively, with respect to the applied transverse acceleration (see Fig.6(a), (b)). In applying Eq.(2),  $E_x$  is assigned + or - when it is in-phase or anti-phase respectively with respect to  $E_y$ . Two quadrants are sufficient when using this new technique.

The test data are conveniently reduced by using a simple computer program which can be made to yield tabulated and/or plotted results.

A more rapid check may be made by scanning through the range of  $\theta$ , while adjusting amplitude and phase to maintain a constant value of A, until a minimum value of  $E_z$  is found. The outputs  $E_x$  and  $E_y$  are read and the angle  $\theta(\text{TSRmin})$  calculated. TSRmax may then be found by increasing or decreasing  $\theta$  by 90 deg.

#### RANGE AND PERFORMANCE OF THE PROTOTYPE CALIBRATOR

The prototype was designed for calibrations at 100 Hz. With the free length  $L_1 = 0.4$  m and a test accelerometer of mass 40 gram, clamping the adjustable collar of mass 104 gram at different positions  $L_2$  along the beam, allowed the resonance frequency to be varied over the range 95 Hz to 103 Hz.

The total range of resonance frequency available with the prototype by varying  $L_1$  in the range 0.3 m to 0.6 m and  $L_2$  over its full range is 39 Hz to 155 Hz.

The maximum acceleration amplitude attainable at 100 Hz with the prototype as described is  $200 \text{ ms}^{-2}$ .

Two examples of calibration results are presented. In Fig.6(a) the full line shows TSR versus  $\theta$  for a relatively inexpensive accelerometer having a high value of TSRmax (13 per cent). For comparison the broken line shows the result obtained for an accelerometer of reference standard quality. As an indication of the resolution of the method, Fig.6(b) is a tracing of the computer printout for the latter.

#### DISCUSSION OF UNCERTAINTIES

##### Input Transverse Vibration

The motion of the point O at the free end

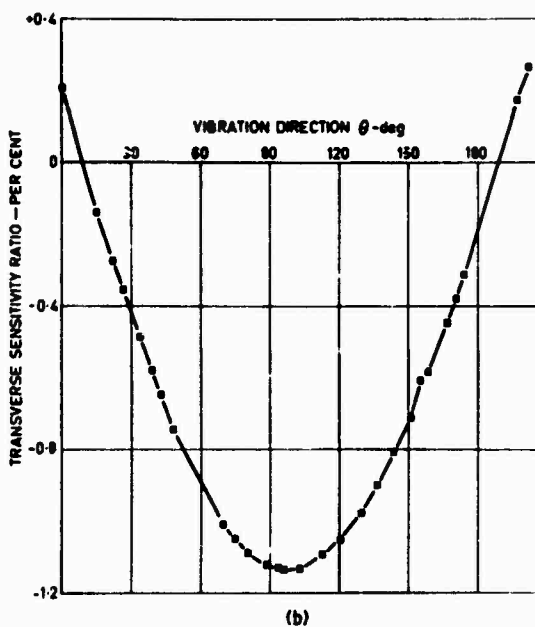
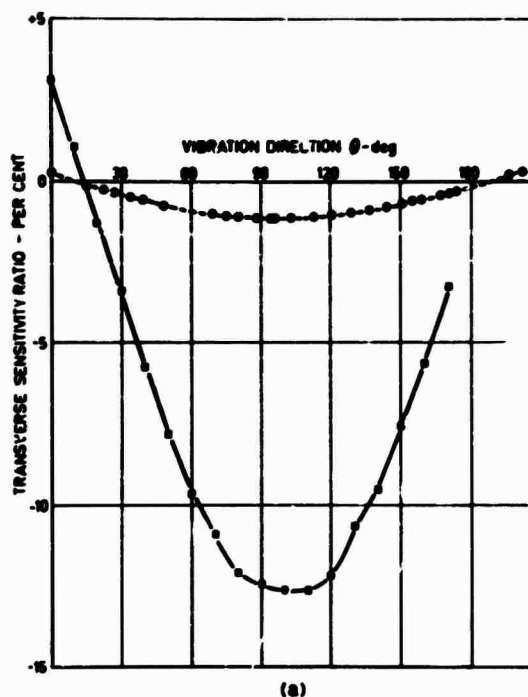


FIGURE 6 Typical Transverse Calibration Results

of the cantilever actually traces out a surface which is approximately spherical, rather than as idealized in the xy plane. The uncertainties

which arise from the consequent non-rectilinearity of the input transverse motion are discussed in the next section.

The X and Y accelerometers which are used to measure the transverse acceleration are themselves subjected to transverse excitation. Uncertainty from this source is discussed in detail in a later section.

The evaluation of A, Eq.(3), is influenced by uncertainties in  $E_x$ ,  $E_y$ ,  $S_x$  and  $S_y$ . To minimize these uncertainties the X and Y accelerometers are calibrated by comparison with a reference accelerometer, measuring the electrical output of each accelerometer with the same digital voltmeter that is used with it on the transverse calibrator. The absolute calibration of the voltmeters thereby becomes inconsequential.

The frequency  $f$  is easily measured to within 0.1 Hz, although a less precise value would be acceptable as the TSR is independent of frequency over a wide range [2, 3].

#### Angle

The evaluation of the direction  $\theta$  of the input transverse vibration is influenced by the uncertainties in  $E_x$ ,  $E_y$ ,  $S_x$  and  $S_y$  (Eq.(2)), which have been discussed above. The residual uncertainty from these sources is mostly attributable to random reading errors.

The polar scale on the oscilloscope is used for setting nominal values of  $\theta$ . If  $\theta$  is read directly from that scale the additional error does not exceed 2 deg.

Some further uncertainty is incurred in relating the test value of  $\theta$  (TSRmin) to a reference mark on the body of the test accelerometer.

The departure of the X or the Y accelerometer mounting face from squareness with the Z accelerometer mounting face, and the departure from mutual squareness between the X and Y mounting faces of the prototype cantilever beam are all less than two minutes of arc. The effects of these small discrepancies can be ignored.

#### Output of Test Accelerometer

Uncertainty in the measurement of the electrical output  $E_z$  resulting from the transverse input acceleration A is influenced by signal-to-noise ratio and by harmonic distortion, particularly from the second harmonic. For improved accuracy a true-rms voltmeter is used; this is explained later in the context of the discussion of non-rectilinearity of transverse acceleration.

To find the electrical output of the test accelerometer resulting from vibration of the same amplitude A and frequency  $f$  applied axially, the accelerometer is calibrated by comparison with the same reference accelerometer as used for

the determination of  $S_x$  and  $S_y$ , measuring the output with the same true-rms meter that is used in the transverse calibration. Only relative values of  $S_x$ ,  $S_y$  and  $S_z$  are required in calculating TSR from Eq.(1).

#### Overall Uncertainty

For an accelerometer with axial sensitivity of the order of 10 millivolts per g (where  $g = 9.8 \text{ ms}^{-2}$ ), and TSRmax of the order of one per cent, the uncertainty in TSRmax was estimated to be  $\pm 2$  per cent (of TSRmax), and  $\theta$  (TSRmin) was determined with an uncertainty of  $\pm 2$  deg, using the prototype calibrator with  $A \approx 200 \text{ ms}^{-2}$ .

#### Non-rectilinearity of Transverse Acceleration

The path of the test accelerometer is assumed to be a circular arc, as shown with greatly exaggerated curvature in Fig.7.

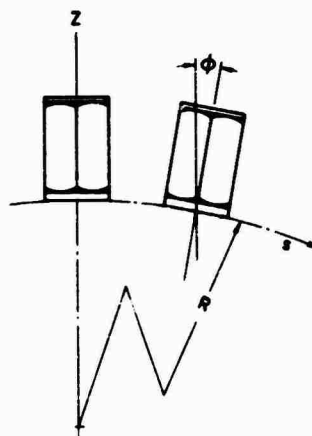


FIGURE 7 Non-rectilinearity of the Transverse Motion

Assuming the displacement(s) along the curved line to be represented by  $s = S \sin \omega t$  the tangential acceleration ( $a_t$ ) is given by

$$\begin{aligned} a_t &= -\omega^2 S \sin \omega t \\ &= A \sin \omega t \end{aligned}$$

The radial acceleration ( $a_r$ ) acting along the sensitive axis of the test accelerometer is given by

$$\begin{aligned} a_r &= (\omega S \cos \omega t)^2 / R \\ &= \omega^2 S^2 (\cos 2\omega t + 1) / 2R \end{aligned}$$

where R is the radius of curvature of the path.

The ratio of radial to tangential oscillatory acceleration amplitude is therefore  $S/2R$ .

If the deflected form of the beam is

assumed to be that of a uniformly loaded cantilever of length  $L_1$  then, at maximum displacement  $S$ ,  $R$  can be shown to equal  $3L_1/4$ . On the prototype, the value of  $R$  was  $0.73 L_1$ , the difference being attributed to the non-uniform loading and the method of driving.

As an example, in a transverse calibration at  $f = 100$  Hz, with  $A = 200 \text{ ms}^{-2}$ ,  $S \approx 5 \times 10^{-4} \text{ m}$ . If  $L_1$  is  $0.4 \text{ m}$ , then  $S/2R \approx 0.0008$ . That is, the oscillatory component of  $a_r$  has a peak value which is 0.08 per cent of  $A$ , and is of frequency  $2f = 200$  Hz. This is negligibly small in comparison with the one per cent limit specified in the American Standard [2].

This effect may be measured directly if  $\theta(\text{TSRmin})$  is first found; with this direction of transverse excitation,  $E_z$  has the dominant component at frequency  $2f$ , as well as random noise, which condition is easily checked on the second oscilloscope screen (Fig.5). If the test accelerometer output is measured throughout the calibration using a true-rms meter, then all  $E_z$  readings can be corrected for these unwanted components, thus improving accuracy.

The axes of the X and Y accelerometers are displaced a small distance  $\delta L$  below the mounting surface of the Z accelerometer (Fig.3). In the prototype  $\delta L = 8.7 \text{ mm}$ , thus the correction factor to be applied to  $A$  as found from Eq.(3) is 1.030, for  $R = 0.302 \text{ m}$ . This factor, the ratio of the transverse vibration amplitude at the Z mounting surface to the amplitude at the junction of the O<sub>x</sub> axis and the X mounting surface, has been determined from direct measurement on the prototype, using an image-shearing microscope. The uncertainty in the determination does not exceed 0.5 per cent.

An end fixture could be designed to make  $\delta L = 0$ , but this would involve increasing the distance of the X and Y mounting faces from the beam axis, which is undesirable.

Curvature of the path also produces an unwanted tangential component due to tilting of the axis of the accelerometer in the earth's gravitational field, but this effect is negligible: in the example  $\phi = S/R \approx 0.0016$  (Fig.7), hence the tangential component from this source is about  $0.016 \text{ ms}^{-2}$ , i.e. 0.008 per cent of  $a_r$ . Likewise the change  $(1 - \cos\phi)$  in the radial acceleration is negligible.

#### Transverse Excitation of the X and Y Accelerometers

With the test accelerometer subjected to a transverse simple harmonic motion represented by the vector  $\vec{A}(\theta)$  in the  $xy$  plane in Fig.3, ideal X and Y accelerometers would have output voltages proportional to  $A \cos\theta$  and  $A \sin\theta$  respectively (see Fig.8). Because the actual X and Y accelerometers do have some transverse sensitivity the outputs are respectively:

$$E_X = A S_X (\cos\theta + \text{TSR}_X \sin\theta) \sin\omega t$$

$$E_Y = A S_Y (\sin\theta + \text{TSR}_Y \cos\theta) \sin\omega t$$

where  $\text{TSR}_X$ ,  $\text{TSR}_Y$ , the transverse sensitivities of the X and Y accelerometers respectively in the  $xy$  plane, may have either + or - sign depending on accelerometer orientation.

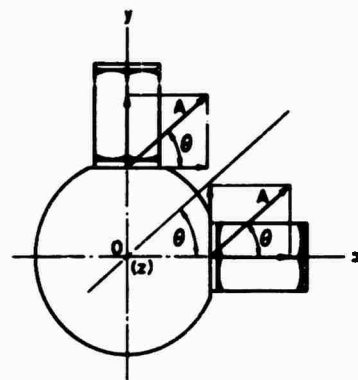


FIGURE 8 Transverse Excitation of Monitoring Accelerometers

If the sign and magnitude of  $\text{TSR}_X$  and  $\text{TSR}_Y$  are known, a correction may be applied when calculating  $A$  and  $\theta$ . For the case where  $S_X = S_Y$  and  $|\text{TSR}_X| = |\text{TSR}_Y| = 0.01$ , the correction to  $A$  is  $\leq 1.0$  per cent, and to  $\theta \leq 0.6$  deg.

Alternatively the X and Y accelerometers may be selected for low  $\text{TSRmax}$  ( $\leq 2$  per cent) and oriented so that their  $\theta(\text{TSRmin})$  directions lie as nearly as practicable in the  $xy$  plane. If they are aligned in this way to within, say,  $\pm 6$  deg, it may be shown that the error due to transverse sensitivity in calculating  $A$  does not exceed 0.2 per cent, and the error in calculating  $\theta$  does not exceed 0.1 deg. This assumes that for each accelerometer  $\text{TSRmin} = 0$ . The signs of  $\text{TSR}_X$  and  $\text{TSR}_Y$  are indeterminate in this case, hence these remaining systematic errors must be treated as further sources of uncertainty.

The effect of radial acceleration  $a_r$  on the X and Y accelerometers is negligible.

#### CONCLUDING REMARKS

A new method of transverse calibration has been presented which allows the transverse response properties of an accelerometer to be evaluated without the resetting of the accelerometer or its mounting fixture that is necessary in methods normally used. Experience to date in using the prototype to calibrate various piezoelectric accelerometers indicates the new method to be accurate, sensitive and easily applied.

When transverse calibration is done

directly on an electrodynamic vibrator, unwanted transverse motion of the vibrator drive may introduce some difficulty: with the new method there is also an unwanted component of motion but this is of small magnitude and is identifiable and measurable as second harmonic of the transverse calibration frequency.

A modification of the calibrator that would appear to be desirable is to mount the monitoring accelerometers on a rotatable fixture so that the transverse acceleration in any direction is measured with an accelerometer aligned in that direction and hence not subjected to transverse excitation. After making tests with such an arrangement it was decided to adopt the simpler design and procedure described in the paper.

Further developments in progress will provide improved clamping of the beam and will extend the frequency range. Obviously, higher resonance frequencies can be attained by changing the length, material and cross section of the beam. Another and more interesting possibility is to operate a cantilever beam at resonance in its higher modes. Preliminary observations with the prototype system driven at its resonance frequency (600 Hz) in its second flexural mode have confirmed that the range can be extended in this manner.

#### REFERENCES

1. American Standards Association, American Standard Methods for the Calibration of Shock and Vibration Pickups, S2.2-1959, (Section 2.8 Transverse Sensitivity Ratio).
2. American National Standards Institute Inc., American National Standard for the Selection of Calibrations and Tests for Electrical Transducers used for Measuring Shock and Vibration, ANSI S2.11-1969, (Section 7.8 Transverse Sensitivity Calibration).
3. D.W. Rockwell and J.D. Ramboz, "Measurement of Accelerometer Transverse Sensitivity", Shock and Vib. Bull., Vol. 35, Pt. 4, pp.73-97, 1966.
4. J.D. Ramboz, "A Proposed Method for the Measurement of Vibration Transducer Transverse Sensitivity Ratio", Instrum. Soc. Am. Trans., Vol. 7, pp.231-236, 1968.
5. T.D. Finley, "A Comparison Method to Measure Accelerometer Transverse Sensitivity", Adv. Instrum., Vol. 24, Pt. 4, Paper 69-666 (Instrum.Soc.Am.),1969.
6. C.M. Harris and C.E. Crede, Shock and Vibration Handbook, (McGraw-Hill, New York), Vol. 1, Ch. 12, p.19, 1961.